nagra.

Arbeitsbericht NAB 16-18

FEBEX-DP

Concrete ageing, concrete/bentonite and concrete/rock interaction analysis

March 2017

M.J. Turrero & V. Cloet (eds.)

National Cooperative
for the Disposal of
Radioactive Waste

Hardstrasse 73
P.O. Box 280
5430 Wettingen
Switzerland
Tel. +41 56 437 11 11

www.nagra.ch

nagra.

Arbeitsbericht NAB 16-18

FEBEX-DP

Concrete ageing, concrete/bentonite and concrete/rock interaction analysis

March 2017

M.J. Turrero & V. Cloet (eds.)

KEYWORDS

OPC-concrete, ageing, bentonite, concrete/bentonite interaction, concrete/granite interaction, Grimsel Test Site

National Cooperative
for the Disposal of
Radioactive Waste

Hardstrasse 73
P.O. Box 280
5430 Wettingen
Switzerland
Tel. +41 56 437 11 11

www.nagra.ch

Nagra Arbeitsberichte ("Working Reports") present the results of work in progress that have not necessarily been subject to a comprehensive review. They are intended to provide rapid dissemination of current information.

Authors

J. Cuevas, A.I. Ruiz, A. Ortega, R. Fernández, D. González-Santamaría and M. Angulo
Autonomous University of Madrid (UAM), Madrid, Spain

"Concrete analysis (C-C-34 core samples)"
"Concrete/bentonite interface analysis (C-C-34-xx, BC-C-35-xx and BC-S-35-xx samples)"

S. Kaufhold, R. Dohrmann and K. Ufer
Federal Institute for Geosciences and Natural Resources (BGR), Hannover, Germany

"FEBEX experiment – Cement/bentonite interface".

S. Miyoshi and M. Fukaya
Obayashi, Tokyo, Japan

"The quantitative approach for the chemical alteration of the interface between bentonite and concrete in FEBEX-DP".

T. Hitomi and M. Uyama
Obayashi, Tokyo, Japan

"Observation of concrete/rock interface using integrated XRD-CT method".

C.F. Jove-Colon[1], L. Zheng[2], M. Voltolini[2] and J. Birkholzer[2]
[1]Sandia National Laboratory, California, USA
[2]Lawrence Berkeley National Laboratory
"Characterisation of the microscopic structure of the concrete/bentonite overcore C-C-32-6-OC using X-ray CT Imaging, SEM/EDS analysis and micro-X-ray Fluorescence".

M.C. Alonso and J.L. García Calvo
Spanish National Research Council (CSIC-IETcc), Madrid, Spain

"Post-mortem analysis of concrete ageing. Identification of the ageing of the concrete plug at micro and macro level, exposed to the in situ conditions of the Grimsel Test Site".

M.J. Turrero, E. Torres, A. Garralón, P. Gómez, L. Sánchez and R. Campos
Spanish Research Centre for Energy Environment and Technology (Ciemat), Madrid, Spain

"In-situ FEBEX test: Post-mortem characterisation of the concrete/bentonite interface after 13 years of interaction from samples C-C-34-xx, BC-C-35-xx and BC-S-35-xx."

U. Mäder and A. Jenni
University of Bern, Bern, Switzerland

Macroscopic observations on the shotcrete plug/Heterogeneity and textures in the shotcrete plug at the macroscopic scale

V. Cloet
Nagra, Switzerland

This document presents a compilation-synthesis report on the post-mortem characterisation of the concrete plug, concrete/bentonite interface and concrete/rock interface of the FEBEX in-situ test after 13 years of operation. The report is an integrated work based on the individual contributions of 7 Research Institutions and Universities. The authors and individual contributions are those referenced above.

Table of Contents

List of Tables

List of Figures

1 Introduction

This report synthetizes the outcomes of the studies on the concrete, concrete/bentonite and concrete/granite samples, coming from the dismantling of the in-situ full-scale FEBEX experiment at the Grimsel Test Site (Switzerland). Contributions have been submitted by the Autonomous University of Madrid (UAM, Spain), the Federal Institute for Geosciences and Natural Resources (BGR, Germany), Obayashi (Japan), Sandia National Laboratory (U.S. Department of Energy, USA), the Spanish National Research Council (Eduardo Torroja Institute, CSIC-IETcc, Spain), the Spanish Research Centre for Energy, Environment and Technology (Ciemat, Spain) and the University of Bern (Switzerland).

After the introduction, which contains the description of the FEBEX project, the construction of the concrete plug and objectives of the report, three main chapters detail the main findings of the above-mentioned investigations.

1.1 The FEBEX Project

FEBEX (Full-scale Engineered Barrier Experiment in Crystalline Host Rock) is a research and demonstration project that was initiated by ENRESA (Spain).

The aim of the project is to study the behaviour of near-field components in a repository for high-level radioactive waste in granite formations. The main objectives of the project may be grouped in two areas:

a) Demonstration of the feasibility of constructing the engineered barrier system in a horizontal configuration according to the Spanish concept for deep geological storage (AGP), and analysis of the technical problems to be solved for this type of disposal method.

b) Better understanding of the thermo-hydro-mechanical (THM) and thermo-hydro-geochemical (THG) processes in the near field, and development and validation of the modelling tools required for interpretation and prediction of the evolution of such processes.

The project consists of two large-scale tests (see Fig. 1) — “in situ” and “mock-up” (the latter is managed by Ciemat in Spain) —, a series of laboratory tests, and THM and THG modelling tasks.

The full-scale heating test (“in-situ” test), to which this document refers, was performed at the Grimsel underground laboratory in Switzerland, also known as Grimsel Test Site (GTS) or Felslabor Grimsel (FLG in German). A complete description of the FEBEX project objectives and test program may be found in Fuentes-Cantillana et al. (1998).

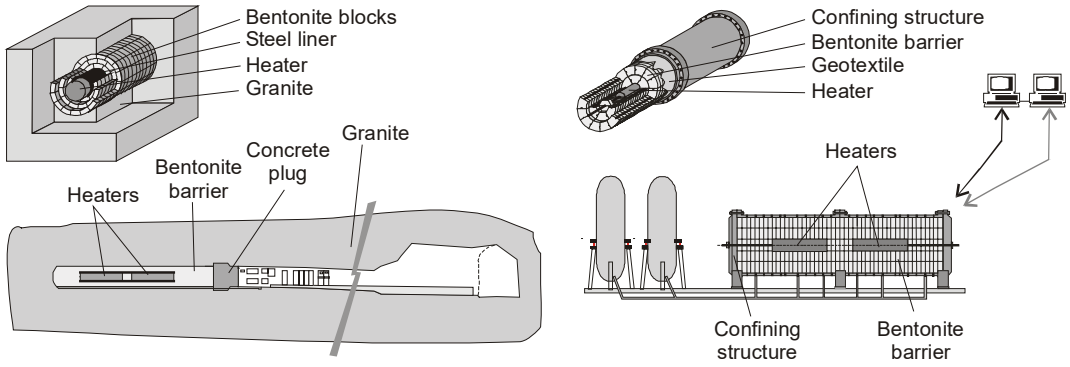

Fig. 1: Overall layout of FEBEX "in-situ" test (left) and "mock-up" test (right)

The project started in 1994 and has been supported by the European Commission through consecutive contracts, identified as FEBEX I (contract nº FI4W-CT-95-0006) for the period January 1996 to June 1999, and FEBEX II (contract nº FIKW-CT-2000-00016), from September 2000 to December 2004. Afterwards, NF-PRO took place from January 2005 to December 2007. Finally, in January 2008 the "in-situ" test was transferred from ENRESA to a consortium composed by SKB (Sweden), POSIVA (Finland), Ciemat (Spain), NAGRA (Switzerland) and more recently KAERI (South Korea), the FEBEXe Consortium, which supports it currently.

The dismantling of the "in-situ" experiment was carried out in 2015. New partners, interested in taking part in the planned sampling and analysis operations, were incorporated into the Consortium (now called FEBEX-DP), namely US DOE (USA), Obayashi (Japan), RWM (UK), ANDRA (France), BGR (Germany) and SURAO (Check Republic).

1.2 Test configuration during FEBEX I

The installation of the "in-situ" test was carried out at the GTS. A horizontal drift with a diameter of 2.28 m was excavated in the Grimsel granodiorite especially for this experiment using a TBM (a tunnel boring machine). Two electrical heaters, of the same size and of a similar weight as the reference canisters, were placed in the axis of the drift. The gap between the heaters and the rock was backfilled with compacted bentonite blocks, up to a length of 17.40 m, requiring a total of 115'716 kg of bentonite. The backfilled area was sealed with a plain concrete plug placed into a recess excavated in the rock with a length of 2.70 m and a volume of 17.8 m^3. Fig. 2 shows the dimensions and layout of the test components schematically.

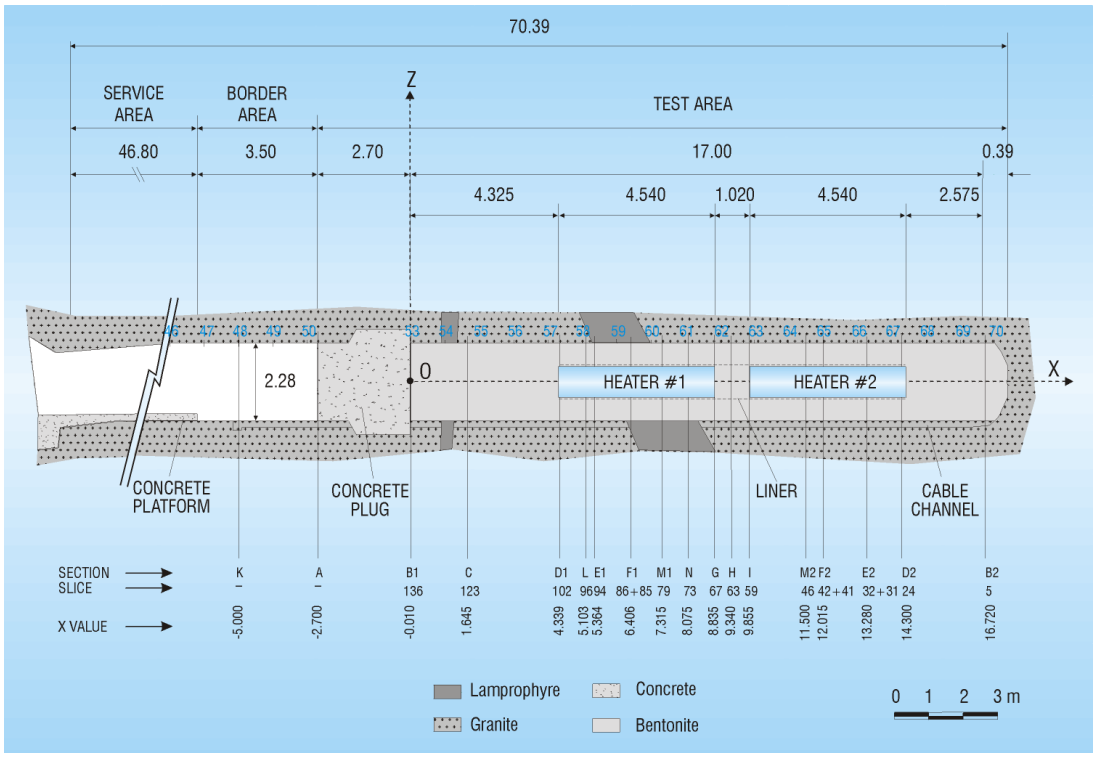

Fig. 2: General layout of the FEBEX "in-situ" test (FEBEX I configuration)

A total of 632 instruments were placed in the system along a number of instrumented sections, both in the bentonite buffer and in the host rock, to monitor relevant parameters such as temperature, humidity, total and pore pressure, displacements, etc. The instruments were of many different kinds and their characteristics and positions are fully described in Fuentes-Cantillana & García-Siñeriz (1998).

A Data Acquisition and Control System (DACS) located in the service area of the FEBEX drift collected the data provided by the instruments. This system recorded and stored information from the sensors and also controlled the power applied to the electrical heaters, in order to maintain a constant temperature at the heaters/bentonite interface. The DACS allowed the experiment to be run in an automated mode, with remote supervision from Madrid. Data stored at the local DACS were periodically downloaded in Madrid and used to build the experimental Master Data Base.

The construction of the concrete plug was completed in October 1996, and the heating operation started on 28 February 1997. A constant temperature of 100 °C was maintained at the heaters/bentonite interface, while the bentonite buffer slowly hydrated with the water naturally seeping from the rock. A complete report that includes both the installation of the test and the results gathered after two years of operation is given in Fuentes-Cantillana et al. 2000.

1.3 Dismantling of heater 1 and test configuration afterwards (FEBEX II)

A partial dismantling of the FEBEX "in-situ" test was carried out during the summer of 2002, after 5 years of continuous heating. The operation included the demolition of the concrete plug, the removal of the test section corresponding to the first heater, and the sealing with a new

shotcrete plug. A large number of samples from all types of materials were taken for analysis. A number of instruments were subsequently dismantled, as well as a few new ones installed. Accordingly, system design was adapted, and the physical layout was changed in order to ease the partial dismantling operation.

The buffer and all components were removed up to a distance of 2 metres from heater #2 to minimize disturbance of the non-dismantled area. A dummy steel cylinder with a length of 1 m was inserted in the void left by heater #1 in the centre of the buffer. Some new sensors were installed in that one additional metre of bentonite buffer.

Additional sensors were introduced in boreholes drilled in the buffer parallel to the drift. To simplify this operation, the new concrete plug was constructed in two phases: an initial temporary plug measuring just 1 m in length, which was built immediately after dismantling, and a second section to complete the plug length to the 3 m planned in the design of the experiment. Unlike FEBEX I, the new plug was a parallel plug, without a recess excavated in the rock, constructed by shotcreting (more details in section 1.5).

The description of the partial dismantling operation is given by Bárcena et al. 2003. The configuration of the test, after completing the partial dismantling operation and construction of the full plug length, is shown in Fig. 3.

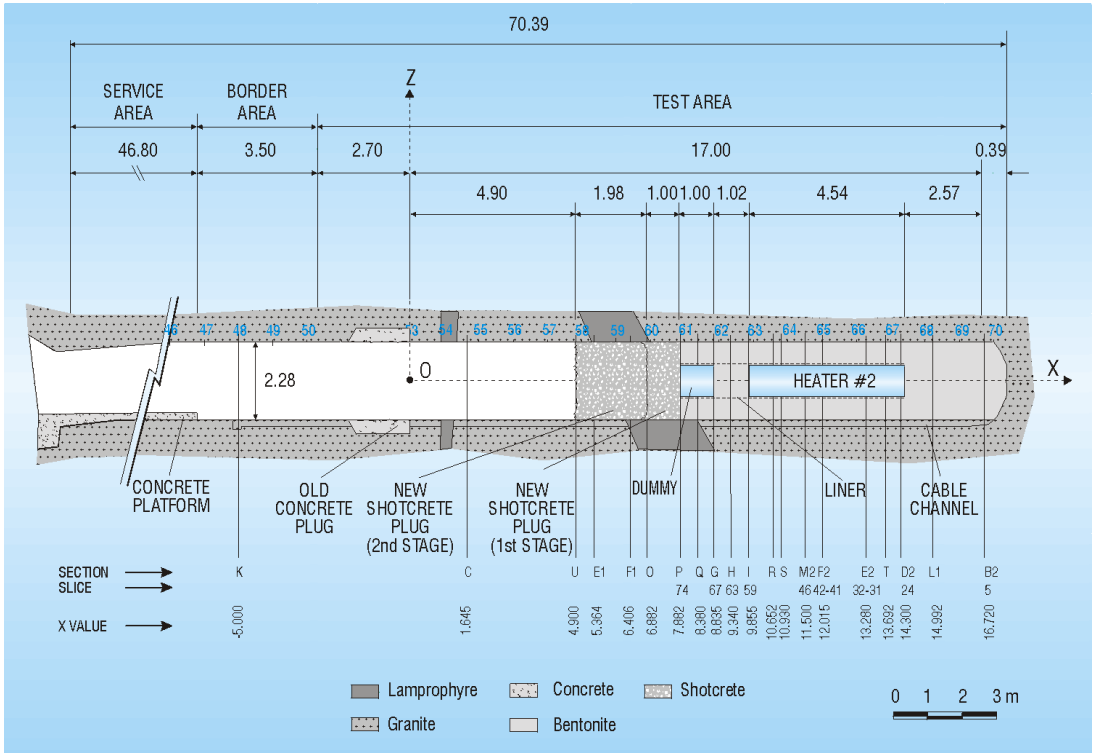

Fig. 3: Status of the FEBEX "in-situ" test after the partial dismantling (FEBEX II configuration)

A more complete report that describes the test from the conception up to two years of operation after the partial dismantling is given in Huertas et al. (2006).

1.4 Concept of the dismantling of heater #2

The objective of the second dismantling operation, carried out throughout 2015, was to dismantle all the remaining parts of the "in-situ" test, including heater #2. This operation includes carrying out a complete sampling of the bentonite, rock, relevant interfaces, sensors, metallic components and tracers allowing the analysis of the barriers' condition after 18 years of heating and natural hydration.

Analytical results will be compared with data obtained from the partial dismantling (Huertas et al. 2006); the monitoring data (Martinez et al. 2016) as well as with the results derived from modelling efforts (Lanyon & Gaus 2013). The results are expected to increase the current knowledge and confidence for the FEBEX-DP partners in bentonite performance with a focus on thermo-hydro-mechanical (THM) and thermo-hydro-chemical (THC) processes as well as on corrosion and microbial activity. The reporting of the laboratory analysis and dismantling results is expected to be complete by the end of 2017 with a final integrated report issued in early 2018.

All details about the planned dismantling operation and sampling program are given in Bárcena & García-Siñeriz (2015a), Bárcena & García-Siñeriz (2015b) and Rey et al. (2015).

All sample logs of the dismantling operation are documented in Abós and Martínez (2015).

1.5 The concrete plug in the FEBEX II configuration

Cementitious materials will be used in fracture grouts, tunnel plugs and backfills in many of the design concepts of geological repositories for radioactive waste. The use of these materials requires understanding the interaction with other components of the repository, e.g. buffer material and host rock, in terms of degradation, new phases formation, changes in porosity, transport properties, etc. In this sense, one point of interest of the FEBEX test is providing data from the investigations on the concrete plug used to seal the experiment and and on its interaction with the bentonite buffer and the surrounding rock.

The concrete plug used for the confinement of the buffer after the first dismantling was designed as a parallel plug (Fig. 4), without anchors in the rock, constructed by the shotcreting technique. The plug was constructed in two stages: a first section (known as Section 1) with a thickness of one metre and a second one of two metres (known as Section 2), giving a total length of 3 metres. A picture of the final appearance of the plug is presented in Fig. 5. Details of the operations for constructing the plug are given in Huertas et al. (2006) and some succinct details about its main characteristics are summarised below.

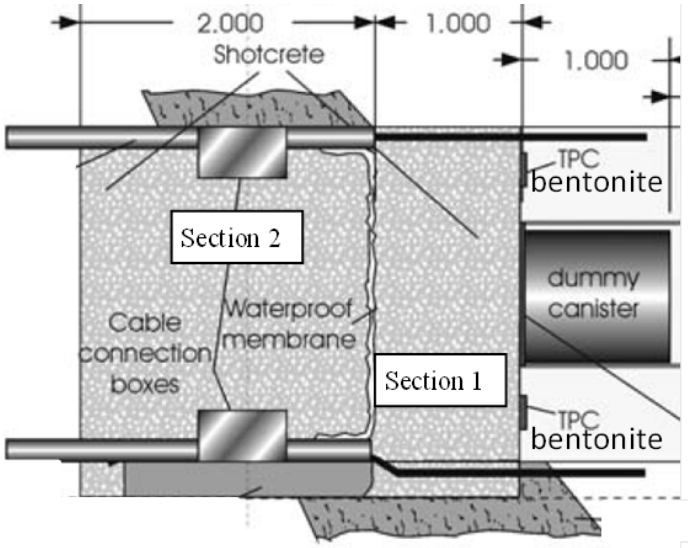

Fig. 4: Design of the concrete plug (shotcreting technique) used for the confinement after the first dismantling (from Huertas et al. 2006).

Fig. 5: Final appearance of the plug with the sensors installed (from Huertas et al 2006).

The first section was constructed in July 2002 with the concrete formulation given in Tab. 1-1. This section served as a temporary plug while new instruments were installed (e.g. cable pipes) after the first dismantling. The concrete was applied using a wet shotcreting pump located at the entrance of the FEBEX area. The first batch of fresh concrete delivered at the site had too high a w/c ratio (0.6) and was inadequate for shotcreting; only a thin shotcreted concrete layer of about 2 cm could be made with this material. The batch was changed to that shown in Tab. 1-1, with a w/c ratio 0.4, and the other layers were constructed. The final configuration of the plug was four concrete layers of 2, 39, 25 and 30 cm, given a total average thickness of 96 cm. Due to abovementioned technical problems the final result had some degree of heterogeneity, discussed further in Chapter 6.1 on macroscopic observations. A quality control was made after 28 days of

hardening. Cores were drilled and mean strength values of 32 MPa and mean permeability values of 4.3E-11 m/s were measured (Huertas et al 2006).

Tab. 1-1: Concrete formulation in the first plug section (from Huertas et al. 2006)

CEM II A-L 32,5 R	430 kg/m3
Nanosilica MEYCO MS 660	30 kg/m3
Steel fibres Dromix ZP 306	50 kg/m3
Polypropylene fibres	800 g/m3
Superplasticiser GLENIUM T803	1.5%
w/c	0.40
Aggregate 0-8 mm	1700 kg/m3
Curing compound MEYCO TCC 735	1%
Accelerant MEYCO SA 160 E	6%

The construction of the second section was made in June 2003 with the concrete formulation indicated in Tab. 1-2. An important difference with the first section is the absence of steel and polypropylene fibres. A layer of approximately 3-4 cm of MASTERSEAL X345 was first applied on top of the existing temporary plug. This material is a sprayable polymer product especially developed for the impermeabilisation of shotcrete lined tunnels, and should improve the water and gas tightness of the test. Then, the concrete was applied in five layers of 43, 67, 30, 30 and 30 cm, giving a total thickness of 2 m. The construction process was efficient and the final concrete section exhibited a very good uniformity. The quality control of this section showed mean strength values of 39.66 MPa and mean permeability values of 9.4E-11 m/s (Huertas et al 2006).

Tab. 1-2: Concrete formulation in the second plug section (from Huertas et al. 2006)

CEM II A-L 32,5 R	475 Kg/m^3
Nanosilica MEYCO MS 660	60 Kg/m^3
Superplasticiser GLENIUM T803	1.5%
W/C	0.46
Aggregate 0-8 mm	1700 Kg/m^3
Curing compound MEYCO TCC 735	1%
Accelerant MEYCO SA 160 E	6%

2 Objectives and contents

The current report presents all results of the post-mortem analysis carried out to check the physical, physico-chemical, mineralogical, chemical and textural changes of the concrete plug of the FEBEX in-situ experiment after 13 years of operation since the first dismantling operation. The report aims at documenting the full set of results obtained by all research partners. A synthesis of all results, including modelling and other lab tests will not be presented in this report, but will be presented in a future synthesis report and/or in peer-reviewed articles. This report documents the investigations of the changes that occurred in the concrete through the interaction with granite and bentonite, and vice-versa, the changes that occurred in the bentonite and the granite through the interaction with the concrete.

Chapters 1 and 2 address the introduction to the FEBEX-DP experiment and the objectives, respectively. Chapter 3 offers a description of the materials studied, including the main work made on them, while Chapter 4 gives a brief relation of the analytical techniques used. Chapter 5 investigates concrete ageing, by analysing the mechanical properties, pH, porosity, carbonation and microstructure. Chapter 6 is dedicated to studying the concrete/bentonite interface, analysing physical properties of both materials from millimetre to centimetre scale, as well as their chemistry, physico-chemistry and mineralogy and to investigating the effects of the interaction between them. Chapter 7 concludes this report with the main results. The results from the granite-concrete interactions are presented in Appendix A. The Appendices B and C contain supporting information such as specific details of some methods and tables with results.

3 Samples

This chapter describes the samples and analytical techniques used for the investigations on concrete ageing and alteration due to the interaction of concrete with other materials, either bentonite or granite. More specifically it looks at these phenomena after 13 years of operation following the first dismantling and installation of the plug in 2002 (Bárcena et al. 2003 and Huertas et al. 2006).

The systematic sampling strategy for the concrete plug was oriented to achieve a good coverage of the whole plug and the interface with different materials. Reports by Bárcena & García-Siñeriz (2015a, b) and Rey et al. (2015) contain all details of the planned dismantling operation and sampling program. Abós & Martínez (2015) document all sample logs of the dismantling operation. García-Siñeriz et al. (2016) collect further details on the activities carried out and the main results gathered during the dismantling.

The concrete plug starts in section 32[1] and ends in section 35 (Fig. 6) (García-Siñeriz et al. 2016). Section 34 is in between both, starting where the water proof membrane was located separating the two plug construction sections (see chapter 2.4). Following Fig. 6, sections 32 to 34 are mentioned in the report as dismantling plan sections, and sections 1 and 2 are referred as plug construction sections, in order to avoid misunderstandings reading the document.

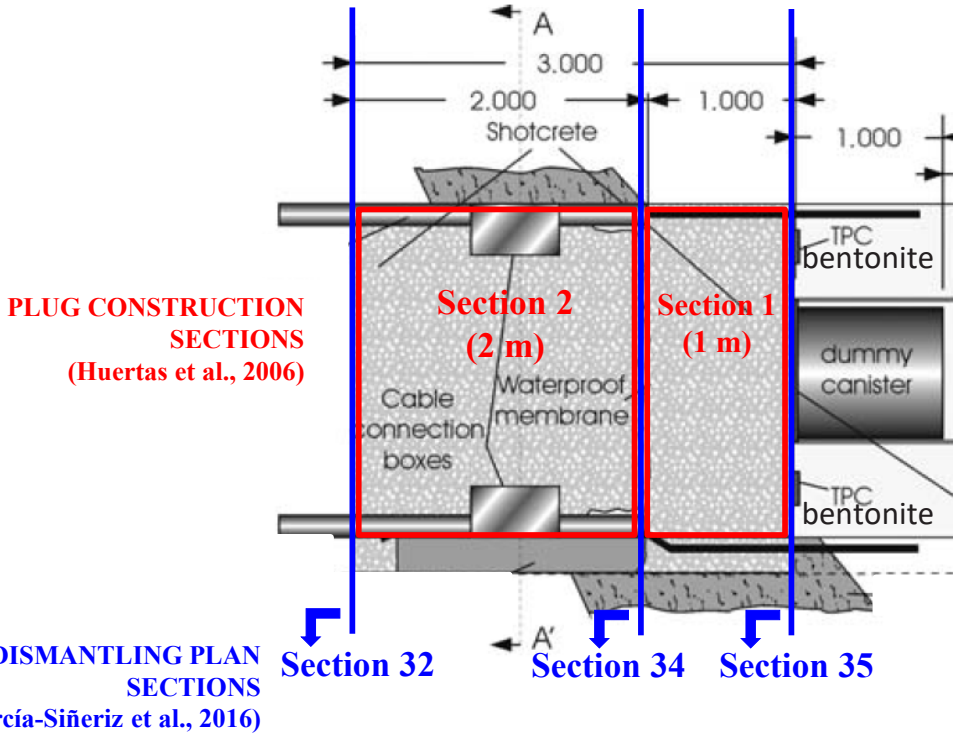

Fig. 6: Sampling layout of the plug (modified from García-Siñeriz et al. 2016) showing the dismantling plan sections and the plug construction sections.

[1] *Dismatling sections* as described and numbered in the dismantling plan (García-Siñeriz et al. 2016) should not be confused with the *construction sections* as can be seen in Figure 6.

Concrete and concrete/bentonite interface samples were taken from section 32 (long cores C-C-32-1 to 3 and overcores C-C-32-4 to 6), section 34 (cores C-C-34-4 to 11) and section 35 (short cores to have additional samples of the concrete/bentonite interface and hand-picked samples taken with the same objective). Parts 3.1 and 3.2 of this chapter provide further details on that. Bárcena & García-Siñeriz (2015b) describe the guidelines for naming the cores in a systematic way; for example for the drill cores C-C-32-1, C-C-32-4-OC, BC-S-35-2, CG-C-32-5-OB and B-B-36-7:

- First letter: C = concrete, BC = bentonite/concrete, CG = concrete/granite, B = bentonite,
- Second letter: C = core, S = slice, B = block
- First number: Section in the dismantling plan (e.g. section 32, 34, 35 or 36)
- Second number: Sample number (e.g. the first, second, third, ….. sample of this type)
- The addition "OC" (or "OB") indicates an overcored drill core to obtain concrete/bentonite (or concrete/rock interfaces).

3.1 Concrete samples

Concrete can deteriorate through the interaction with surrounding materials; in the case of the FEBEX test those are the Grimsel granite and the FEBEX bentonite. As a result of the chemical interactions between both materials, the physical and/or mechanical properties of the concrete will change. For example, the infiltration of ions as sulphates or chlorides from the bentonite to the concrete will cause new minerals to be formed, which could influence the transport properties of the concrete. Therefore, dilute water from the Grimsel granite can provoke the leaching of alkalis and the dissolution of portlandite. CSIC-IETcc was in charge of studying specific aspects of the concrete plug that can serve to evaluate its performance after 13 years of interaction with the surrounding materials. CSIC focused on the analysis of the mechanical strength, porosity, hydraulic conductivity, capillary suction capacity and physico-chemistry of a number of samples coming from both plug construction sections. CSIC also investigated carbonation, soluble salt migration and solid phase alteration in the plug construction section 1. Additional carbonation and mineralogical analyses were carried out by UAM on samples CC-34-4 to CC-34-11, these results are discussed together with the other samples from section 34 (Chapter 6).

Physical and physico-chemical characterisation of the concrete plug was addressed by CSIC by analysing 3 cores (C-C-32-1, 2 and 3) drilled from section 32 between 17 and 20 February 2015. Fig. 7A shows the location of the cores.

The three cores go through the two plug construction sections (Fig. 7B) having an outer diameter of 78 mm and a total length between 2.91 – 2.99 m, of which the first 2.70 to 2.80 m were drilled in wet conditions whereas the last 10 to 20 cm, close to the bentonite buffer, were drilled under dry conditions.

Cores C-C-32-1 and 3 were ≈ 20 cm far from the granite wall and the end of the cores almost form the contact with the bentonite face. During dry drilling of the last centimetres of core C-C-32-3 a constant backflow of water occurred. However, the backflow of water stopped 24h after ending the drilling (García-Siñeriz et al. 2016). Core C-C-32-2 is 10 cm down the central gallery axis and the end of the core is at the contact of the plug with the dummy. García-Siñeriz et al. (2016) collect specific details on drilling, samples and preservation.

The distribution of cores C-C-32-1 to 3 covers the following scenarios:

(a) Influence of the granite groundwater on the concrete performance by studying the complete C-C-32-1 and 3 cores.

(b) Influence of the bentonite pore water on the concrete by studying the fragments of concrete closest to the bentonite in the plug section 1 of cores C-C-32-1 and 3.

(c) Study of a concrete apparently not influenced by the granite groundwater or by the bentonite pore water, which is core C-C-32-2, drilled in the middle of the plug. That core is "far" from the granite and is not directly contacting the bentonite, that is why CSIC considered it as reference material to check alteration in the other two.

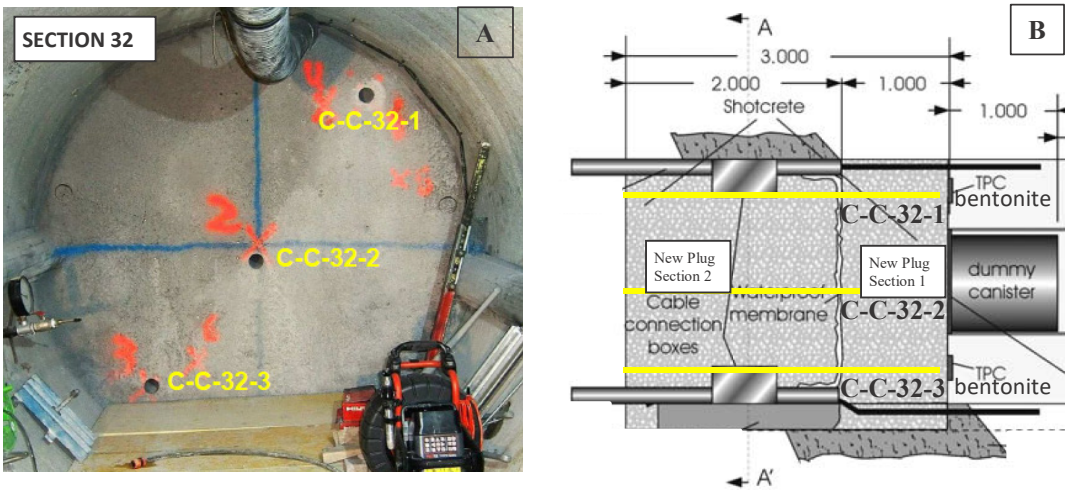

Fig. 7: A. Picture of section 32 with the position of the C-C-32-1 to 3 long cores going through the two plug construction sections. B. The cross-section shows the approximate location of the cores with respect to the granite wall, the bentonite and the dummy.

A set of subsamples of each core (example in Fig. 8) was used to analyse the concrete at macro- and microscale to evaluate its performance. Appendix B provides details about subsamples (part B.1, Tab. B-1 to B-3).

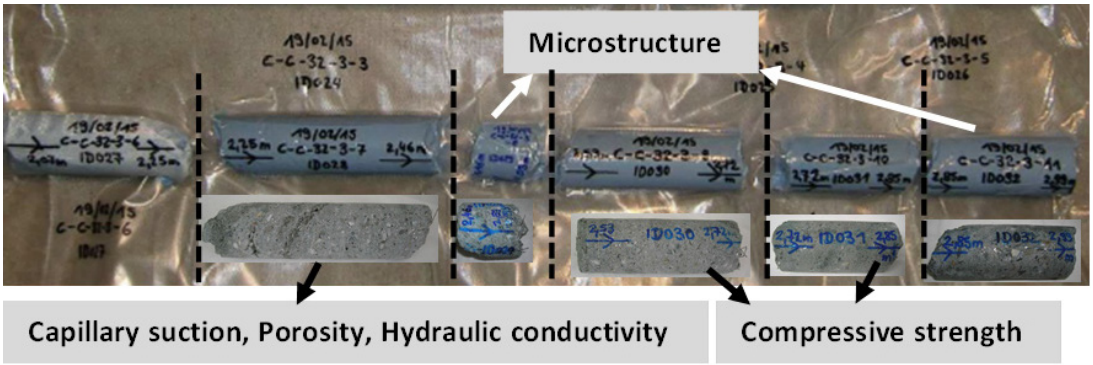

Fig. 8: Example of subsampling core C-C-32-3 (2.07-2.93 m) to cover the analyses planned by the CSIC.

3.2 Concrete/bentonite interface

Partners involved in the study of the concrete/bentonite interface were BGR, Ciemat, Obayashi, Sandia, UAM and UniBern. BGR, Ciemat, Obayashi, Sandia and UAM analyses focused on the geochemical reactions taking place at the bentonite/concrete surface. Furthermore, Ciemat, UniBern, Sandia and UAM addressed the physical properties of the concrete/bentonite interface as well, e.g. porosity distribution and specific surface area. Fig. 9 and Fig. 11 show the set of samples used for the analysis of the concrete/bentonite interface.

Concrete cores and concrete/bentonite dry-drilling cores

Fig. 9 shows the location of the concrete cores C-C-34-4 to 11 (Appendix B, Tab. B-4) drilled and named following the FEBEX-DP Sampling Book (García-Siñeriz et al. 2016). Concrete cores with an outer diameter of 78 mm and a total length between 0.92 – 0.99 m were drilled under wet conditions until 5-10 cm before achieving the interface. The drilling was performed between 21 and 23 April 2015.

Cores C-C-34-10 and 11 were drilled ≈ 25 and 10 cm away from the granite wall, respectively, and their ends are close to the bentonite contact. Cores C-C-34-5 to 7 are located towards the gallery axis where the plug is in contact with the dummy. Cores C-C-34-4 and 8 are located close to the triple concrete-dummy-bentonite point. García-Siñeriz et al. (2016) provide additional details on drilling, samples and preservation.

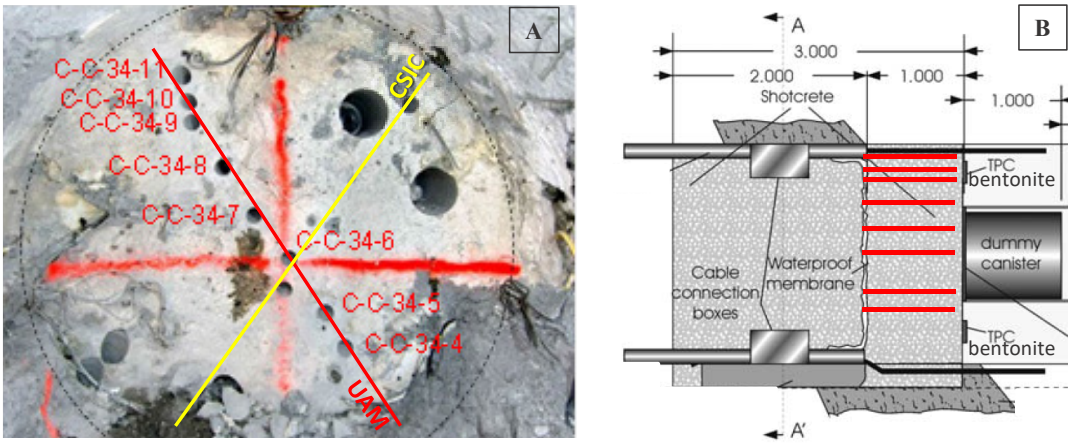

Fig. 9: A. Picture of section 34 with the position of the C-C-34-4 to 11, close to 1 m length cores, going through construction plug section 1. Red and yellow lines represent the radius of UAM and CSIC samples, respectively. B. Cross-section showing the approximate location of the cores with respect to the granite wall, bentonite and dummy.

A set of subsamples of cores C-C-34-4 to 11 (Fig. 10) was used to analyse the source of inorganic carbon by different methods to evaluate carbonation and salt migration related to the influence of bentonite and/or granite on the concrete. A perpendicular dry cut to the interface was performed in each fragment to distribute samples for further mineralogical and geochemical analysis. In order to obtain a more detailed characterisation of the resulting cement paste, a special grinding procedure was used. The concrete samples were crushed with a vice clamp obtaining small-sized samples. These crushed samples were ground in a Herzog

ring mill at three different grinding times (2, 5 and 10 s), obtaining samples of different sizes. After sieving, the fractions were hand-ground in an agate mortar and stored in open polycarbonate tubes during > 48 h in a 50% relative humidity chamber (controlled by $MgNO_3$ saturated solution at 25 °C and by a deposit of NaOH pellets as CO_2 absorbing material). Then, the sieved fractions were analysed.

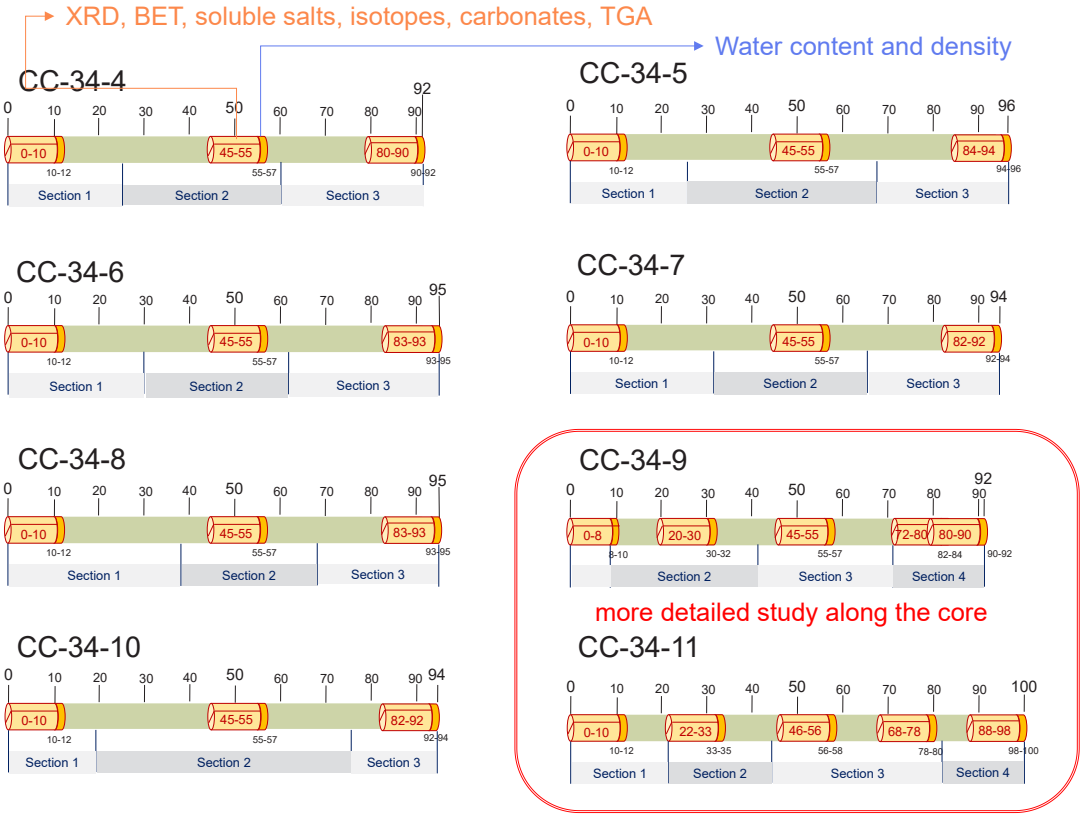

Fig. 10: Systematic sampling for cores C-C-34-4 to CC-34-11 The scheme of a more detailed sampling for cores C-C-34-9 and CC-34-11 is shown at the bottom right side.

Aitemin used dry-drilling to extent cores C-C-34-8 and 10 until getting 5-8 cm deep into the bentonite, with the objective of having samples of the concrete/bentonite interface (e.g. Fig. 11). Aitemin drilled the cores with a diamond coring Hilti machine that was also used for drilling three additional short cores named C-C-34-12 and BC-C-35-1 and 2 to get extra concrete/bentonite interface samples in the zone close to the dummy and to the granite, respectively (see location in Fig. 12). The samples were immediately sealed under vacuum in Al-sheets for further investigations on the interface. Ciemat and UAM focused their studies of the concrete/bentonite interface on those samples.

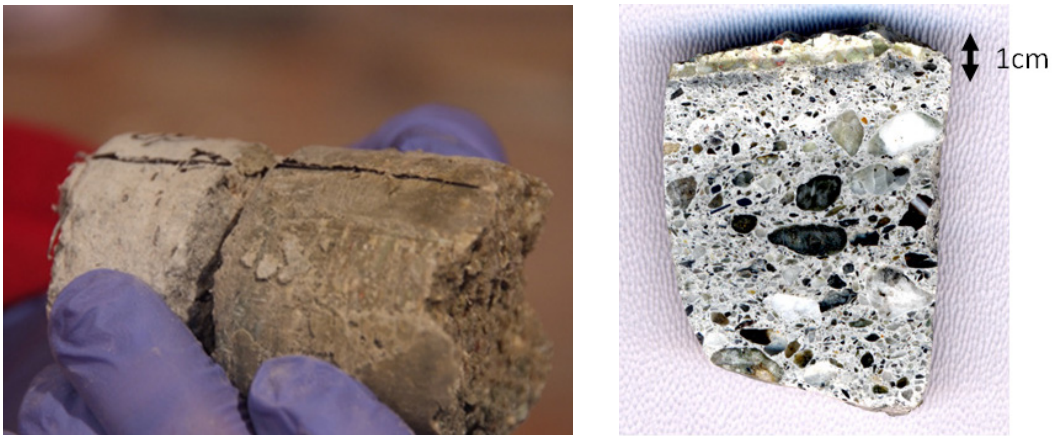

Fig. 11: The picture on the left shows the concrete/bentonite sample BC-C-35-1. The right image displays a cross section of the sample with the interface in the upper part.

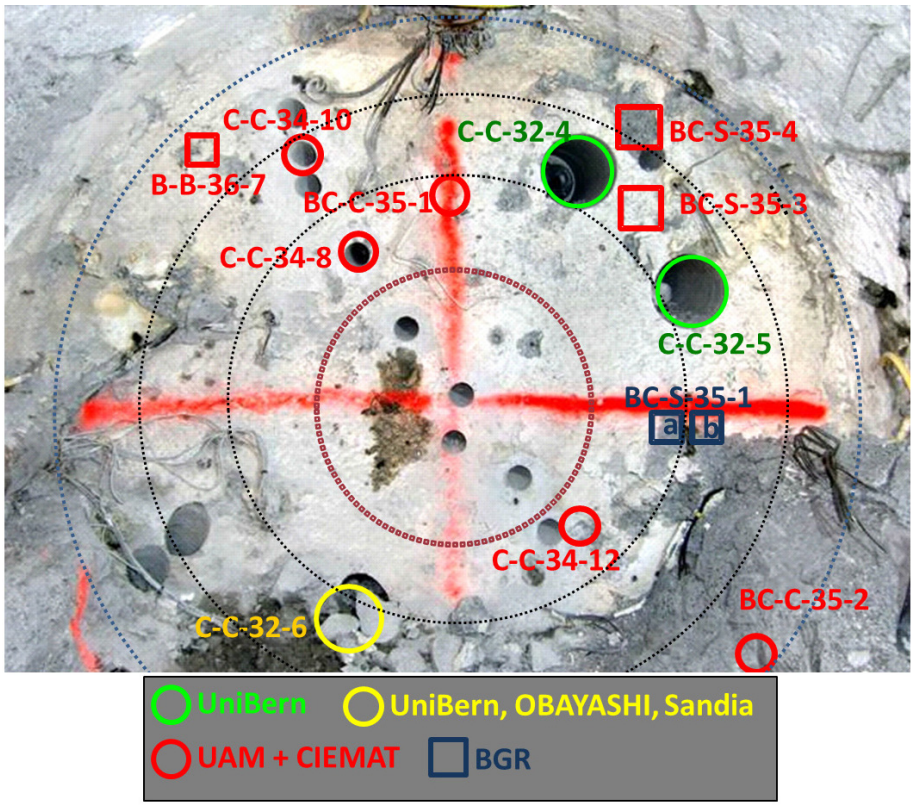

Fig. 12: The picture corresponds to section 34 and shows the position of the samples used for the analysis of the concrete/bentonite interface. Different colours identify the samples analysed by each partner.

Stabilized overcoring

The University of Bern used the stabilized overcoring technique to get the samples named C-C-32-4-OC, C-C-32-5-OC and C-C-32-6-OC containing the concrete/bentonite interface (Mäder et al. 2016). The overcoring was done before starting the FEBEX-DP dismantling operations in order to avoid disturbance of the interface with the hydraulic hammer used to take down the plug. Mäder et al. (2016) offer an abundant compilation of schemes and pictures with the details of the overcoring procedure and Fig. 12 shows the location of those samples. The cores obtained by this drilling procedure were exceptionally well preserved and of excellent quality (e.g. Fig. 13).

The samples were packed under vacuum at the FEBEX location, kept in cold storage and moulded entirely in epoxy resin at the University of Bern, as described in Mäder et al. (2016). Cylindrical samples that contain the concrete/bentonite interface were cut into half cores (Fig. 13A). The freshly cut surfaces were protected with Araldite resin XW 396. The half cores were further cut into quarter cores and these surfaces were simply vacuum-sealed in plastic to make subsequent analytical work easier (Fig. 13B). The University of Bern also measured the temperature in situ at the position of the concrete/bentonite interface in the three overcores. Mäder et al. (2016) provide the temperature data, which are quite similar in the three samples, 28-29 °C.

Parts 5.1 and 6.1 of this report give details on macroscopic observations of the concrete and concrete/bentonite interface during and after the plug overcoring. UniBern made the macroscopic description of the samples based on cores C-C-32-4, 5 and 6. Furthermore, UniBern, Obayashi and Sandia investigated more in detail the sample C-C-32-6.

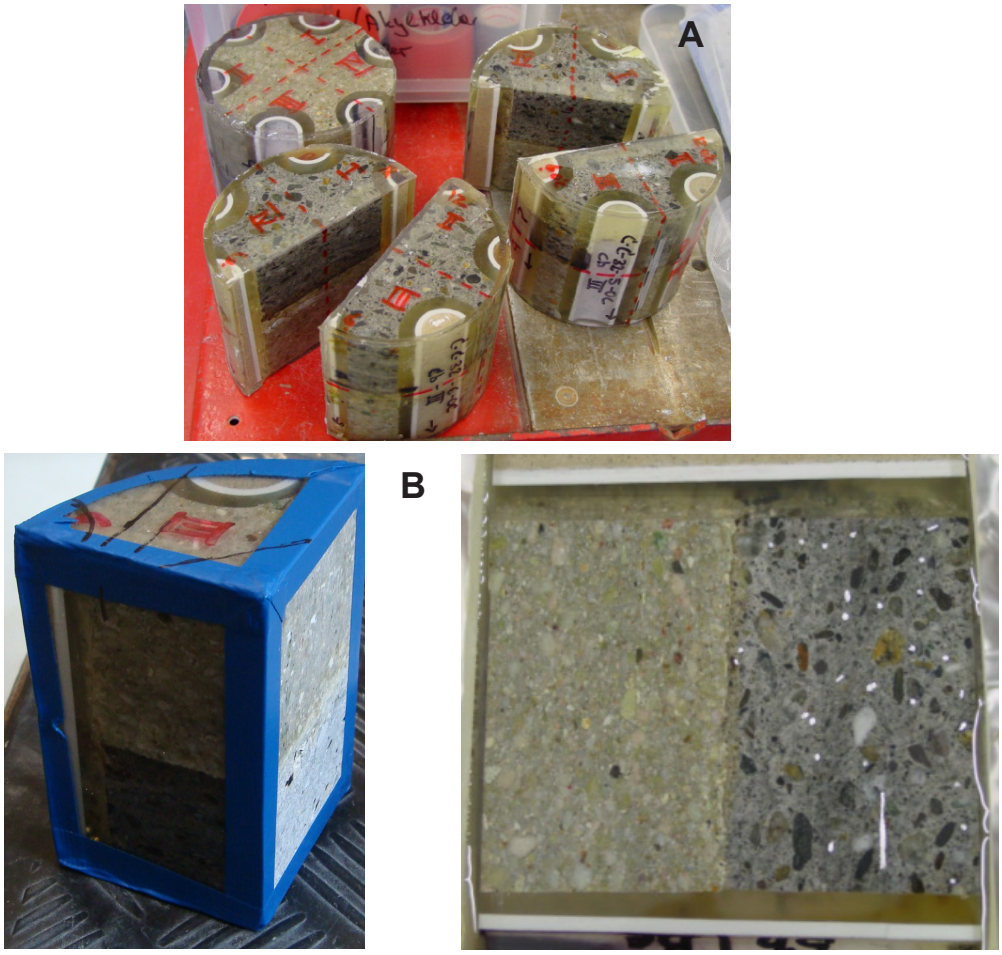

Fig. 13: A. Image showing the sections of the three overcores containing the concrete/bentonite interface (from Mäder et al. 2016). Each piece contains 5 cm of bentonite plus 5 cm of concrete. B. Pictures show an example of the concrete/bentonite interface of the overcoring C-C-32-5 with 5 cm of each material.

Hand-picked samples

When the demolition of the last centimetres of the concrete plug was in progress, pieces of concrete were easily detachable and hand-picked concrete samples were recovered as well as the bentonite contacting them, which was cut with a knife and extracted. These concrete/bentonite bulk samples were referenced as BC-S-35-1 (a,b), 3 and 4 (e.g. Fig. 14). Initial visual inspection revealed that all concrete specimens were grey-coloured and without any visible crack or deterioration. Steel fibres were clean, no oxidation was observed as the sample was taken off, but as the sample remained in contact with air the fibres became rapidly oxidized. The samples were immediately sealed under vacuum in Al-sheets for further investigations on the interface. BGR, Ciemat and UAM worked on those samples.

Fig. 14: Hand-picked concrete/bentonite interface sample named BC-S-35-4. The picture on the left shows the piece of concrete with some remains of bentonite. The image on the right depicts the hole after the bentonite extraction.

The dispersion of samples has allowed covering the following scenarios at the interface level:

(a) Influence of the granite on carbonation and dissolution/precipitation processes in the concrete (core C-C-34-11) and in the concrete/bentonite interface (cores B-B-36-7, BC-S-35-4 and BC-C-35-2).

(b) Samples close to the dummy served to check how the bentonite affected by temperature from heater #1 in the past behaves after interacting with the concrete (cores BC-C-35-1, C-C-34-8 and C-C-34-12).

(c) Samples at a certain distance from both the dummy and the granite allowed investigating the effect on the concrete (cores C-C-34-10, C-C-34-9, C-C-34-4) and the concrete/bentonite interaction (cores C-C-34-10, BC-S-35-1, BC-S-35-3 and C-C-32-6) excluding the influence of both the granite and past temperature effects on the bentonite a priori.

(d) Samples of concrete far from the bentonite and the granite (C-C-34-5, C-C-34-6 and C-C-34-7) are analysed as reference material for comparison effects.

The sample B-B-36-7 represented in Fig. 12 corresponds to a block of bentonite sampled for thermo-hydro-mechanical analysis (Villar 2017). A piece of the block contained remains of concrete and Ciemat used it for soluble salts and porosity analysis on the bentonite side, given its location close to the granite.

While the short-core drilling operations were in process a water spill occurred (Fig. 15, left). It happened specifically while drilling the extension of core C-C-34-4 (see location in Fig. 9). It was not possible to obtain a reliable core at that point, but instead core C-C-34-12 was drilled 2-3 centimetres away from it. The water spill was collected in a polypropylene bottle of 30 mL (Fig. 15, right) and analysed in the Ciemat laboratories. Tab-1 includes the analytical results of the sample. Carbonate and sodium dominates the water composition, although chloride, sulphate and potassium are also in relatively high concentration. Note the low concentration of Mg compared to the rest of ions in the water.

Fig. 15: Left: plug during dismantling operations. A square marks the area of the water spill. Right: a detail of the water spill and the sample collected for the chemical analysis.

Tab. 3-1: Chemical composition of the water spill that occurred during the short-cores drilling operations in the concrete plug in May 2015.

E.C.	**pH**	**Cl^-**	**HCO_3^-**	**SO_4^{2-}**	**F^-**	**CO_3^{2-}**	**OH-**
µS/cm		meq/L	meq/L	meq/L	meq/L	meq/L	meq/L
10850	10.18	23.01	4.90	18.01	10.25	55.20	5.8

Na^+	**Mg^{2+}**	**Ca^{2+}**	**K^+**	**NH_4^+**
meq/L	meq/L	meq/L	meq/L	meq/L
114.46	0.31	3.10	13.46	4.94

The water analysis gives some clues on the range of granite groundwater interaction with the EBS. To put the composition of the water in context, a rough comparison with physico-chemical data from radial and parallel boreholes around the gallery is made. The pH values of the water samples coming from parallel boreholes drilled in the FEBEX gallery is 7.4 ± 0.7 and from radial boreholes is 8.1 ± 0.7, indicating that waters are generally neutral to slightly alkaline (Garralón et al. 2017). A pH of 10.18, as measured in the water spill, seems to indicate some interaction with concrete, which should provide a higher pH. In the same way, the electrical conductivity of the water samples coming from parallel boreholes is 238 ± 163 µS/cm and from radial boreholes is 101 ± 31 µS/cm (Garralón et al. 2017). Those values are far from the electrical conductivity measured in the water spill, which is two orders of

magnitude higher (Tab. 3-1). The increase in this parameter suggests interaction of the granite groundwater with both the concrete and the bentonite. In fact, the granite water analysed in sections of the radial boreholes far from the experiment is dominated by bicarbonate and calcium/sodium ions and contains very low concentrations of other anions and cations. The high concentration of chloride, sulphate, sodium and potassium in the water spill may also reflect the interaction of the granite groundwater with the concrete plug and the bentonite buffer.

A variety of sampling strategies was planned for each working group, but a general trend towards a very detailed study of the 0-3 cm close to the interface in both materials was common to all teams. The methodology and techniques used to conduct the physical, chemical and mineralogical analysis of the concrete/bentonite interface are described in Chapter 4 and results are given in Chapter 6.

3.3 Concrete/rock interface

Eleven cores containing the concrete/rock interface were drilled by stabilised overcoring between 21 and 23 September 2015. Obayashi was in charge of the sampling. It was made after the dismantling of the plug and the bentonite barrier, during which remains of concrete as "islands" in different locations were left for a subsequent sampling of the concrete/rock interface. This fact made the sampling difficult for several reasons: disturbances created by the hydraulic hammer used to dismantle the plug, which created cracks, and a long exposition of the remaining concrete pieces to the air. A brief summary of the procedure followed is given below, whereas specific details can be obtained elsewhere (in Kober & Van Meir 2018).

Cores with a diameter of 25 mm were drilled with a manual drilling machine up to the rock surface. The space left between the sample and the rest of the concrete (Fig. 16 – left) was filled with resin Sika®. After one day, resin was hardened and sampled were taken by overcoring (Fig. 16 – middle).

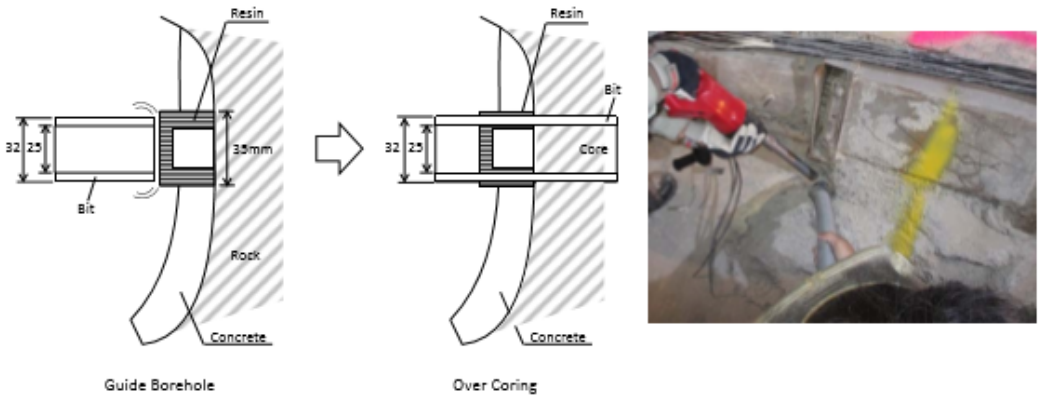

Fig. 16: Schematic of the sampling procedure used to extract concrete/rock cores (see details in Kober & Van Meir 2018).

The results presented in this report (Appendix A) are based on the analysis of two concrete/rock samples: CG-C-31-OB1 and CG-C-32-OB5 (see location of point 1 and 5,

respectively, in Fig. 17). CG-C-31-OB1 belongs to the old plug demolished in 2002 (dismantling of heater #1) and CG-C-32-OB5 to the 2015 dismantling (dismantling of heater #2). The simultaneous study of both samples was made with the objective of comparing alteration after 5 years and 13 years of plug operation. Fig. 18 shows two photos and schematics of the sample conditions. Although pieces are quite small and contain voids, they are suitable for XRD-CT analysis, since the required size for it is small.

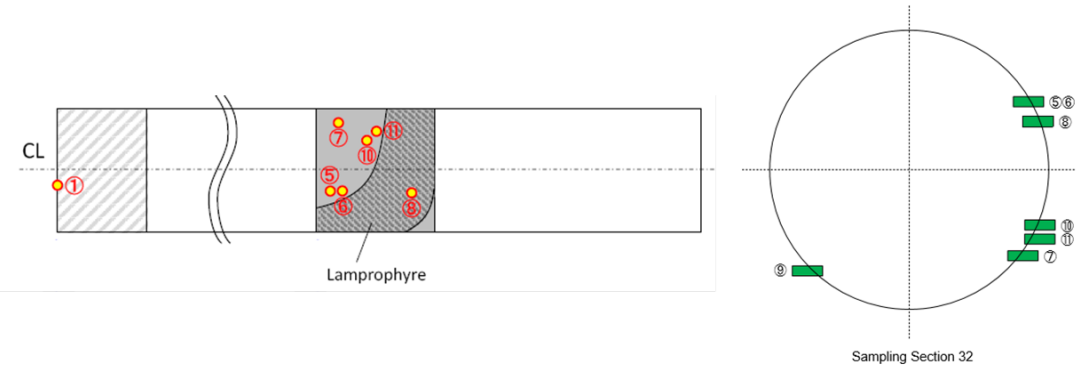

Fig. 17: Location of the concrete/rock interface samples CG-C-31-OB1 and CG-C-32-OB5 (number 1 and 5, respectively, in the left image) analysed in this report (see details in Kober & Van Meir 2018). Both samples were taken on the upper-right side of the gallery.

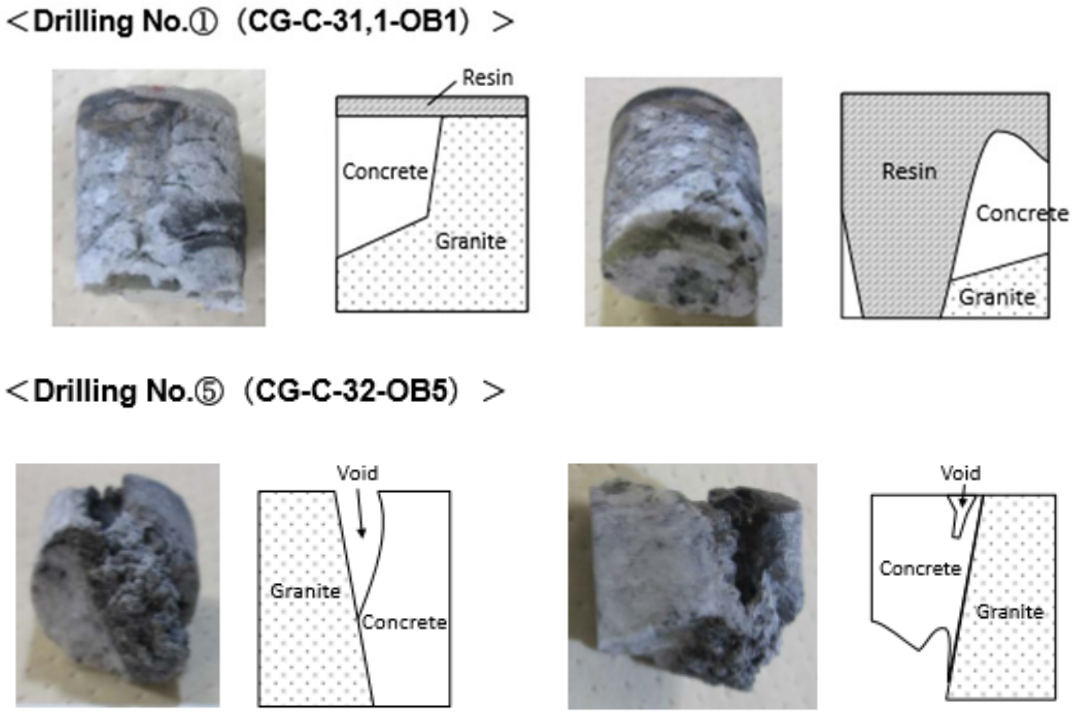

Fig. 18: Images showing the sections of the samples CG-C-31-OB1 (up) and CG-C-32-OB5 (down) containing the concrete/rock interface (see details in Kober & Van Meir 2018). Pieces are quite small and contain voids, but are suitable for XRD-CT analysis since the required size is very small.

Fig. 19 shows the preparation steps of the samples for the XRD-CT equipment. First of all, the samples were stabilised with a resin (Fig. 19 left), then cut with a high precission wire cutter to obtain a piece 20 mm length x 3.5 mm width x 1.5 mm height containing the interface (approx. 1 cm concrete and 1 cm rock) (Fig. 19 middle) and finally they were wrapped in aluminum tape and mounted on the device to be introduced in the equipment (Fig. 19 right).

Fig. 19: (Left) Stabilisation of the concrete/rock sample with resin; (Middle) Final appearance of the specimen that has around 1cm of concrete and 1 cm of granite; (Right) Specimen mounted on the device for introducing in the equipment.

4 Analytical methods

4.1 Concrete

4.1.1 Physical properties

CSIC determinations

The compressive strength was determined in samples of 60 x 120 mm following standard UNE-EN 1015-11. Some ultrasound characterisation was performed to identify differences in quality of the concrete and to determine the concrete's dynamic modulus of elasticity.

Hydraulic conductivity tests were performed in cores of 50 x 50 mm drilled from the original cores. The samples were placed between two cylinders of methacrylate with devices for water in- and outlet. The device and the methodology used are described in García-Calvo et al. (2010). Granite water from the GTS was used for the tests since hydraulic conductivity is influenced by the water chemistry. An air pressure of 0.5 bars was employed to accelerate the water "flow" through the concrete sample.

For the capillarity tests, samples of 60 x 50 mm were used. Water absorption rate was determined by means of the capillarity test UNE 83982 and capillary suction coefficient and accessible porosity were calculated.

Total porosity and pore size distribution were analysed by using a Mercury Intrusion Porosimeter (MIP, Micromeritics porosimeter Model 9320). A piece of concrete with approximately 1cm3 was used.

UAM determinations

The specific surface area was determined by N_2-BET analysis (analysis of the adsorption isotherm of nitrogen gas) by UAM in samples C-C-34-4 to 11 (Fig. 9). It was performed using Micromeritcs® GEMINI V equipment, and a program of standardised analysis in order to obtain an isotherm of five points (0.05-0.25 P/P0 relative pressure). The degassing phase, which takes place before obtaining the isotherm, was carried out from a 0.2 g sample heated to 90 ºC for 18 hours (Norm UNE 22-164/94). The analysis is performed on the bulk sample ground to < 5 µm size.

4.1.2 Mineralogy and carbonation

CSIC determinations

Microstructure and analysis of the solid phases of cores C-C-32-1 to 3 were evaluated on both plug construction sections and on subsamples as those in Fig. 8 under the label "Microstructure". The rapid phenolphthalein test looking for carbonation on the zones of the concrete cores closest to the bentonite was carried out. The first 1.5 cm of concrete of the C-C-32-3 core remained almost colourless suggesting carbonation. From 1.5 cm the sample turned purple indicating the absence of carbonation (Fig. 20).

For the water soluble concrete components of cores C-C-32-1 to 3, a portion of powdered concrete was mixed with deionized water to a solid:liquid ratio =1 and the slurry was stirred for 30 min. The suspension was vacuum filtered and the pH and the ionic composition were determined. In order to prevent the carbonation of the cementitious material samples, both the leaching tests and the pH measurements were performed under nitrogen atmosphere. Pore fluid pH was measured accordingly to the ex-situ leaching method developed by IETcc-CSIC and validated through a Round Robin test (Alonso et al. 2013). Na, K, Ca, Si, Al, Mg, S contents were determined using a inductively coupled plasma optical emission mass spectrometer (ICP-OES 725-ES-Varian). The total chloride content was determined after total dissolution of the solid using nitric acid followed by a potentiometric titration of Cl. The results are expressed as % of cement (or binder) mass.

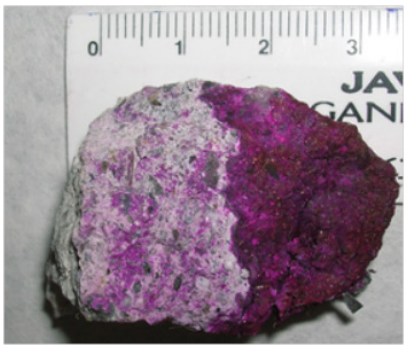

Fig. 20: End of core C-C-32-3, just at the contact with the bentonite. Phenolphtaleine test indicates carbonation of the concrete in the first 1.5 cm from the interface.

The mineralogical composition of the formed/altered concrete phases was evaluated by XRD, TG/DTA, BSEM (SEM-backscattering) with EDS. XRD patterns of cores C-C-32-1 to 3 were recorded by using an X D8 Advance X-ray diffractometer from Bruker with a Cu source of 2.2 kWand an ultra-fast RX Lynxeye detector with a Ni K-beta filter. DTA/TG data were obtained using a STD Q600 V 20.9 Build 20. The samples were heated to 1000 ºC at a heating rate of 10 ºC/min using nitrogen as a medium under static conditions. Alumina powder was used as a reference material. Backscattered electron microscopy (BSEM) images were obtained using a Hitachi S-4800 scanning electron microscope equipped with a Bruker 5030 energy dispersive analyser under the following conditions: 20 kV accelerating voltages and a beam current of 20 mA. The samples were embedded into an epoxy resin, cut, polished and then coated with carbon.

UAM determinations

Aqueous extracts were obtained from 0.05 mm sieved samples of concrete. Then, they were placed in contact with deionized and degassed water in sealed polypropylene bottles at a solid to liquid ratio of 1:8 (2g of solid material in 16 mL of water). Cations and anions were analysed using ion chromatography (Metrohm® 882 IC and C4 (cations) A5supp (anion columns)). Carbonates were determined by the calcimeter (Bernard) method measured as $CaCO_3$ weight %. Then, it is complementary to calcite semi-quantification by XRD. The method compares the volumes of CO_2 that degas after the acid reaction of a sample of known weight, with standard weights of calcium carbonate, under the same conditions of T and P. Carbon and oxygen isotopes ($\delta^{13}C$ and $\delta^{18}O$) were measured by Isotope-Ratio Mass

Spectrometry (IRMS). Measurements were performed on GB/GC-Thermo Delta V Advantage equipment coupled to a Gas Bench II (Thermo) system. Analytical precision (2 sigma) is ± 0.1‰.

The mineralogical composition of the concrete matrix was determined by X-ray diffraction (XRD). To quantify cement phases, the combination of the Rietveld Structure Refinement (RSR) and semi-quantitative Reference Intensity Ratio (RIR) methods were used. The morphology, chemical composition and microstructure of selected samples of concrete were performed by INCAx-sight Oxford Instruments® Energy Dispersive X-ray analyser coupled to a Hitachi S-3000N Scanning Electron Microscope (SEM-EDX). Thermogravimetric (TG) Analysis and Differential Scanning Calorimetry (DSC) analysis were performed in several samples on a simultaneous DSC-TGA analyser (SDT Q600, TA Instruments Co.). Details are explained in Appendix B (part B.2).

4.2 The concrete/bentonite interface

4.2.1 Physical properties

The concrete/bentonite interaction may cause the alteration of the physical properties of both materials, e.g. porosity, surface area, flow paths, etc., affecting the transport properties. Since one of the key functions of the materials used as barriers is limiting the transport of dissolved components, it is important to assess the performance of these materials to maintain this function. Ciemat, Sandia, Obayashi, UAM and UniBern have measured some of these properties in selected concrete/bentonite samples, at the interface level. Parts below give a brief summary of the measured properties.

4.2.1.1 Porosity and pore size distribution

The pore size distribution of selected samples was measured by Ciemat by Mercury Intrusion Porosimetry (MIP). This technique allows the determination of porosity and pore size distribution by injecting mercury into the sample at different pressures while controlling the intruded volume. A Micromeritics AutoPore Series IV 9500 porosimeter was used, allowing the exploration of pore diameter sizes between 0.006 and 600 μm. Samples were previously lyophilised to eliminate the water in the pores. Measurements were made on samples C-C-34-10 and BC-C-35-2 in equal measure in concrete and bentonite. Samples BC-C-35-1 and BC-S-35-3 were used to measure porosity only in the concrete. Bentonite of sample B-B-36-7 located close to the concrete plug surface was recovered after the THM studies for measuring porosity instead of bentonite from sample C-C-34-8 because that sample had been used for other analyses.

4.2.1.2 Specific surface area (SSA)

Classical nitrogen adsorption/desorption isotherms were obtained by Ciemat on a Micromeritics ASAP 2020 (discontinuous volumetric sorptometer). Measurements were made on samples C-C-34-10 and BC-C-35-2 in equal amounts in concrete (cement paste without aggregates) and bentonite. Approximately 2-4 grams of total sample were ground in an agate mortar. The samples were dried at 90 °C during for 24 h. prior to the nitrogen adsorption, the samples were degassed by heating at 90 °C for 18 hours using a mixture of helium and nitrogen under a residual vacuum between 500 and 6-10 mmHg.

Specific surface area was also measured by UAM by BET N_2 isotherm on the concrete (cement paste) and the bentonite on samples C-C-34-8, 10 and 12, BC-C-35-1 and 2 and BC-S-35-3. It was performed using a Micromeritcs GEMINI V equipment, using a program of standardised analysis in order to obtain an isotherm of five points (0.05-0.25 P/P0 relative pressure). The degassing phase, which takes place before the realization of the isotherm, was carried out on a 0.2 g sample heated to 90 ºC for 18 hours (UNE 22-164/94). The analysis was performed on the bulk sample ground to < 5 µm size.

4.2.1.3 Clay mineral surface imaging (AFM)

Obayashi used the Atomic Force Microscope (AFM) for molecular scale imaging of the bentonite that has been in contact with the concrete plug. The measurement of the montmorillonite crystals' dimensions using AFM can provide information on crystal dissolution and dissolution rate. To check dissolution processes, the bentonite of core C-C-32-6-OC closest to the concrete was compared to a reference bentonite sampled far from the concrete, apparently unaffected by the concrete.

An AFM Keyence VN-8000 was used for the studies. A bentonite powder sample was dispersed in 0.02% pyrophosphoric acid solution and was diluted by water. 0.0005 wt% slurry was thus obtained. Previous studies have confirmed that the sheets of montmorillonite are separated one by one using this procedure. The slurry was dropped onto a mica slide and was dried in the atmosphere. The crystals on the slide were observed. The crystals with a thickness between 1.0 and 2.0 nm were chosen for the analysis and the circumference and area were measured using a cantilever in the DFM mode. 100 crystals were analysed for each sample.

4.2.1.4 X-ray computed microtomography imaging (X-ray CT)

The application of X-ray CT imaging is well-suited for core samples due to its non-destructive nature, excellent scanning resolution (e.g., 10 microns), the ability to analyse relatively large specimens (in the order of cm in length), and the generation of 2D-3D digital image data for textural evaluation. Sandia and UniBern used the overcore C-C-32-6-OC to perform image analyses with this technique.

The X-ray CT imaging setup used by Sandia in this study is a North Star Imaging Inc. X50 system. It uses a Comet 225kV constant potential X-ray Source in conjunction with a Varian 2520V flat panel detector. North Star Imaging Inc. software was used for 3D-reconstruction and to create 2D slices of the 3D volume-rendering. The 2D image slices were subsequently used as input for further image post-processing using North Star Imaging Inc. software and the open source ImageJ/Fiji software package (http://imagej.net/Fiji; http://fiji.sc/). The scanning resolution is 10.5 microns in a helical step scan mode. This scanning resolution was deemed sufficient to resolve textural features down to the sub-millimetre scale and it is focused on the concrete/bentonite interface region.

UniBern performed X-ray computed tomography at the University of Fribourg, Department of Geosciences, with a latest-generation Bruker Skyscan 2211 Multi-Scale nano-CT instrument. Imaging was performed with a 11 Mp cooled CCD camera. Data were reconstructed with Bruker NRecon software optimised for GPU support. Data analysis and visualisation was performed with Bruker CTAn software. Examples applied to cement/clay interaction and methods and limits of quantification are detailed in Dolder et al. (2014, 2016).

4.2.2 Geochemical measurements

The chemical characterisation of the concrete and bentonite is necessary to give an idea of the behaviour and distribution of some elements under the FEBEX experimental conditions. For this reason, soluble ionic composition as well as elemental mapping and X-ray fluorescence on solid phases was made on a number of samples. Furthermore, changes in the cation exchange capacity and the exchangeable cations can influence the swelling properties of the bentonite. Several groups addressed the measurement of this variable. Thermogravimetric analysis, carbon content and analysis of stable isotopes were addressed as well. Below, some details about the techniques and groups involved are given.

4.2.2.1 Soluble ions by aqueous leaching

Ciemat obtained aqueous extracts from both concrete and bentonite on samples C-C-34-8, 10 and 12, BC-C-35-1 and 2, BC-S-35-3 and 4 and B-B-36-7. Powder samples were obtained by grinding the samples in a Retsch RM200 mortar grinder with an agate pestle to a size of less than 63 μm after drying them overnight in an oven at 105 °C. In the case of concrete, large aggregates were avoided. Then, they were placed in contact with deionised and degassed water in hermetically-sealed polypropylene bottles at a solid to liquid ratio of 1:8 (5 g of clay in 40 mL of water), shaken end-over-end and allowed to react for 24 hours. Separation was done by centrifugation (30 minutes at 12500 rpm) and the supernatant was filtered using a 0.45-μm pore size filter and analysed. pH and Eh were not determined in the extracts because they do not represent reliable environmental conditions regarding the actual cell system, but the method is assumed to be a useful indicator for the content of soluble ions. Duplicates were made for all the samples. Cations in supernatants were analysed by ICP-OES in a Spectro ARCOS spectrometer after acidification of the samples to pH<2 with HNO_3 (8 mL/L). Anions were analysed using ion chromatography (Dionex DX-4500i).

4.2.2.2 Cation exchange capacity (CEC) and exchangeable cations (EC)

Different methods were used for the determinations of cation exchange capacity and distribution of exchangeable cations by the three institutions involved in these analyses, BGR (samples BC-S-35-1a and 1b), Ciemat (samples C-C-34-8, 10 and 12, BC-C-35-1 and 2 and BC-S-35-3 and 4) and Obayashi (sample C-C-32-6-OC). All groups made measurements at different distances of the interface to get an idea of the effect of the interaction with the concrete on this variable. Different methods may give slightly different results, although great variations are not expected. The reason is the different replacement capacity of the replacing cations used, besides the pH buffering or the extraction method. Thus, any discrepancy should be carefully evaluated.

BGR and Ciemat analysed the CEC using the Cu-Triethylenetetramine (Cu-trien) method (Meier & Kahr 1999), although the treatment of the samples was different. BGR employed the same method for the EC while Ciemat used a $CsNO_3$ solution to displace the exchangeable cations as explained below.

The BGR procedure for both CEC and EC consisted in analysing the samples using 30 mL Cu-trien solution and no additional water. Two different sample masses were analysed and average values were calculated. The error (± 3 sigma) of values determined using Cu-trien method for bentonites (Dohrmann & Kaufhold 2009) is different for different cations and the CEC. The scattering is the lowest for K^+ (±0.3 meq/100 g), followed by Mg^{2+} (±0.8 meq/100 g), Ca^{2+} (±0.8 meq/100 g), Na^+ (±1.9 meq/100 g), and the CEC (±3.1 meq/100 g). These values can be used to evaluate differences in this study approximately.

Ciemat also measured Cation Exchange Capacity (CEC) using the copper triethylenetetramine method (Cu-trien). For this determination, 200 mg of clay sample were added to 35 ml of distilled water and dispersed by ultrasonic treatment for 5 min. The suspension was diluted in a 50 mL volumetric flask, and then transferred into a 100 mL beaker. While stirring the suspension, 10 mL of Cu-trien solution was added. After 3 minutes of reaction time, the suspension was centrifuged at 13000 rpm for 10 minutes. The supernatant solution was carefully removed and the extinction was measured at 620 nm by spectrophotometry.

Ciemat used a $CsNO_3$ solution to displace the exchangeable cations (Sawhney 1970) for EC analysis. Bentonite powdered and dried samples were equilibrated with $CsNO_3$ 0.5 N at pH 8.2 at a solid to liquid ratio of 0.25 kg/L. After phase separation by centrifugation, the supernatant solutions were filtered at 0.45 μm and the concentration of the major cations was analysed by Inductive Coupled Plasma - Optical Emission Spectrometry (ICP-OES) in a Spectro ARCOS spectrometer after acidification of the samples to pH<2 with HNO_3 (8 mL/L).

Obayashi used the monovalent organic cation benzyltrimethylammonium (BTMA) to displace exchangeable cations of the bentonite. The method is often used for the quantification of exchangeable cations in bentonite because BTMA is highly exchangeable in the interlayer and the extracting solution is neutral so that the alkali minerals such as carbonate are not dissolved.

4.2.2.3 X-ray fluorescence spectroscopy (XRF)

BGR made chemical determinations of samples BC-S-35-1a and b by XRF with a PANalytical Axios spectrometer (ALMELO, The Netherlands). Samples were prepared by mixing the sample with a flux material (lithium metaborate Spectroflux, Flux No. 100A, Alfa Aesar) and melting it into glass beads. The beads were analysed by wavelength-dispersive XRF. To determine loss on ignition (LOI), 1000 mg of sample material was heated to 1030 °C for 10 min.

4.2.2.4 Carbon content and stable isotope analysis

BGR measured the organic carbon (OC) content of sample BC-S-35-1a and b with a LECO CS-444-Analyser after dissolution of the carbonates. Carbonates were removed by treating the samples several times at 80 °C with HCl until no further gas evolution could be observed. Samples of 170-180 mg of the dried material were used to measure the total carbon (TC) content. TIC (total inorganic carbon) was calculated by the difference of TC-TOC. The samples were heated in the device to 1800-2000 °C in an oxygen atmosphere and the CO_2 was detected by an infrared detector. The device was built by LECO (3000 Lake Avenue, St. Joseph, Michigan 49085, U.S.A).

Carbon and oxygen isotopes ($\delta^{13}C$ and $\delta^{18}O$) were measured by UAM on samples C-C-34-8, 10 and 12, BC-C-35-1 and 2 and BC-S-35-3 by Isotope-Ratio Mass Spectrometry (IRMS). Measurements were performed on GB/GC-Thermo Delta V Advantage equipment coupled to a Gas Bench II (Thermo) system. Analytical precision (2 sigma) is ± 0.1‰. The fraction >0.05 mm in concrete samples was discarded for the analysis of stable isotopes, in order to obtain representative measurements of the cement matrix.

4.2.2.5 Elemental mapping on polished sections

Energy dispersive X-ray analysis coupled to a scanning electron microspope (SEM-EDX)

UAM made elemental mapping in perpendicular areas to the concrete/bentonite interface. The concrete and bentonite subsamples were dry cut in slices with a diamond wire saw, freeze-dried in liquid nitrogen, dried in vacuum with P_2O_5 dehydrated atmosphere until 10^{-4} Pa, and finally polished. Using this preparation method the bentonite slices maintained their consistency in the polishing operation without disaggregation. Therefore, embedding in resin was not required for elemental profiles or mapping. The chemical profiles at both sides of the interface, in concrete and bentonite, were performed on those dry polished sections as a function of distance from the interface to represent the geochemical perturbations at the µm-mm-cm scale. The first 100 µm of sample from the interface were measured by 5 EDX analyses with high resolution (20 µm in perpendicular length from the interface). The next 5 analysis were extended to approximately a whole length of 250 µm. From that distance to the end of each sample, a constant resolution of approximately 400-500 µm was considered per analysis to represent the chemical profiles. These sections allowed producing chemical composition maps and revealed microstructural features of concrete/bentonite contact. An INCAx-sight Oxford Instruments® Energy Dispersive X-ray analyser coupled to a Hitachi S-3000N Scanning Electron Microscope (SEM-EDX) was used to perform the analyses. For the analysis of the concrete, coarse aggregate grains were intentionally avoided with the aim of obtaining a better-averaged chemical profile of the cement paste matrix.

UniBern used uncoated sample surfaces for elemental mapping by SEM (Zeiss EVO-50 XVP) equipped with a backscattered electron (BE) and an EDAX Sapphire light element detector in the low vacuum mode (10 Pa) with a beam acceleration of 20 keV and a working distance of 8.6 mm. The beam current was adjusted to yield a dead time of 10–20% for EDX. EDX element maps with a resolution 3 µm/pixel were acquired using a dwell time of 400 µs, repeating 64 frames. The total measuring area was divided into fields of 733 × 573 µm that were merged after acquisition. Normalisation of each field to total counts is necessary to compensate for filament weakening, which is significant when the total measurement time is approximately 50 h. Summation EDX spectra of each field measured for the element maps can be analysed semi-quantitatively without standardisation using the EDAX Genesis software (ZAF matrix correction). All detected elements heavier than fluorine are normalised to 100 mol%, in contrast to methods with standardisation that result in absolute concentrations (e.g., electron microprobe). Absolute errors (accuracy) are below 3 mol% in low-vacuum mode. When comparing measurements within the same material acquired at the same conditions (e.g., chemical gradients in a fine-grained matrix), differences as low as 0.1 mol% can be resolved (precision).

Sandia performed SEM/EDX analyses on polished thin sections using a TESCAN (Warrendale, PA) Vega 3 LMU tungsten filament scanning electron microscope (SEM) operated at 30 kV accelerating voltage. Backscattered electron imaging (BSEI) was conducted under low vacuum mode and micrographs were collected using an annular YAG scintillator backscatter electron detector. EDX analyses were obtained using an EDAX® Element fixed working distance silicon drift detector with a 25 mm^2 sensor.

Electron probe microanalysis (EPMA)

This method used by Obayashi analyses the samples by recording the X-ray photoelectron spectrum, a quantitative technique that gives an accurate chemical composition of the selected areas in a sample. A polished section of the concrete/bentonite interface from sample C-C-32-4-OC was used to obtain the distribution maps of different elements.

The equipment used was a JXA-8100 of JEOL. The measurement conditions are shown in Tab. 4-1. The target elements are Si, Al, Ca, Mg, Fe, S, Na and K. The measured spots are located with the same intervals in the parallel and the vertical direction to the interface of both materials. The measured values are shown as a contour map for each element. In addition, the line-averaged value for every line that is parallel to the interface is obtained as the average of the values of the measured spots on the line. Then, for each element, the line-averaged values are plotted as a function of the distance from the interface.

Tab. 4-1: Measurement condition for EPMA

Spot size	For the measurement of large area, 40μm x 40μm For that of local area, 4μm x 4μm
Beam diameter	For the measurement of large area, 20μm x 20μm For that of local area, 2μm x 2μm (The beam is irradiated at the center of each spot.)
Acceleration voltage	15kV
Current	5x10-2 μA
Irradiation duration	40 msec for one spot

Sandia used micro–X-ray Fluorescence (XRF) on polished thin sections to obtain maps on elemental composition. Micro-XRF allows for micron-scale compositional analysis but covering a larger scan area. The micro-XRF analysis was performed using a Bruker M4 Tornado micro-XRF mapping system. The instrument was equipped with a micro-focused Rh source (50 kV, 600 μA) with a poly-capillary optic (~30 μm spot-size). The detector system employed a silicon-drift detector to collect fluorescence spectra from the specimen. The specimen was secured to the x-y translation stage within the M4 chamber, and XRF spectra were collected under vacuum conditions (~10^{-3} Torr). The XRF-mapping dataset for the thin-section specimen was collected as a large datacube with full X-ray spectra (4096 channels, 0 to 40 keV range) collected at each pixel in a 2D array. The step size employed for the micro-XRF spatial map was 50 μm. This resulted in a 502 × 860 matrix for the map which covered an area ~24 × ~35 mm^2, thus incorporating the entire cross-sectioned specimen.

4.2.3 Mineralogy

The mineralogy of concrete and bentonite was addressed in different ways by the teams contributing to this report.

4.2.3.1 X-ray Diffraction (XRD)

X-ray diffraction was used by UAM to identify the mineralogical composition of concrete and bentonite. The XRD patterns registered from bulk, randomly oriented, dried powders were recorded in an angular range of 3-70º using a θ/2θ X-PERT PANalytical instrument with an X-CELERATOR detector (Co-Kα radiation generated at 40 kV and 40 mA). The equipment uses monochromatic radiation provided by a Ge 111 single crystal face. The slit settings were: soller slit (0.04 rad); divergence and anti-scatter slits both of 0.50º.

The <2μm fractions were extracted by the dispersion of bentonite in distilled water using an ultrasonic tip. The dispersion was let to settle in a 25 cm high flask during 14 h at 20 ºC in order to aspirate the liquid up to 20 cm height measured from the initial level of the liquid surface. Suspensions in the flask were maintained tightly closed to atmospheric contact with paraffin film in order to avoid carbonation. Flocculation of clay particles occurred after adding ethanol and then centrifugation was made. Basal spacings of smectite in samples were measured by the preparation of oriented aggregate films using a 0.05g/ml dispersed slurry that was smeared on a 2 cm^2 glass tile, letting it to dry in laboratory ambient conditions. Ethylene Glycol (EG) solvation was performed inside a closed plastic box adding a few drops of EG impregnating a filter paper inside. EG vapour enters the clay film deposited in the glass tiles lying on the paper (48 h). These samples were scanned from 3º to 40º in the same conditions as the powder patterns.

BGR recorded XRD powder patterns using a PANalytical X'Pert PRO MPD θ-θ diffractometer (Co-Kα radiation generated at 40 kV and 40 mA), equipped with a variable divergence slit (20 mm irradiated length), primary and secondary soller, diffracted beam monochromator, point detector, and a sample changer (sample diameter 28 mm). The samples were investigated from 1° to 75° 2θ with a step size of 0.03° 2θ and a measuring time of 12 s per step. For specimen preparation, the back loading technique was used.

Oriented mounts for XRD (texture slide XRD) were prepared using 15 mg of clay per cm^2. An aliquot of 1.5 mL of suspension was deposited on the circular (diameter = 2.4 cm) ceramic tiles which were 3 mm thick. The suspension was filtered through the tile using a vacuum filter apparatus. XRD pattern of the oriented mounts were recorded using a PANalytical X'Pert PRO MPD θ-θ diffractometer (Co-Kα radiation generated at 40 kV and 40 mA), equipped with a variable divergence slit (20 mm irradiated length), primary and secondary soller, diffracted beam monochromator, and a point detector. The air dried samples were investigated from 1° to 65° 2θ with a step size of 0.03° 2θ and a measuring time of 5 s per step. Furthermore, the specimens were stored overnight in an ethylene glycol atmosphere at 60°C. The clay films were measured from 1° to 40° 2θ (stepsize 0.03° 2θ, 5 s per step) after cooling to room temperature, representing EG conditions.

XRD analysis was also carried out by Obayashi. The measurement conditions for random and oriented powders are shown in Tab. 4-2. In addition to these, oriented XRD measurement was done in the condition that relative humidity (RH) is 40%. The basal spacing of montmorillonite in an RH condition varies by the dominating interlayer cation. That of Na-montmorillonite at 40% RH is around 1.26 nm while that of Ca-montmorillonite is around 1.50 nm.

Tab. 4-2: XRD measurement condition for random and oriented bentonite powders

Items		Random	Oriented
Machine		Rint2500 Rigaku	Rint1200 Rigaku
Slits	Divergence and scattering slits	0.25o	0.5 o
	Receiving slit	0.15 mm	0.15 mm
Tube	Voltage	40 kV	30 kV
	Current	100 mA	20 mA
Scan	Speed	0.2 degree/min	1.0 degree/min
	Pitch	0.02 degree	0.05 degree
	Range	4 - 70 degree	2 - 40 degree
Monochrometer		ON	OFF

4.2.3.2 Thermo-gravimetric (TG) and Differential Scanning Calorimetry (DSC)

Thermal analysis is usually done to study phase transition, structural collapses or weight changes of the sample during heating, as well as to determine the water content as a function of temperature.

UAM made TG-DSC analyses on samples C-C-34-8, 10 and 12, BC-C-35-1 and 2 and BC-S-35-3. 0.1 g of bulk sample was ground to < 5 μm. TGA and DSC were carried out on a simultaneous DSC-TGA analyser (SDT Q600, TA Instruments Co.). In each experiment, an alumina (Al_2O_3) crucible and nitrogen gas purge delivered at a constant rate of 100 mL/min were used. Samples were heated from room temperature (~25 °C) to a maximum temperature of 1000 °C at a rate of 10 °C/min. In all DSC curves presented, upward peaks indicate heat release from the sample and downward peaks indicate heat absorption.

BGR carried out thermal analyses on samples BC-S-35-1a and b using a Netzsch 449 F3 Jupiter thermobalance equipped with a DSC/TG sample holder linked to a Netzsch QMS 403 C Aeolus mass spectrometer (MS). 100 mg of powdered material previously equilibrated at 53 % relative humidity (RH) was heated from 25 to 1150 °C with a heating rate of 10º K/min. Netzsch (Gebrüder-Netzsch-Straße 19, 95100 Selb, Germany) manufactured the devices.

4.2.3.3 Scanning electron microscopy (SEM) and Transmission electron microscopy (TEM)

Different teams (UAM, BGR and Ciemat) used electron microscopy to study the morphology, mineralogy and microstructure of some samples. Furthermore, transmission electron microscopy provides morphologic, compositional and crystallographic information on samples of interest. Ciemat used TEM on specific samples trying to observe crystal structure, texture and size as well as to analyse selected crystals.

UAM made SEM studies on samples C-C-34-10 and C-C-34-12 prepared as explained in Section 3.2. The morphology, chemical composition and microstructure on those dry polished

sections were analysed by an INCAx-sight Oxford Instruments® Energy Dispersive X-ray analyser coupled to a Hitachi S-3000N Scanning Electron Microscope (SEM-EDX).

Ciemat selected small fresh pieces of samples C-C-34-10, BC-C-35-2 and BC-S-35-3 to examine the interface by SEM. Prior to SEM imaging, samples were dried at 60 °C during 48h and sputter-coated with gold to reduce sample charge and improve secondary electron emission. A SEM JEOL JM-6400 coupled to a dispersive X-ray energy spectrometer X LINK LZ_5 was used at the National Centre for Electron Microscopy of the Complutense University of Madrid. For TEM examination, bentonite samples were dispersed in acetone and dropped on a carbon-coated copper grid. A JEOL 2100FX with 200 kV acceleration voltages (3.4 Å point- to-point resolution) coupled to an OXFORD ISIS X-ray energy dispersive spectrometer, giving a resolution of 136 eV at 5.39 keV, was used at the National Centre for Electron Microscopy of the Complutense University of Madrid.

BGR used a FEI Quanta 600 F operated in low-vacuum mode (0.6 mbar) for SEM investigation. Therefore, sputtering of the samples with gold or carbon was not necessary. The microscope is equipped with the EDX-system Genesis 4000 of EDAX. A freshly broken surface of the unprocessed air-dried sample BC-S-35-1 was fixed on carbon grid and used for SEM inspection.

4.2.3.4 Fourier transform infrared spectrometry (FTIR)

BGR and Ciemat used FTIR to observe possible compositional and structural changes in the clay and concrete as a consequence of chemical modifications due to the concrete/bentonite interaction. FTIR was also used to look for the formation of new phases (e.g. calcite).

Ciemat homogenized slices taken at different distances from the interface of the samples C-C-34-10 and 12 in a Retsch RM200 mortar grinder with an agate pestle. The different fractions were then mixed with KBr, i.e. 2 mg of clay or concrete and 100 mg of KBr. FTIR spectra were obtained using a Nicolet 6700 FTIR spectrometer in transmission mode with a DTGS KBr detector and recording over the middle-IR region spectral range (4000-400 cm^{-1}) with a resolution of 2 cm^{-1} in an atmosphere continuously purged from water and atmospheric CO_2. Measured FTIR spectra were processed by Omnic (version 3.1) software (Nicolet Instruments Co., Madison, USA).

After homogenizing sample BC-S-35-1 BGR mixed the sample with KBr (1 mg sample / 200 mg KBr) and collected the FTIR Spectra on a Thermo Nicolet Nexus FTIR spectrometer (MIR beam splitter: KBr, detector DTGS TEC). The resolution was adjusted to 2 cm^{-1}. Measurements were conducted before and after drying the pellets at 150°C in a vacuum oven for 24 h. Nicolet Instruments (Madison, Verona Road, Wisconsin, USA) built the spectrometer.

4.3 The concrete/rock interface

A synchrotron-based imaging technique named X-ray diffraction computed tomography (XRD- CT) developped by Hitomi and collaborators (Kajiwara et al. 2013) at the synchrotron facility Spring-8 in Japan was used to study the samples CG-C-31-OB1 and CG-C-32-OB5. Fig. 21 shows the conceptual diagram of XRD-CT. It is a non-destructive evaluation technique that combines the principles of X-ray diffraction and computed tomography to generate high-resolution images of spatial structure and mineral composition of samples.

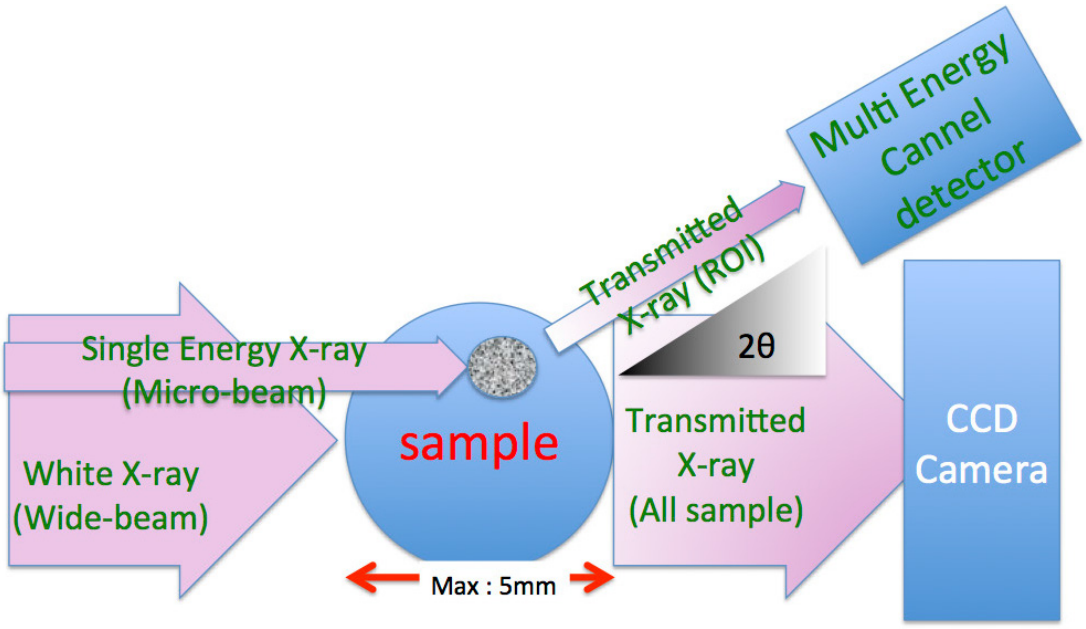

Fig. 21: Conceptual scheme of the XRD-CT functioning

In a first step, spatial structure observation by X-ray computed tomography allowed identifying irregularities, cracks, voids, etc. The samples were located in a rotating stage and for each complete 180º scan, 1500 projections with acquisition time 0.15 s were recorded. The reconstruction of the cross-sections was made from the transmission images using in-house software distributed by Spring-8. These served as basis for the selection of regions of interest or observation points.

The second step was the analysis of those regions of interest by XRD to get mineralogical data. The experimental set-up for XRD-CT includes a monochromatic (E=20 keV) 0.15 mm beam and a charge-coupled device (CCD) for data acquisition. A single mineral database was generated converting angle-intensity to energy-intensity from the ICSD (Inorganic Crystal Structure Database). Diffraction patterns were then compared with the database to identify minerals.

Fig. 22 shows an example of raw data on different points of one of the samples of the concrete/rock interface. Some key features can be highlighted in the XRD profiles. One is that due to the lower energy absorption of X-ray inside the sample, X-ray intensity at 0~20 keV is relatively weak compared to a higher range of X-ray. Another is that there is a broad peak 20~50 keV called ‘halo’. The ‘halo’ is related to short range order of amorphous materials and measuring systems. For the mineralogical analysis, the location and intensity of the peaks is important, so the peak profile is generated by substracting the ‘halo’. Fig. 23 shows the peak processing. Halo fit line (red dash line) was calculated connecting low points of raw data. The final peak profile was produced by substracting ‘halo’ from raw data.

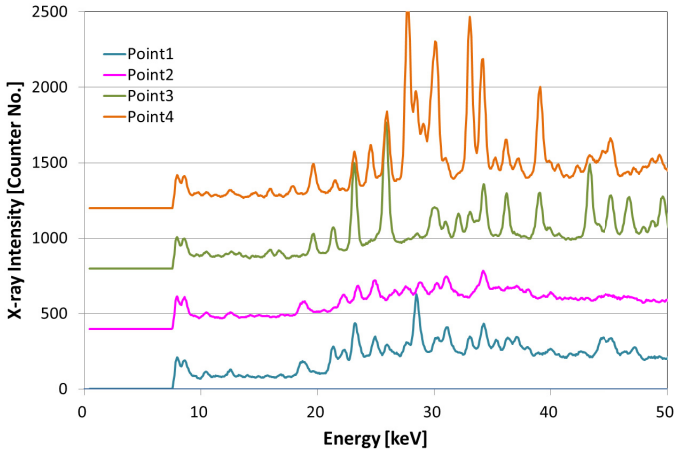

Fig. 22: Example of diffraction profiles by XRD-CT of 4 points on a concrete/rock sample.

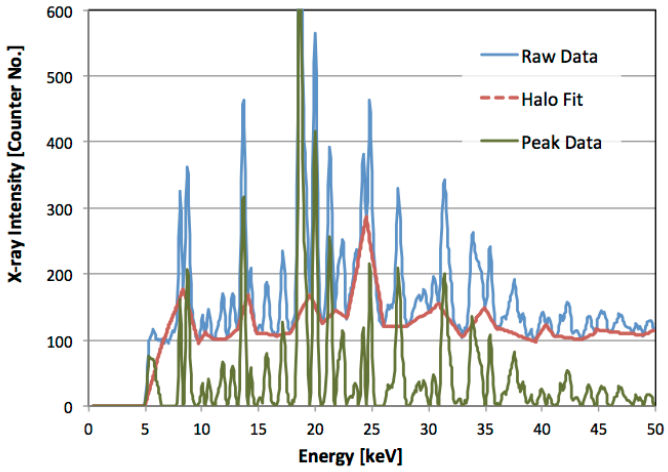

Fig. 23: Peak processing in the samples. The final peak profile is generated by substracting the 'halo'(non-crystaline mineral phases) from the raw data.

Mineral data was generated by converting angle-intensity to an energy-intensity relation from the ISCD database. Finally, mineral data were stored as indeces of peak energy. Analyses were performed using these mineral data. Fig. 24 shows the example of an analysis of calcite. Several peaks agree with calcite although many of them present weak intensity; probably, the calcite content is low. The diffraction profiles of the samples analysed were compared with database of quartz, cement hydrates, clay and feldspar.

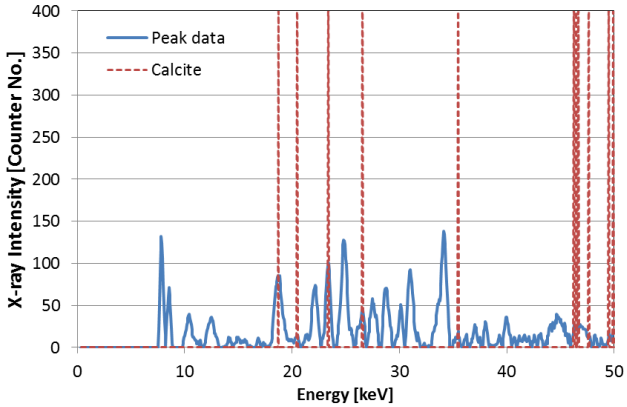

Fig. 24: Example of typical XRD analysis of calcite.

4.4 Summary of samples' characterisation

Fig. 25 and Fig. 26 summarise the concrete and concrete/bentonite interface samples, together with the type of characterisation applied on each sample and the partners in charge of those characterisations. Results are compiled in Chapters 5 and 6.

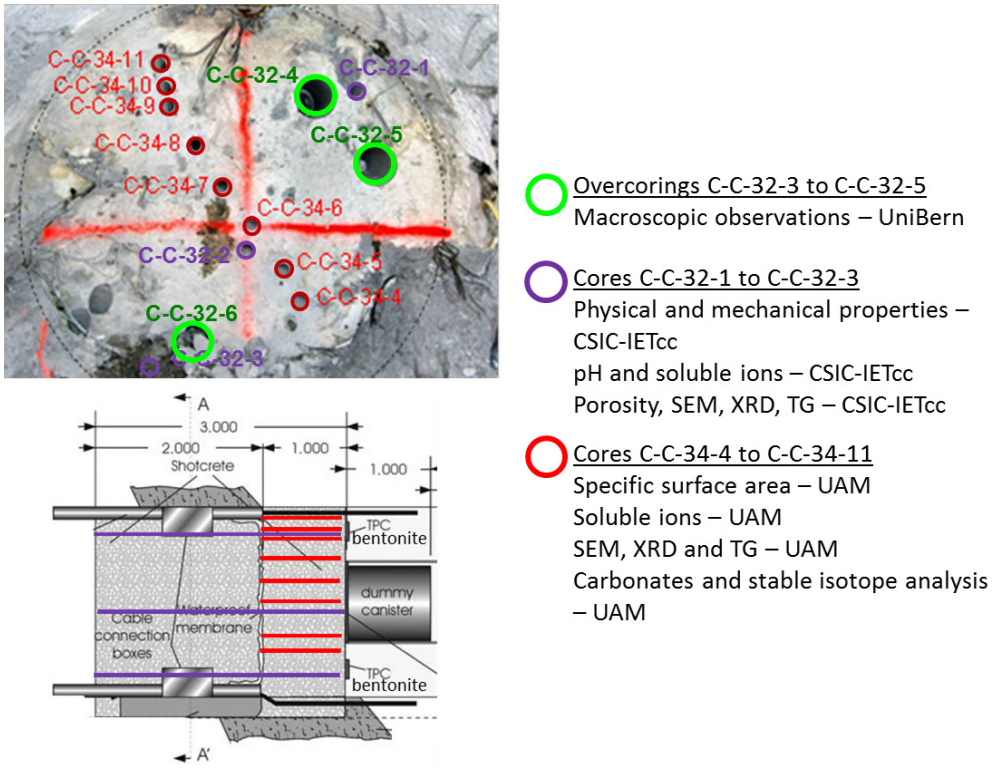

Fig. 25: Summary of samples of concrete analysed for macroscopic observations by UniBern (Chapter 5) and physical and mineralogical determinations by CSIC (Chapter 5) and UAM (Chapter 6) laboratories

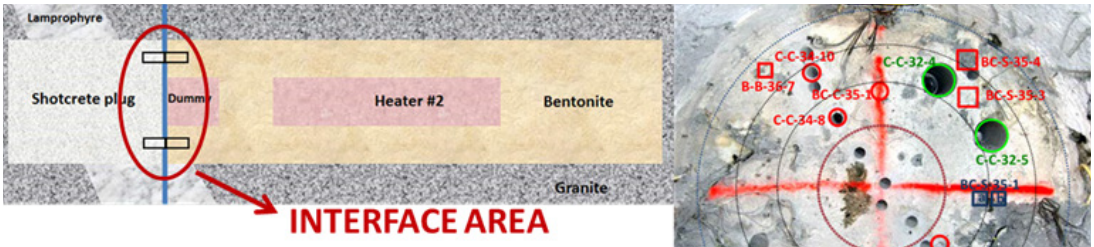

Overcorings C-C-32-4 and C-C-32-5
Macroscopic observations – UniBern
Additional studies of these samples will be made in the context of the EC CEBAMA project

Overcoring C-C-32-6
Macroscopic observations – UniBern
X-ray CT – UniBern and Sandia
Elemental mapping analysis – UniBern, Sandia, Obayashi
AFM, CEC and exchangeable cations and XRD – Obayashi
Additional studies will be made in the context of the EC CEBAMA project

Cores C-C-34-8, C-C-34-10, C-C-34-12, BC-C-35-1, BC-C-35-2 and hand-picked samples BC-S-35-1, BC-S-35-3 and BC-S-35-4
Water content, dry density and MIP – Ciemat
Specific surface area – UAM and Ciemat
Soluble ions – Ciemat
CEC and exchangeable cations – Ciemat and BGR
Carbonates and stable isotope analysis – UAM
Chemical analysis (XRF) – BGR
Elemental mapping analysis – UAM
XRD and TG – UAM and BGR
SEM (UAM, BGR and Ciemat) and TEM (Ciemat)
FT-IR – BGR and Ciemat

Fig. 26: Summary of samples of the concrete/bentonite interface analysed for physical, chemical and mineralogical determinations by different laboratories. Details on the specific characterisation of each sample and the partners involved in it are in Tab. 6-1 and the results are compiled in Chapter 6.

5 Concrete analysis: results

In this chapter, results from the cores C-C-32 are described. These cores were drilled with the main purpose of investigating the concrete evolution as a function of distance to both the bentonite and the granite boundaries. Although this chapter describes mainly the concrete properties, reference to the boundaries of the experiment are also made where appropriate. The observations closer to the interfaces should therefore also be compared to the results presented in Chapters 6 (bentonite) and Appendix A (granite). Tab. 5-1 summarises the samples used for concrete investigations, partners involved in the studies and type of analysis performed by each partner.

Tab. 5-1: Summary of samples, partners and analysis for concrete investigations

Reference	Type of sample	Partner studying the sample	Analysis
C-C-32-1 to 3	Core	CSIC	Permeability, mechanical properties, capillary suction, microstructure
C-C-32-4 to 6	Overcoring	UniBern	Internal structure, macroscopic aspects

5.1 Macroscopic observations (UniBern)

Observations of concrete were made during overcoring. Core segments extracted from drilling the 220 mm OD approach borehole C-C-32-4 in the concrete plug (Fig. 27) are compact, displaying the usual macro-porosity common to shotcreted concrete. While the second plug section (0-1.95 m) is textureless, the first section (1.95 – 2.75 m) displays a layered texture arising from shotcreting. The white sealing layer that separates the two plug sections is extremely well-bonded to the shotcrete, and did not separate during core wedging and extraction. Details of the flat-end steel fibres (Fig. 27, lower right) explain why core separation was difficult: the wedge-shaped ends are firmly held in the concrete, and fibres bridging a fractured core still provide a lot of strength. All fibres have a fresh, uncorroded appearance.

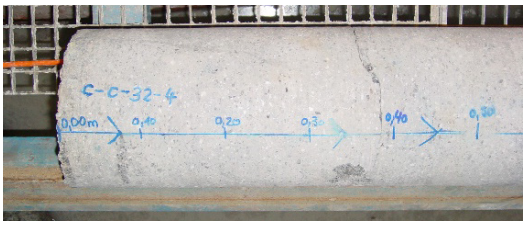

Concrete, second section, 0-0.55 m

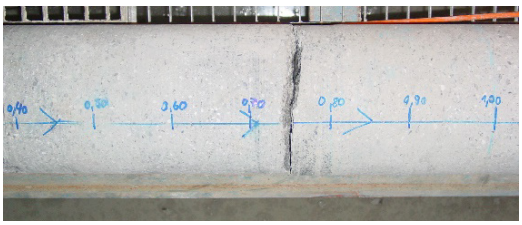

Concrete, second section, 0.4-1 m.

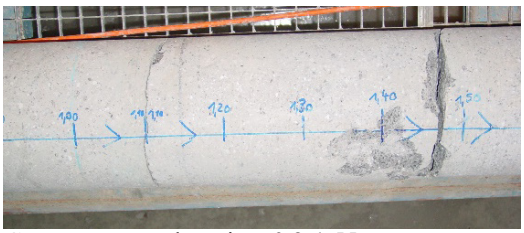

Concrete, second section, 0.9-1.55 m.

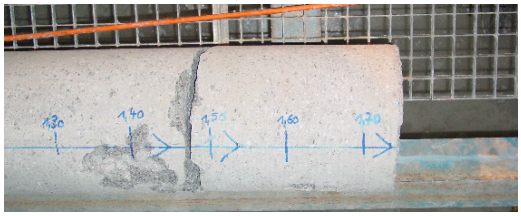

Concrete, second section, 1.25-1.75 m.

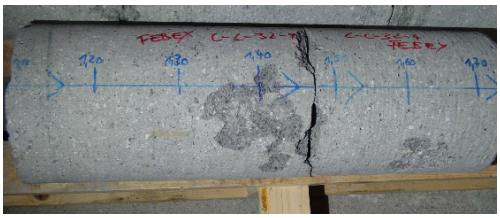

Concrete, second section, 1.1-1.75 m, moist surface

Concrete, second section, 1.85-1.65 m, wet surface. White sealing layer between plug sections.

Concrete plug, section without steel fibres, but with polymer fibres. Moist surface.

Concrete plug, section with flat-end steel fibres. Wet surface.

Fig. 27: Images of samples from a 220 mm approach borehole, C-C-32-4. Arrows point towards the plug/bentonite interface. The scale is drawn along the hinge line

The appearance of core segments from borehole C-C-32-5 is very similar to that from C-C-32-4 described above (Fig. 28). Some steel lines for sensors were caught in the shotcreting action just in front of the first core section, and these were intersected during drilling.

Concrete core from 0-270 cm. The white sealing layer separates the two plug sections at 195 cm.

Detail of deep end of concrete core with steel fibres.

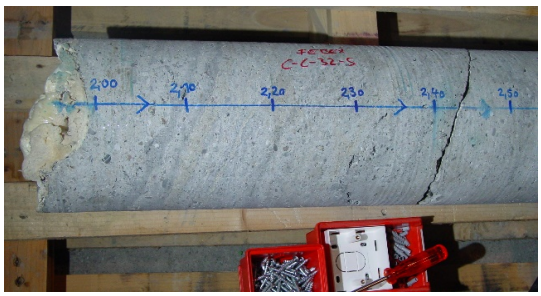

Detail of first plug section, starting at sealing layer at 195 cm. Layering from shotcreting is well visible.

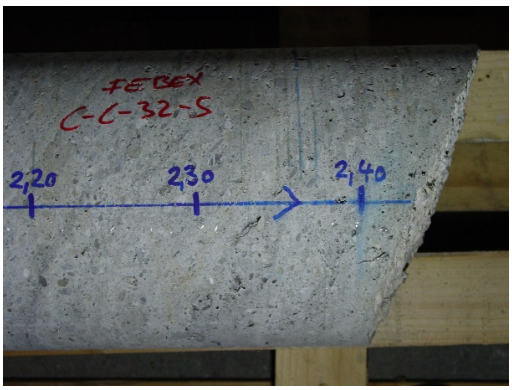

Detail of image on left side.

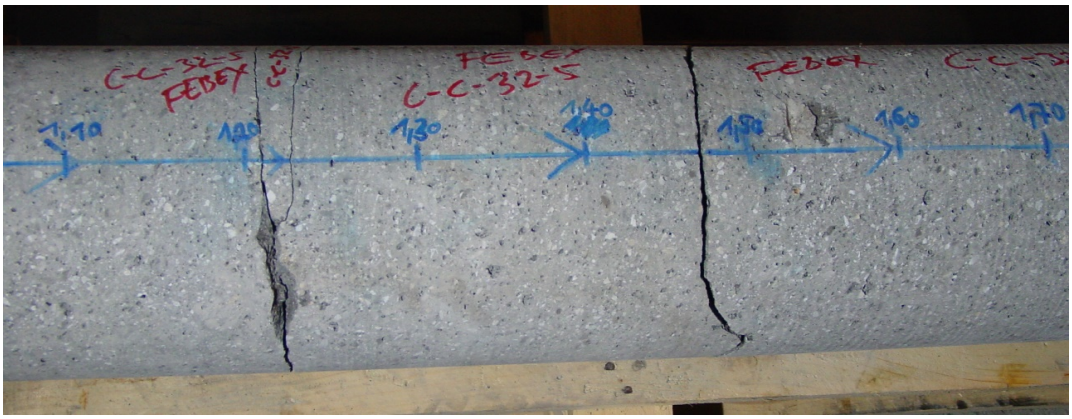

Detail of second plug section with massive texture, from 105-170 cm.

Fig. 28: Images of samples from the 220 mm approach borehole, C-C-32-5. Arrows point towards the plug/bentonite interface. The scale is drawn along the hinge line.

Core segments extracted from drilling the approach borehole in the concrete plug for C-C-32-6 (Fig. 29) are similar in appearance to the second plug section (0-1.85 m). The first section (1.85 – 2.75 m) displays a layered texture arising from shotcreting, but is more heterogeneous compared to the other two sampling locations (details below).

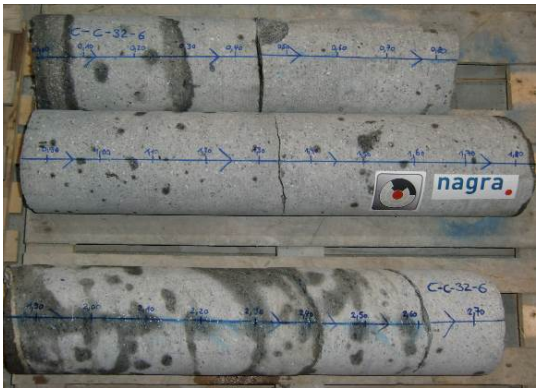

Concrete core from 0-275 cm. The white sealing layer separates the two plug sections at 185 cm.

Detail of deep end of concrete core in first plug section. Steel fibres are well visible. White surface represents a parting surface, freshly broken surface is grey.

Detail of region at interface between first (on right side) and second plug section, with a sealing layer at 185 cm. Layering from shotcreting is well visible.

Detail from first plug setion. Layering from shotcreting is well visible. Scale is marked along hinge.

Fig. 29: Images of samples from 220 mm approach borehole, C-C-32-6. Arrows point towards the plug/bentonite interface. The scale is drawn along the hinge line.

There is a pronounced difference in texture between the first and second plug section. The second section, nearly 2 meters in thickness is massive with only a weak layered texture in some areas. The core had to be forcefully broken in this section and broken surfaces invariably have a “fresh” aspect.

The first plug section, containing steel fibres, displays a layered aspect from the shotcreting, but also contains parting surfaces that most likely relate to some hiatus in shotcreting action. Near the plug base (location of C-C-32-6) coarse and porous or rubbly rebound layers (Fig. 30) are entwined in compact layered shotcrete. Rebound is material that gets deflected during shotcreting and accumulates at the base. Normally, for best results, such loose rebound

material is removed, but this can be difficult to achieve. The net result is a more porous and locally more permeable region at the base of the plug.

Fig. 30 (A and B) illustrates the difference between a “fresh” surface on breaking core, and a parting surface (a weak zone) from borehole C-C-32-4. Well visible is that bridging fibres are evident in case of a “fresh” surface, but no fibres are visible at the parting surface. Such surfaces may indicate – as stated above – a hiatus in the shotcreting action or some adjustments to fibre supply. Images C and D show a similar situation in sample C-C-32-5, again from the first section of the plug. Image E is a nice illustration of rubbly layers of rebound located in between normal and compact layered shotcrete observed in C-C-32-6, near the base of the plug. The rubbly rebound layers are widening towards the base of the plug and may be significantly more prominent further below the sampling location. Finally, image F illustrates a clump of steel fibres that was also observed in these heterogeneous areas of C-C-32-6.

A: Broken concrete with bridging steel fibres, C-C-32-4.

B: Parting surface, without steel fibres, C-C-32-4.

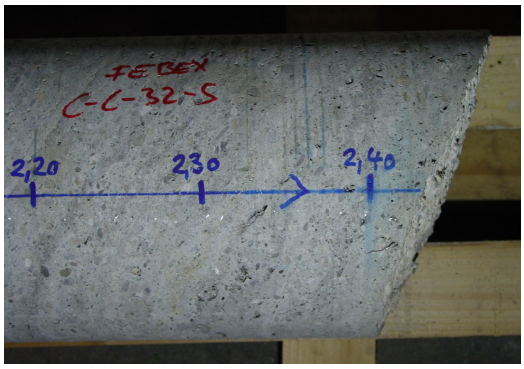

C: Layering in C-C-32-5. Location of image D is at the right end of the core (2.45 m).

D: Parting surface, C-C-32-5, without steel fibres.

E: Course rebound forming several rubbly layers within layered but compact concrete, C-C-32-6. The core is in upside-down position, with the hinge along the base of the image.

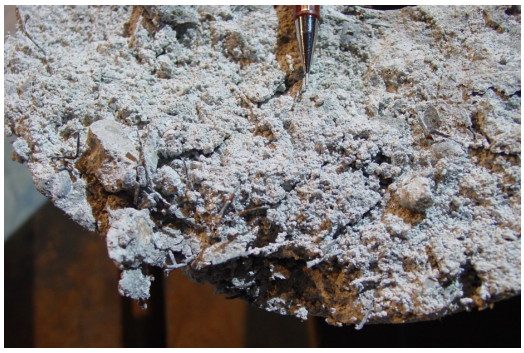

F: Details of a clot of steel fibres, C-C-32-6.

Fig. 30: Samples from all three boreholes illustrating interfaces and heterogeneities within the first part of the concrete plug.

Temperatures at the deep end of the boreholes and near the interface with bentonite are 26 - 28 °C measured at a distance of 25 cm from the interface (details in Mäder et al. 2016). The measurements were done after sampling the plug/bentonite interface, but when the heater was still in operation. Temperatures may have slightly cooled off during drilling operations.

These are purely qualitative observations and it is difficult to associate any variation in hydraulic or mineralogical properties with the observed heterogeneities. Nevertheless, it is important to consider that operational aspects may have a strong influence on the implementation of the engineering objectives locally.

5.2 Physical and mechanical properties (CSIC)

This section investigates the physical and mechanical properties of the plug construction sections 1 and 2. Compressive strength, dynamic elastic modulus, water absorption and capillary suction were determined in core C-C-32-2. This core is used as “reference material” because it is in the middle and hence, is a priori less affected by granite groundwater or bentonite porewater. The result is then compared with cores C-C-32-1 and 3, sampled in points of each section influenced either by granite or bentonite porewater.

Fig. 31 shows the mechanical properties of plug sections 1 and 2 of core C-C-32-2. The compressive strength of concrete from section 2 is higher than that measured in section 1, in agreement with the higher binder content used. Similar differences are observed in the dynamic elastic modulus obtained from ultrasound measurements. The differences between both sections were already observed during a quality control 28 days after plug installation (Huertas et al. 2006) and are maintained after 13 years. Although a slight decrease in compressive strength is observed in both sections after 13 years, this is a minor or even negligible difference. Thus, according to the results, concrete of both sections have not suffered from any significant alteration that would limit their mechanical properties during these 13 years.

Fig. 32 shows the water absorption curves obtained in plug sections 1 and 2 of core C-C-32-2 and Fig. 33 depicts the accessible porosity for water and the capillary suction coefficients calculated from the obtained water absorption curves. The samples of section 1 have slightly higher water absorption rates than those measured in section 2. Thus, the corresponding calculated accessible porosity for water and capillary suction coefficient are also higher in the concrete of section 1. Based on porosity and capillary suction, the potential durability of concrete from plug section 1 would be lower than that of concrete from plug section 2.

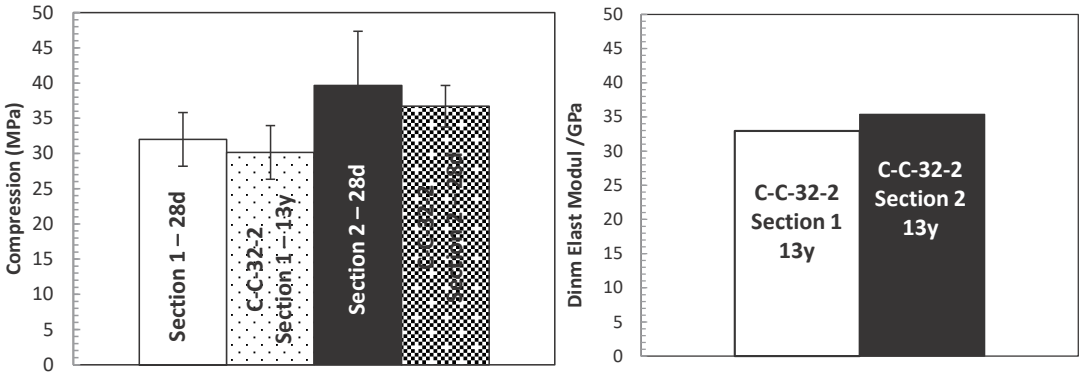

Fig. 31: Graphs show the mechanical properties of the concrete from the C-C-32-2 core. Left: compressive strength after 28 days (Huertas et al. 2006) and 13 years (C-C-32-2); Right: dynamic elastic modulus after 13 years in core C-C-32-2.

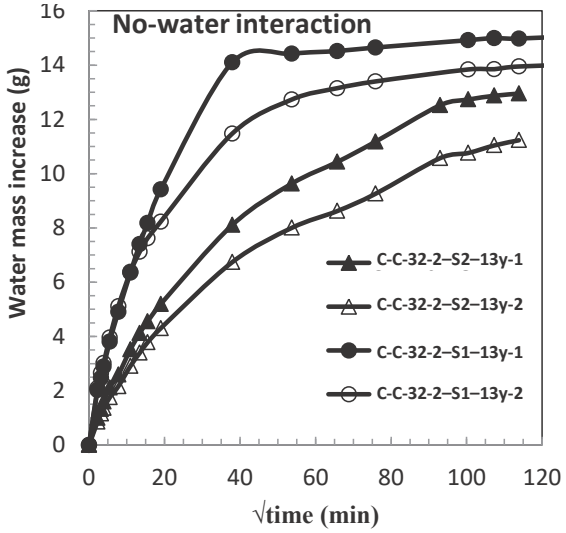

Fig. 32: Water absorption rates of the samples from sections 1 and 2 of core C-C-32-2.

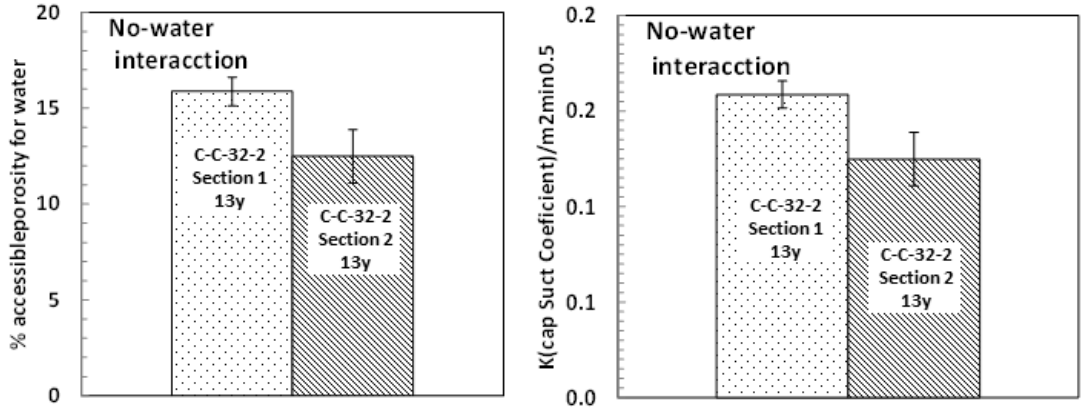

Fig. 33: Accessible porosity for water and capillary suction coefficients calculated in samples from sections 1 and 2 of core C-C-32-2.

Mechanical properties have also been measured on the concrete close to the granite wall, where it can be affected by the interaction with granite groundwater. Analyses of those parts of the plug far from the direct contact with the bentonite barrier were made in samples from cores C-C-32-1 and 3. The results are then compared with those obtained from core C-C-32-2.

Fig. 34 shows the mechanical properties of sections 1 and 2 of the three cores. Compressive strength of section 2 is slightly higher than that of section 1 in all cases, which could indicate a higher quality of the concrete in section 2 of the plug. There is not a clear influence of the granite groundwater attack in the concrete, since the values measured in samples from C-C-32-1 and 3 are similar to those measured in core C-C-32-2 (reference). Although granite groundwater has reached the cores, the leaching is probably not relevant at the analysed distance from the rock (around 20 cm). A similar trend was observed for dynamic elastic modulus calculated from ultrasound velocity and density of concretes.

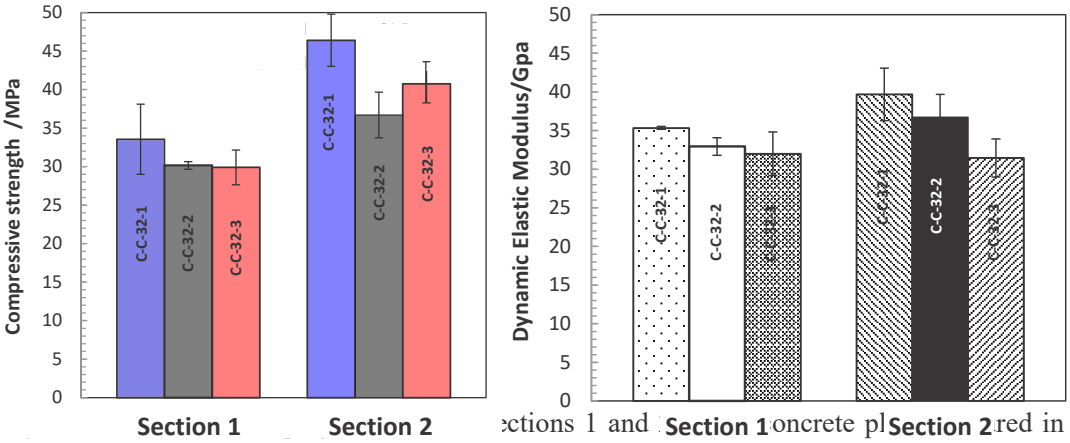

ections 1 and oncrete pl red in cores C-C-32-1 to 3 in zones far from the bentonite barrier. Left: compressive strength and right: dynamic elastic modulus. Data from core C-C-32-2 (reference) are depicted for comparison.

The water absorption curves obtained in these samples are presented in Fig. 35. In general, samples from section 1 show higher and faster water absorption rates than samples from section 2. Again, this indicates a higher quality of the concrete of section 2 of the plug. Comparing the results of the same section, there is no clear evidence of poorer quality of the samples from core C-C-32-1 (upper part) or core C-C-32-3 (lower part) of the plug. On the other hand, similar accessible porosity for water and capillary suction coefficients are calculated for sections 1 and 2 of each core (Fig. 36).

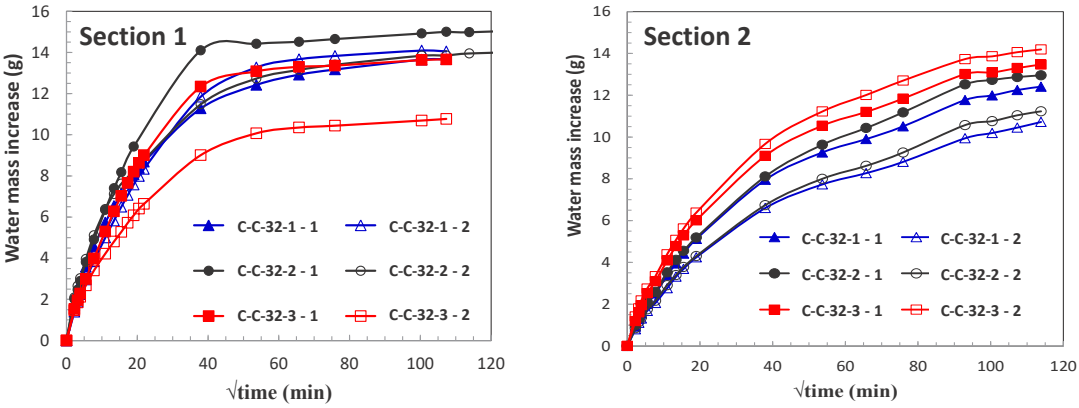

Fig. 35: Water absorption rates of concrete distant from bentonite barrier. Left: samples from plug section 1; Right: samples from plug section 2. Numbers 1 and 2 behind the core name indicates two analyses for each core.

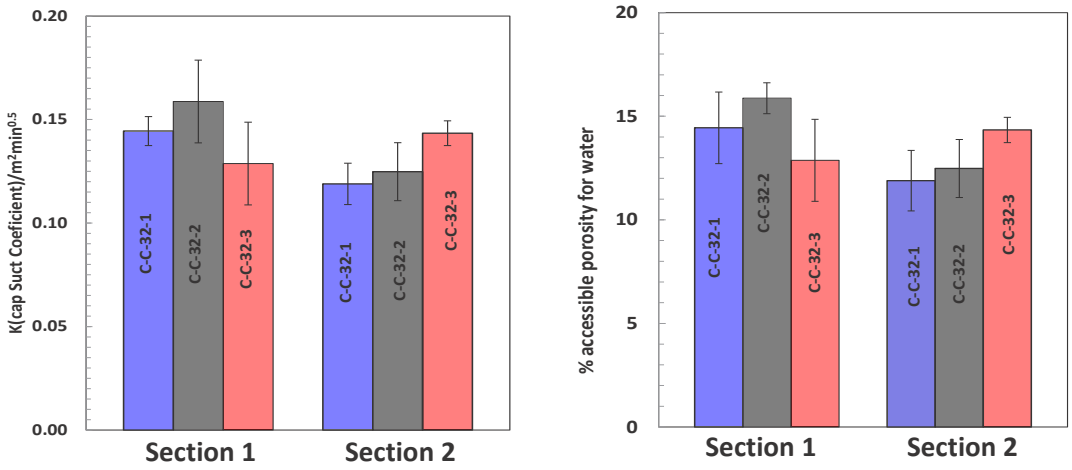

Fig. 36: Left: calculated capillary suction coefficient; Right: accessible porosity for water.

The water permeability tests were carried out in samples of section 1 of cores C-C-32-1 and 2. A typical Grimsel granite groundwater coming from the BO-ADUS borehole (Garralón et al. 2017) was used as eluent. The results are presented in Fig. 37. The water permeability coefficient (K) at the stationary state is in the order of 10^{-10} m/s.

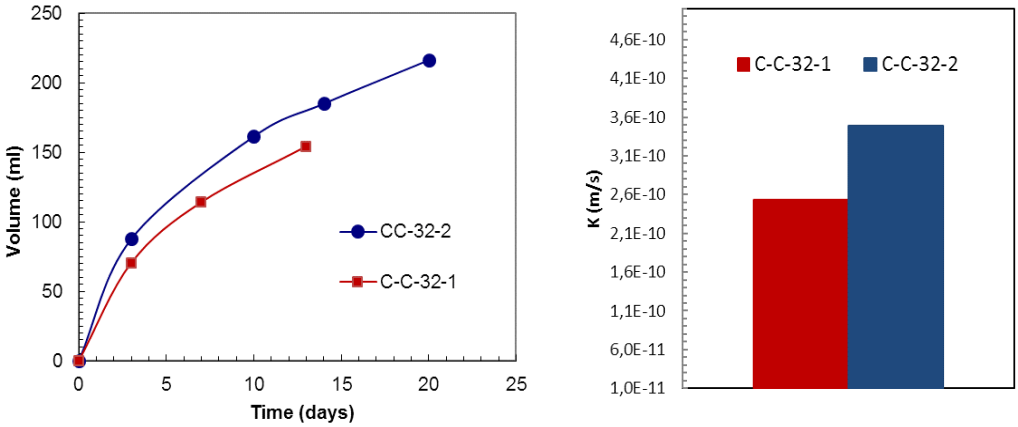

Fig. 37: Left: water volume taken up by samples, right: water permeability coefficient from section 1 of cores C-C-32-1 and 2.

5.3 Microstructural properties

5.3.1 Porosity and pore size distribution (CSIC)

Fig. 38 shows the total porosity and pore size distribution of sections 1 and 2 of core C-C-32-2 (reference) of the concrete plug. Concrete from section 2 has a slightly lower total porosity and a more refined pore size distribution for pore sizes higher than 0.1 µm than concrete from section 1. In fact, section 1 has a higher content of pores with diameter size between 0.1 and 5 µm than section 2. These results agree with the higher accessible porosity for water and capillary suction coefficients of concrete from section 1 and with the compressive strength results.

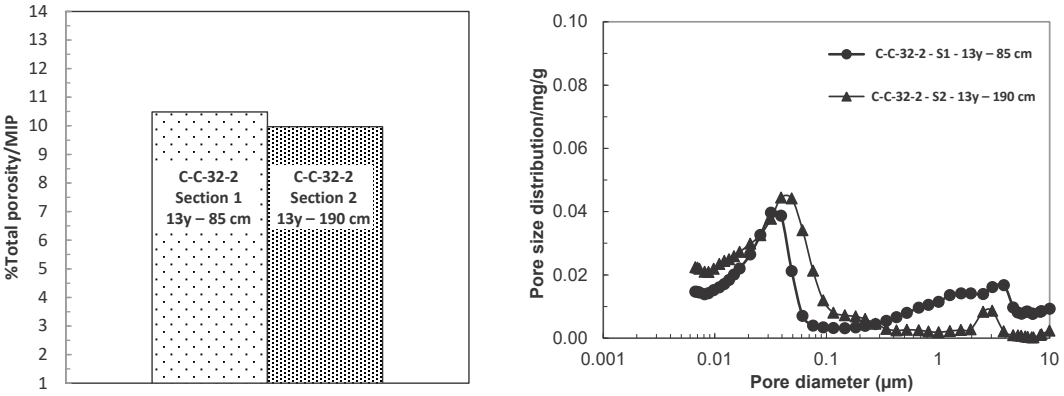

Fig. 38: Total porosity (left) and pore size distribution (right) of the samples of core C-C-32-2 in both sections by mercury intrusion porosimetry.

The total porosity and the pore size distribution of cores C-C-32-1 and 3 in zones far from the bentonite and influenced by granite groundwater are depicted in Fig. 39. Regarding the

differences between concrete plug sections 1 and 2, the concrete of section 2 has lower total porosity and more refined pore size distribution than the concrete of section 1 in all the evaluated core locations. Comparing the samples from a same section, the total porosity of section 1 of cores C-C-32-1 and 3 is slightly higher than the porosity measured in the C-C-32-2 (reference). The interaction of the concrete with the granite groundwater can enhance dilution processes that decrease the hydrates content, thus increasing the total porosity of the cementitious matrix. The differences in section 2 are less significant although the concrete from core C-C-32-3 has the highest total porosity. The porosity investigations of concrete-bentonite interfaces confirm this observation (see section 6.2.2).

Regarding the pore size distribution, the main differences are observed in the concrete of core C-C-32-3. In fact, the lower quality of the lower part of the concrete plug was evident during the dismantling operations. However, this poorer quality of the lower part of the plug can be due also to the use of the shotcreting technique as this is a phenomenon usually observed in the construction of different shotcreted concrete plugs.

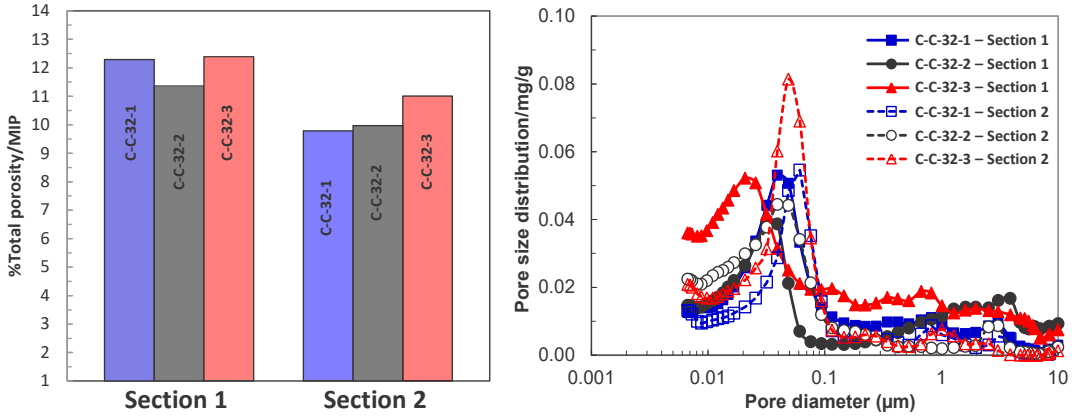

Fig. 39: Total porosity (left) and pore size distribution (right) of the samples far from bentonite barrier.

To check the influence of the bentonite porewater on the concrete porosity, the porosity results of concrete from cores C-C-32-1 and 3 close to the bentonite buffer (section 1) and the results of section 1 of reference core C-C-32-2 are compared.

The interaction of the bentonite porewater with the concrete alters the concrete's pore structure. Two processes could lead to the observation in Fig. 40 (left); 1) an increase of total porosity as consequence of leaching, and 2) new phase formation in the concrete near the bentonite interface (0-1 cm). A densification is also detected at a distance of 3 cm, associated with the advance of the concrete hydration in the presence of water and the subsequent precipitation of new phases. The analyses of the dedicated concrete-bentonite samples confirm this change in microstructure (see section 6.2.2).

Related to the increase in total porosity, an increase in capillary pores is detected in the altered concrete near the bentonite where most interaction reactions of the concrete plug with bentonite water take place (Fig. 40, right). Two regions of capillary porosity are altered; pores <0.1 µm, probably as a consequence of phase dissolution, and larger pores (0.1 to 1 µm) as a consequence of microcracking in the cement paste.

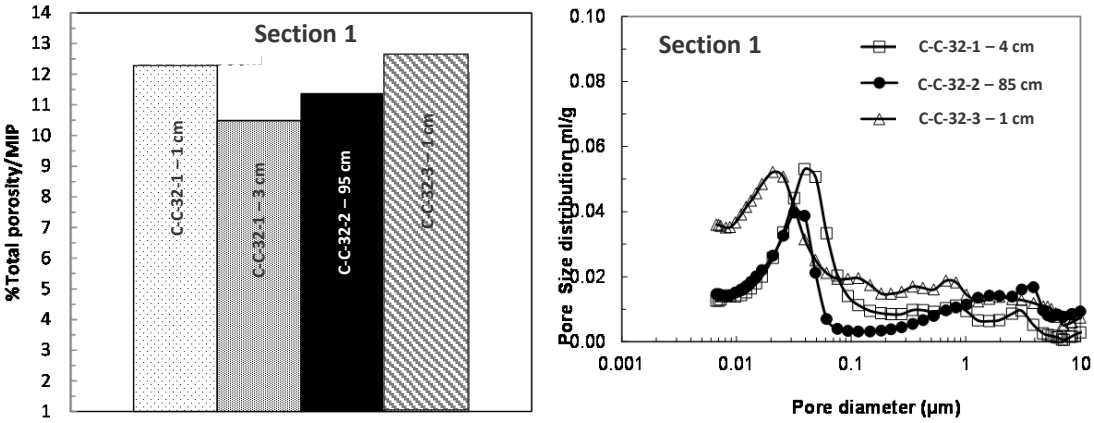

Fig. 40: Total porosity (left) and pore size distribution (right) of the samples near the bentonite barrier. Cores C-C-32-1 and 3 are compared with core C-C-32-2 (reference). Distances (cm) refer to distance from the interface with bentonite.

5.3.2 Pore solution pH (CSIC)

The pore solution pH of different points of sections 1 and 2 of core C-C-32-2 (reference) are shown in Fig. 41(left). Similar values are obtained in both sections and in all cases the pH is above 12.5, as usually obtained in conventional concretes based on Ordinary Portland Cement and low content in supplementary cementitious materials with high silica content. The results suggest that the cementitious matrix of the concrete has portlandite.

Fig. 41 (middle) shows the pore fluid pH of the samples of sections 1 and 2 of cores C-C-32-1 and 3 in those points far from the bentonite to check the influence of granite groundwater on the concrete. Results are compared with those of core C-C-32-2 (reference). The pH measured in section 2 in the three cores is similar. However, the pH of section 1 of the reference core (C-C-32-2) is higher than in the other two, core C-C-32-1 being the lowest (12.5). The lower pH values agree with possible dissolution of hydrates.

Fig. 41 (right) depicts the pore fluid pH of samples of section 1 of cores C-C-32-1 and 3 close to the bentonite to check the influence of bentonite porewater on the concrete. A decrease of the concrete pore solution pH is observed in the zones closest to the bentonite. The pH of the core C-C-32-2 (reference) is 12.80 ± 0.05, while the pH values of the concrete from cores C-C-32-1 and 3 at 1, 3 and 4 cm from bentonite are lower, and below 12 at 1 cm in core C-C-32-1. The direct action of granite groundwater and the influence of the bentonite porewater have both favoured the dissolution of soluble components in the concrete followed by a decrease of the concrete pore solution pH.

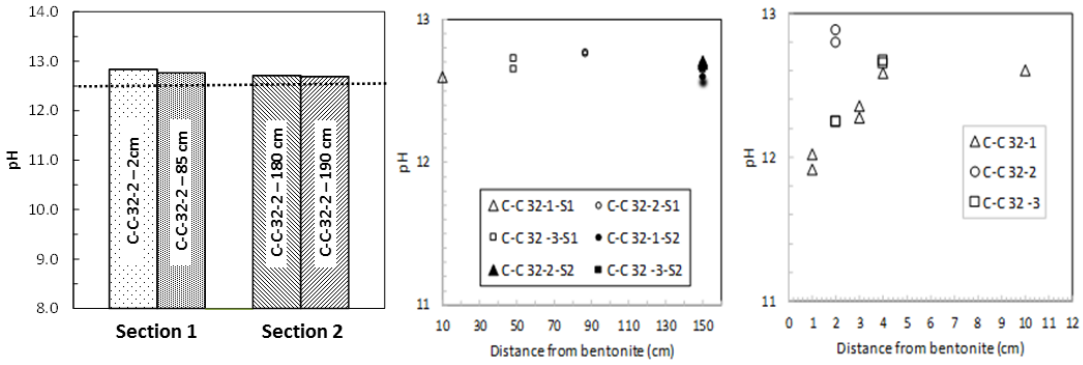

Fig. 41: Pore fluid pH values measured in the samples from sections 1 and 2 of core C-C-32. Distances (cm) refer to distance from the interface with the bentonite. Left) C-C 32-2 No water interaction (Sections 1 and 2). Middle) Granite water interaction (Sections 1 and 2), Right) Bentonite water interaction (Section 1).

5.3.3 Soluble ionic composition (CSIC, UAM)

The ionic composition of sections 1 and 2 of core C-C-32-2 (reference) is shown in Tab. 5-2. Ca and alkali ions Na and K are the main components, typical of a pore solution composition of Portland cement pastes. Sulphates are present in low concentration and probably come from the dissolution of gypsum used for setting control. The concentration of Si, Al and Mg is practically negligible (see also section 6.3.1).

Tab. 5-2: Soluble ionic composition of concrete from sections 1 and 2 of core C-C-32-2. No water interaction

Sample C-C-32-2	Total Cl (% binder mass)	SO_3	Ca	Na	K	Si	Al	Mg
		Water soluble (ppm)						
Section 1 close to the dummy	0.04	14	269	159	296	0.76	0.4	0.06
Section 1 (85 cm)	0.04	22	142	347	589	0.70	0.4	0.04
Mean	0.04	18 *±6*	205 *±90*	253 *±133*	442 *±207*	0.73 *±0.04*	0.4 *±0,0*	0.05 *±0.01*
Section 2 (190 cm)	0.04	49	247	234	964	1.03	0.2	0.01

Pore solution of samples C-C-32-1 and 3 in those points far from the bentonite and influenced by the granite groundwater is depicted in Fig. 42. The soluble content is dominated by SO_3, Ca and alkalis (Na and K), as in core C-C-32-2. However, Ca, Na and K concentration of cores C-C-32-1 and 3 in section 1 is lower than in core C-C-32-2, which can be associated to an incipient leaching process that starts dissolving and leaching the more soluble components of the concrete. Such differences are less evident in section 2, with a large scatter in the measurements, probably as a consequence of a better quality concrete of this section, already mentioned in section 0.1. Minor ion components Si and Al do not show relevant changes.

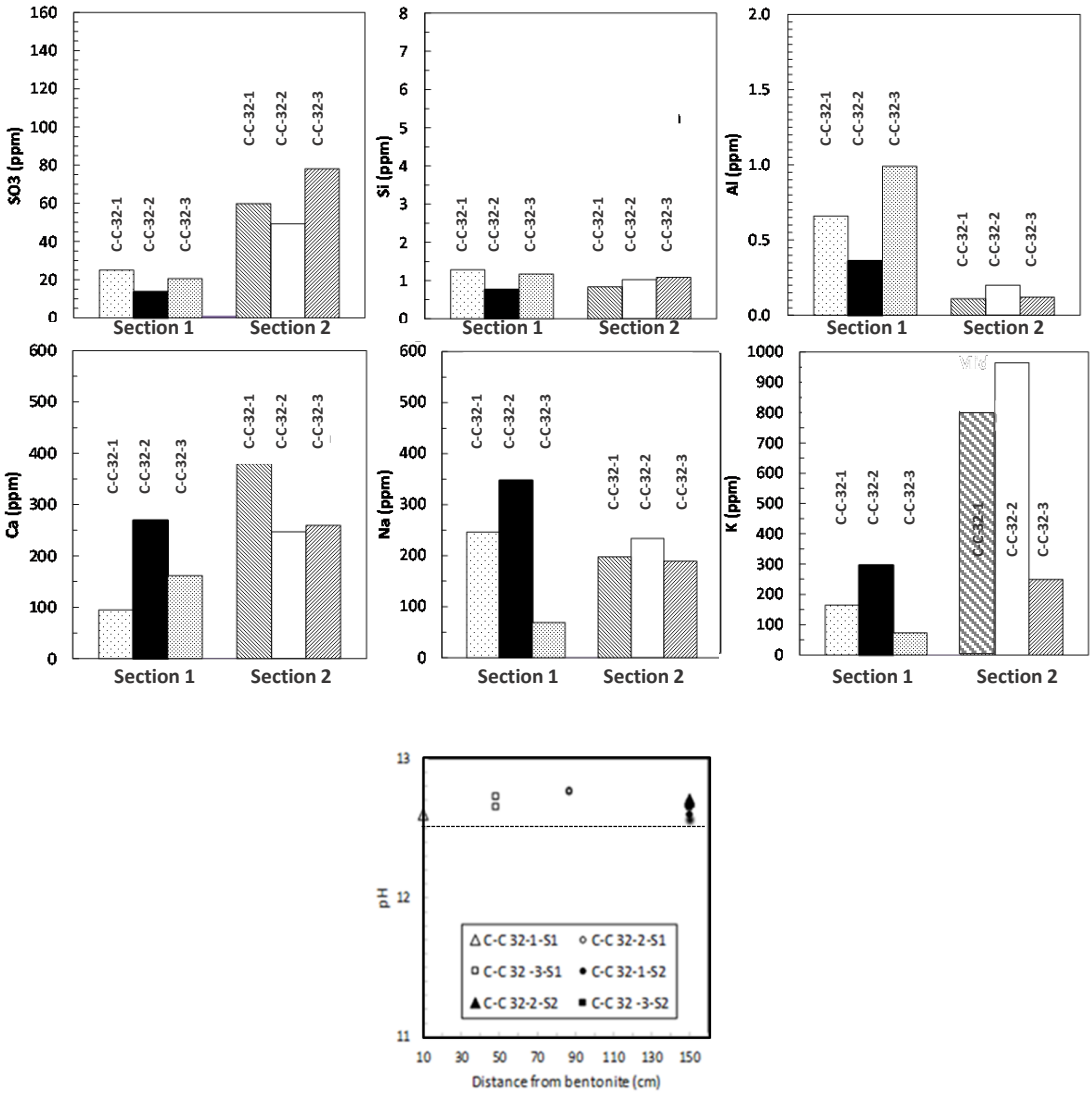

Fig. 42: Soluble ion contents in the samples far from the bentonite buffer in sections 1 and 2 of the three cores C-C-32-1 to 3. Results reflect the interaction with the granite water. Graph in the bottom shows the pH measurements in those samples.

The main water soluble ions of concrete close to the bentonite in Section 1 (Na, K, Ca, SO3, Cl) are represented in Fig. 43. There are clear differences between core C-C-32-2 (reference) and cores C-C-32-1 and 3. The results suggest the coupling of different processes depending on the source of water interacting with the concrete and their composition.

A decrease in the alkali content, both Na and K, is observed in cores C-C-32-1 and 3 compared to those measured in concrete from core C-C-32-2 (reference). It confirms the leaching of alkali ions due to the action of granite groundwater which agrees with the decrease of pH observed in Fig. 41. However, the concentration of soluble Ca is higher in cores C-C-32-1 and 3 compared to core C-C-32-2, even when considering the large variability of the results obtained for this ion (Fig. 43). This increase in the soluble Ca can be explained by Ca coming from the bentonite once it is saturated with granite groundwater and when some

redistribution in the filling of cation exchange sites occur. Porewaters from the FEBEX bentonite are rich in Ca ions (Fernández & Villar 2010; Garralón et al. 2017). Thus, Ca diffusion from the bentonite porewater into the concrete porewater has to play an important role in explaining the results. In fact, there is evidence from the $\delta^{13}C$ isotopic signature in bentonite carbonates indicating calcite redistribution from the bentonite to the concrete interface (Fernández et al. 2017). The interaction of bentonite porewater with the cement paste concrete is further confirmed by the analysis of dissolved sulphates and total chlorides in cores C-C-32-1 and 3 near the bentonite. Both anions are present in those cores at depths close to bentonite while their content is very low in core C-C-32-2 (reference) at similar depths (with no direct contact with bentonite or granite waters). Nevertheless, a clear difference can be seen in the penetration depth between both anions. While Cl penetrates faster, even up to 5 cm from the bentonite barrier, the high sulphate contents can only be detected in the very first centimetres of the concrete close to the bentonite. The studies of several interfaces with bentonite (see part 6 of this report) reveal high sulphate concentrations close to the bentonite surface, while for chloride, the distribution is more heterogeneous, in agreement with its more mobile behaviour (Cuevas et al. 2016). The different reaction capacity of the cement for the two anions must also influence the different penetration depths detected. Moreover, although the cement used in the construction of the plug has a high Ca content (around 20% of limestone filler) this may not be contributing to solubility of Ca due to the lower values measured in core C-C-32-2.

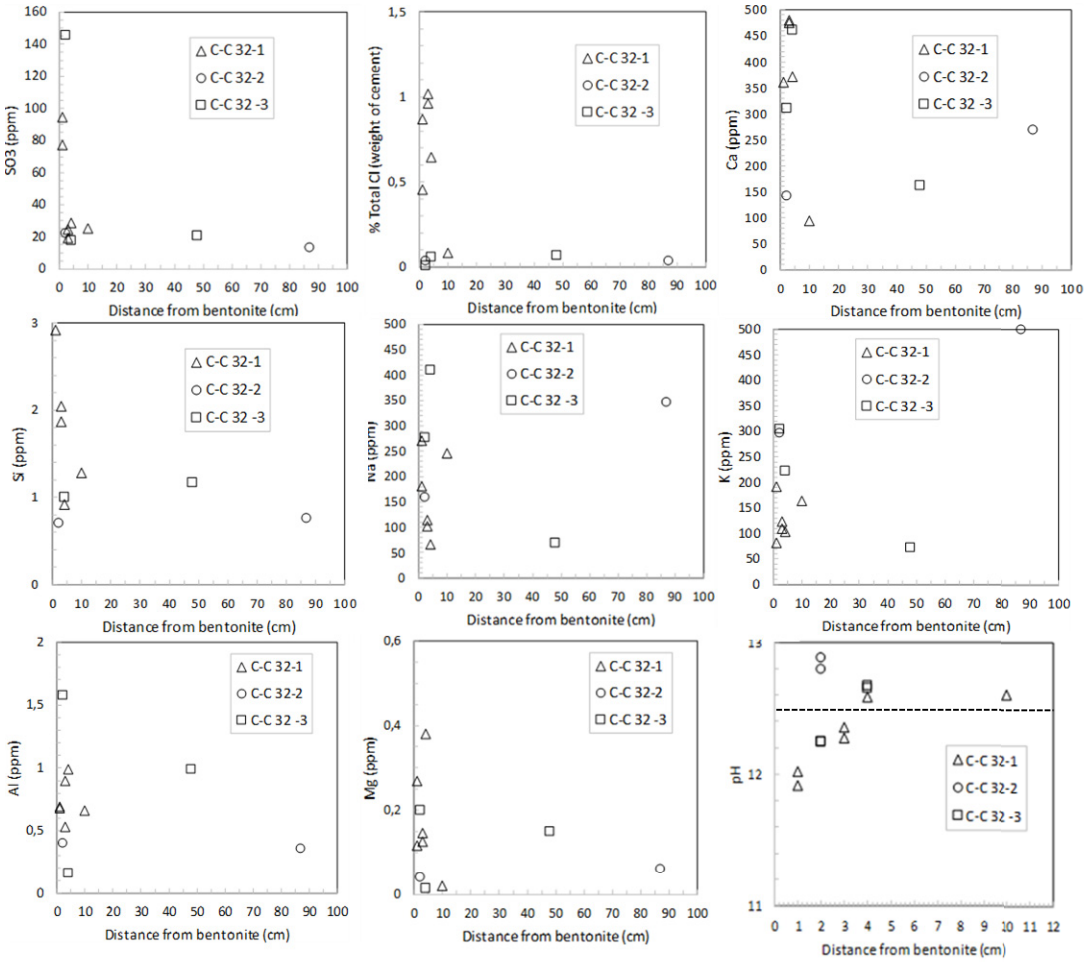

Fig. 43: Soluble ion contents in the samples of the cores C-C-32-1 and 3 near bentonite compared to core C-C-32-2 (reference). Measurements of pH are in the bottom-right of the figure. Distance (cm) refer to the interface with the bentonite, being 0 the point of contact concrete/bentonite.

Other differences are observed in the soluble contents of Si, Al and Mg, although they are in concentrations below 5 ppm in all cases. Their presence is practically negligible in core C-C-32-2 (reference) (0.07, 0.04 and 0.05 ppm, respectively). After interaction with granitic and bentonite waters (cores C-C-32-1 and 3), an increase is detected in all elements up to concentrations of 7, 1 and 0.3 ppm (Si, Al and Mg, respectively). Certainly, these concentrations are not significant compared to those of Na, K, Ca, SO_3 and Cl, but in all cases the concentrations are at least two orders of magnitude higher than the values measured in core C-C-32-2. Consequently, these elements will diffuse from the bentonite barrier into the concrete.

5.3.4 Mineralogical studies (CSIC)

5.3.4.1 X-ray diffraction analysis

The X-ray diffractograms of the concrete samples from sections 1 and 2 of core C-C-32-2 (reference) are shown in Fig. 44. The length value specified in each XRD indicates the distance to the dummy. Most of the obtained peaks refer to the minerals of the aggregates used in concrete, but portlandite and ettringite peaks are clearly identified. The ettringite peak is equally large as the portlandite peak in the concrete of section 1, which is very remarkable. This could be related to an ettringite content higher than the one usually found in a conventional Portland cement concrete.

The X-ray diffractograms of the concrete samples affected by the granite groundwater interaction but not by the bentonite contact are shown in Fig. 45. The most relevant information obtained in the XRD pattern is the decrease in the portlandite peak detected in the C-C-32-1 and 3 cores of section 1, which agrees with dissolution processes of this hydrate due to the interaction of the concrete plug with the surrounding groundwater. In fact, in section 1 of core C-C-32-1 the portlandite peak cannot be detected in agreement with a pore solution pH value of 12.5. The pH decrease shown in part 5.4.2 can be a consequence of several processes, mainly alkali (Na and K) leaching followed by portlandite dissolution. It is well known that at pH < 12.5 the presence of portlandite is limited or even invisible in the cementitious matrix.

Again, it is remarkable that the intensity of the ettringite peaks are higher than expected, as previously mentioned. Regarding the XRD patterns obtained in the concrete of section 2 of the plug, the decrease of the portlandite peak is less clear. The lower alteration of the concrete of this section of the plug is, therefore, demonstrated again.

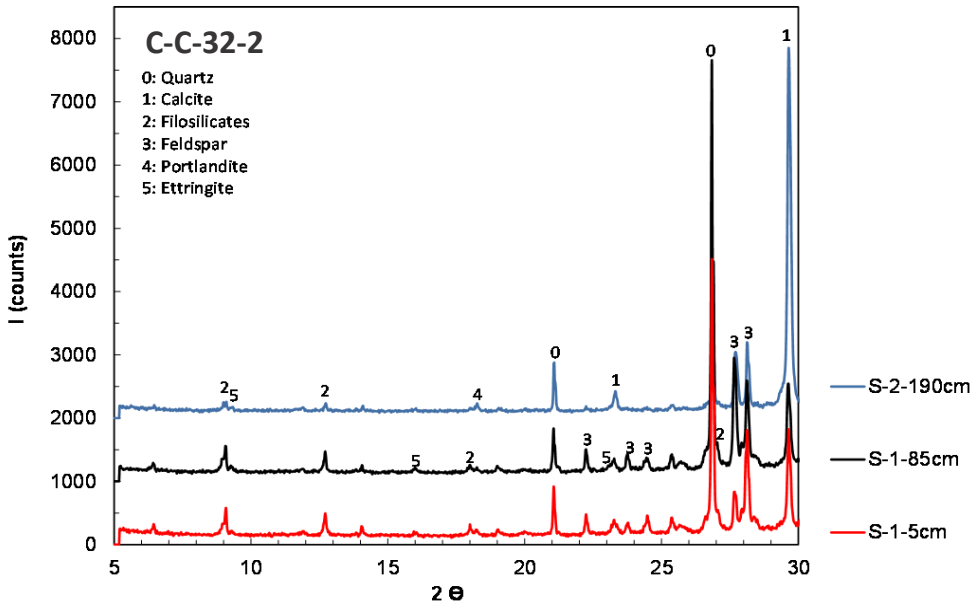

Fig. 44: XRD patterns of the concrete samples from sections 1 and 2 of the core C-C-32-2. Minerals of the cement paste are identified.

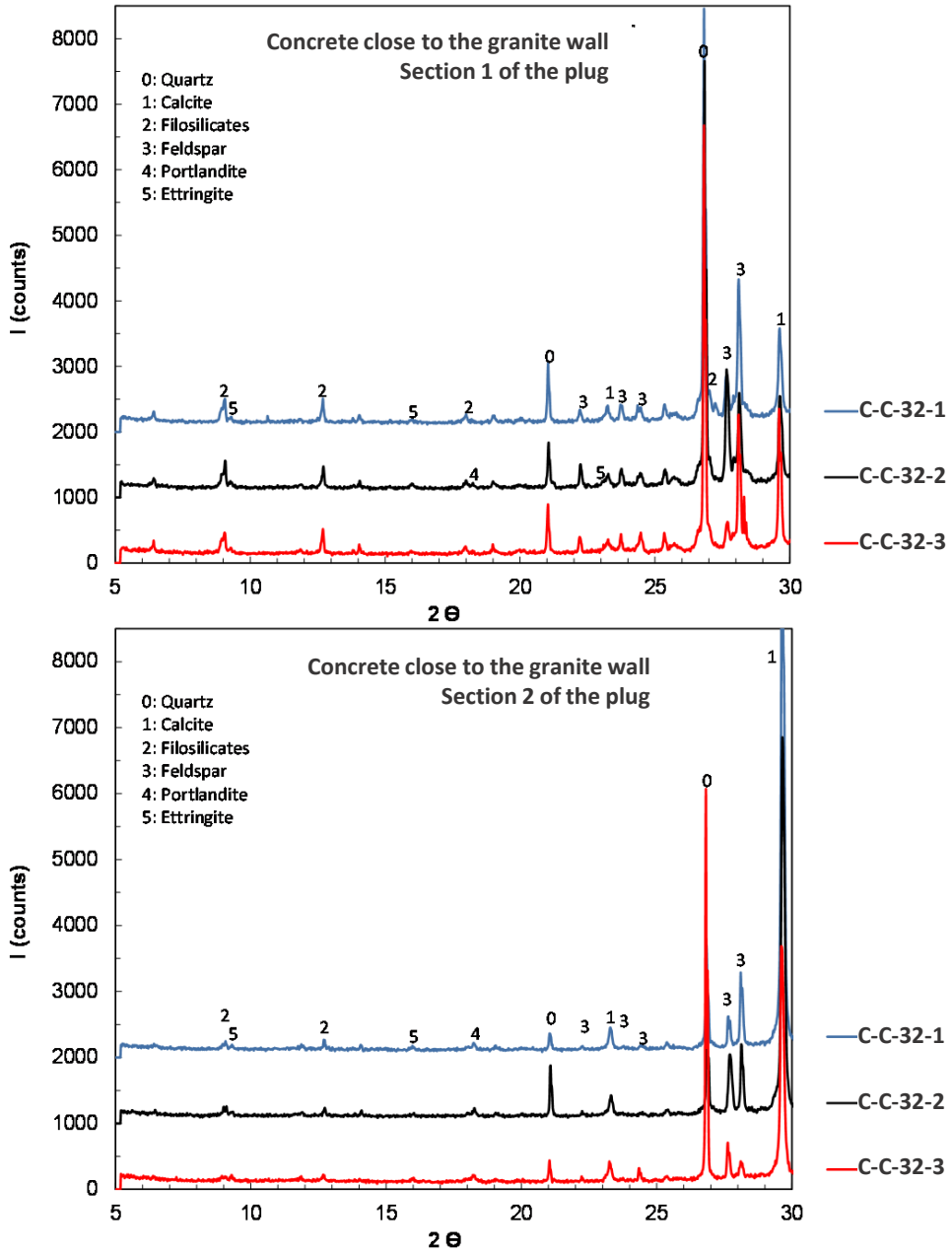

Fig. 45: XRD patterns of the sections 1 (upper) and 2 (lower) of the cores C-C-32-1 and 3 in the zones of the concrete plug closest to the granite. Spectra of core C-C-32-2 are shown as reference.

Fig. 46 shows the XRD pattern of the concrete from section 1 of cores C-C-32-1 and 2 at different distances from the bentonite interface (<1 – 4 cm). They are compared to the XRD pattern of the concrete sampled from core C-C-32-2 (reference) at 85 cm from the dummy. The objective is to check the influence of the bentonite on the concrete.

The XRD patterns are shown between 2θ values of 5° and 20° in order to remark the more interesting peaks. The Portlandite peak, disappears close to the bentonite barrier (<1cm) while

it is detected at further distances. Therefore, apart from a portlandite dissolution promoted by the interaction of the concrete with the granite groundwater, the interaction of the concrete with the bentonite water accelerates this process. However, the most relevant alteration promoted by the interaction of the concrete with the bentonite barrier is the increase in the ettringite content. High amounts of this phase are observed along all the concrete core lengths. In fact, the intensity of the ettringite peaks (2θ = 9.2 and 19) are as important as the intensity of the second portlandite peak (2θ = 18.09) and even more important close to the bentonite barrier. This high intensity of the ettringite peaks is related to the use of the shotcreting technique to construct the plug that implies the use of accelerator admixtures. Although the cement composition was unknown Tab. 1-1 indicates that at least a 6% of accelerator was used to shotcrete the concrete. According to the producer identification this accelerator had high Al content, thus promoting the initial ettringite formation to obtain the fast hardening required in the concrete after shotcreting. Fig 40 demonstrates that the closer the concrete is to the bentonite the higher the intensity of the ettringite peaks. In fact, the maximum intensity of these peaks are detected just in the concrete/bentonite interface (few mm from bentonite).The peak associated with the presence of Friedel salt (2θ = 11.2) is clearly observed at certain distances from the bentonite interface larger than 2 cm; this also corresponds with a decrease in intensity of the ettringite while close to the bentonite the ettringite peak is higher.

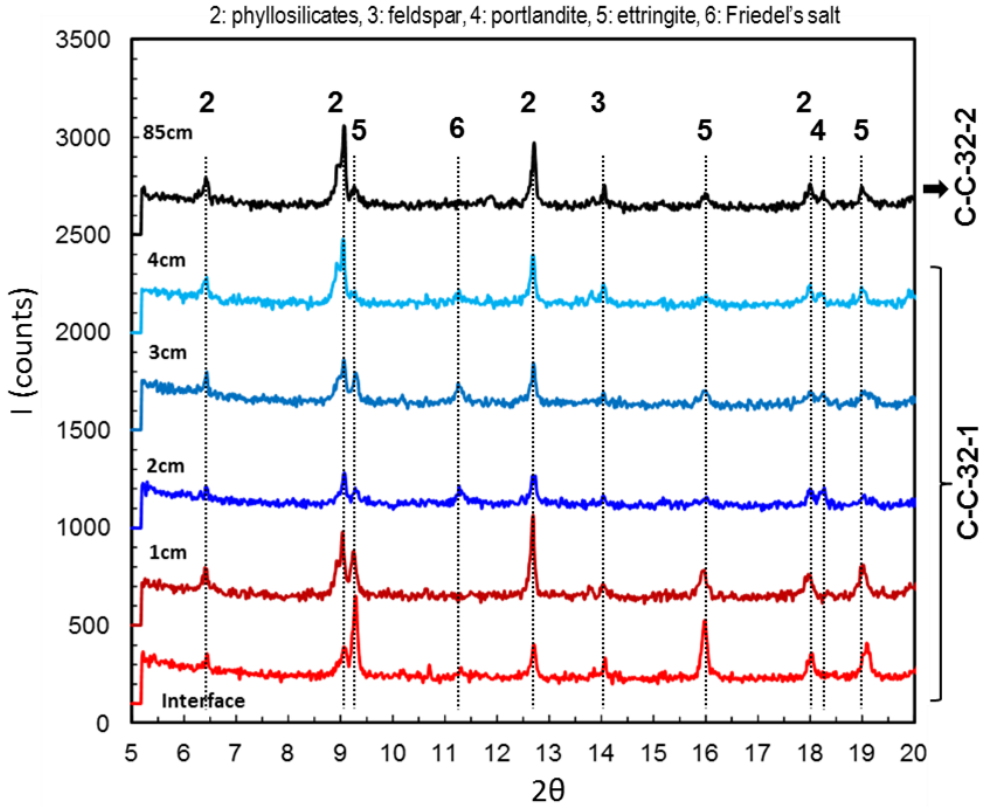

Fig. 46: XRD pattern of the concrete close to the bentonite affected by interaction with bentonite porewater compared to the XRD of C-C-32-2 sample.

5.3.4.2 Scanning Electron Microscopy analysis

SEM images and analyses of sections 1 and 2 of core C-C-32-2 (reference) are shown in Fig. 47 and Fig. 48. The main feature to point out is the high amount of ettringite crystals detected along the two sections. Ettringite nodules of at least 100 μm are clearly observed and they are filling air voids in many cases (Fig. 47A and Fig. 48). Some microcracks are detected but these cannot always be attributed to ettringite since they are also present in the bulk cement paste. These microcracks are probably shrinkage phenomena as a consequence of drying or heat during hardening and hydration or because of sample preparation. In this sense, the initial ettringite formed in the concrete plug does not seem to induce expansive phenomena.

EDS microanalyses are shown below the pictures in Fig. 47 and Fig. 48. The x-axis of the figures has no title or scale since each result refers to a specific EDS analysis made in the cement paste (green spots in the pictures). Concerning the cement paste the percentage of SiO_2 corresponds with common values found in C-S-H gels of a conventional Portland cement paste, but the content of CaO is too high as a consequence of the limestone filler present in the cement. It results in C/S ratios between 2 and 3, while in a common OPC this ratio ranges from 1.5 to 2. Therefore, the calcium content of the calculated C/S ratios can be overestimated due to the size of microanalysis area and the presence of limestone filler microparticles within the cementitious matrix. Some Al and S (<5%) is always found with local EDS analysis. According to the results obtained it seems evident that concrete not affected by granite groundwater has not suffered any significant alteration in the 13 years of operation of the FEBEX plug. Analyses on the bottom of Fig. 47 and Fig. 48 correspond to different nodules of sections 1 and 2 of the core C-C-32-2 which confirm the ettringite structure.

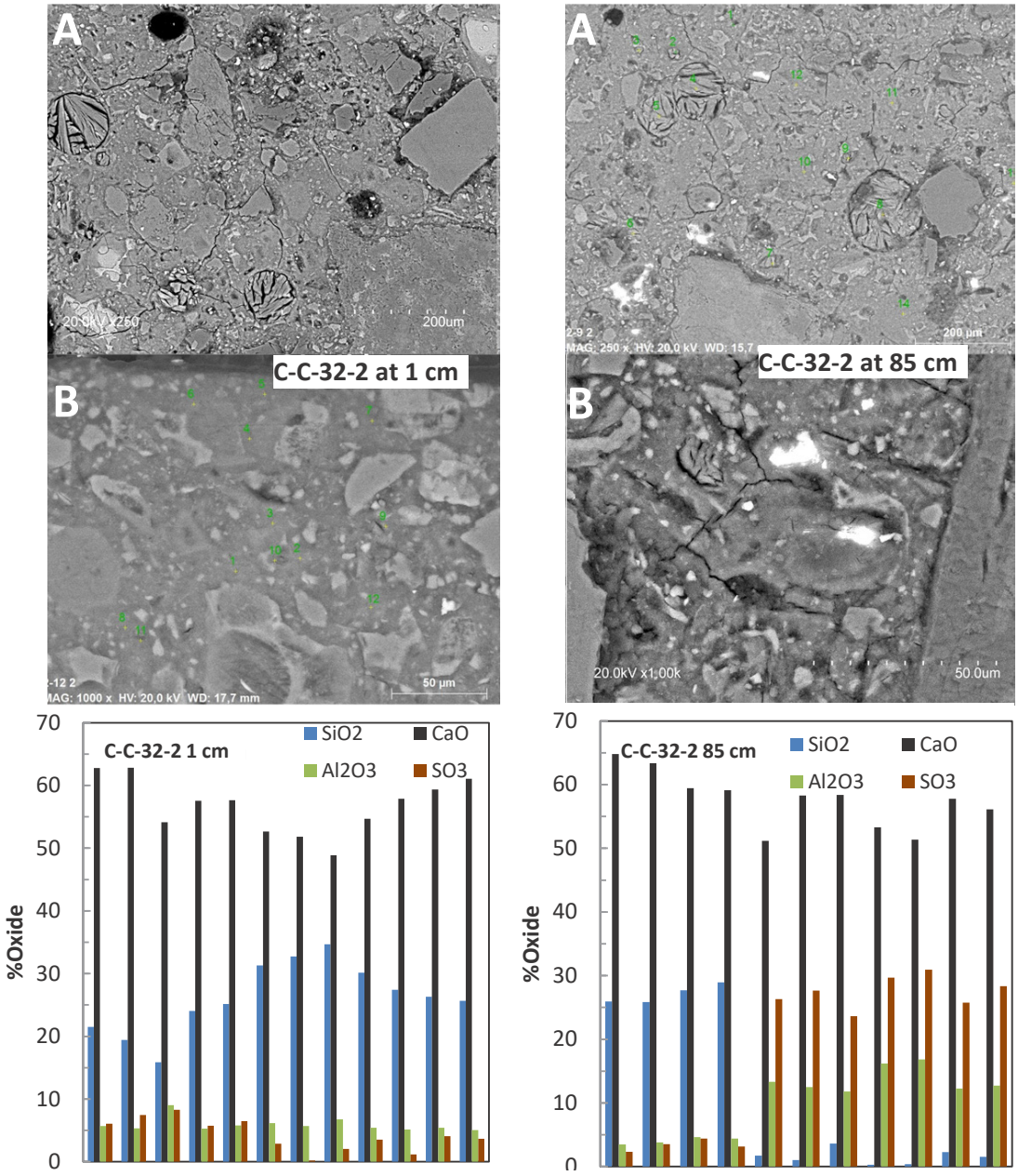

Fig. 47: BSEM (back-scattered SEM) images of samples from section 1 of core C-C-32-2 at 1 cm (left) and 85 cm (right) from the bentonite. Analysis (% oxides) of C-S-H (left) and C-S-H and ettringite (right) in the cement paste are shown below. Analyses correspond to green spots in the pictures.

SEM images and analyses of sections 1 and 2 of cores C-C-32-1 and C-C-32-3 in those zones far from the bentonite influence are shown in Fig. 49 and Fig. 50, respectively. In the SEM images the typical ettringite nodules found in core C-C-32-2 (reference) are clearly observed in samples from sections 1 and 2 of the concrete, although some microcracks grow from them to the cement paste, more than in the concrete analysed from core C-C-32-2; they are filling air voids in many cases. Microcracks can be a consequence of leaching and shrinkage, but loss

of density of cement paste is not observed, neither in concrete from section 1 or 2 of these cores, nor in zones close to the granite compared with the reference concrete (C-C-32-2).

EDS microanalysis of all different phases mentioned above are shown in Fig. 49 and Fig. 50 (bottom part of the figures). The x-axis of the figures has no title or scale since each result refers to a specific EDS analysis made in the cement paste (green spots in the pictures). The % of element, expressed as oxide, indicate that the SiO_2 is similar to that of the reference core (C-C-32-2). The CaO content also indicates that C-S-H is not significantly affected. The presence of ettringite in nodules is analysed as well. Certain levels of Al and S (<5%) are also found with local EDS analysis of C-S-H in both sections.

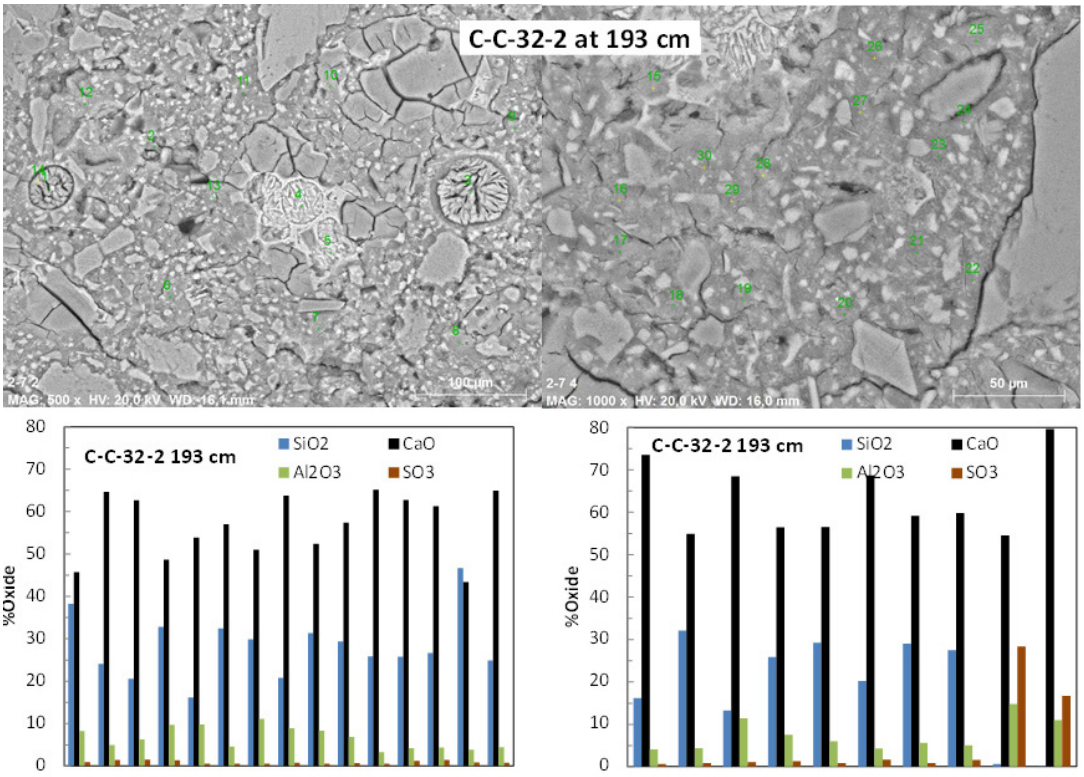

Fig. 48: BSEM images of a sample from section 2 of core C-C-32-2 at 193 cm from the bentonite. Analysis (% oxides) of C-S-H (left) and C-S-H and ettringite (right) in the cement paste are shown below. Analyses correspond to green spots in the pictures.

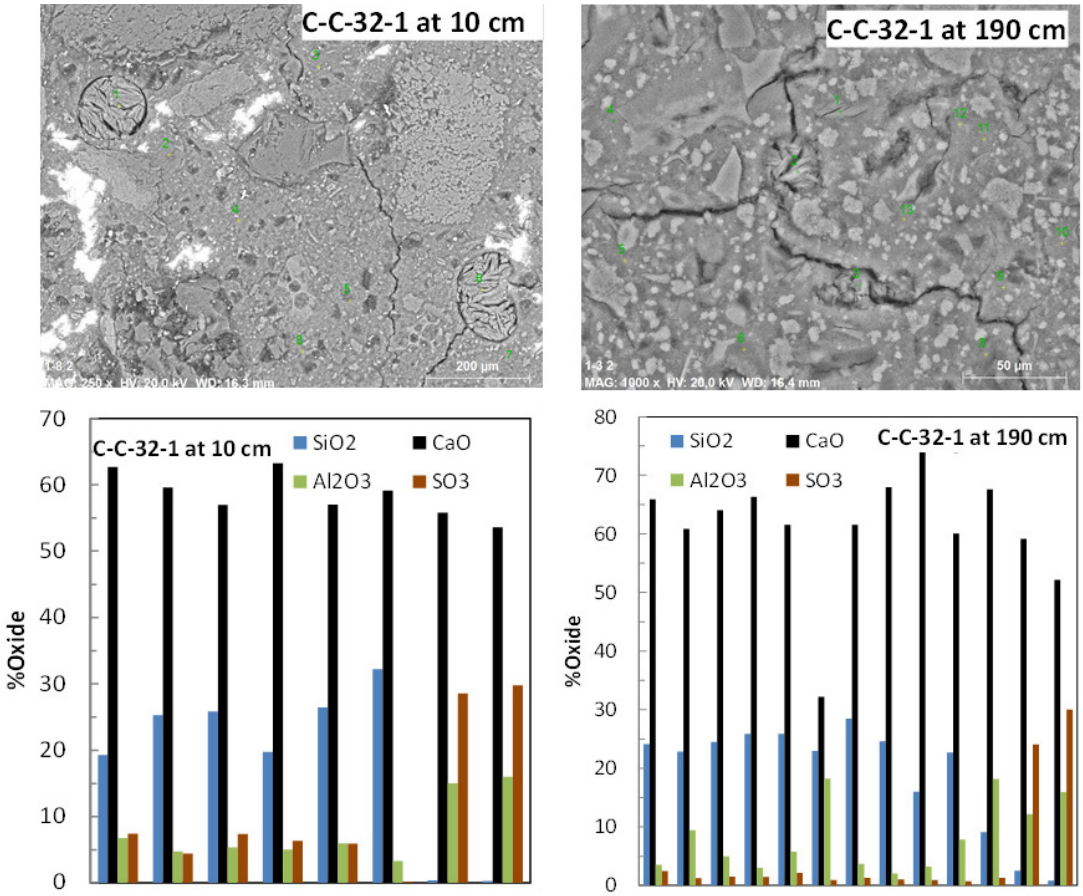

Fig. 49: BSEM images of samples from sections 1 (left) and 2 (right) of core C-C-32-1 at 10 cm and 190 cm from the bentonite interface, respectively. Analysis (% oxides) of C-S-H and ettringite in the cement paste are shown below. Analyses correspond to green spots in the pictures.

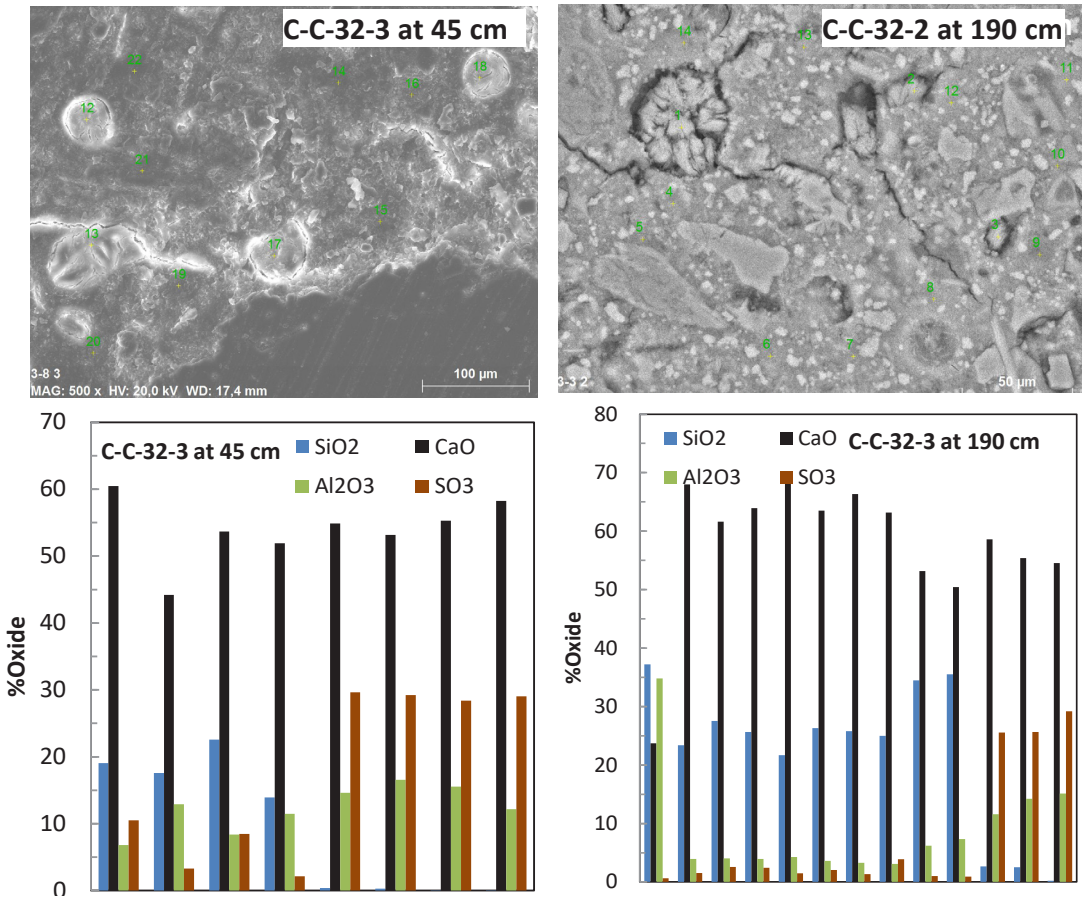

Fig. 50: BSEM images of samples from sections 1 (left) and 2 (right) of core C-C-32-3 at 45 cm and 190 cm from the bentonite interface, respectively. Analysis (% oxides) of C-S-H and ettringite in the cement paste are shown below. Analyses correspond to green spots in the pictures.

5.3.5 Thermogravimetric analysis (CSIC)

The DTA of core C-C-32-2 at different distances from the dummy is shown in Fig. 51. No relevant alteration is detected from these results and the high content of ettringite in the cement matrix at different distances from the dummy can be deduced from the curves between 100-150 ºC (detail in Fig. 51 right).

The DTA analysis of the samples from cores C-C-32-1 and 3 close to the granite and far from the bentonite are shown in Fig. 52 for sections 1 and 2. Detail of the DTA results between 300 °C and 500 ºC is presented on the right side in the figure, to better visualize any change that can be attributed to granite groundwater leaching. In the detailed figures the thermogravimetric curves in wt-% mass loss are also represented. The decrease in the portlandite peak in C-C-32-1 and C-C-32-3, which was also observed by XRD, is evident in the DTA analysis. In fact, the percentage of weight loss associated to portlandite in section 1 of cores C-C-32-1 and 3 is very low compared to the mass loss obtained in section 1 of core C-C-32-2. The dissolution of portlandite in these two cores could be a consequence of granite groundwater interaction. However, this leaching effect is not evident from concrete of section

2 and similar portlandite peaks and weight losses are measured in cores C-C-32-1 and 3 compared to core C-C-32-2.

The main DTA results in those zones of cores C-C-32-1 and 3 close to the bentonite are presented in Fig. 53. Three regions can be distinguished. Concrete at 2-4 cm from the bentonite is shown in Fig. 53A, the three main phases observed in the reference core also appear at 2 cm from bentonite. These phases are represented by exothermal peaks attributed to ettringite (100-150ºC), portlandite (350-450ºC) and calcite (650-750ºC). However, differences are observed in samples from the concrete/bentonite interface up to 1 cm (Fig. 53B). A wider peak associated to ettringite is observed. The higher weight loss of Fig. 53C from 100-150 ºC confirms the increase in ettringite content in the region near the concrete/bentonite interface.

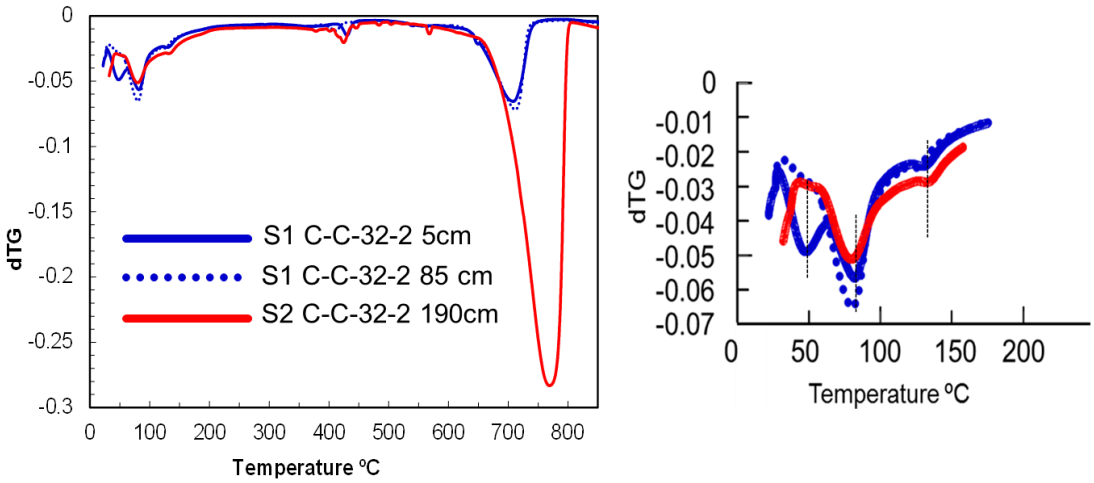

Fig. 51: DTA of the core C-C-32-2 at different distances of the dummy. On the right the peaks corresponding to the 50-150 ºC have been enlarged.

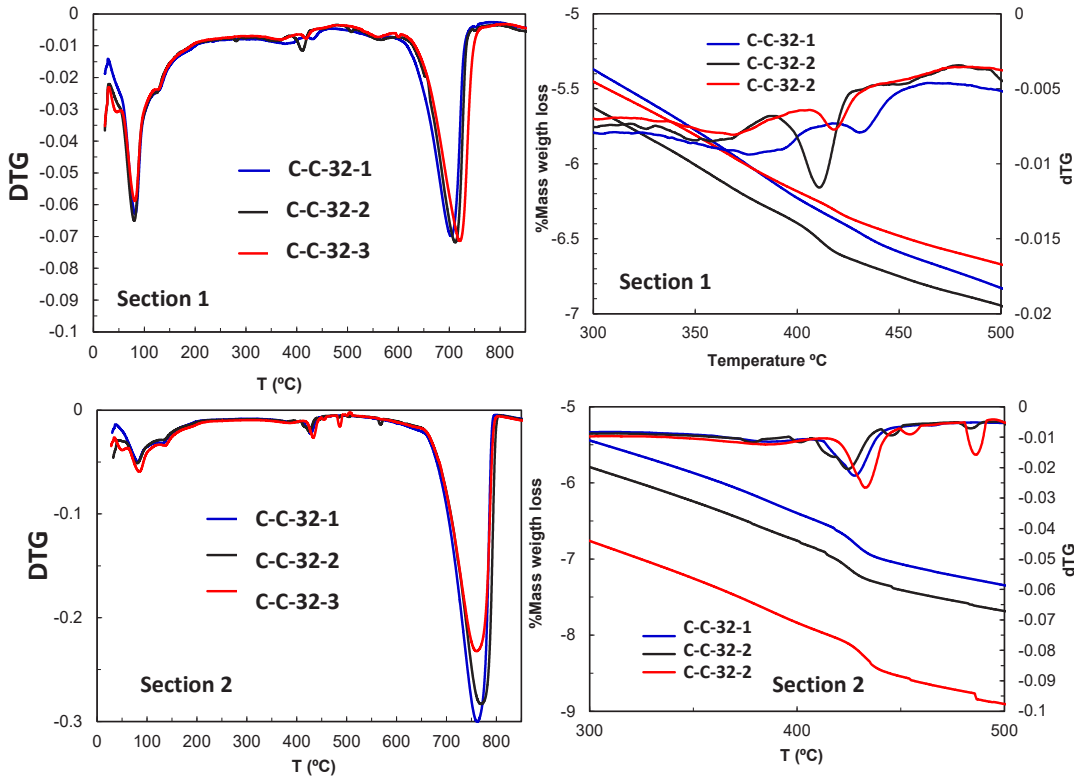

Fig. 52: DTA of the sections 1 and 2 of cores C-C-32-1 and 3 in those zones close to the granite and far from the bentonite interface. Comparison is made with core C-C-32-2 (reference). On the right hand side the detailed results between 300 °C and 500 ºC as well as thermogravimetric curves in wt-% mass loss are represented.

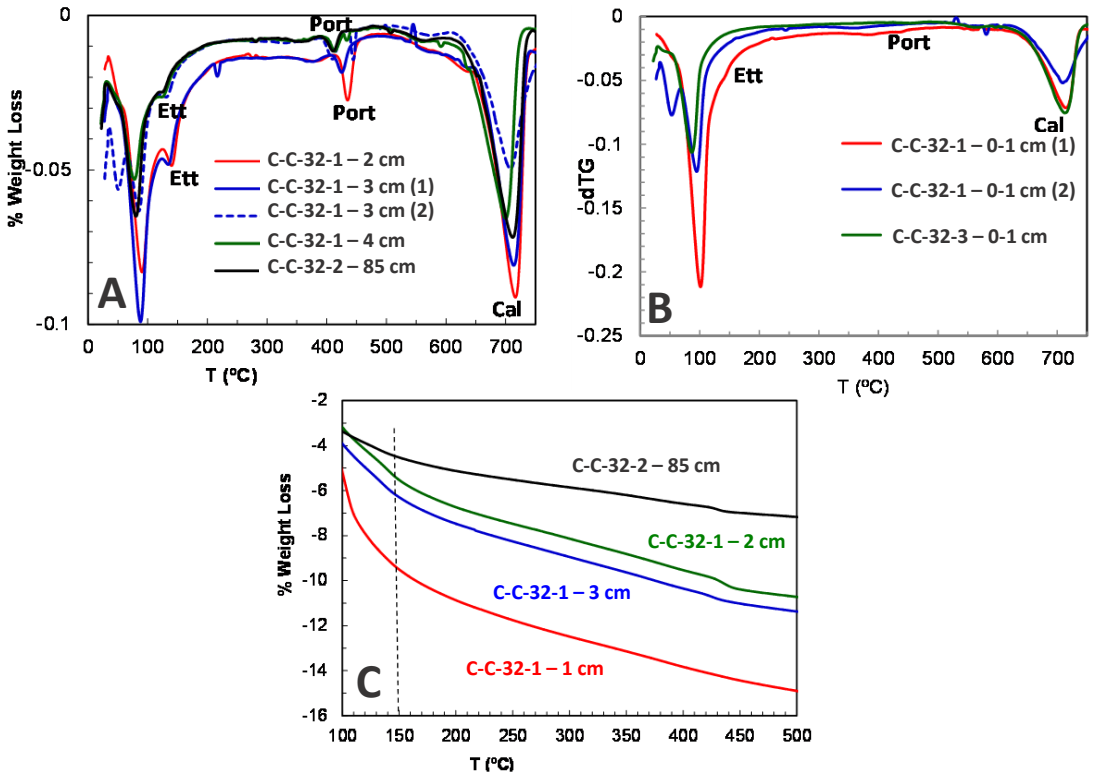

Fig. 53: TGA-DTA analysis of concrete from section 1 of cores C-C-32-1(A) and 3(B) in those zones closest to the bentonite. Comparison is made with core C-C-32-2 (reference).

5.4 Summary of concrete analysis

Macroscopic observations

The most significant macroscopic observation of the concrete plug, obtained from cores C-C-32-4 to -6, is the difference in shotcreting quality between section 1 and 2. Section 1 displayed a more layered texture from the shotcreting, while section 2 was very dense and only weakly layered. Between both sections, a clear white sealing layer was observed. Because a lot of rebound material was accumulated at the base of the tunnel and incorporated in the shotcrete layer, the lower part of section 1 was seemingly more porous and permeable (see C-C-32-6). Plenty of steel fibres (not visually oxidized) were found in section 1 of the cores. The operational aspects of the shotcreting may in this way also have an impact on the observed results from section 1.

Physical and mechanical properties of intact concrete

The cores C-C-32-1 to -3 were investigated for their compressive strength, dynamic elastic modulus, water absorption and capillary suction. As these cores pass through section 1 and 2, they provide an insight in the differences due to plug construction. Section 2 from core C-C-32-2 serves as a reference sample, as in this concrete the impact of granite groundwater or bentonite porewater is assumed to be negligible. Section 1 of this core, is located closer to the

bentonite interface. The compressive strength of section 2 in C-C-32-2 was higher than in section 1, this difference was observed after 28 days and also after 13 years. The water absorption curves also suggest a higher quality concrete in section 2 compared to section 1, but could not identify an influence of the granite interface. The accessible porosity for water and the capillary suction was slightly lower in section 2 compared to section 1. This result corresponds well to the total porosity measurements, which show a higher porosity in section 1 than in section 2. The concrete alkalinity, particularly the pH, indicates that it is a medium-high alkaline concrete with a pH below 13 (12.8±0.05). These observations suggest that some interaction in section 1 between the bentonite and concrete has occurred, while section 2 remained largely unaffected.

Geochemical perturbations

The impact of the granite porewater in section 2, where no impact from bentonite is present, can be deduced by comparing the core in the middle (C-C-32-2) to the two other cores (C-C-32-1 and C-C-32-3). The impact of the bentonite porewater in section 1 can be concluded from samples at reducing distances to the bentonite interface within the same core. The combined impact of the bentonite and granite porewaters can be seen when looking at all three cores from section 1.

The impact of the granite groundwater on the mechanical and microstructural properties of the concrete can be observed by comparing the results from three different cores (C-C-32-1, C-C-32-2 and C-C-32-3). The pH of the concrete in section 2 of these three cores remains around 12.5. The water accessible and total porosity in section 2 was slightly higher in C-C-32-3 compared to the other two cores. In terms of soluble ions, a slight increase in sulphate was observed in C-C-32-3, while the potassium concentration was significantly lower in this core. The calcium concentration in section 2 of C-C-32-1 was higher than in the other two cores. Ettringite is present in all three cores as seen by XRD and SEM-EDX. Only with TGA-DTA a slight increase in section 2 of C-C-32-3 was seen. Also portlandite was observed in all three cores to the same extent. These results suggest that the interaction with the granite rock is limited to the formation of calcite and the leaching of potassium towards the granite.

The impact of the bentonite interface on the properties of the concrete was also studied. Soluble ions were measured in C-C-32-2 at three different distances from the dummy interface: 1) in close proximity to the bentonite; 2) at 85 cm from the bentonite (section 1); and 3) at 190 cm from the bentonite interface (section 2). For sulphate, sodium and potassium, a strong decrease at the bentonite interface was observed, while the calcium concentration was much higher at the interface. Precipitation of ettringite took place in both sections 1 and 2, as confirmed by XRD, SEM-EDX and TGA-DTA. The dissolution of portlandite at the interface with the bentonite could be observed by XRD, while carbonates were increasingly found in section 2 (observed by TGA-DTA). The mineralogical study gives little evidence for the presence of C-S-H, as this is amorphous in nature. However, the CaO and SiO_2 distribution and ratio as a function of distance away from the bentonite become more homogeneous and decrease, suggesting a decreasing C/S ratio. Meanwhile, calcite, portlandite and ettringite were clearly identified in the cement matrix. More portlandite is formed when ettringite decreases. These observations suggest that the concrete was strongly leached by the contact with the bentonite and precipitation of minerals in the concrete such as ettringite and carbonates occurred. Depending on the mineral, precipitation occurs preferentially closer or further away from the interface.

The vicinity of the bentonite and granite interaction can be observed clearly in the increased total porosity of section 1 in C-C-32-1 and -3. The water permeability coefficient (K) has

increased in C-C-32-2 compared to C-C-32-1 (section 1), from 10^{-11} m/s at 28 days to 10^{-10}m/s after 13 years. The interaction of the granite and bentonite with the concrete has promoted leaching processes in the concrete matrix with the subsequent dissolution of the portlandite content (see XRD analysis). Pore solution pH values near or even below 12.5 have been measured in the corresponding affected concrete (section 1 of C-C-32-1 and C-C-32-3). The analysis of the soluble ions shows that the lower Ca and alkaline content (Na and K) is linked to the pH decrease. Conservative anions as chloride show the highest concentrations near the granite boundary, but have been detected as far as 5 cm from the interface. Small crystals of Friedel's salt were found in section 1 of C-C-32-1. In addition, an increased concentration of Mg was observed in SEM-EDS mapping of this section. Besides, the main precipitation and dissolution processes have been located near the granite and bentonite boundaries. The upper part of the dummy was less affected by these processes. Despite the leaching, significant damage in the cementitious cement paste matrix has not been observed at 15 cm from the host-rock.

Tab. 5-3: Summary of analyses in sections 1 and 2 of C-C-32-1 to C-C-32-3. Section 2 of core C-C-32-2 serves as a reference concrete, as this concrete is believed to be the least affected by granite or bentonite interaction.

	C-C-32-1 (upper right)		**C-C-32-2 (centre of cavern)**		**C-C-32-3 (lower left)**	
	Section 1	**Section 2**	**Section 1**	**Section 2**	**Section 1**	**Section 2**
Compressive strength	0	+	-	0	-	+
Accessible porosity	+	-	+	-	0	+
Total porosity	++	-	+	-	++	+
Pore solution pH	12	>12.5	>12.5	>12.5	12	>12.5
Aluminium	++	0	+	0	++	0
Sulphate	0	+	0	+	0	++
Sodium	0	0	+	0	-	0
Potassium	-	++	0	++	-	0
Calcium	-	+	0	0	-	0
XRD						
-portlandite	-	+	+ [1]	+	-	+
-ettringite	+	+	+ [1]	+	+	+
SEM						
-ettringite	+	+	+	+	+	+
TGA-DTA						
-portlandite	-	0	+	0	-	0
-ettringite	+	0	+	0	0	+
-carbonate	0	+++	0	++	0	+

[1]decrease towards bentonite

6 The concrete/bentonite interface analysis: results

Tab. 6-1 summarises the samples used for concrete investigations, partners involved in the studies and the type of analysis performed by each partner.

Tab. 6-1: Summary of samples, partners and analyses for concrete/bentonite interface analysis.

Reference	Type of sample	Partner studying the sample	Analysis
C-C-32-1 and 3	Core	CSIC	Geochemical modifications (concrete)
C-C-32-6	Overcoring	Obayashi, Sandia, UniBern	Internal structure, mineralogy, elemental distribution, exchangeable cations
C-C-34-4 to 11	Core	UAM	Mineralogy, carbonation, soluble salt migration, specific surface area (concrete)
C-C-34-8 and 12	Core	Ciemat, UAM	Specific surface area, soluble salts exchangeable cations, mineralogy, geochemical modifications
C-C-34-10	Core	Ciemat, UAM	Porosity, specific surface area, soluble salts exchangeable cations, mineralogy, geochemical modifications
BC-C-35-1	Core	Ciemat, UAM	Specific surface area, soluble salts, exchangeable cations, mineralogy, geochemical modifications
BC-C-35-2	Core	Ciemat, UAM	Porosity, specific surface area, soluble salts, exchangeable cations, mineralogy, geochemical modifications
BC-S-35-1(a,b)	Hand-picked	BGR	Exchangeable cations, mineralogy, geochemical modifications
BC-S-35-3	Hand-picked	Ciemat, UAM	Porosity, specific surface area, soluble salts exchangeable cations, mineralogy, geochemical modifications
BC-S-35-4	Hand-picked	Ciemat	Soluble salts, exchangeable cations
B-B-36-7	Block	Ciemat	Porosity, soluble salts

6.1 Macroscopic appearance of the concrete/bentonite interface (UniBern)

Since overcores are the best preserved concrete/bentonite samples, UniBern, in charge of the plug overcoring (Mäder et al. 2016), made a very detailed description of the macroscopic aspect of the concrete/bentonite interface based on sample overcore C-C-32-6-OC. The description is given below and further details of concrete can be found in chapter 5.

FEBEX bentonite is quite a coarse-grained material (Fig. 54) with grain sizes up to ca. 6 mm. The different grains are mostly composed of smectite aggregates and reflect presumably different minerals and/or different alteration mechanisms in the volcanic precursor rock. The overall fabric is homogeneous at the coarse grain scale. Fig. 54 shows cut surfaces after producing half cores from C-C-32-6-OC, just after applying a protective covering of Araldite XW 396 epoxy resin. Textures are displayed extremely well through the liquid resin. Steel fibres are not corroded. Some faint alteration zones are visible in both concrete and bentonite, and this is detailed further below.

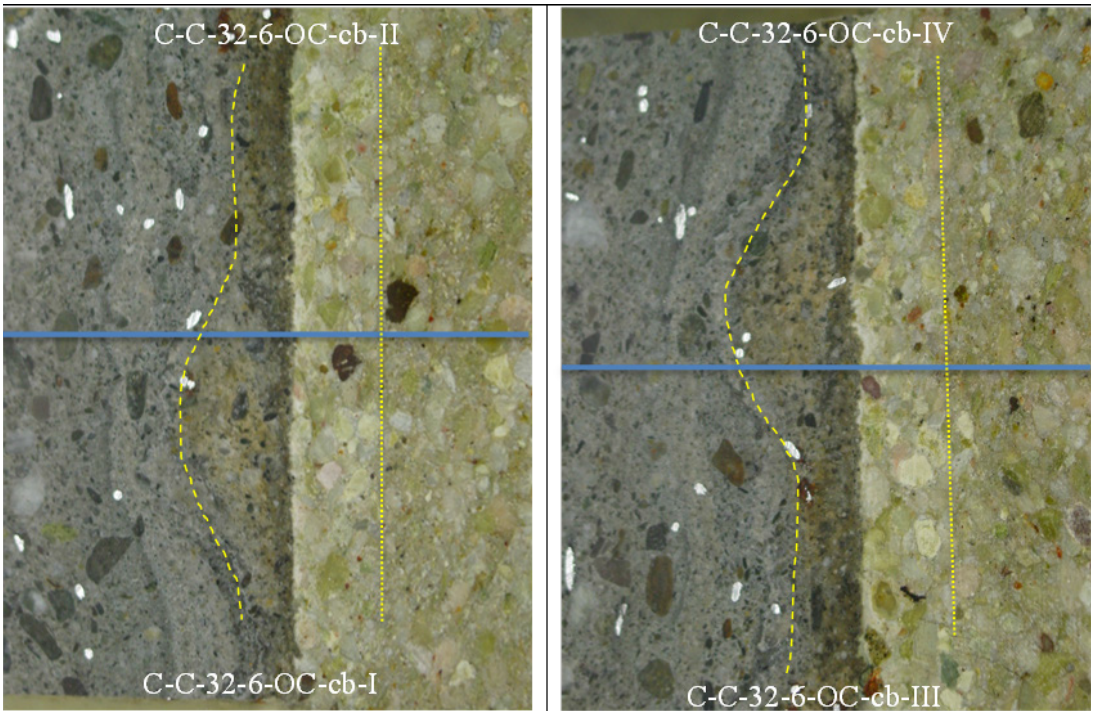

Fig. 54: Images of cut surfaces of half cores from C-C-32-6-OC-cb viewed through liquid epoxy layer. Left: C-C-32-6-OC-cb-I&II; Right: C-C-32-6-OC-cb-III&IV. Blue lines indicate subsequent cuts to produce quarter cores. Field of view is ca. 60x75 mm. Glossy components in concrete (left side) are steel fibres.

Fig. 54 illustrates the layered aspect of concrete as a consequence of the application method (shotcreting technique). It also contains more or less randomly distributed steel fibres. There is a faint brownish discoloration of the concrete part next to the bentonite, 6-12 mm in width, outlined by a yellow dashed line in the figure. This zone is also present at the interface in core sample C-C-32-5, but it is much narrower, only 3-4 mm (images in Appendix B of Mäder et al. 2016). It can be assumed that this discoloration is related to the presence of bentonite and the resultant geochemical interactions. There is also a very faint zone, ca. 12 mm wide, within the bentonite and adjacent to the concrete with a slightly lighter-coloured bentonite matrix (dotted yellow line in the figure). This zone was clearly visible at the time of sample cutting but was difficult to capture by photography afterwards. Such zones of similar dimension were also observed along the interface in C-C-32-5 and C-C-32-4 (images in Appendix A and B of Mäder et al. 2016). It is not entirely clear if this zone is related to interaction with concrete, because the bentonite block surfaces were exposed to ambient conditions for some time before shotcreting was applied.

The interface itself appears to be physically very well preserved, without any obvious fractures or joints, and without any obvious altered material, except perhaps for a very thin (<1 mm) light-coloured irregular skin on the bentonite side.

The macroscopic appearance of the sample prepared for X-ray CT work (Fig. 55) also attests of a firm contact between bentonite and concrete. The bentonite matrix between the coarser grains appears to be lighter coloured in the vicinity of concrete, as illustrated in Fig. 54. The brownish discoloration in concrete near the interface as seen in Fig. 54 is not obvious in this subsample (images taken more than 1 year later). The layered texture in concrete is due to the application procedure (shotcreting technique). Image C of Fig. 55 appears a bit clouded because it is a view across the original epoxy resin applied when moulding the entire cores, whereas A and B are viewed only through freshly applied resin.

A

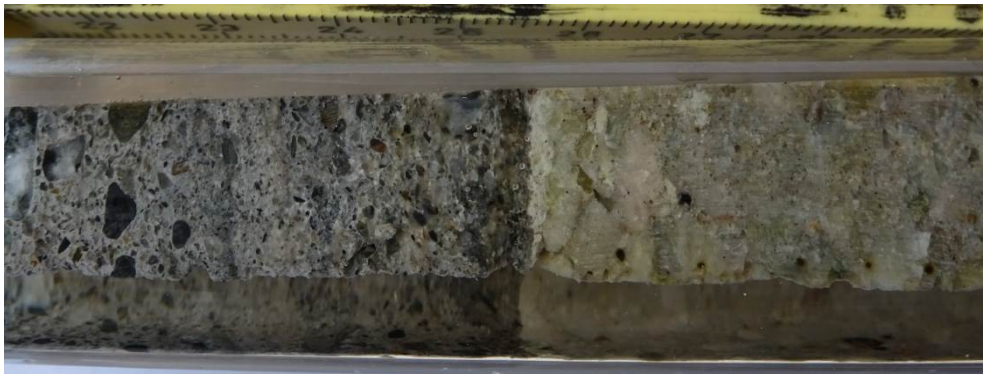

B

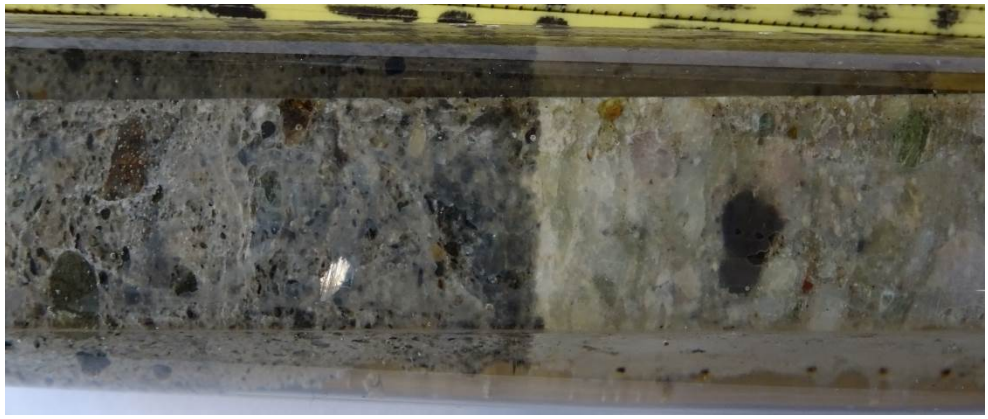

C

Fig. 55: Photographs of the three main facets of the prismatic sample prepared for X-ray CT. The scale bar is labelled in cm. Concrete is on the left-hand side.

6.2 Physical parameters

6.2.1 Water content and dry density of bentonite section closest to the concrete (Ciemat)

An exhaustive analysis of water content and dry density of the bentonite section just contacting the concrete plug (section 36) can be found in Fig. 56 (Villar 2017). The results indicate that the water content decreases from the granite towards the inner part of the barrier whereas the dry density increases. It is important to remember that the physical state of section 36 was affected by heater #1 for five years followed by 13 years of cooling. Furthermore, a slight increase of the water content and decrease of the dry density in those samples close to the dummy (central axis of the gallery) is observed. As explained in section 3.2 a water spill occurred during dry drilling of cores to obtain samples of the concrete/bentonite interface. The spill was located almost at the contact with the dummy and may be that "accumulation" could explain that slight increase of water content and decrease of dry density in those points closest to the dummy.

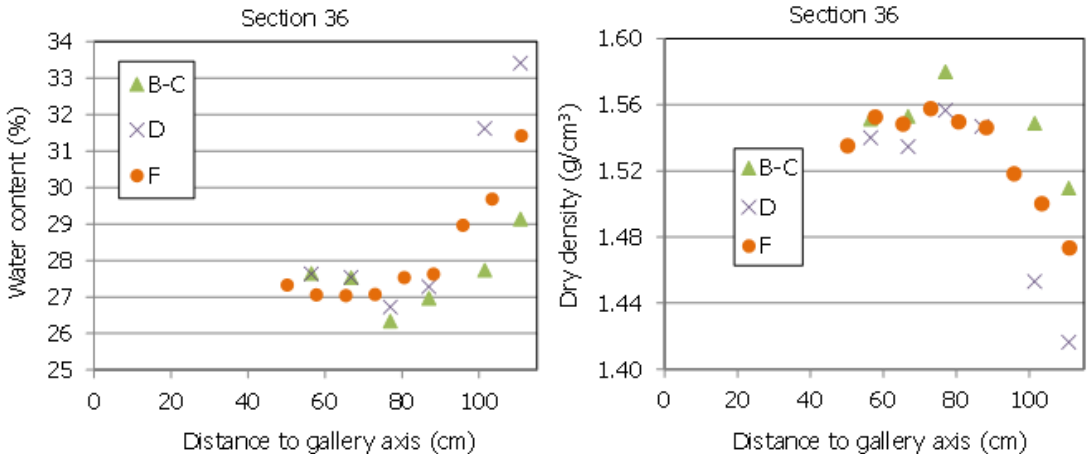

Fig. 56: Water content and dry density measured in the laboratory in blocks taken from the three radii sampled in section 36; the section next to the concrete plug (from Villar 2017).

Concrete/bentonite interaction processes may affect the mechanical properties of the bentonite, particularly its swelling behaviour. In order to check this impact, the swelling capacity of six samples taken in dismantling plan section 36 close to the concrete plug was determined in oedometers according to the methodology described in Villar (2017), where the results are presented. The swelling strain values measured are 1% lower than the values expected for the reference sample with the same initial state in terms of dry density and water content. However, for the rest of samples tested not affected by interfaces, the decrease in swelling capacity with respect to the theoretical one was even higher. Hence, it is considered that the concrete interface had no effect on the swelling capacity of the bentonite. Nevertheless, it is also acknowledged that the number of samples analysed was small. Details on samples, methods and results on swelling of samples close to the concrete (section 36) are discussed in detail in Villar et al. 2018.

6.2.2 Pore size distribution (Ciemat)

The pore size distribution of samples C-C-34-10 and 12, BC-C-35-1 and 2, BC-S-35-3 and B-B-36-7 was determined by Mercury Intrusion Porosimetry (MIP). Various subsamples of concrete and bentonite were taken from the interface up to 4 cm away. Due to the limitation of the method in the bentonite only inter-aggregate porosity, specifically part of the macropores (>50 nm) and mesopores (6-50 nm), is accessible. However, the percentage of pores less than 6 nm can be important, so assuming that the percentage of pores not intruded by mercury corresponds entirely to the micropore size, an estimation of the percentage of micropores can be made from the percentage of pores intruded. The methodology used was the same as used by Villar (2017) and it consists of recalculating the total porosity and the percentage of each pore size by comparing the actual void ratio of the samples (computed from their dry density and density of solid particles) and the apparent void ratio calculated from mercury intrusion. Fig. 57 shows the total concrete and bentonite porosity recorded just at the concrete/bentonite interface and some millimetres further.

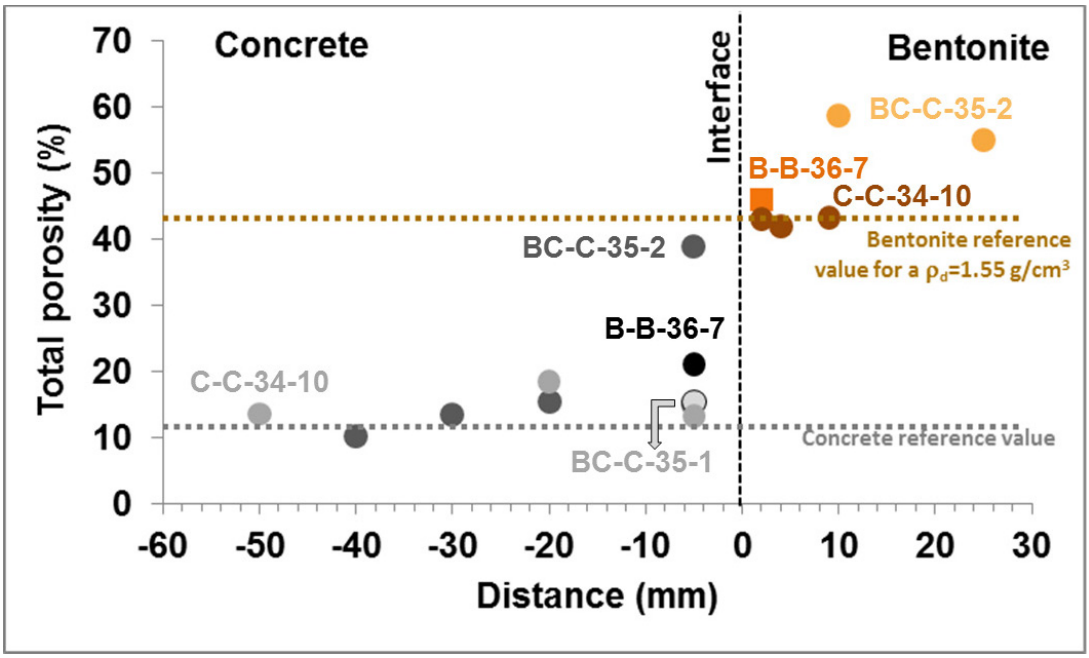

Fig. 57: Total porosity (MIP) of the concrete and the bentonite as a function of distance to the interface in dry-drilled samples C-C-34-10 and 12, BC-C-35-1 and 2, BC-S-35-3 and B-B-36-7. Average reference values for concrete and bentonite are plotted for comparative purposes.

Porosity of the bentonite

The average porosity of the bentonite is 42.7 ± 0.7 % in samples C-C-34-10 and B-B-36-7, similar to the reference value (≈ 42 %) for a dry density of 1.55 g/cm^3 (Fernández & Rivas 2005), and higher (56.8 ± 2.6 %) for sample BC-C-35-2, the sample closest to the granite wall. The increase of porosity in this sample agrees with a higher percentage of macropores (Fig. 58) and a decrease of the micropores. It is noticeable that there is a linear relationship between the decrease in microporosity and the increase of macroporosity, while the percentage of mesopores is quite stable (21 ± 1 %).

The micropores were predominant in all bentonite samples analysed. In sample B-B-36-7 the macroporosity is slightly higher than the mesoporosity and the biggest differences are in sample BC-C-35-2 with a macroporosity quite high compared to the mesoporosity. A relationship was established by Villar (2017) between proximity to the granite and higher macroporosity. However, the number of samples analysed in this report is small and unrepresentative for the inner parts of the barrier so that a trend cannot be confirmed.

Close to the interface (1 cm) the percentage of macropores and mesopores is approximately the same in all the bentonite subsamples taken from sample C-C-34-10. Moreover, there is an important difference in the mode of macropores as the distance to the interface is higher; there is a sharp increase of the intrusion curve (Fig. 59) in those diameters corresponding to the larger macropores (mode 71 ± 30 µm) in the zones closest to the interface with the concrete, and as the distance to the interface is higher macropores mode decreases (21 ± 3 µm). This could mean that changes in the bentonite pore size distribution are related to the interaction with the concrete.

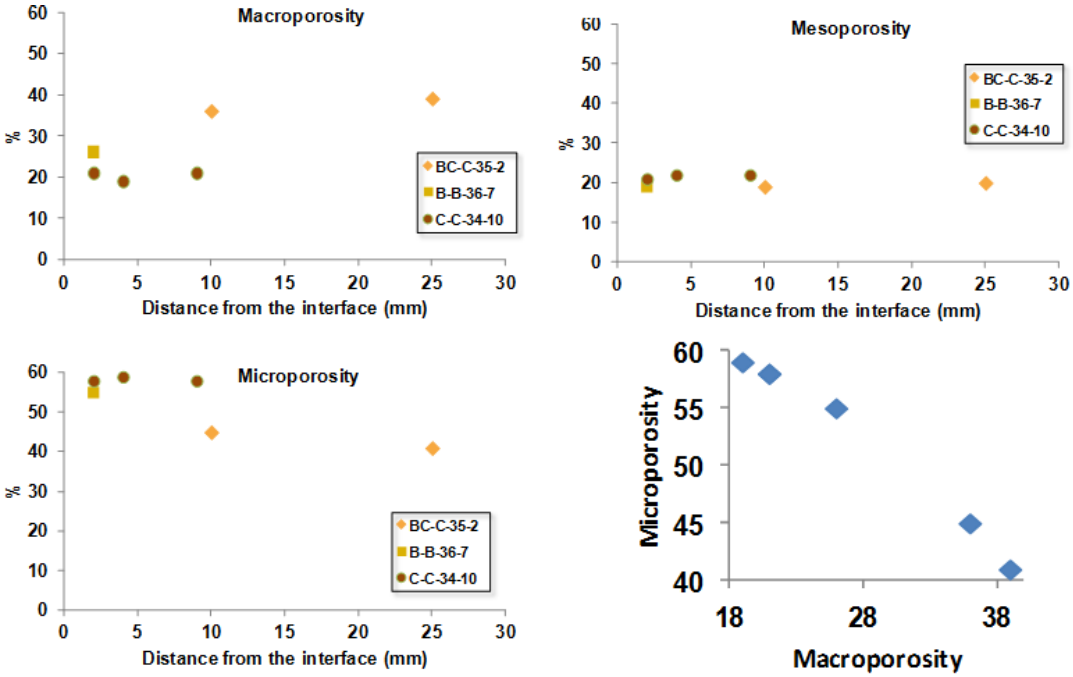

Fig. 58: Percentage of macropores and mesopores in the bentonite up to 3 cm from the interface, measured in samples BC-C-35-2, B-B-36-7 and C-C-34-10.

Another increase in the intrusion curve is observed in the diameter attributable to the mesopores. This increase occurs in all the samples independently of the distance to the concrete or granite interface (mode 13 ± 3 nm). The final draw is a bimodal distribution related to macro- and mesopores. The bimodal distribution obtained by MIP is quite typical of the FEBEX bentonite, as well as the percentage of each type of pores: macropores 27 ± 9 %, mesopores 21 ± 1 %, and micropores 53 ± 8 %. Additional data of porosity of other sections of the bentonite buffer can be found in Villar (2017). This report mentions a bimodal distribution with sizes in the range of those presented in this report, and no spatial changes in the mean pore size of the mesopores as well.

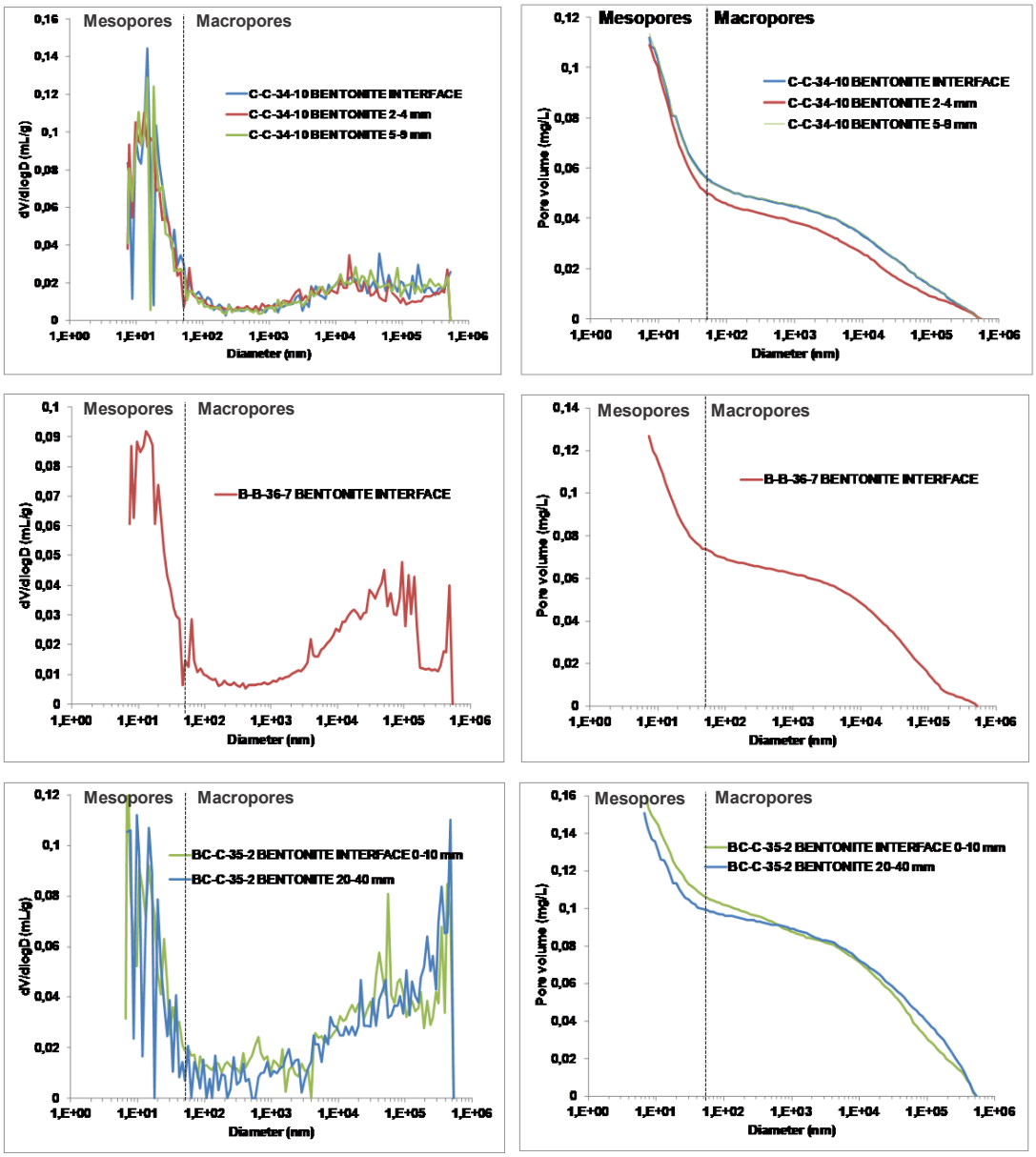

Fig. 59: (Left) Pore size distribution (log differential intrusion) and (Right) Intrusion volume curves of bentonite samples C-C-34-10 and BC-C-35-2 at different distances from the concrete.

Porosity of the concrete

The porosity of the concrete ranges from 10.09 % to 38.92 %; the higher values are those recorded just at the interface in the samples closest to the granite (BC-C-35-2 and B-B-36-7). Porosity at 3 cm from the interface and further is lower, and similar to the reference values for concrete, as those presented in section 5.3.1.

The pore-size distribution of the concrete side of the samples is bimodal, with a population of macropores, corresponding to inter-aggregate pores (> 50 nm), and a population of mesopores

(2.5-50 nm), corresponding to intra-aggregate pores, which would include small (gel) capillaries (2.5-10 nm). The delimitation has been made following the classification by Mindess et al. (2002) who notes that the pores affecting the resistance of the concrete are those >10nm.

There is a sharp increase of the intrusion curve (Fig. 60 and Fig. 61) in those diameters corresponding to the larger macropores just at the interface with the bentonite in all samples (mode 0.5 μm in B-B-36-7, 6 μm in BC-C-35-1 and 77 μm in BC-C-35-2), except in C-C-34-10 (mode 59 ± 4 nm). Mode of the macropores of sample BC-C-35-2 in zones far from the interface with the bentonite is 57 ± 5 nm. The information available about the shotcreting procedure (chapter 1) and porosity data presented in this part indicate that a link between porosity of the concrete and interaction with the granite or the bentonite is difficult to establish for two reasons: (1) the shotcreting technical difficulties in the first 2 cm of concrete led to a non-homogeneous and quite porous layer of concrete; and (2) the number of samples analysed in this report is small and only one is located in the lower half of the plug. Chapter 5 described some of the macroscopic features in the concrete samples, as a layered aspect and a more porous and locally more permeable region at the base of the plug. The data from the sample analysed at the base of the plug (BC-C-35-2) would support this appreciation (Fig. 61 – bottom – see the sharpe increase in the intrusion curve in the first 2 cm) that is probably more related to technical issues than interaction of concrete with other materials.

Another increase in the intrusion curve corresponds to the mesoporosity. The samples at distances > 20 mm from the interface with the bentonite has a mode 9 ± 3 nm which would correspond to the typical sizes of the space between the C-S-H particles (gel capillaries), while in the rest of samples the mode is 43 ± 6 nm, quite close to the mode of the macropores.

Fig. 62 shows SEM images of the concrete of sample C-C-34-10 close to the bentonite interface illustrating different pore sizes. All of them correspond to the macropore range: inter-crystal pores in the scale of tens of nanometres, air voids around 20-50 μm, or cracks around 5 μm width. Although the proportion of pores with sizes around mode 59 ± 4 nm is the highest, in Fig. 60 a small percentage of pores in the range of tens of microns can be observed as well.

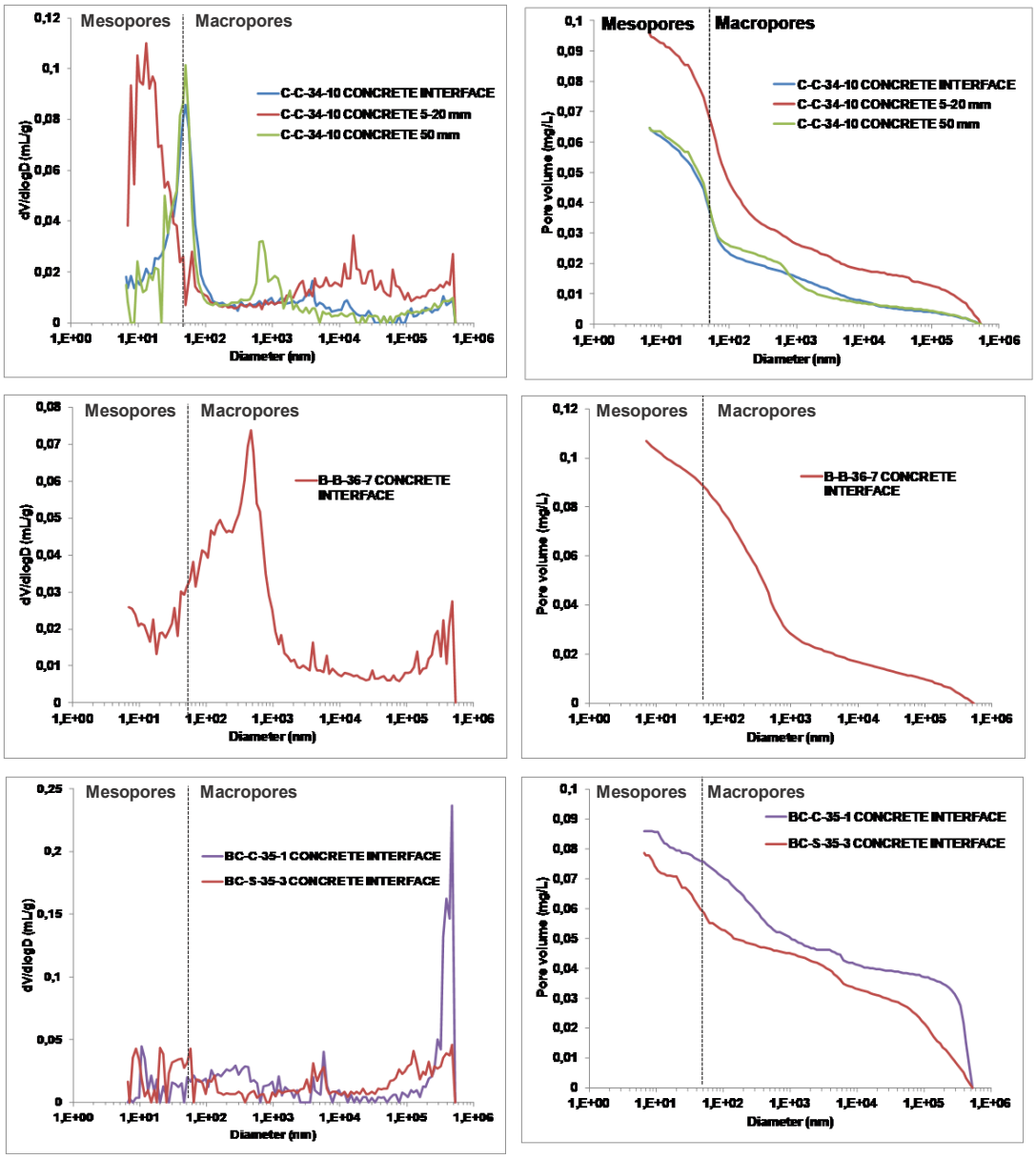

Fig. 60: (Left) Pore size distribution (log differential intrusion) and (Right) Intrusion volume curves of concrete samples B-B-36-7, BC-C-35-1, BC-S-35-3 and C-C-34-10 at different distances from the bentonite.

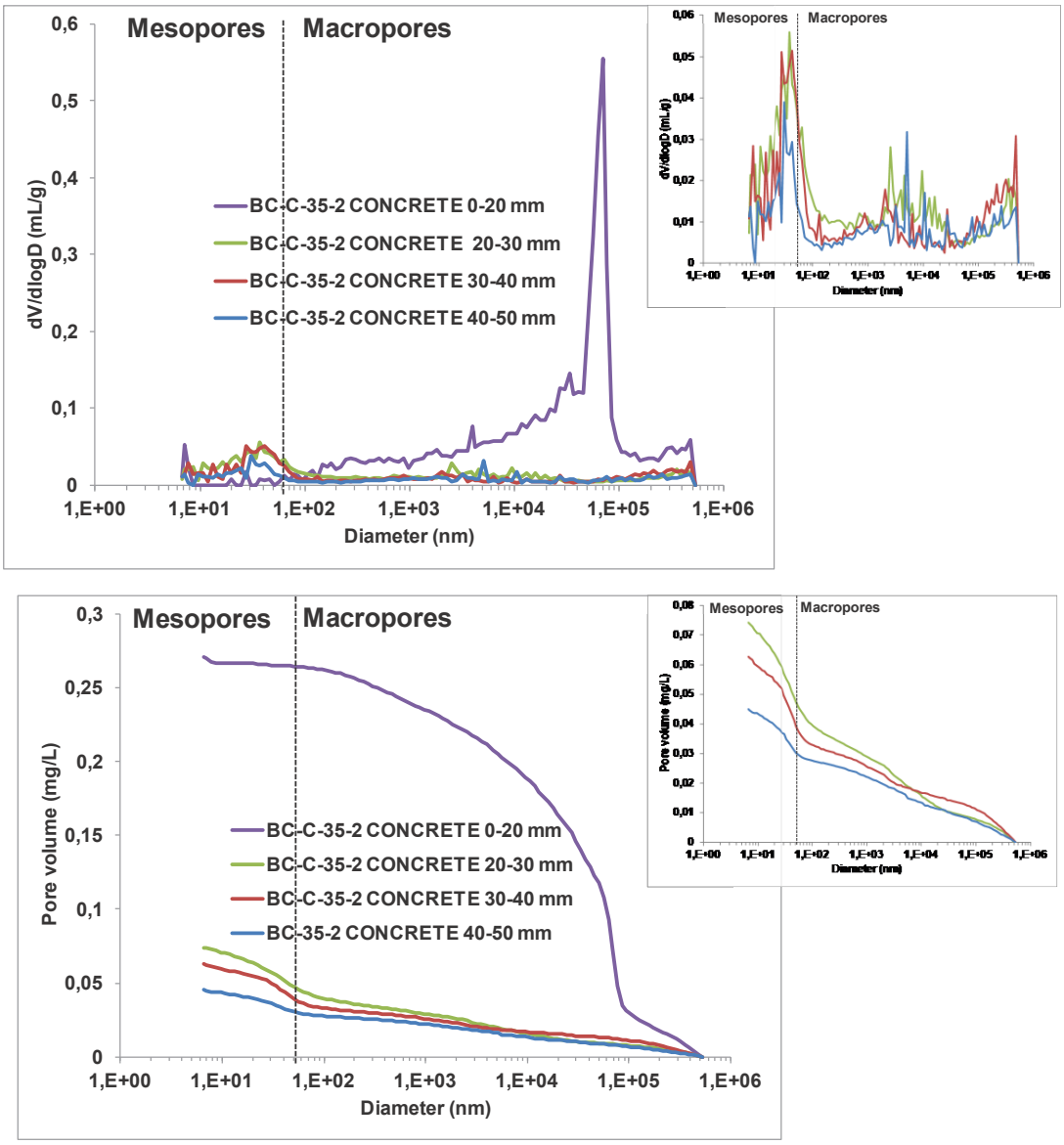

Fig. 61: (Left) Pore size distribution (log differential intrusion) and (Right) Intrusion volume curves of concrete sample BC-C-35-2 at different distances from the bentonite.

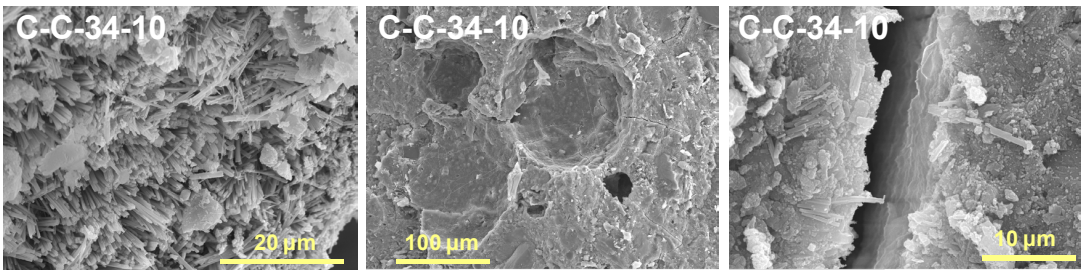

Fig. 62: SEM images of sample C-C-34-10 close to the bentonite interface, showing an example of different pore sizes: inter-crystal pores, in the scale of tens of nanometers, air voids, around 20-50 µm, or cracks around 5 µm width.

6.2.3 Specific Surface Area (SSA) (UAM, Ciemat)

Bulk concrete

The specific surface area (BET surface) of the cement paste of bulk concrete samples C-C-34-4 to 11 was measured. The surface area is lower near the granite or bentonite boundaries (Fig. 63). These areas were characterised as zones of carbonate dissolution/precipitation (see part 6.3). In a first attempt to explain the differences in measured BET surface, this parameter is crossed with the calculated C-S-H (calcite DRX-calcite calcimeter) (Fig. 63 left – data in Appendix B – part B.5, Tab. B-10 and additional details in part 6.3). No significant trends were found, presumably due to the amorphous nature of some of the C-S-H phases. It is, nevertheless, suggested to link the decalcification of C-S-H and potential crystal growth processes to the decrease of BET surface.

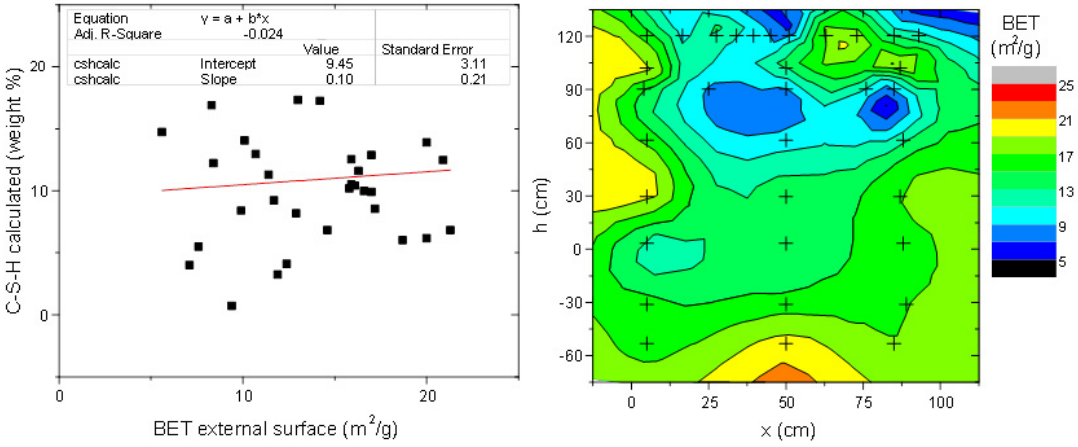

Fig. 63: Distribution map of BET surface and dispersion plot versus calculated C-S-H (see mineralogy paragraphs) as function of distance to the bentonite and the dummy front (higher x indicates proximity to the bentonite) and the distance from the axis of the gallery following the line where the samples were taken (higher h indicates proximity to the granite).

Concrete/bentonite interface

Very detailed sampling for the measurement of specific surface area was carried out on both concrete and bentonite. Data are represented in Fig. 64. Results on the bentonite side are slightly lower than those of the FEBEX reference (close to 62 m^2/g represented by a dotted line in the figure). However, they evolve from relative low values at the very interface to a maximum near 1-2 mm after the interface and stabilization to slightly low values far from the interface. The highest values in the bentonite may be related to high specific surface minerals near the interface. These results will be further discussed in the mineralogy section (part 6.3).

On the concrete side the minimum SSA values are near 2 mm before the interface and they tend to increase at the interface. Dissolution of ettringite and precipitation of calcite can be responsible for such a minimum (see section 5.3.4 on concrete mineralogy close to the interface); the precipitation of high specific surface minerals could be the cause of the increase

of the BET surface towards the interface. It will be further discussed in the mineralogy section (part 6.3). This result would agree with the presence of pores around 9 nm in the zones closest to the interface, which usually correspond to the typical sizes of the space between the C-S-H particles (Fig. 65) (see section 6.2.2).

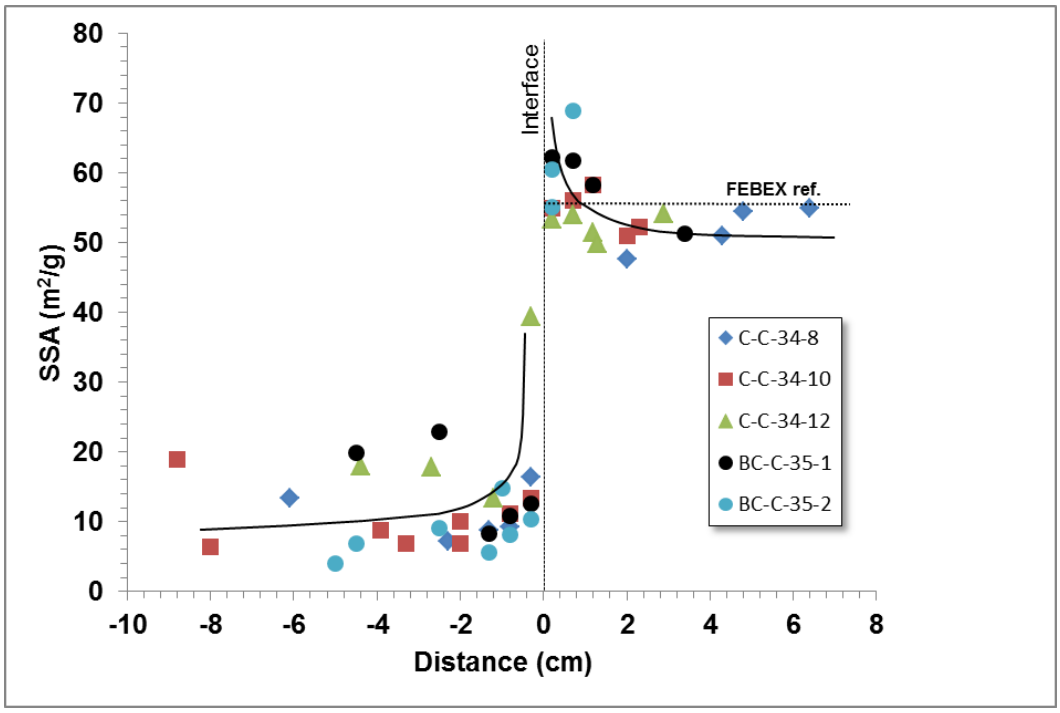

Fig. 64: Specific surface area of the concrete and the bentonite in samples C-C-34-8, 10 and 12, and BC-C-35-1 and 2.

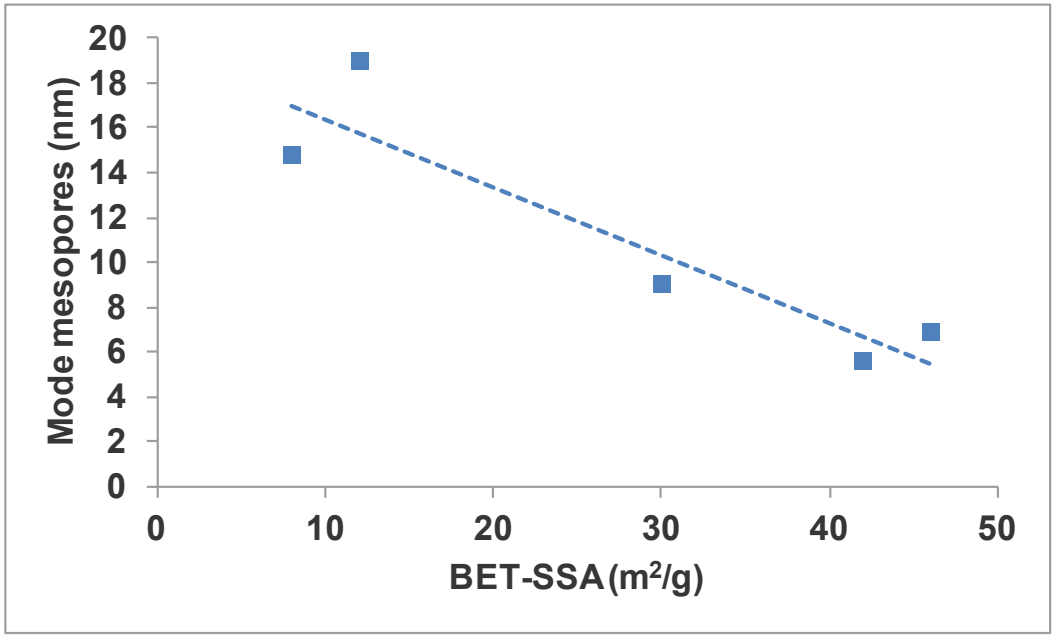

Fig. 65: Relationship between mode of mesopores in samples of concrete just at the interface with bentonite and BET surface area.

6.2.4 Clay mineral surface imaging by AFM (Obayashi)

Morphological and structural changes on smectite were checked by Obayashi on sample C-C-32-6 using atomic force microscopy (AFM). The study was based on quantifying smectite nanoparticles dimensions by measuring the perimeter, basal surface area and thickness of particles of samples taken at different distances from the interface (Fig. 66).

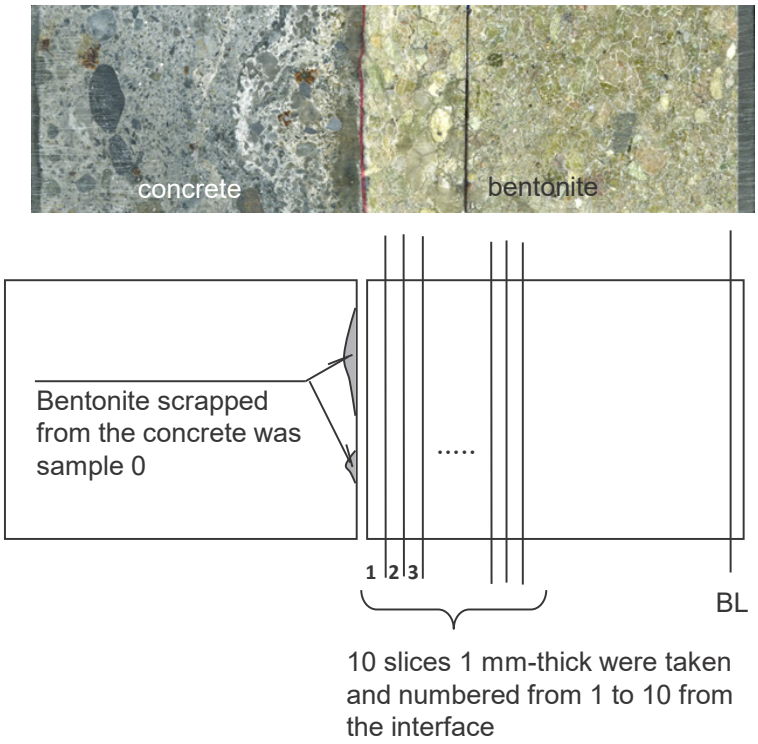

Fig. 66: Sampling of bentonite close to the interface in core C-C-32-6.

The AFM images of smectite crystals are shown in Fig. 67, where the nanocrystals of sample 0 (scrapped from the concrete), sample 1 (1 mm from the interface) and sample 10 (10 mm from the interface) can be observed. The slanted white lines in the pictures are noise. The crystals with a thickness between 1.0 and 2.0 nm were chosen for the analysis and the circumference and area were measured using a cantilever in the Dynamic Force Microscopy (DFM) mode. 100 crystals were analysed for each sample.

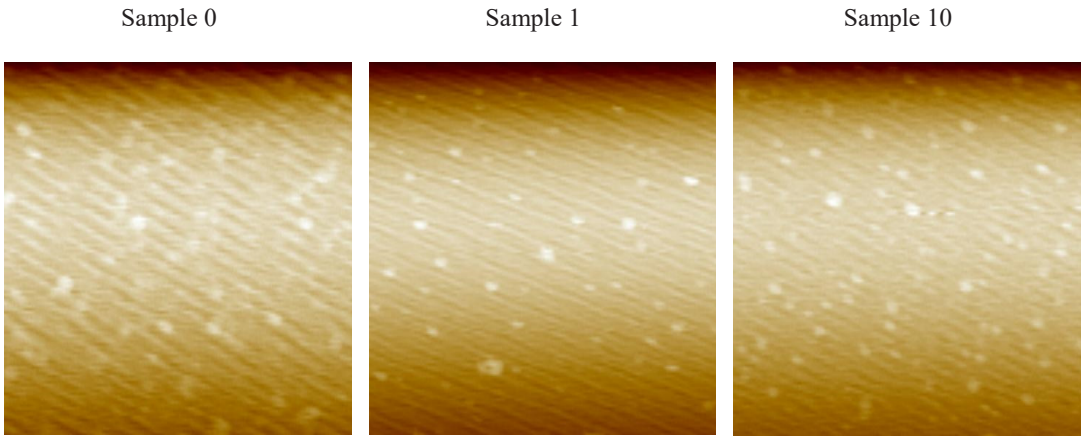

Fig. 67: AFM images of smectite crystals of Sample 0 (left) Sample 1 (middle) and Sample 10 (right). Slanted white stripes are noise.

The average results of measurements in various crystals of each sample are presented in Tab. 6-2 and Fig. 68. Sample 10 was used as reference as it is furthest from the interface. A decrease in the dimensions of montmorillonite crystals was not observed. However, a much more detailed analysis must be done, and additional samples at different points of the concrete plug and at different distances from the granite and the heater, should be analysed to ensure that there are no morphological or structural changes of the clay.

Tab. 6-2: Results of AFM measurements.

C-C-32-6	**Thickness (nm)**	**Area (µm^2)**	**Circumference (µm)**
Sample 0 average	1.70	4.99 x10^{-3}	0.283
variance	0.09	6.81 x10^{-6}	5.49 x10^{-3}
Sample 1 average	1.77	4.56 x10^{-3}	0.263
variance	0.09	1.38 x10^{-6}	9.60 x10^{-3}
Sample 10 average	1.57	3.73 x10^{-3}	0.253
variance	0.11	5.03 x10^{-6}	5.04 x10^{-3}

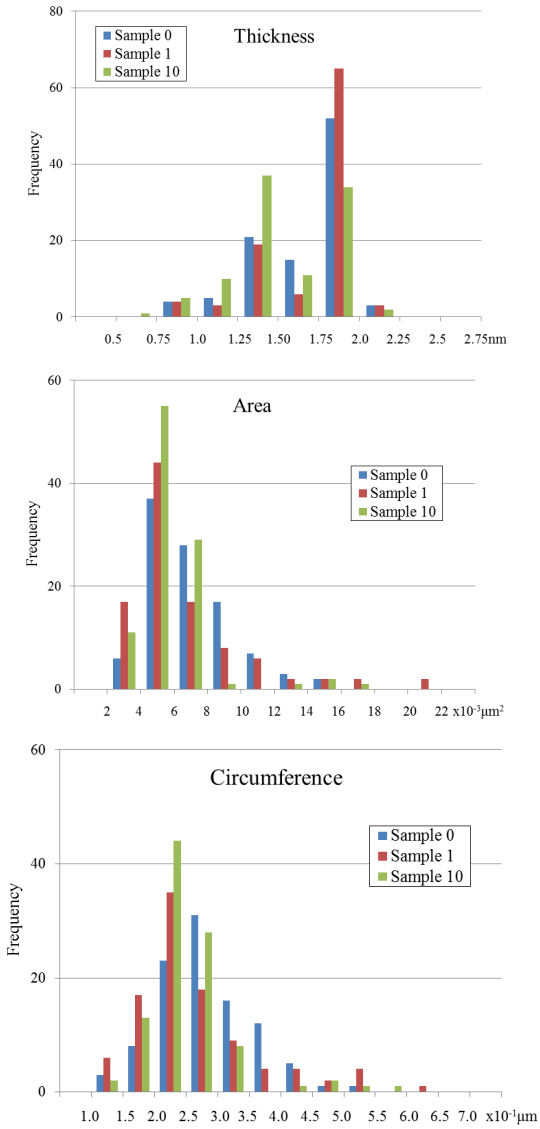

Fig. 68: Histograms showing the quantification of smectite particles dimensions by AFM

6.2.5 X-ray computed microtomography imaging (X-ray CT) (Sandia, UniBern)

Both Sandia National Laboratory and UniBern studied sample C-C-32-6 (overcoring) focusing on the interface region. Both laboratories include a preliminary evaluation and give input about major features observed by CT-imaging, although both agree that further work on data should be made for optimizing data acquisition and reconstruction and, for example, quantifying the crack network. Separate results of both laboratories are presented below.

Sandia analysis

The main objective of this characterisation study (Jové Colón et al. 2016) is to (1) identify spatial heterogeneities of barrier materials near and far from EBS interfaces that can inform process models (e.g., porous media transport). Fig. 69 illustrates the concrete/bentonite sample analysed by Sandia and the interface region on which analyses were made. Although the integrity of the sample in hand specimen is remarkable, some minor cracks are visible particularly along the interface between the epoxy and bentonite clay. Still, the state of the retrieved core sample is very good and makes it ideal for obtaining thin sections for X-ray CT imaging. The reported results are presented next.

The salient feature from the analysis of 2D-slices is the common occurrence of microcracks in bentonite and pores (no cracks) in concrete. Gaping cracks and pores in bentonite tend to form near or at the concrete/bentonite interface whereas in other cases these are found at the interface of dissimilar materials (bentonite-epoxy).

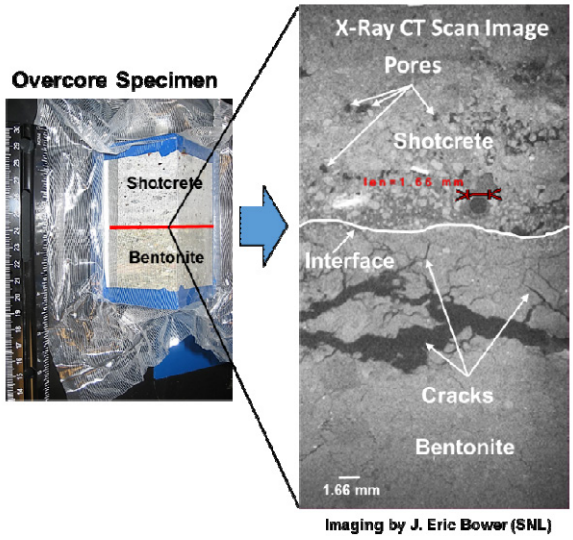

Fig. 69: Photographs of the C-C-32-6 concrete/bentonite overcore sample (left) and the X-ray CT image (right) focusing on the interface region.

Crack formation is not only restricted to areas close to material interfaces but are common to bulk bentonite regions as well. The cracks seen in the Fig. 70 have nominal apertures ranging from a few hundred microns up to about a millimetre for large cracks. Most crack apertures fall within the micron/sub-millimetre scale range. The 3D-projection of the CT scan slice stacks shows the extent and connectivity of cracks in the bentonite phase. Connected crack lengths can extend to length distances exceeding 1000 microns, in some cases evolving to or terminating into large pores. There is no discernable preferred orientation for cracks at the scale of these analyses.

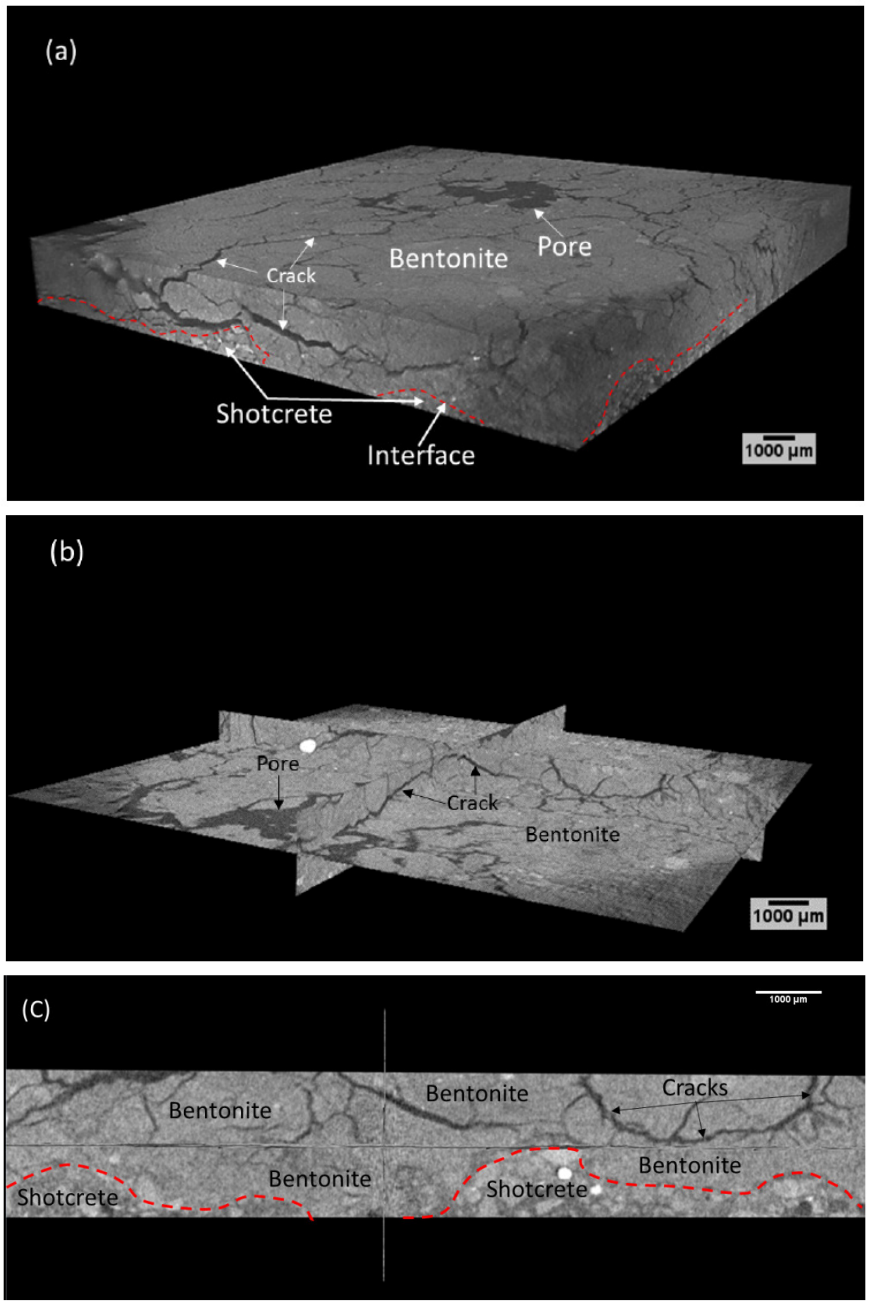

Fig. 70: (a) 3D-rendered volume of X-ray CT image data for sample C-C-32-6 at the concrete/bentonite interface (red dashed line) region. Notice the 3D-crack network connectivity to other cracks and large pores in the bentonite region; (b) orthoslice projection of the volume in (a) with the horizontal plane near the concrete/bentonite interface; (c) 2D-orthoslice (plan view) projection of the concrete showing its irregular nature. The length of the rectangular front face in (c) is ~1.3 cm.

However, typical crack pattern characteristics resemble that of a “tree” branch network with smaller-aperture cracks forking from a larger-aperture branch. Further analysis of 2D-3D

image stacks show these “tree” branch networks evolving into craquelure or “chickenwire” patterns in many cases connected by rectilinear and jagged segments (Fig. 71). The bentonite also has minor embedded granular material from which cracks either radiate towards the clay matrix or surround the grains. It should be noted that the rather heterogeneous nature of microcracks distribution also gives rise to localized regions without pores or crack features at interfaces and the bulk bentonite. This is indicative of apparent localized “sealed” regions at the interface. Similar observations from experiments involving FEBEX bentonite interactions with cementitious materials have been described by Fernández et al. 2009 and Cuevas et al. 2016.

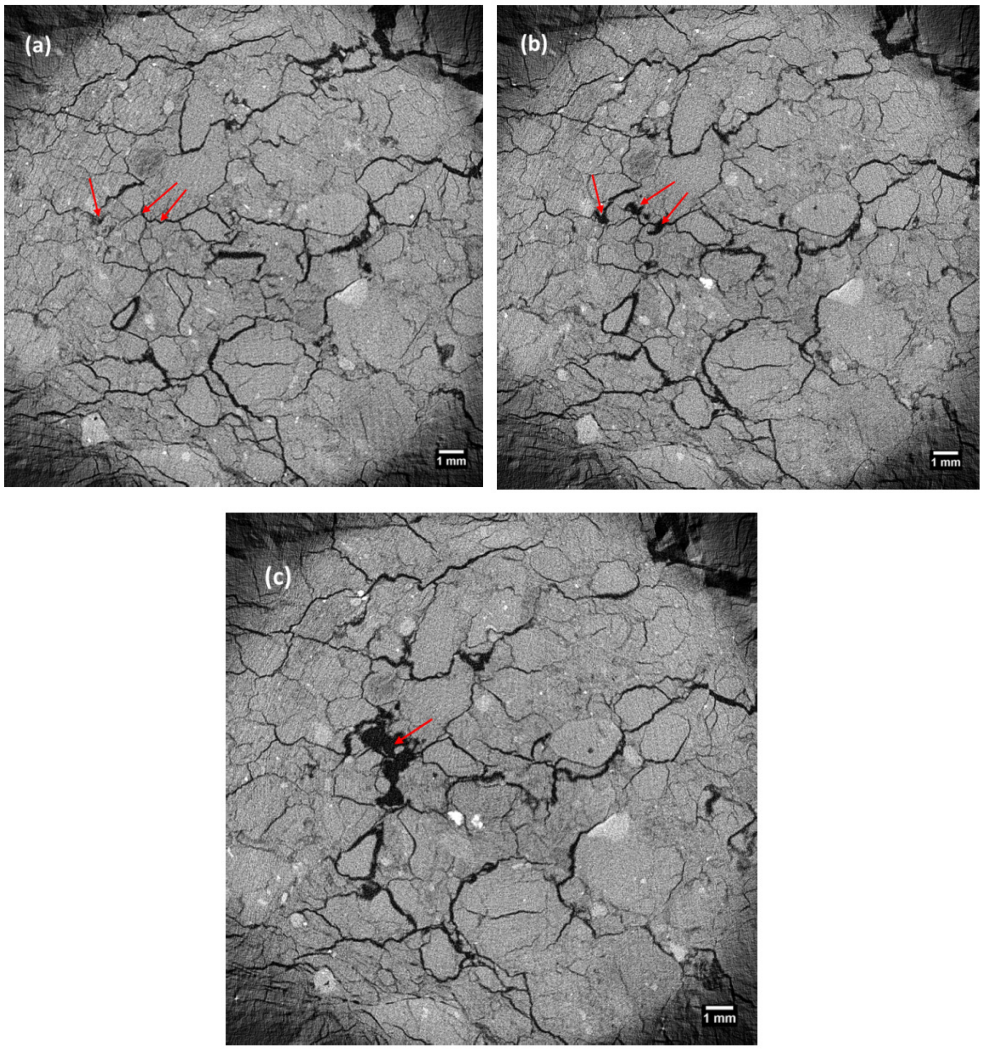

Fig. 71: CT image XY slice sequence (down z axis) of FEBEX bentonite showing the craquelure or “chickenwire” patterns of cracks evolving into pores. Red arrows in panels a-c delineate: (a) cracks, (b) small pores, and (c) large pores.

The concrete texture tends to be more regular with granular material embedded in a fine-grained matrix with dark spots interpreted as round-shape pores/voids having a wide size range (Fig. 72). The shapes and sizes of these pores/voids plus the apparent lack of secondary solid precipitation suggests these are the result of entrapped air during the concrete

emplacement. No microcracks at the scale of those observed in bentonite were resolved in concrete, even at the interfaces of large pores or grains. 3D pore/void connectivity still needs to be assessed from the digital image analysis. However, a preliminary assessment of the extent of void connectivity in concrete suggests these are often isolated except when localized at the concrete/bentonite interface.

The origin of microcracks in bentonite as observed in the concrete/bentonite core can be difficult to assess given the number of potential mechanisms in the creation of such features. For instance, sampling artefacts during overcore retrieval or desiccation and shrinkage due to in-situ or ex-situ drying conditions could induce crack formation in bentonite. It should be noted the overcoring technique employed in obtaining this sample is remarkable in preserving core material in the least disturbed state. Regardless of the origin of cracks, which in many cases is based on subjective criteria by the observer's evaluation, a description of microcracks patterns in bentonite is still very valuable in advancing common traits to similar structures observed in other environments. For example, desiccation cracks on clay surfaces or commonly known as "mud cracks" as a result of dehydration and shrinkage have been studied for decades motivated by the performance of clay-bearing geotechnical covers/liners and its importance to soil management (Corte & Higashi 1964, Gebrenegus et al. 2011, Kulander et al. 1990, Morris et al. 1992).

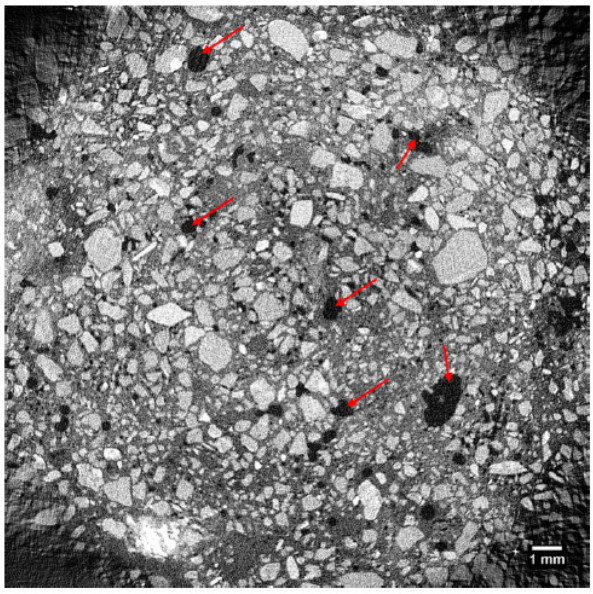

Fig. 72: CT image of concrete showing typical texture of angular grains in a fine matrix. Dark spots marked by the red arrows are interpreted as pore spaces based on preliminary evaluation of digital image stacks.

CT-imaging methodologies have been applied to studies of bentonite clay mixtures that have undergone drying/shrinkage to examine structural features such as desiccation crack morphology and dynamics under various conditions (DeCarlo & Shokri 2014, Gebrenegus et al. 2011, Gebrenegus et al. 2006, Tuller et al. 2013). The overall morphological features observed in the current analysis and the CT-imaging study of Gebrenegus et al. (2011) in sand-bentonite mixtures share some remarkable similarities, particularly the craquelure pattern and other microcrack network characteristics. Their study assessed the evolution of 3D networks of desiccation cracks in sand-bentonite mixture under controlled conditions of

temperature, pore solution chemistry, and bentonite content (Gebrenegus et al. 2011). They concluded that crack porosities (or pore volume fraction occupied by cracks) increased with bentonite content for samples exposed to drying. This is consistent with the occurrence of these features in the samples considering that FEBEX bentonite content is about 92% smectite clay. However, Gebrenegus et al. 2011 observed a decrease in hydraulic conductivity with increasing bentonite content in bentonite/sand mixtures. These authors also point to drying rates as an important factor in controlling crack porosities, whereas pore solution chemistry has less influence.

The occurrence and distribution of these microcracks in bentonite due to drying/shrinkage is important for evaluating the clay barrier performance given its strong influence on moisture transport, clay swelling, and therefore the permeability/porosity properties of the barrier. This is particularly important in the assessment of barrier performance during dry/wet cycles as anticipated for HLW upon emplacement in disposal galleries. Some key aspects of CT-imaging studies are the quantification of crack apertures and porosities based on 3D-image treatment algorithms and corrections to eliminate noise and other artefacts. This operation is necessary to attain the required resolution of crack networks and perform segmentation thresholding to resolve features of interest. Currently, image smoothing and thresholding tools in the ImageJ-Fiji software package seem adequate to qualitatively resolve major 2D-3D morphological features and patterns. However, automatic segmentation and quantification of crack apertures can be quite a difficult process given the complexity of recognizing and separating phases of interest with the obtained resolution, plus the huge demand on computational resources in handling massive amounts of data.

UniBern analysis

A preliminary evaluation of the data collected to date from the analysis of sample C-C-32-6 (Fig. 55) is presented in this part. Originally, two regions of the prismatic sample cut across the concrete/bentonite interface were scanned, one covering the immediate interface region, and one imaging bentonite ca. 30-55 mm away from the interface. The latter one showed very strong artefacts (ring artefacts and beam hardening) and hence was not evaluated. Also, only the CCD detector could be used and not the flat panel detector (under repair), and were consequently a bit limited in contrast.

The primary data consists of a data stack with a pixel/voxel size of 3.2 µm, with 2641 X-Y sections of 4032x4032 pixels in BMP format, each 15.6 MB in file size. Thus, the entire stack is ca. 41.2 GB. Two sections of the primary data (Fig. 73) show a section across concrete (left) and bentonite (right). Bright specks represent small inclusions of phases with very high X-ray attenuation, such as Fe-oxides/hydroxides or Fe-sulphides.

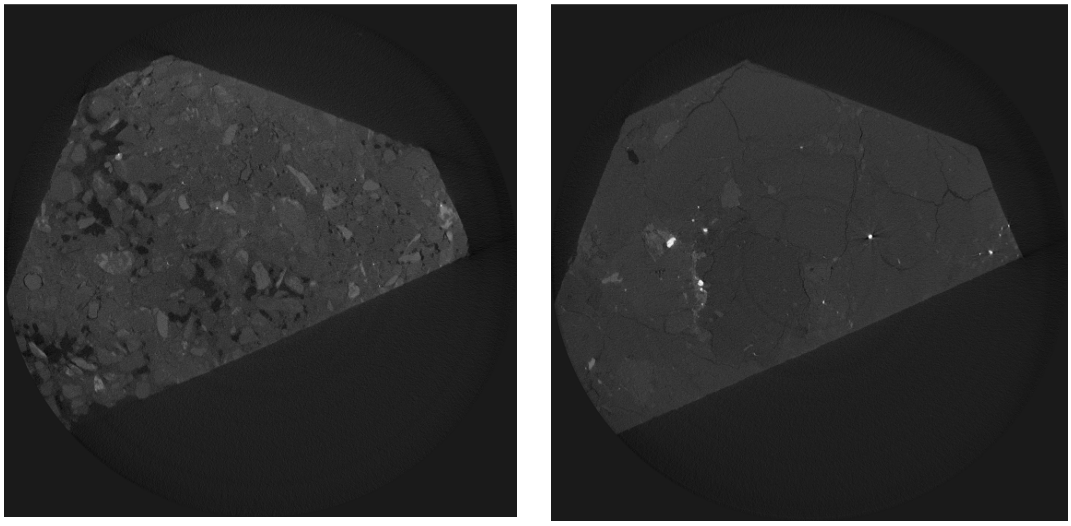

Fig. 73: CT sections parallel to the concrete/bentonite interface. Left: within concrete, right: within bentonite. The images are 12.9 x 12.9 mm.

A cylindrical volume of interest was cut from within the prismatic sample for easier handling. It is composed of 2309 X-Y sections, each 3.2 µm apart, measuring 6.60 mm in diameter, or 2064x2064 pixels, of 3.2 µm. A section across the concrete parallel to the interface (Fig. 74), at a distance of 15 mm from the interface, shows aggregate and gas/water voids quite irregularly distributed. Brighter grains have higher X-ray attenuation. Some minute bright specks are most likely composed of Fe-rich phases, and these commonly show star-shaped artefacts. This image also suggests that it may be difficult to resolve details from the cement matrix itself.

An image across bentonite, 35 mm from the interface (Fig. 75) indicates that some of the granular nature of FEBEX bentonite (optical imaging, SEM BS and EDX maps) is also visible in CT. The networks of fractures are artefacts due to sample storage. Dehydration may not necessarily be significant, but unloading and some minor shrinkage does result in these obvious features. Bright specks represent most likely Fe-rich accessory phases. It is of course impossible to resolve details at the pore-scale of bentonite. Nevertheless, slight differences seen here in grey scale (X-ray attenuation) of otherwise homogeneous smectite-rich regions must reflect either slight differences in density/water content, differences in the composition of the silicate sheets, or any submicron size evenly-distributed phases.

It may be possible to further refine the data set by thresholding and gain more information relevant for textural and compositional details. Semiquantitative evaluation of macroporosity (at the 3 µm scale) should be possible in concrete, irrespective of whether pores are gas-filled, water-filled or resin impregnated. Porosity characterisation is not possible in the bentonite part.

The 3D-model explained above (volume of interest) was serially sectioned parallel to the z-direction (perpendicular to the X-Y sections shown in Fig. 74 and Fig. 75 to obtain a view of the interface region (Fig. 76). It is a section exactly across the middle of the cylindrical volume of interest, oriented according to the X-Y axis of the FEBEX gallery in Fig. 74 and Fig. 75. The interface region (Fig. 76) shows a layer of bentonite, 1-1.5 mm wide with a mottled appearance, a relatively dense interface itself, and an adjacent porous region within the shotcrete. There is no clear skin developed at the interface; but a thin discontinuous zone

with a slightly higher X-ray attenuation is associated with the bentonite-side of the interface. This zone is only ca. 0.3 mm wide. It is evident, that the interface region did not suffer from obviously induced artefacts arising from sample preparation.

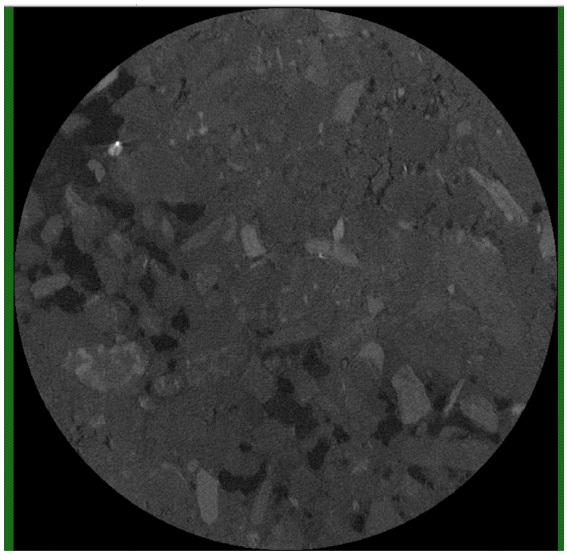

Fig. 74: CT-section across concrete parallel to the concrete/bentonite interface at a distance of 15 mm from the interface. The image is 6.60 mm in diameter.

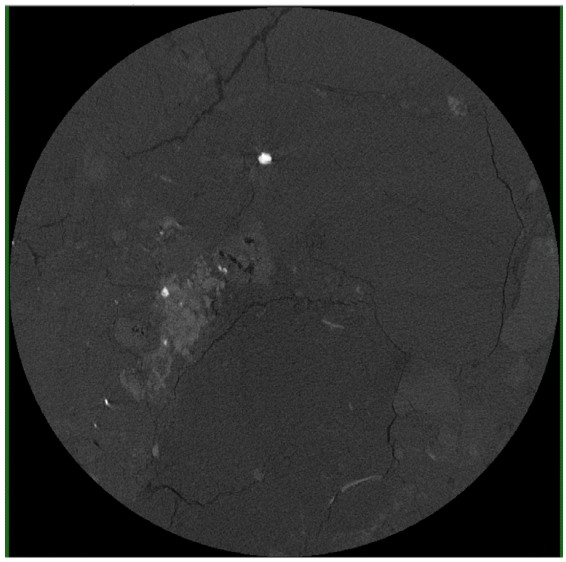

Fig. 75: CT-section across bentonite parallel to the concrete/bentonite interface at a distance of 35 mm from the interface. The image is 6.60 mm in diameter.

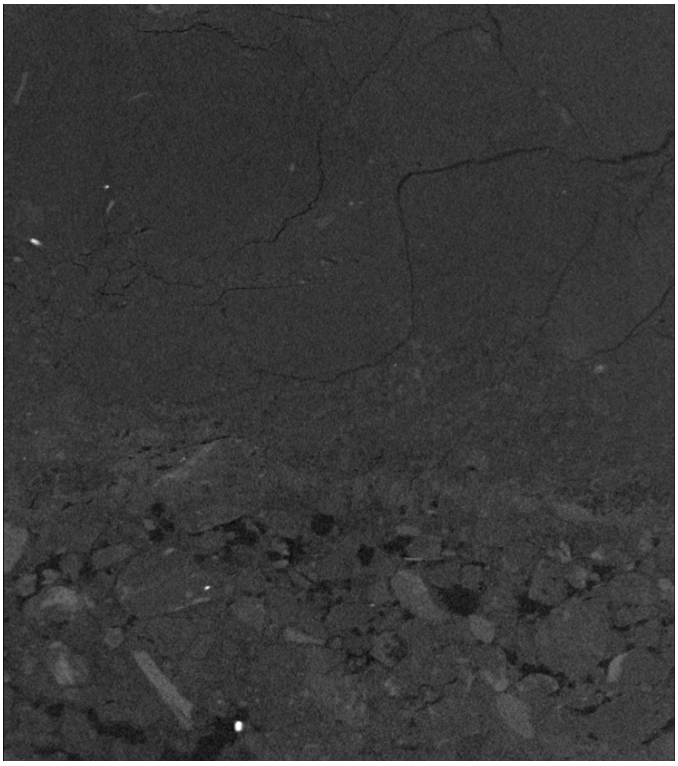

Fig. 76: CT-section perpendicular to the concrete/bentonite interface with concrete at the base. The image is 6.60 mm wide, and 7.39 mm high.

Serial sectioning of the same volume of interest perpendicular to the interface was performed. In this way 20 sections were produced, each 320 µm apart. A subset of 6 sections (Fig. 77), each section 960 µm apart, shows the heterogeneity of the interface region at the mm scale.

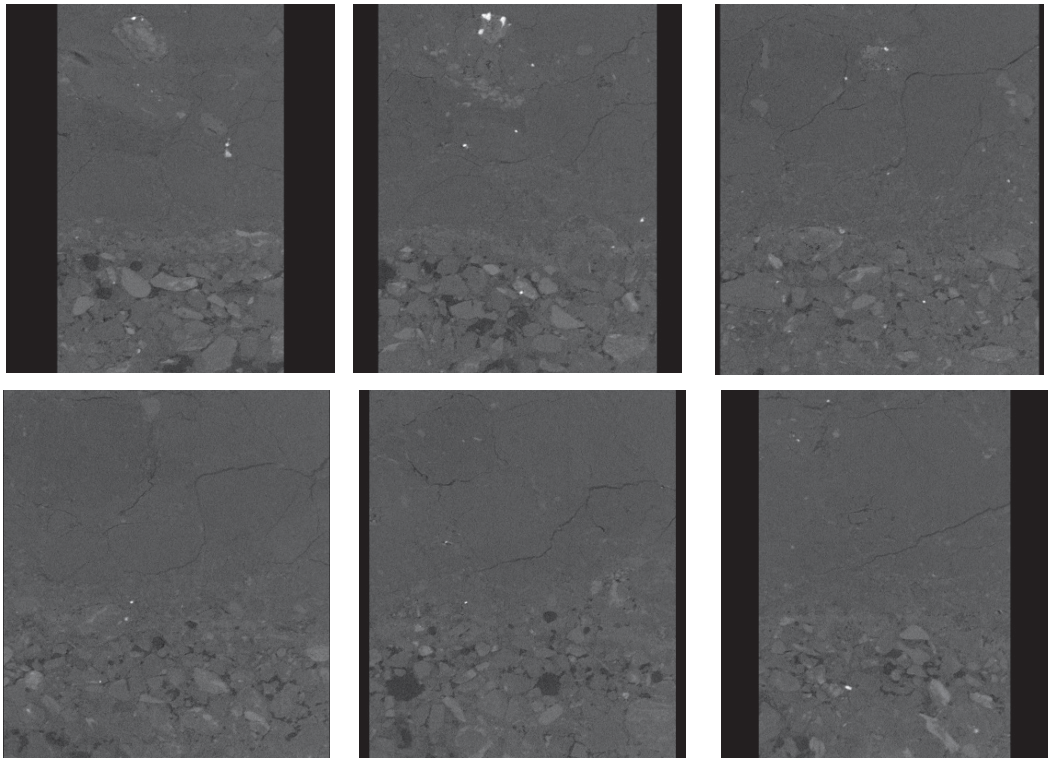

Fig. 77: CT serial sections perpendicular to the concrete/bentonite interface with concrete at the base. The images are up to 6.60 mm wide, and 7.39 mm high. The distance between the sections 0.96 mm.

Close-ups of the immediate interface region are shown in Fig. 78. Despite heterogeneity – particularly with respect to the concrete porosity – all sections across the interface region have a common character as described above (Fig. 76). The region with enhanced porosity in concrete is presumably due to the shotcreted concrete application. It should be possible to characterise the porosity distribution and connectivity at this scale by appropriate segmentation and volume rendering. The overall texture of concrete (such as layering) would need to be imaged at a larger scale.

The mottled region in bentonite adjacent to the interface (Fig. 78) is composed of thin particles of a phase with higher X-ray attenuation than smectite, which are arranged around the granular bentonite and outline this texture. This looks very similar to the Ca-distribution seen on the EDX map (further section 6.4.5.2, Fig. 143) where Ca does not penetrate smectite granules either, but accumulates along grain boundaries. It may be possible to even better resolve these small differences in X-ray attenuation and its texture by further optimization of the data acquisition and reconstruction, as well as to image at an even higher resolution.

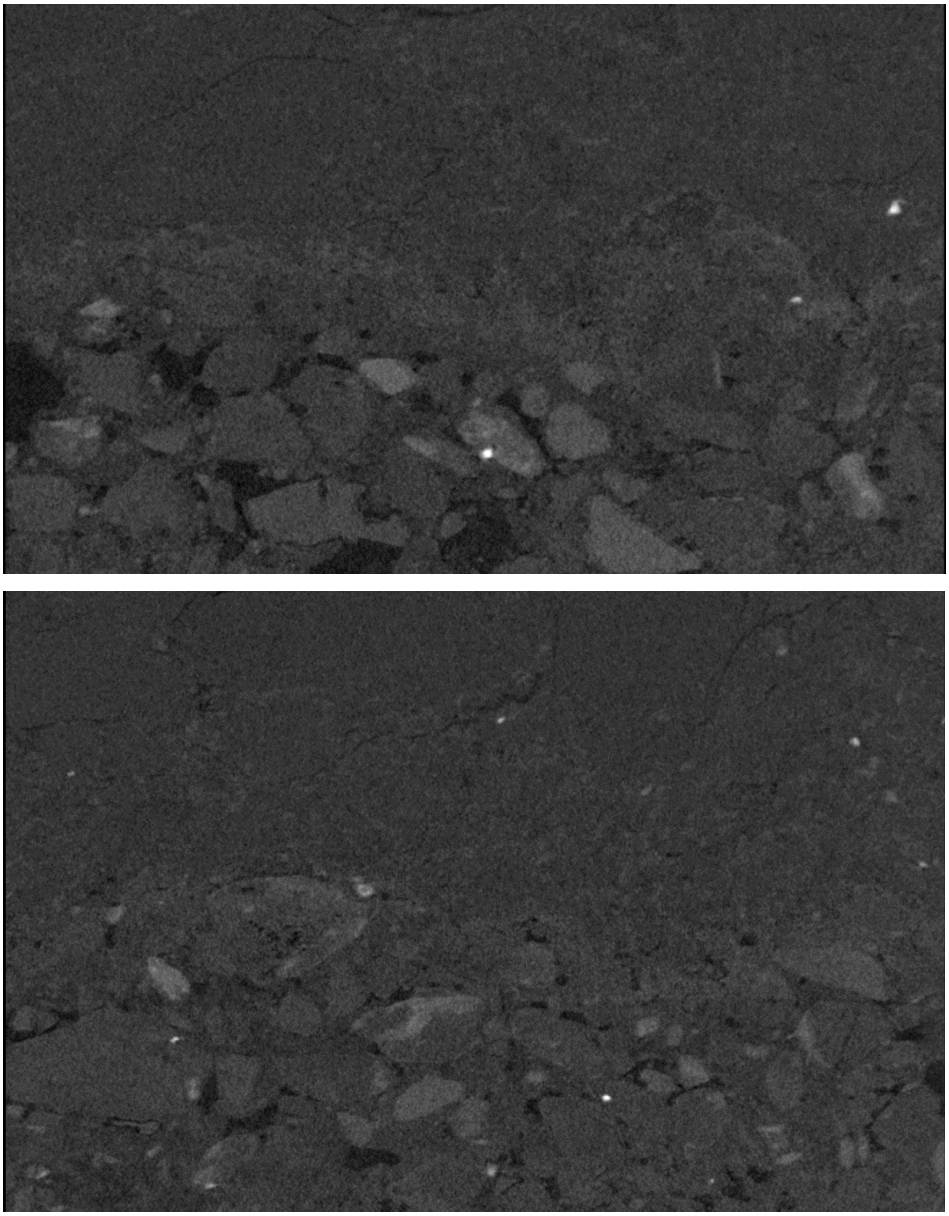

Fig. 78: Close-up of the interface region of some images from Fig. 77. The width is 6.6 mm. The distance between the sections is 0.96 mm. Images shows thin particles of a phase with higher X-ray attenuation than smectite.

6.3 Mineralogy

The mineralogy of the bentonite and the concrete was determined by most of the groups involved in the concrete/bentonite characterisation. The results are based on X-ray diffraction analysis, thermogravimetric analysis and differential scanning calorimetry, electron microscopy and infrared spectroscopy.

6.3.1 X-ray diffraction (UAM, Obayashi, BGR)

6.3.1.1 Results on samples C-C-34-4 to 12, BC-C-35-1 and 2, and BC-S-35-3 (UAM)

Concrete mineralogy

The quantification of the mineral phases in the concrete was done in section 1 of the plug in core samples that were drilled up to a distance of 10 cm from the interface. The results of the samples closest to the interface are presented in the part below this.

The quantification of the concrete mineralogy, specifically in terms of cement paste mineral phases, is characterised by the apparent lack of C-S-H phases. This can be attributed to the overlapping of C-S-H reflections and calcite (3.02-3.05Å) and presumably to the amorphous character of these minerals, not detectable by XRD. Fig. 79 shows the aspect of the XRD random powder patterns taken along the radius by cores C-C-34-4 to 11 at a distance of 50 cm from the bentonite-dummy front. Appendix B (part B.4, Tab. B-8) contains the results of the characterisation.

Calcite, ettringite and portlandite spatial distributions are represented in Fig. 80, Fig. 81 and Fig. 82. The figures are intended to represent the distribution of these minerals in all of section 1 of the plug, but it should be remembered that the samples do not reflect the mineralogy of the interface itself since the cores were drilled up to a distance of 10 cm from it. Therefore, the interpolations of the areas closest to the interface should be considered with caution. A detailed study of the interface will be presented in the part below this.

The calcite distribution is random and it has no apparent relationship with the main distinct boundaries: granite at the top, bentonite at the top x near 100 cm, and the iron dummy at the bottom x near 100 cm. Portlandite and ettringite exhibit certain dependences with boundary conditions. Portlandite tends to be depleted from the dummy to the bottom part (maybe related to the water spill observed to drain through the bottom part of the dummy, through the liner) and ettringite has slightly lower concentrations at the top part of the section, near the bentonite, although it is rather randomly distributed.

Calcite has been alternatively quantified by the calcimeter method by measuring outgassed CO_2 content. Fig. 83 shows the mapping of outgassed calcite revealing the increase of carbonates across the granite boundary and the decrease near the bentonite. In order to calculate an indicator for C-S-H, calcite determined in the calcimeter was subtracted from XRD calcite yielding a number that would be related to calcium silicate hydrates. The Pearson correlation coefficients were calculated for the variables portlandite, ettringite, outgassed calcite and calculated C-S-H (Fig. 83). The most significant correlation comes from portlandite and ettringite, which are anti-correlated. More portlandite is formed when ettringite decreases. This must be related to heterogeneities of the bulk concrete as near the bentonite contact both phases tend to decrease. New determined carbonates are correlated with portlandite, which is obviously anti-correlated with C-S-H. Carbonation should be more related to C-S-H decalcification than to portlandite dissolution.

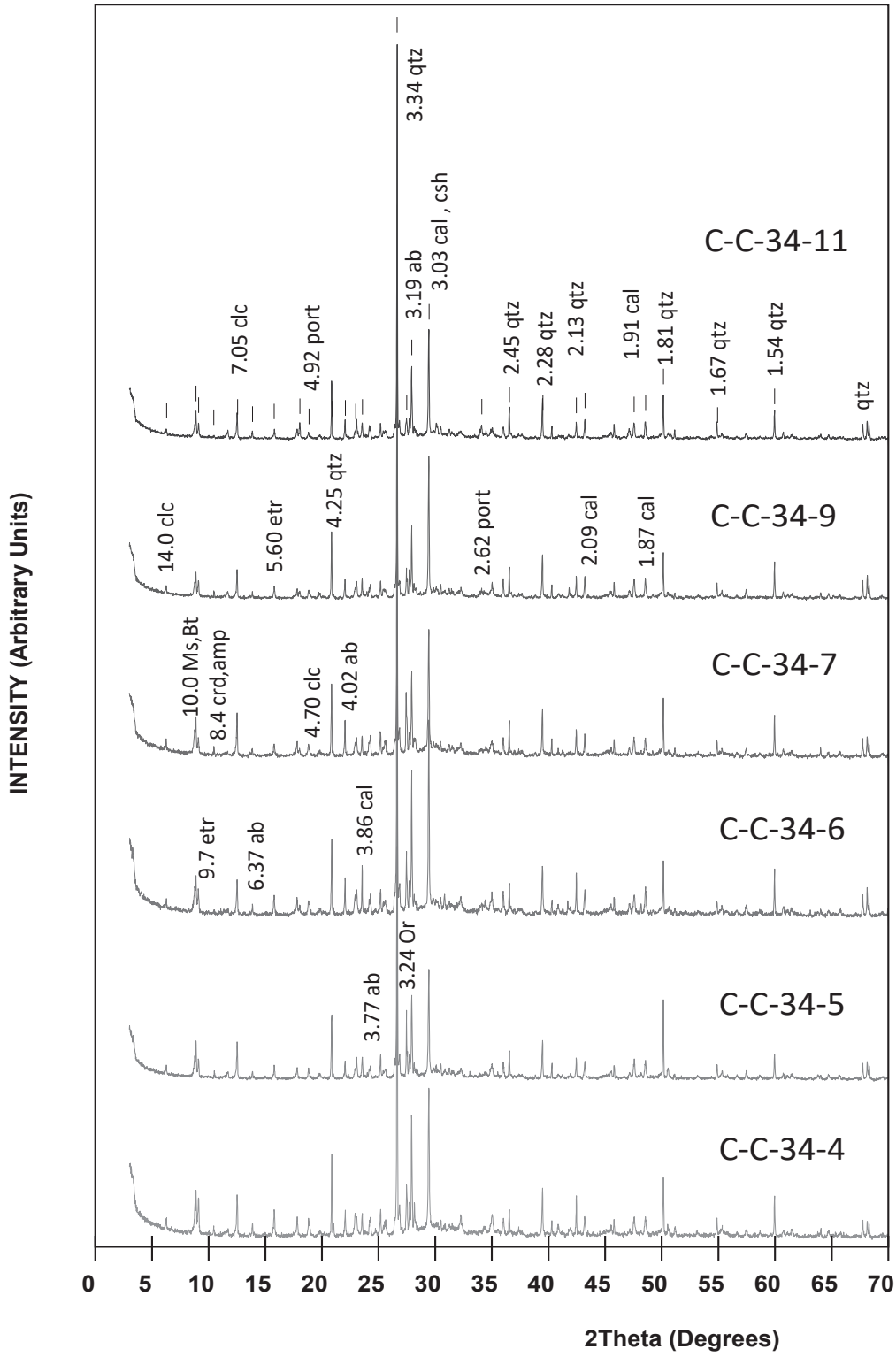

Fig. 79: XRD random powder patterns of samples C-C-34-4 to C-C-34-11 at 50 cm from the dummy-bentonite front. Peak numbers are d-spacings in Å. Clc: clinochlore, Ms: muscovite, Bt: biotite, crd: cordierite, amp: amphibole, ab: albite, or: orthoclase, port: portlandite, qtz:quartz, cal: calcite, etr: ettringite, csh: C-S-H.

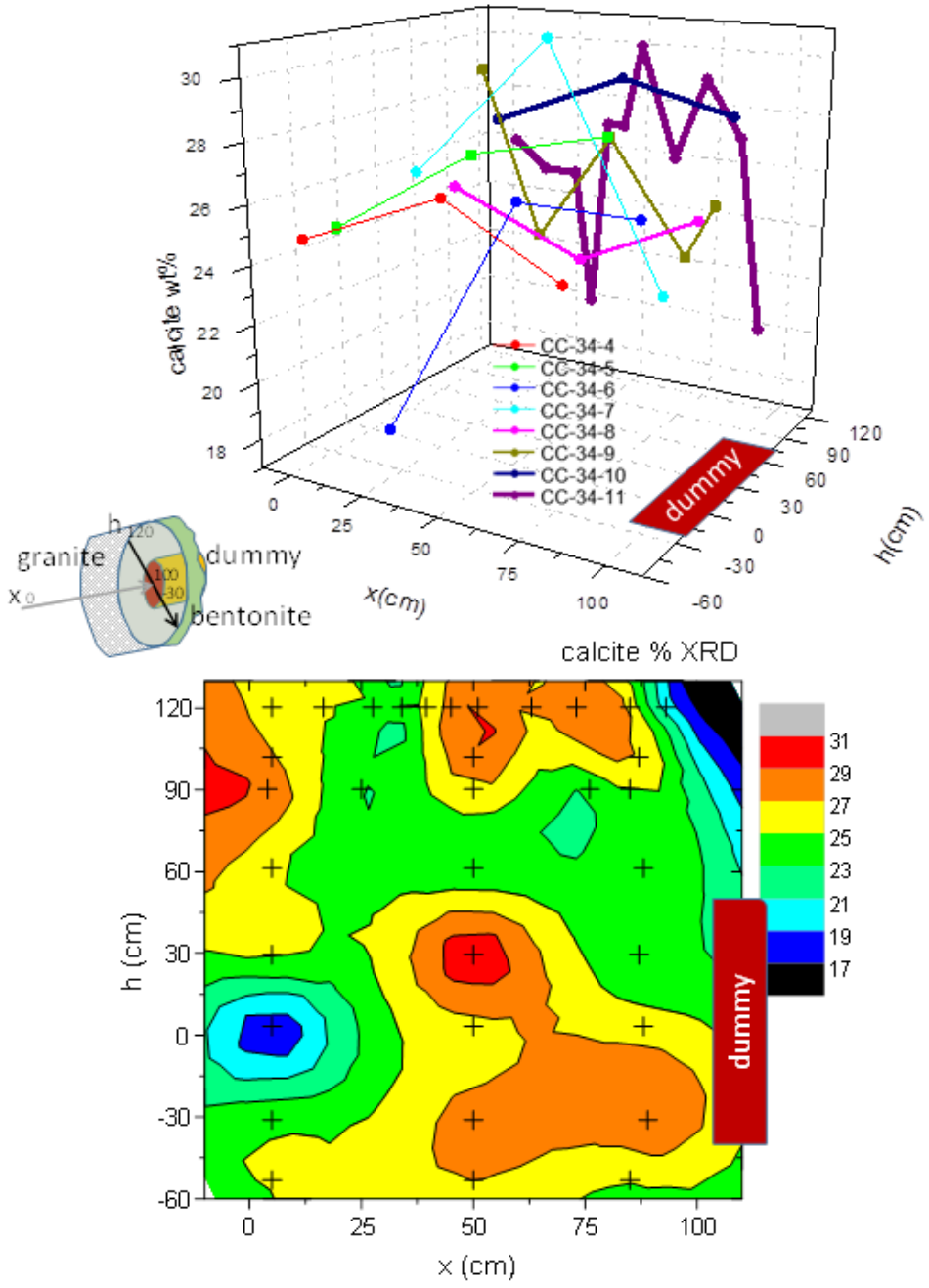

Fig. 80: 3D-representation of calcite determined in the concrete by XRD (upper part) as function of the distance to the bentonite and the dummy front (higher x indicates proximity to the bentonite) and the distance from the axis of the gallery following the line where the samples were taken (higher h indicates proximity to the granite) (see intermediate picture). Below: 2D-contour mapping for the calcite distribution. Note that the analysed samples are at a distance between 10 and 100 cm from the interface.

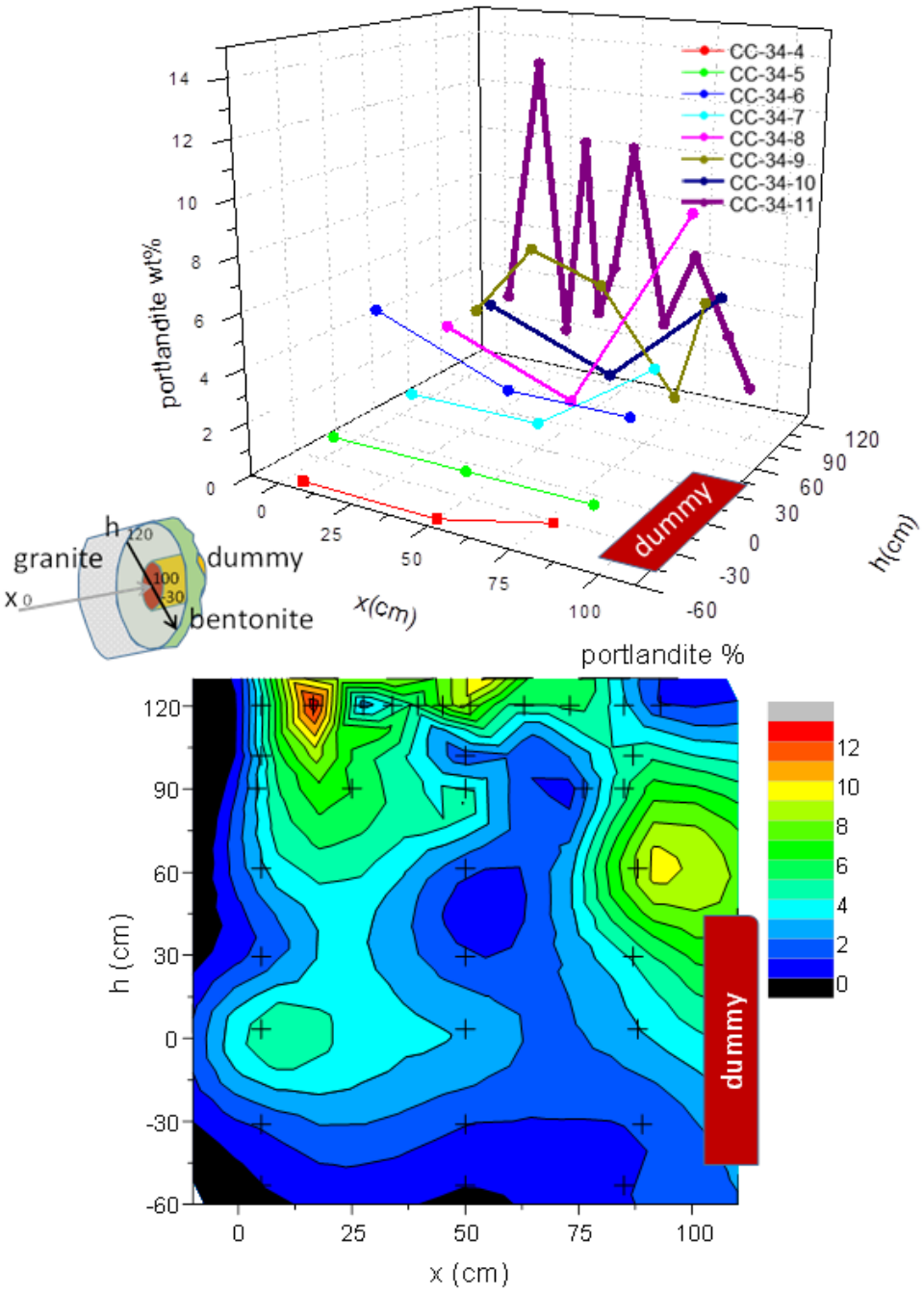

Fig. 81: 3D-representation of portlandite (upper part) determined in the concrete by XRD as function of the distance to the bentonite and the dummy front (higher x indicates proximity to the bentonite) and the distance from the axis of the gallery following the line where the samples were taken (higher h indicates proximity to the granite) (see intermediate picture). Lower part: 2D-contour mapping for the portlandite distribution. Note that the analysed samples are at a distance between 10 and 100 cm from the interface.

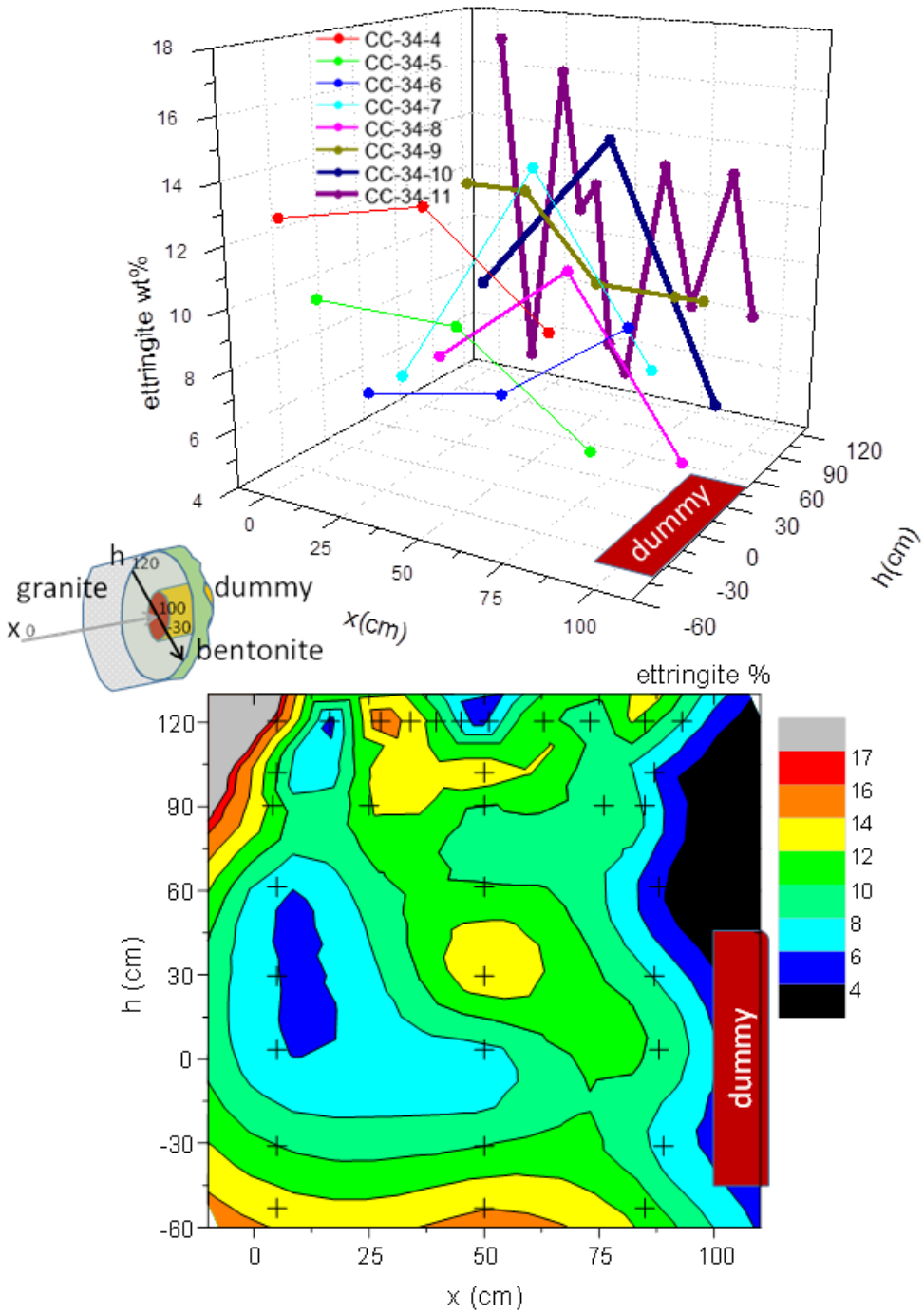

Fig. 82: 3D-representation of ettringite (upper part) determined in the concrete by XRD as function of the distance to the bentonite and the dummy front (higher x indicates proximity to the bentonite) and the distance from the axis of the gallery following the line where the samples were taken (higher h indicates proximity to the granite) (see intermediate picture). Lower part: 2D-contour mapping for the ettringite distribution. Note that the analysed samples are at a distance between 10 and 100 cm from the interface.

	etr	port	calco2	cshcalc
etr; r pearson	1	-0.46887	-0.19342	0.23279
sig lev.	--	0.00516	0.27306	0.1852
port; r pearson	-0.46887	1	0.37464	-0.39286
sig lev.	0.00516	--	0.02904	0.02154
calco2; r pearson	-0.19342	0.37464	1	-0.81665
sig lev.	0.27306	0.02904	--	3.88E-09
cshcalc; r pearson	0.23279	-0.39286	-0.81665	1
sig lev.	0.1852	0.02154	3.88E-09	--

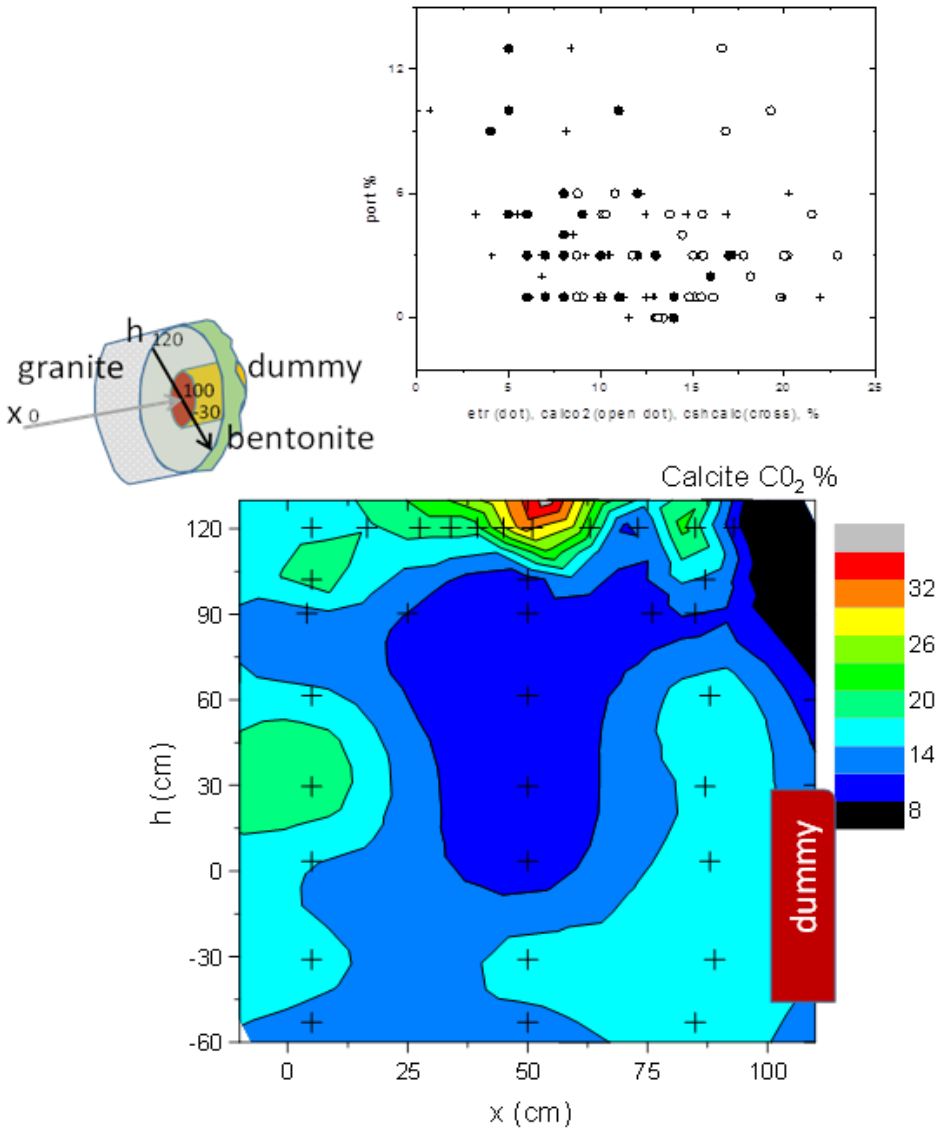

Fig. 83: Correlation statistics and scatter diagram for ettringite (etr), outgassed calcite (calco2), portlandite (port) and calculated C-S-H (cshcalc). Lower part: 2D-mapping of degassed calcite is shown at the bottom of the figure. Note that the analysed samples are at a distance between 10 and 100 cm from the interface.

Concrete/bentonite interface

Appendix C (part C.5) details the sampling sections and mineralogical quantification made on concrete/bentonite samples for XRD quantification. The quantification of XRD random powder patterns reveals the characteristic presence of relatively high contents of calcite and sometimes gypsum at the concrete side of the interface. C-(A)-S-H phases become more representative than in the bulk concrete, and portlandite is detected in low quantities; i.e. similar or less than the contents detected in most parts of the bulk concrete (< 5%; see chapter 5). The presence of ettringite on the concrete side is relevant when gypsum is not detected. Calcite and less frequently gypsum are also concentrated in a 1 mm thickness at the bentonite side of the interface, where C-(A)-S-H and M-S-H trioctahedral 2:1 sheet silicates are abundant in the scrapped "zero" mm zone of the interface. The characteristic presence of gypsum, calcite, C-(A)-S-H and M-S-H minerals is shown in Fig. 84 (left) for BC-C-35-1 core interface samples, where ettringite is absent. Fig. 84 (right) illustrates the case for BC-S-35-3 in which gypsum is not present in the concrete interface and ettringite is concentrated. The quantification data for the characterised samples are listed in Appendix C (part C.5, Tab. C-12).

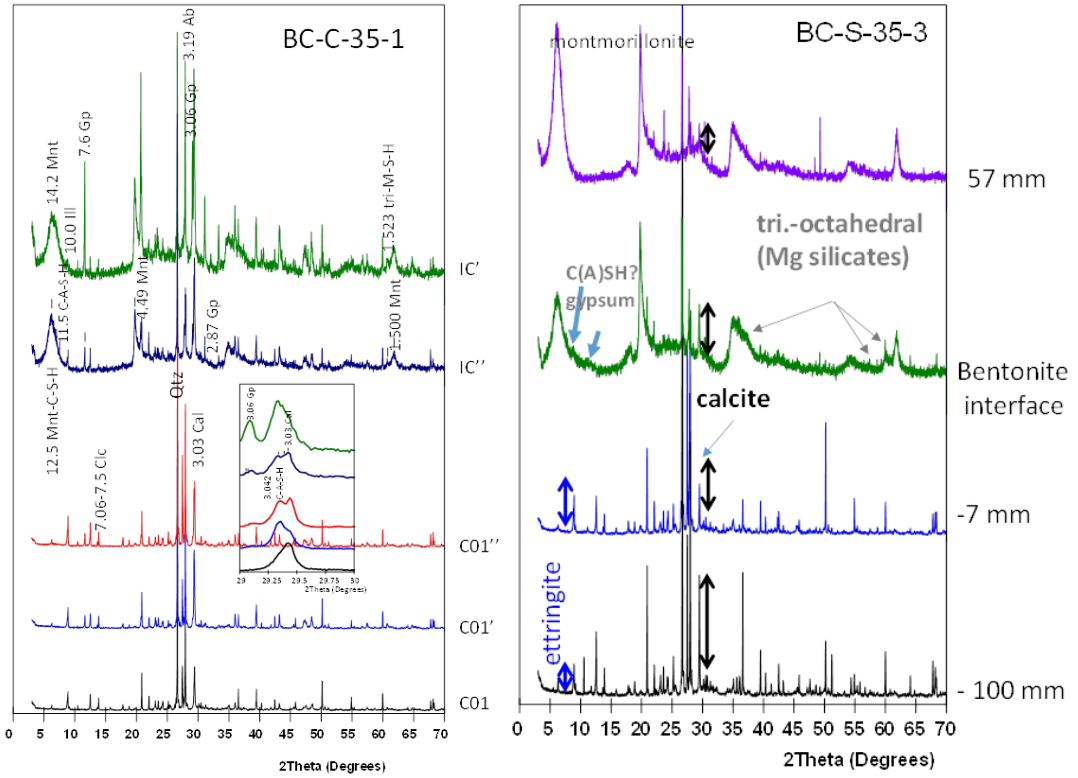

Fig. 84: Main representative mineral phases identified in random XRD powder patterns in the concrete interface sampled in core BC-C-35-1. Peak reflections are numbers in Å. Minerals' abreviations are the same as in Appendix C (part C.5, Tab. C-12) where explanation on C-A-S-H and M-S-H adjusting is made.

Calcite decreases to < 20% when compared to the bulk concrete (30-20 %) and becomes concentrated towards the interface. Fig. 85 shows the % of calcite at one or the other side of the interface. Carbonate content was determined by XRD RIR semi-quantification and

calcimetry and although XRD tends to overestimate the calcite in the concrete material (see Appendix B, B.2 Tab B-5) the results are very comparable, which provides confidence in the carbonate content profiles across the concrete/bentonite interface. Calcite content decreases from about 1cm in the bentonite towards the interface. Then it increases to 30 (± 5) %. This calcite concentration front sometimes passes the first 4 mm of bentonite, especially in the upper part cores in the gallery, e.g. samples C-C-34-10 and 34-8.

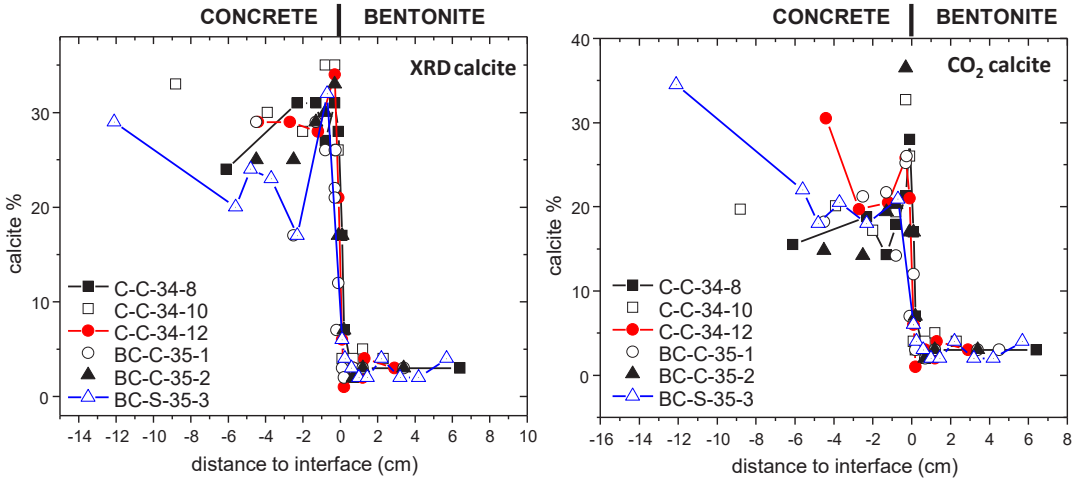

Fig. 85: Calcite distribution at the concrete/bentonite interface. Concrete calcite content has been determined by XRD (left) and calcimetry (right, only for the concrete).

On the bentonite side the montmorillonite content decreases at the interface due to the presence of trioctahedral magnesium silicates (Appendix C, part C.5, Tab. C-12). Fig. 86 shows details of the bentonite sampled at the concrete contact. The basal XRD reflection region exhibits a lot of complexity compared to the original bentonite. Within the region of 12 to 7 Å diffraction reflections have several maxima which may indicate the presence of 11-Å tobermorite type C-A-S-H minerals, 10Å mica, ettringite in the case of C-C-34-10, 9-Å tobermorite type C-S-H and 7.6 Å gypsum. The wide reflections at 11-11.5 Å could be indicative of tobermorite-type calcium aluminate silicate hydrates (C-A-S-H) (Fernández et al. 2014; Fernández et al. 2016). Reflections observed in the region 7-7.5 Å may indicate the intercalation of brucite in montmorillonite or the possible formation of serpentine-like minerals (Fernández et al. 2013b). In fact, the formation of trioctahedral sheet silicates is confirmed by the presence of at least two bands at 1.53-1.52 Å and by the shoulder to lower angles of the 2.57 Å reflections. These reflections form part of the h-k non-basal reflections of 2:1 and 1:1 sheet silicates and the new positions, although related to broad maxima, are compatible with the presence of M-S-H disordered phases structurally described by Roosz et al. (2015). A typical profile from these phases has been included in Fig. 86. It has to be outlined that the presence of montmorillonite introduces a lot of difficulty in the M-S-H determination due to important overlapping in h-k bands.

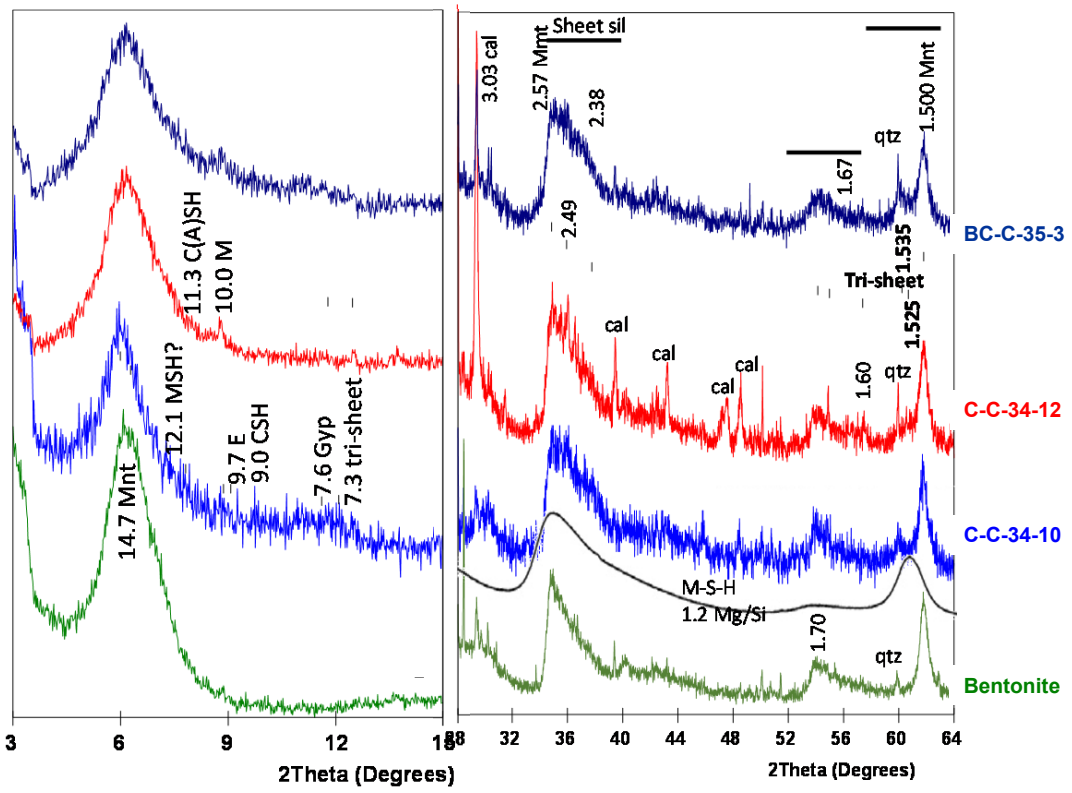

Fig. 86: XRD details from random powder patterns of bentonite scrapped at the concrete interface. (Left) Basal reflection °2θ range for sheet silicates. CSH, C(A)SH: C-S-H minerals 11 to 9Å tobermorite type. M: mica, E: ettringite, Gyp: gypsum, Mnt: montmorillonite. Tri-sheet: trioctahedral sheet silicates of the serpentine group. (Right) h-k non-basal reflections range within 28-64 °2θ. Numbers are positions of the diffraction reflections in Å. Sheet sil: h-k non-basal reflections of sheet silicates. Tri-sheet: 060 reflection from trioctahedral sheet silicates. Cal: calcite, Mnt: montmorillonite, qtz: quartz; M-S-H: XRD pattern of M-S-H with 1.2 Mg/Si composition as taken from Roosz et al. (2015).

The above described bulk mineralogy identifies typical alteration patterns for concrete and bentonite at or near the interface (Fig. 87). Concrete exhibits an increase of C-S-H, although less when calcite is formed, and an increase of ettringite that is less when gypsum is formed. On the other hand, bentonite is characterised by the formation of M-S-H and C-A-S-H minerals. This fact causes a slight decrease of the montmorillonite content in the first 4-8 mm thickness of the bentonite.

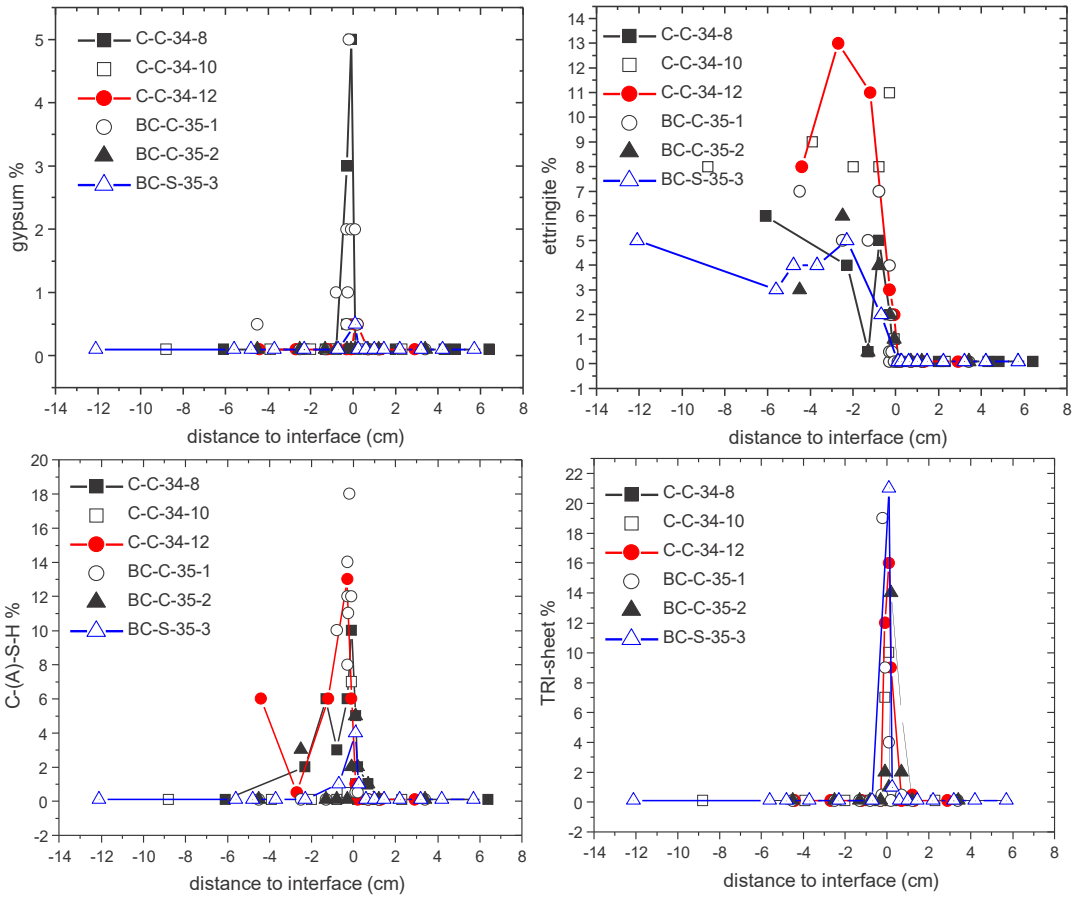

Fig. 87: Gypsum, ettringite, C-(A)-S-H and trioctahedral M-S-H 2:1 sheet silicate phase disitribution at the concrete bentonite interface.

Oriented films of < 2µm clay fractions were prepared on glass slides. These clay fractions were not obtained by adding any dispersing agent nor were homoionised in any index exchangeable cation as calcium or magnesium. The basal spacing of air dried films is hence, related to the redistribution of the exchangeable cations at the interface. 15.0, 14.5 and 12.0 Å are the basal spacing positions for Ca-, Mg- or Na- homoionised FEBEX montmorillonite. As a rule, FEBEX smectite in the studied samples maintains the regularity of the different orders of basal reflections and the predominance of the divalent cations in the exchange complex. The main feature observed is the sharpening and symmetry of the basal reflection in B01 samples near the concrete interface. These reflections are also fixed at 15.0-15.03 Å, indicating the presumable predominance of calcium. Samples situated progressively further from the interface exhibit a characteristic asymmetry to higher angles (Na-contribution) and a slight decrease of the value determined for the basal spacing to 14.5 Å (Fig. 88). Illite presence (9.9-10.0 Å reflection) is detected in the air-dried oriented aggregates, usually in samples B01. These reflections are not evident in the EG-treatment which can be attributed to the expansion of small quantities of high-charged collapsed interlayers of montmorillonite.

Ethylene-glycol treated samples show the homogenization of basal spacing to their regular symmetric shapes and virtually the same thickness. The regularity and similarity of most of the patterns indicates minor or no changes in the characteristics of montmorillonite at a distance of 1-2 mm away from the interface into the concrete.

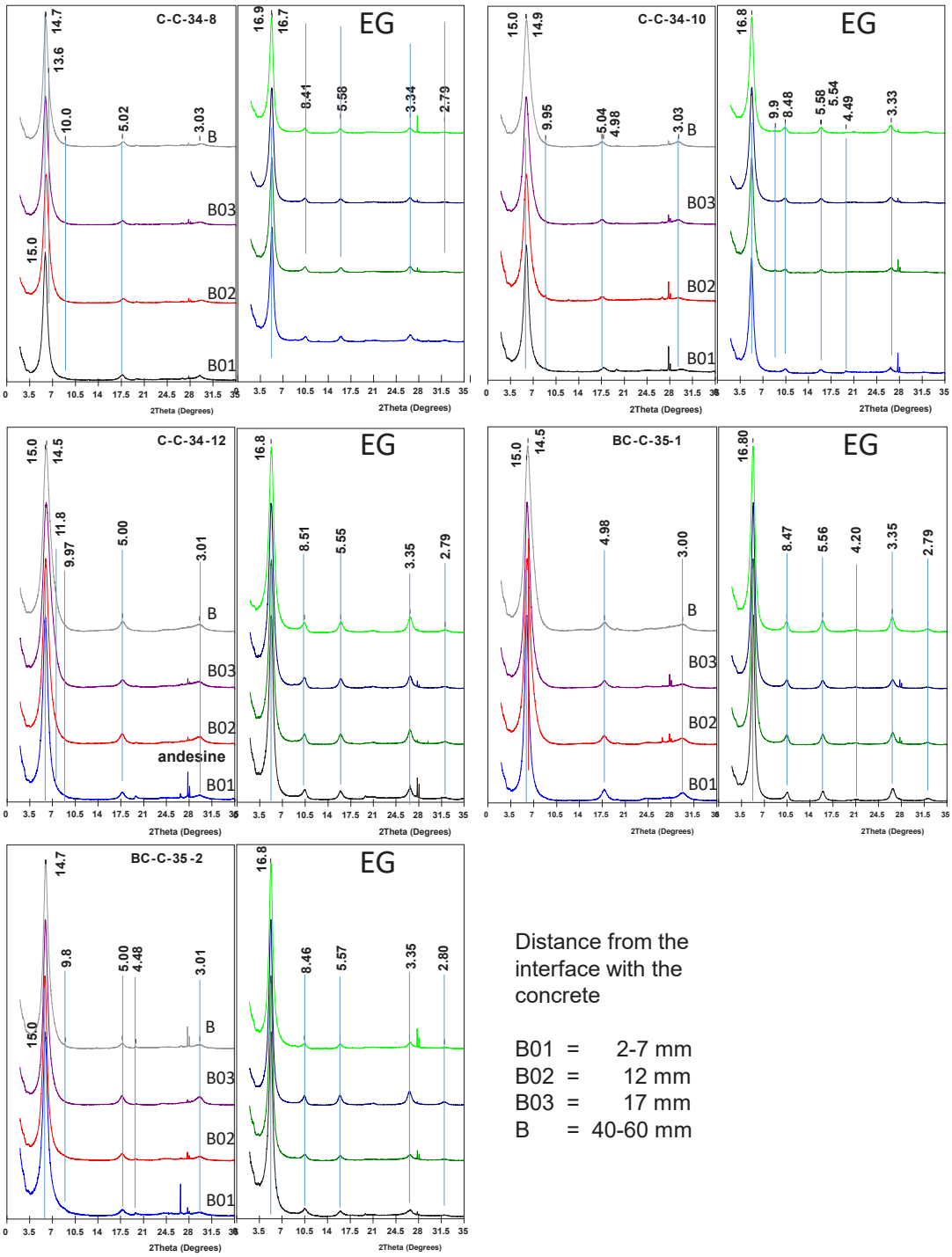

Fig. 88: XRD powder patterns performed on oriented air dried (left side of each sample) and ethylene-glycol solvated clay (<2µm size fraction) (right side of each sample). Numbers are peak reflections in Å.

6.3.1.2 Results on sample C-C-32-6 (Obayashi)

The XRD patterns for random powder samples 0 to 10 and BL (reference) (Fig. 66) are shown in Fig. 89. For sample 0, mica, chlorite, and feldspars were identified and quartz shows a higher peak than the other samples. The reason for this is that sample 0, obtained at the interface, contains a small portion of concrete. Samples 1 to 10 show peaks of calcite not identified in sample BL. The closer to the interface, the greater the intensity of the calcite peaks. That implies that calcite was precipitated as a secondary mineral under the influence of the alkali leachate from the concrete. In addition, the intensity of smectite near the interface is lower than that of sample BL. That also implies that smectite was influenced by the alkali leachate.

The XRD patterns for the twelve oriented powder samples are shown in Fig. 90. The basal spacing of the samples is 1.50 nm, which means that the dominating interlayer cation is Ca. The peak intensity of smectite of samples 1, 2 and 3 are lower than in sample BL. That again implies that smectite in the sample was influenced by the alkali leachate, consistent with the results of the XRD measurement on random powder samples.

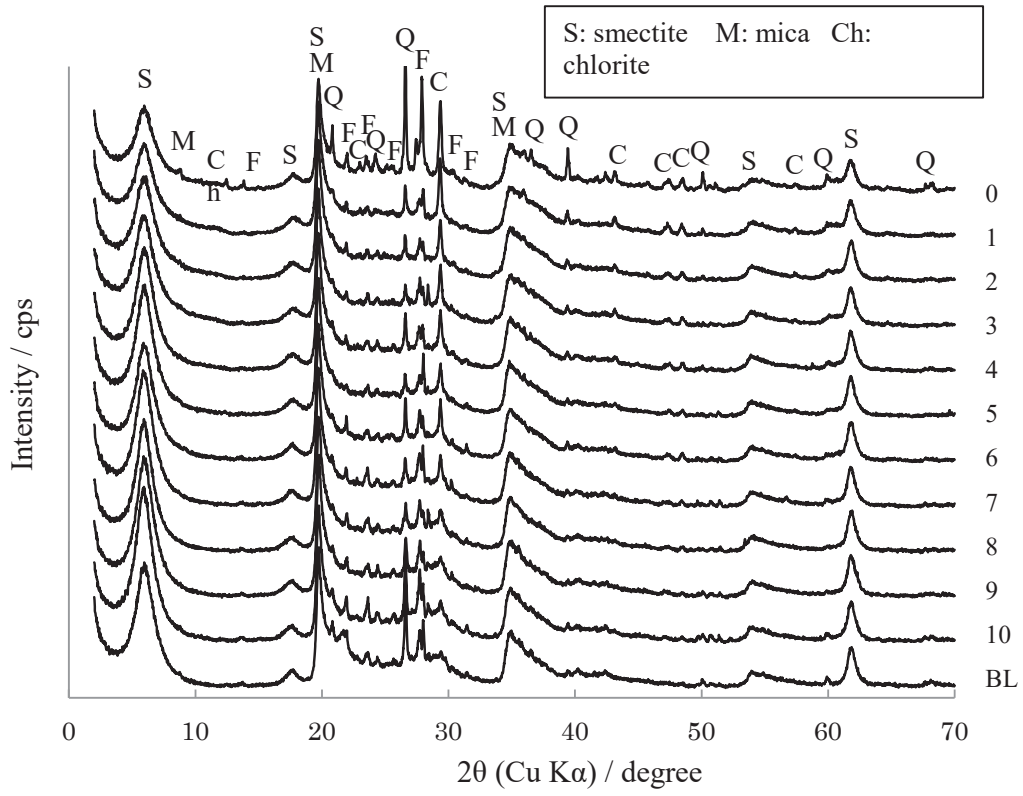

Fig. 89: XRD patterns for the sliced random powder samples of bentonite.

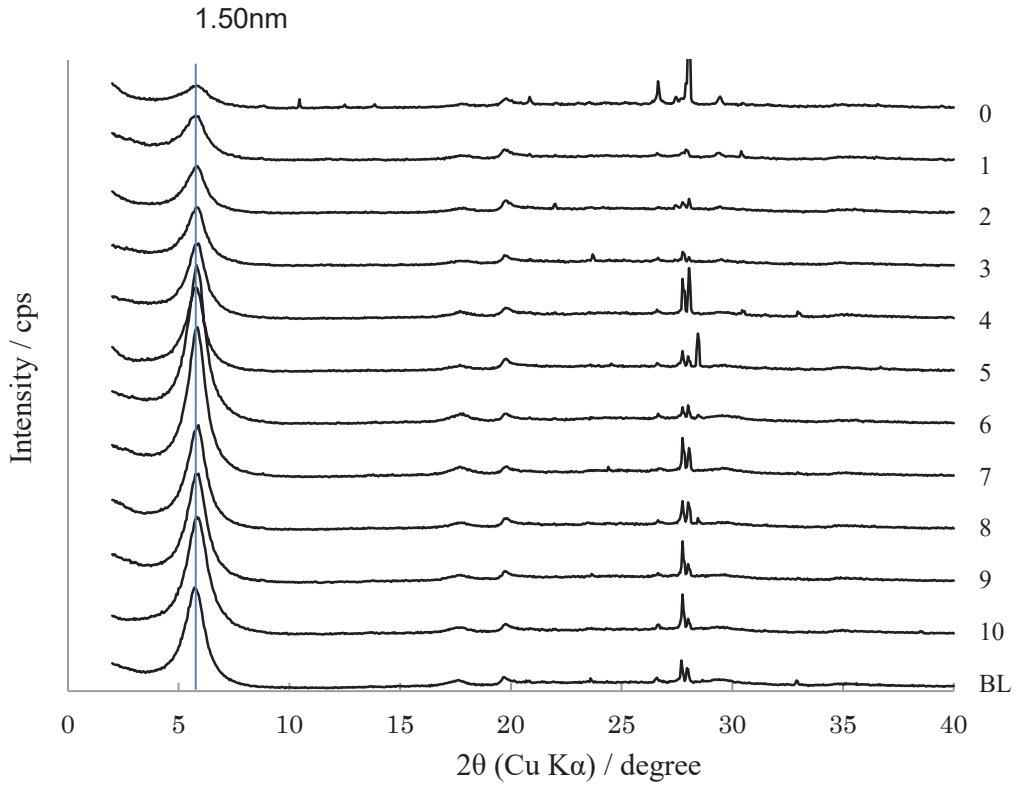

Fig. 90: XRD patterns for the sliced oriented powder samples of bentonite.

6.3.1.3 Results on sample BC-S-35-1a and b (BGR)

XRD powder patterns of the contact samples and the reference material (21-FEB) are shown in Fig. 91. A larger calcite peak was found for both contact samples (around 34 °2θ). Also, more pronounced quartz peaks were found for the contact samples (at almost 60 °2θ). Both calcite and quartz, contribute to the peak at about 46 °2θ. The peak at about 71°2θ can also be assigned to quartz rather than to trioctahedral layer silicates. The increased quartz intensity at that position is probably not related to an increased content of quartz but to single crystal reflections. Clay mineral abundance was further investigated by XRD texture slides (Fig. 92). The XRD analysis after ethylene-glycol intercalation showed that sample BC-S-35 1b 1mm has still the same expendability to 16.9 Å as the reference sample. However, the peaks of the basal series were broadened. Rather small amounts of muscovite and a 7 Å mineral (kaolinite, serpentine) were found. The peaks, however, correspond to 3 to 5 times the signal noise ratio and hence should not be over-interpreted. The decrease in exchangeable Na^+ (Appendix C, part C.2, Tab.C-3) could explain the small peak shift of the d_{001}-reflection to larger basal distances.

All qualitative information was used to calculate a quantitative mineral composition by Rietveld analysis (Tab. 6-3). Rietveld analysis, however, did not provide further information on the presence of either brucite or kaolinite/serpentine. Although peaks are at different positions, some brucite or kaolinite/serpentine is found depending on which structural reference is used.

Rietveld analysis found a slightly lower smectite content (only BC-S-35-1a), more carbonate (only BC-S-35-1b), and possibly some brucite/7Å-clay mineral in the contact samples. The brucite/7Å-clay mineral content of sample BC-S-35-1b is low (about 0.3 mass %) and hence at the detection limit. Larger brucite/7Å-clay mineral content was found for sample BC-S-35-1a which also showed the most significant increase of the band at 3698 cm^{-1} of the IR analysis (section 6.3.4, Fig. 121). This sample shows the most significant Mg increase (section 6.4.3, Tab. 6-5) which would speak for brucite. On the other hand a weak 7Å reflection was found in the XRD. Therefore, it is impossible to state whether a trace of brucite or kaolinite/serpentine was formed (or even both).

Tab. 6-3: Mineralogical composition of samples from section 35 (XRD Rietveld analysis) compared with the reference material (FEB). 0 means < 1 mass %.

	BC-S-35-1a 1mm	BC-S-35-1b 1mm	BC-S-35-1a 3Cm	BC-S-35-1b(2) cement 1cm	FEB
	[mass %]	[mass %]	[mass %]	[mass %]	[mass %]
Quartz	5	3	2	23	1
k-feldspar	3	4	5	14	5
Smectite	79	83	84		84
Plagioclase	10	8	9	22	9
Calcite	1	2	1	12	1
Goethite				2	
Aragonite				4	
Brucite/7Å-clay mineral	2	0			
Muscovite				6	
Gypsum				10	
Chlorite				6	
Siderite				1	
Total	**100**	**100**	**100**	**100**	**100**

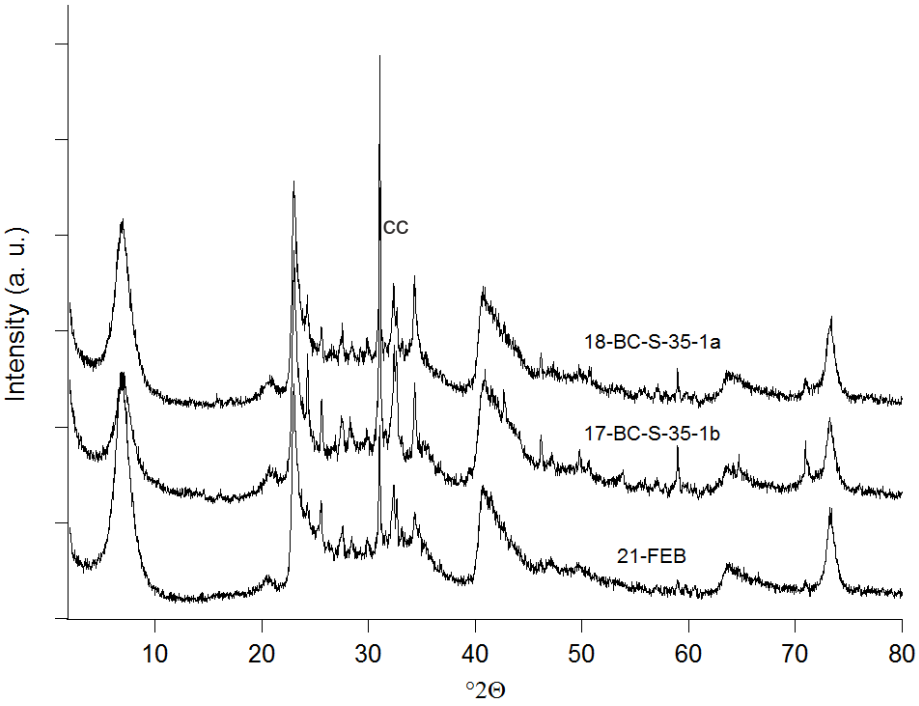

Fig. 91: XRD pattern of selected samples from section 35 (cc indicates the position of calcite).

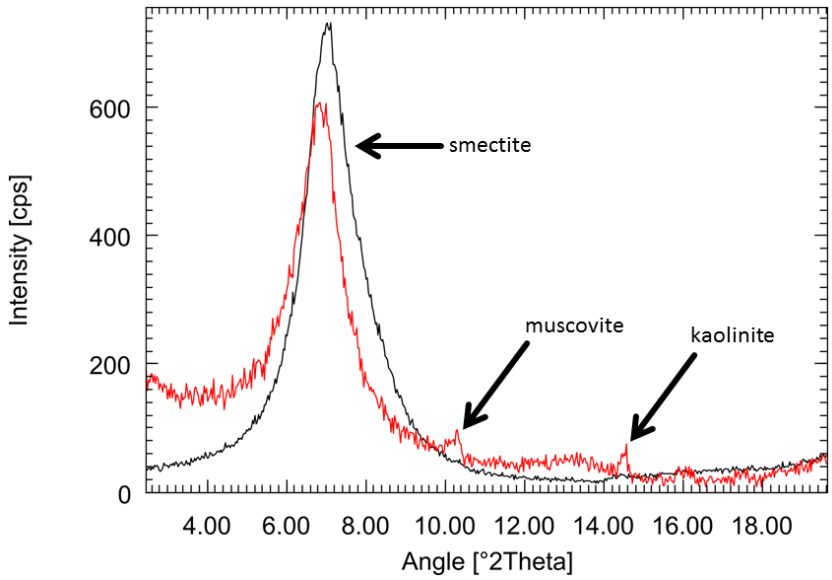

Fig. 92: XRD texture slide pattern of the reference (black) and sample BC-S-35 1b 1mm (red) after drying at air.

6.3.2 Thermogravimetric Analysis and Differential Scanning Calorimetry (UAM, BGR)

6.3.2.1 Results on samples C-C-34-4 to 12, BC-C-35-1 and 2, and BC-S-35-3 (UAM)

Bulk concrete

Thermogravimetric (TG) and derivative thermogravimetric (DTA) analyses were performed within two transects in samples C-C-34-11 and C-C-34-9. Both samples represent a line from the granite towards the bentonite. Appendix B (part B.4, Tab. B-9) contains the main temperature maxima for mass loss as indicated in the example of Fig. 93. In addition, weight % losses for several intervals are given: 25-300 ºC (adsorbed or free water loss: CSH, ettringite); 300-500 ºC (hydroxides (portlandite), organics); 500-800 ºC (dehydroxilation of 2:1 sheet silicates; carbonates); 800-1000 ºC (structural decomposition, crystallization of new phases; Emmerich, 2011).

The DTA data from the analysed samples indicate that most of the weight loss is associated to dehydration in the region of 25-300 ºC; and degassing of CO_2 centred at 700 ºC. This temperature is indicative of fine-grained carbonates, either incorporated in the CEM-II formulation or redistributed by actual dissolution/precipitation processes (Villain et al. 2007). In fact, dehydration has the most significant correlation coefficient with the total loss of weight measured in the samples. There is a significant trend of the less hydrated from the concrete towards the bentonite face (Fig. 94). There were good correlations between the ettringite presence and the mass loss on dehydration and between the total mass loss and the calcite content determined by calcimetry (Fig. 95). It is worth mentioning that there was no significant relationship between portlandite content and the thermal loss at 300-500 ºC. From Fig. 94 it becomes clear that a DTA peak overlaps with the 410 ºC portlandite dehydration maxima; this is interpreted as the decomposition of organics in pyrolysis. Another peak near 500 °C agrees with the decomposition temperature of polypropylene (Beyler & Hirsler 2002).

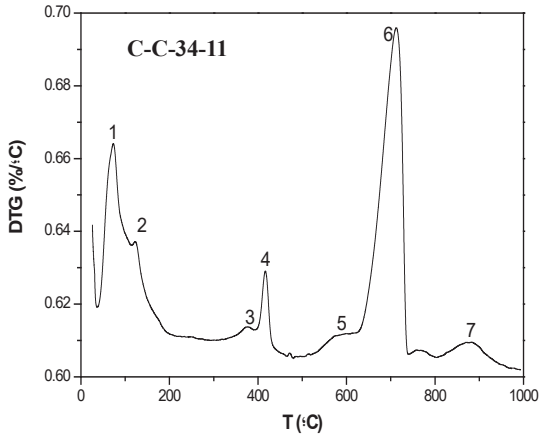

Fig. 93: Example of Derivative thermogravimetric analysis (DTA) showing the main temperature maxima of mass loss in concrete during heating. Numbers in the figure are related to temperatures listed in Appendix B (part B.4, Tab. B-9). Numbers correspond to the following mass/weight loss: 20-200 ºC (1, 2): loss of adsorbed water, dehydration of calcium silicate hydrates, dehydration of ettringite (80-150ºC); 300-400ºC (3): dehydration of silicate hydrates; 400-500 ºC (4): dehydroxylation of calcium hydroxide; 500-600 ºC (5): quartz phase change; 600-900 ºC (6, 7): second phase of C-S-H decomposition and decarbonation of carbonate phases.

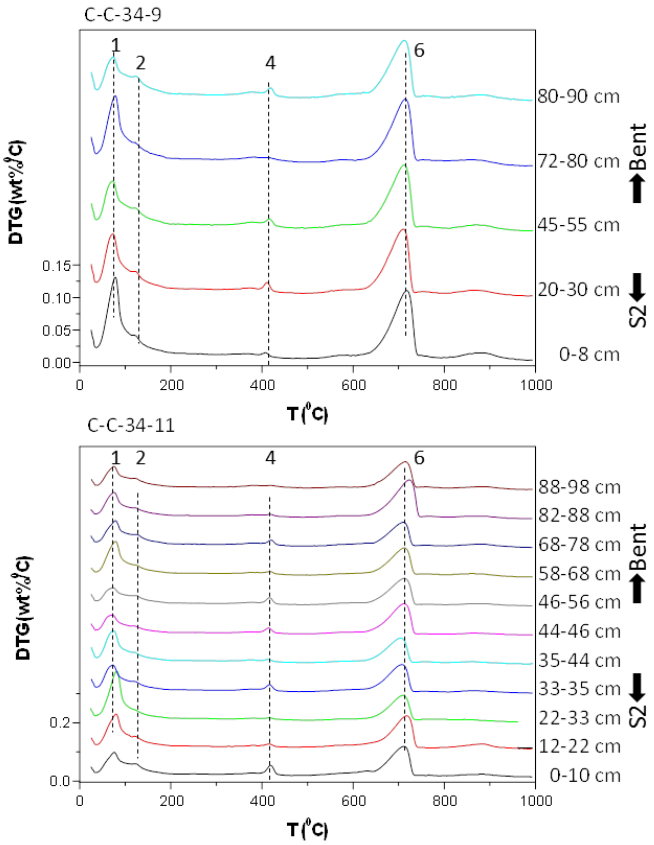

Fig. 94: Differential thermogravimetric (DTA) data as function of the x coordinates (increasing as they approach the bentonite) of the C-C-34-9 and C-C-34-11 cores. The same number legend as in Fig. 93.

According to the TGA interpretation, the corresponding DTA curves at the top part of the concrete plug (C-C-34-11 and C-C-34-9) show three similar peaks in all studied samples, during heating, (1, 2 and 3) near 100, 415 and 715 ºC. These peaks are downward peaks and hence show endothermic reactions (Fig. 96).

The first endothermic peak, peak 1, is the result of dehydration reactions due to the loss of water from C-S-H. The second major peak, peak 2, corresponds to the dehydroxilation of $Ca(OH)_2$, a hydration product and the third peak, peak 3, corresponds mainly to the decarbonation of calcium carbonate. This is in agreement with the mineralogical and thermogravimetric interpretations.

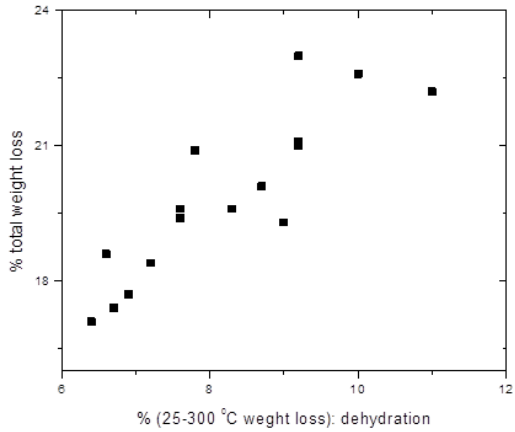

Pearson Correlations

		coordx	coordz	25-300	300-500	500-800	800-1000	% tot	etr	port	calco2
coox	Pearson Corr.	1	0.0091	-0.5101	0.07192	-0.1949	-0.37996	-0.50584	-0.31597	-0.30211	-0.11711
coordx	Sig.	--	0.97332	0.04352	0.79126	0.46947	0.1466	0.0456	0.23318	0.25543	0.66579
cooz	Pearson Corr.	0.0091	1	0.33074	-0.32944	0.12741	-0.07351	0.228	0.02193	0.19007	0.55475
coordz	Sig.	0.97332	--	0.21085	0.21276	0.63818	0.78674	0.39572	0.93576	0.48077	0.02572
h20	Pearson Corr.	-0.5101	0.33074	1	0.0282	0.14765	0.46955	0.87077	0.53587	-0.02168	-0.03265
25-300	Sig.	0.04352	0.21085	--	0.91744	0.58527	0.0665	1.13947E-5	0.0324	0.93647	0.90445
	Pearson Corr.	0.07192	-0.32944	0.0282	1	-0.13648	0.00355	0.12266	-0.0164	0.08178	-0.45905
300-50	Sig.	0.79126	0.21276	0.91744	--	0.61426	0.98958	0.65087	0.95194	0.76335	0.07368
	Pearson Corr.	-0.1949	0.12741	0.14765	-0.13648	1	0.3889	0.56742	0.35209	-0.04816	0.14174
500-80	Sig.	0.46947	0.63818	0.58527	0.61426	--	0.13655	0.02188	0.18109	0.85942	0.60055
str	Pearson Corr.	-0.37996	-0.07351	0.46955	0.00355	0.3889	1	0.66896	0.3944	-0.12008	-0.33624
800-10	Sig.	0.1466	0.78674	0.0665	0.98958	0.13655	--	0.0046	0.13061	0.65778	0.2029
	Pearson Corr.	-0.50584	0.228	0.87077	0.12266	0.56742	0.66896	1	0.6	-0.043	-0.09282
% tot	Sig.	0.0456	0.39572	1.13947E-5	0.65087	0.02188	0.0046	--	0.01401	0.87438	0.73241
etr	Pearson Corr.	-0.31597	0.02193	0.53587	-0.0164	0.35209	0.3944	0.6	1	-0.54165	-0.10613
	Sig.	0.23318	0.93576	0.0324	0.95194	0.18109	0.13061	0.01401	--	0.03023	0.69566
port	Pearson Corr.	-0.30211	0.19007	-0.02168	0.08178	-0.04816	-0.12008	-0.043	-0.54165	1	0.37074
	Sig.	0.25543	0.48077	0.93647	0.76335	0.85942	0.65778	0.87438	0.03023	--	0.15747
calco2	Pearson Corr.	-0.11711	0.55475	-0.03265	-0.45905	0.14174	-0.33624	-0.09282	-0.10613	0.37074	1
	Sig.	0.66579	0.02572	0.90445	0.07368	0.60055	0.2029	0.73241	0.69566	0.15747	--

2-tailed test of significance is used

Fig. 95: Pearson's correlation coefficient calculation for thermogravimetric variables and determined percentages of ettringite (etr) and portlandite (port); XRD, and calcite (calcimeter data).

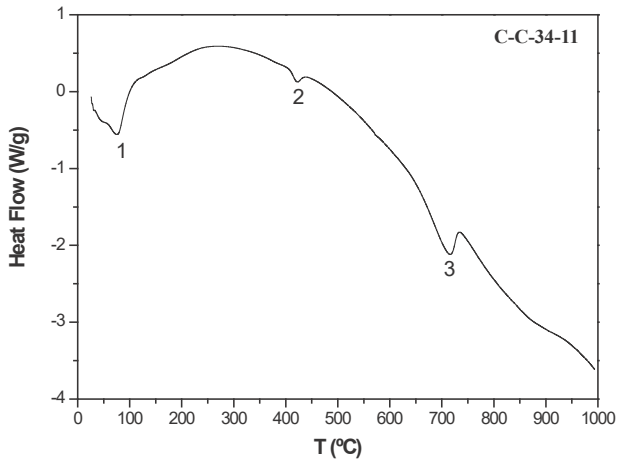

Fig. 96: DSC spectra of sample C-C-34-11. Peak 1 (dehydration of C-S-H); peak 2 (dehydroxylation of Ca(OH)2); peak 3 (decarbonation).

Concrete/bentonite interface

The TGA data at the concrete–bentonite interface is presented as derivative thermogravimetric data (DTG) in Fig. 97. Appendix C (part C.5, Tab. C-13) contains the main temperature maxima for mass loss. % weight losses for several intervals are assigned in Figure 97: 25-300 ºC (adsorbed or free water loss: C-S-H, ettringite, smectite); 300-500 ºC (hydroxides (portlandite, brucite), organics); 500-800 ºC (dehydroxilation of 2:1 sheet silicates; carbonates); 800-1000 ºC (structural decomposition, crystallization of new phases; Emmerich 2011). The low temperature range 25-300 ºC shows the loss of loosely-bonded interlayer water, both in the montmorillonite of bentonite (65 and 135 ºC; indicative of the heterovalent composition of exchangeable cations) and C-S-H (70-80 ºC) in the cement matrix. The presence of ettringite and portlandite is detected near 120 and 410 ºC, respectively, in the concrete far from the bentonite. In contrast, in the samples representing the first 2 mm of concrete in contact with bentonite the 120 ºC ettringite shoulder is not well resolved and the portlandite dehydroxilation effect is absent. In the medium temperature range a differentiated maximum of water loss near 490 ºC in the bentonite at the interface (B01) is in agreement with the presence of M-S-H with 0.8-1.3 Mg/Si (Dauzères et al. 2016; Lothenbach et al. 2015; Nied et al. 2016). This effect is also close to the dehydroxilation temperature of $Mg(OH)_2$ (Bai & Koster van Groos 1998). Montmorillonite is characterised by a broad dehydroxilation peak at 620 ºC (trans-vacant montmorillonite; Wolters & Emmerich 2007). Above this temperature carbonate decomposition can be traced by the presence of peaks at 700-800 ºC. These temperatures are low compared to those reported when limestone aggregates are present and are typical for fine-grained carbonates (Villain et al. 2007). The studied interfaces present distinct features as far as in sample C-C-34-12 the interface concrete shows the predominance of the carbonate phase (80 % of the total weight loss, not shown) in agreement with the relatively high contents of calcite in this interface determined by XRD. In C-C-34-10, C-S-H and other hydrates (52 % of the total weight loss in the < 120 ºC temperature range) are mixed with carbonates.

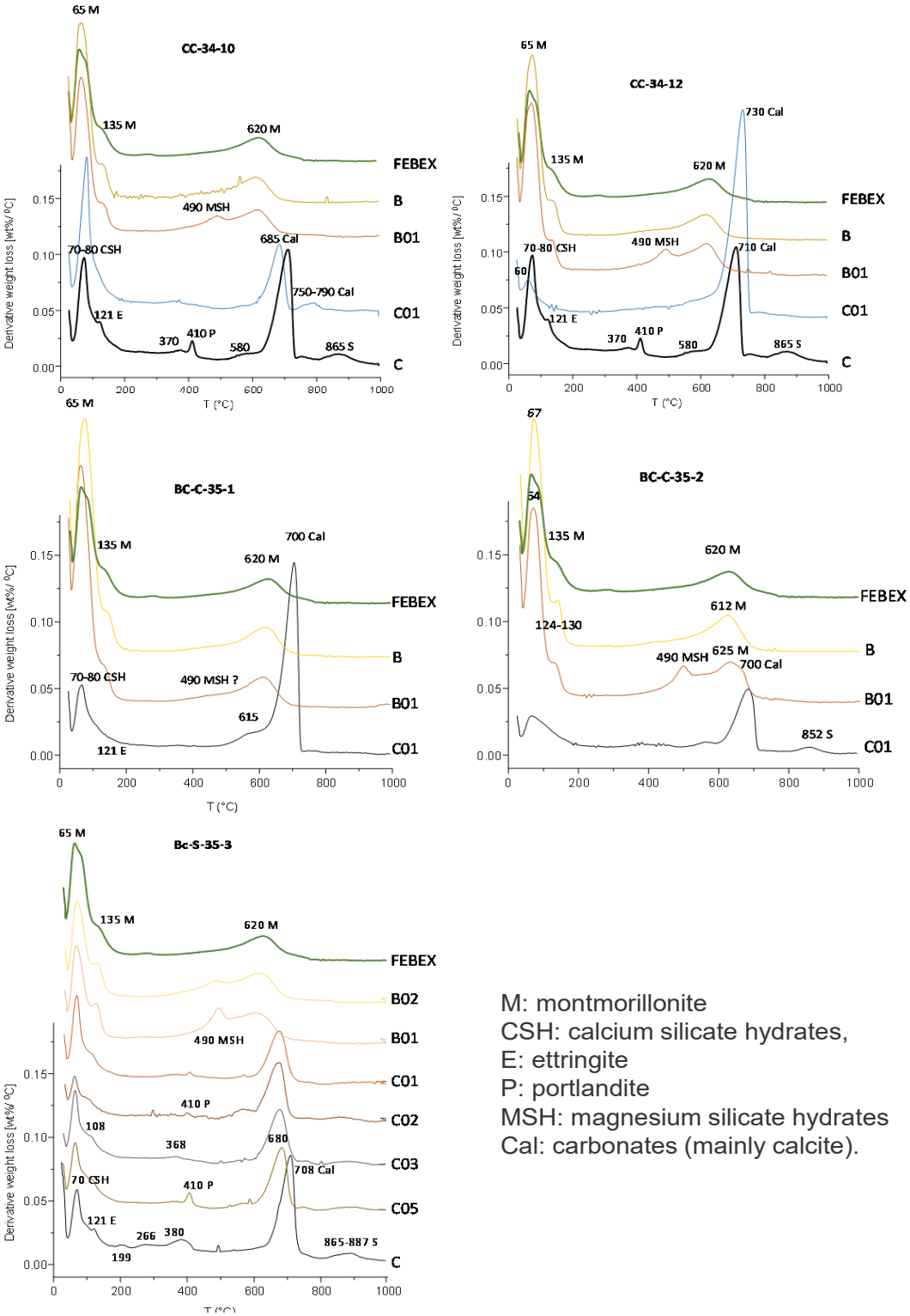

Fig. 97: Derivative thermogravimetric data (DTG) in concrete and bentonite samples compared to the reference FEBEX bentonite and with a concrete sample taken at 90 cm from the interface, near the centre of the gallery. Number labels are the temperatures for DTG peaks.

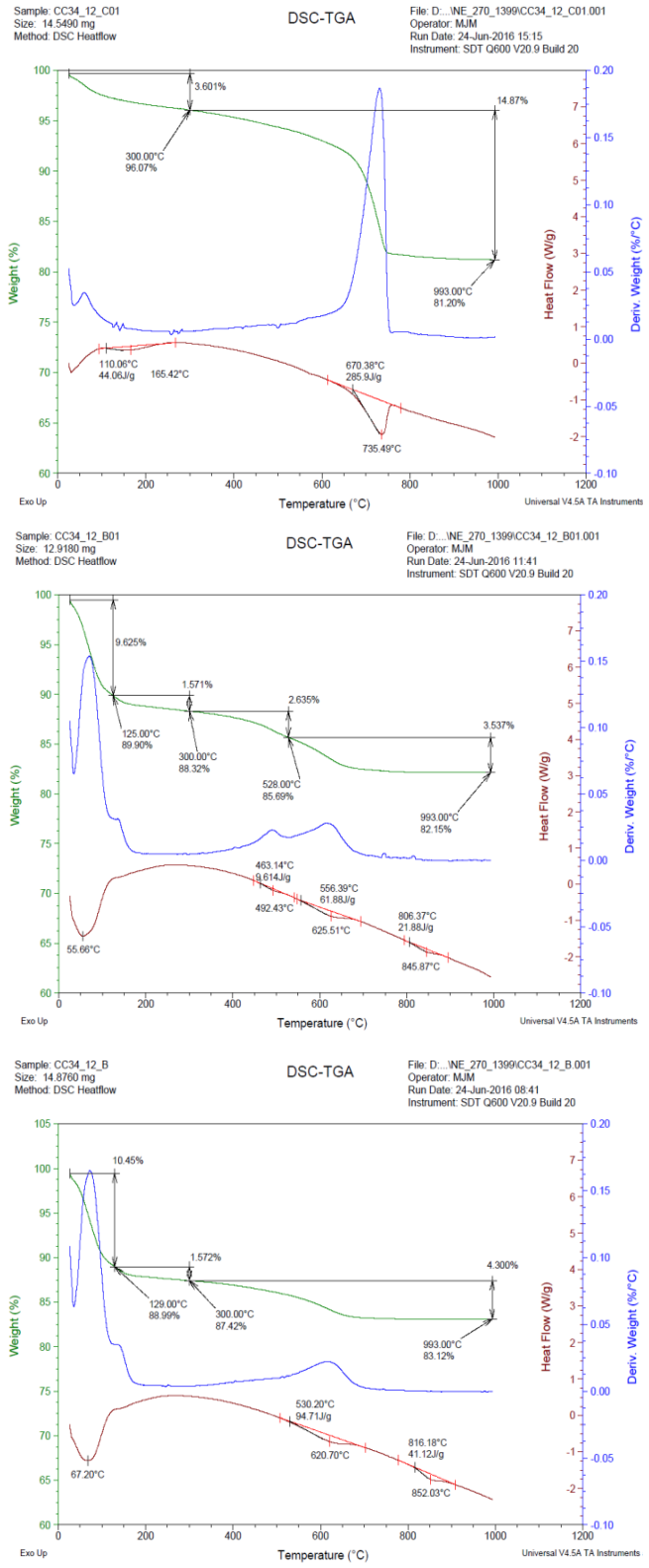

Fig. 98: Thermal analysis of C-C-34-12 C01 concrete interface sample. TG (green), DTG (blue) and DSC (red).

Fig. 97 shows the DTG data in which bentonite, interface bentonite (M-S-H effect) and interface concrete can be compared. Samples from the BC-S-35-3, allow a more detailed comparison. The uneven decrease of portlandite and the M-S-H influence in at least 4-5 mm of interface (B01-B02 samples) can be seen. From all these data it is derived, in agreement with XRD and SEM-EDX results, that M-S-H-like phases are not produced in the concrete but in the bentonite, in which carbonation is not deeply penetrating.

Fig. 98 shows the TG, DTG and calorimetric data (DSC) from bentonite, altered bentonite and concrete interface materials. Their comparison demonstrates the new phase precipitation in the bentonite and how it contributes to the evolution of the heat flux in addition to dehydroxilation and high temperature structural change. In the concrete the CO_2 outgassing is responsible for the main heat flux maxima.

6.3.2.2 Results on sample BC-S-35-1b (BGR)

The bentonite sample of BC-S-35-1b taken near the contact of the cement interface was analysed by Simultaneous Thermal Analysis (STA) coupled to a mass spectrometer. Results are shown in Fig. 99. The samples analysed (1 mm and 3 cm from the interface) were compared with the FEBEX reference (REF).

The contact sample (1 mm) shows a new dehydroxylation peak at about 530°C (compared to the REF or the sample at 3 cm distance). This peak can be assigned to either kaolinite or brucite. The CO_2 curve (not shown) shows a slight increase of the carbonate peak and the SO_2 curve confirms increased sulphate content (decomposition temperature > 800°C).

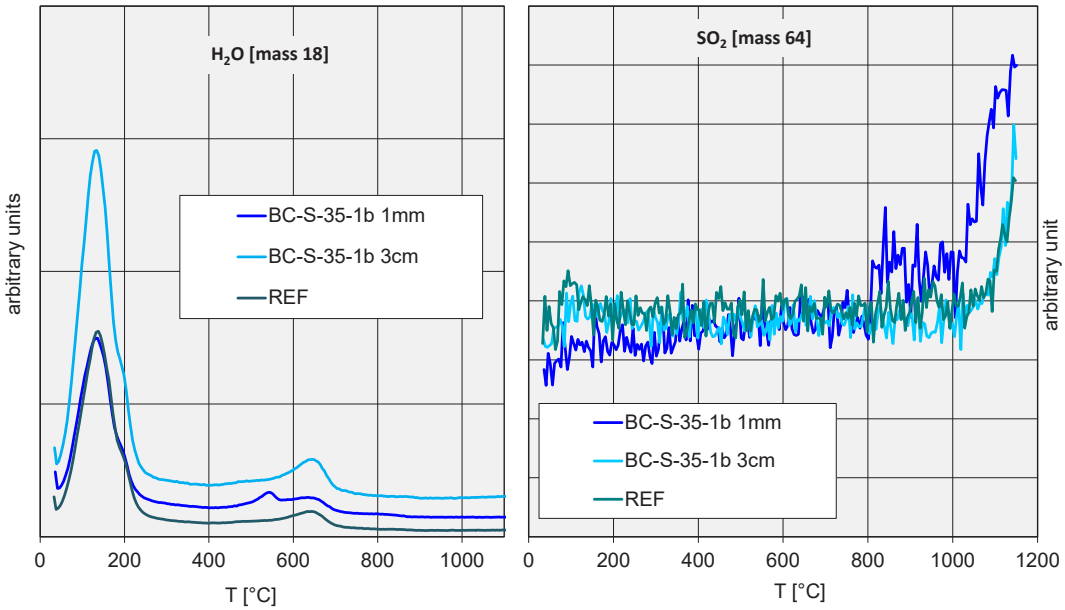

Fig. 99: STA-mass spectrometer curves of subsamples of bentonite (1 mm and 3 cm from the interface with concrete) coming from sample BC-S-35-1b.

6.3.3 Textural and mineral phases by SEM and TEM (UAM, Ciemat, BGR)

SEM analysis of the bulk concrete

Two selected concrete samples located near the interface (10 cm) with the granite and close to the bentonite (10 cm), C-C-34-11 (82-88 cm), and near the middle of the gallery, close to the dummy-bentonite front, C-C-34-4 (10 cm far from the interface), were examined by SEM in order to identify characteristic morphologies and chemical compositions of concrete.

Both samples presented some Mg and S content in the cement matrix, Mg probably higher than in the original samples. Tabular morphologies were observed on the surface in sample C-C-34-11 at micrometric scale (Fig. 100). They correspond to ettringite with contents of Ca higher than that in sample C-C-34-4, where fibrous and needle morphologies with chemical composition characteristics of ettringite were more abundant on the surface of the concrete aggregates (Fig. 101). In general, more ettringite can be seen near the dummy-bentonite front, and mixed phases higher in Ca content (calcite or portlandite) seem to be best represented in the samples near the granite-bentonite zone. This is in agreement with the relatively high concentration of ettringite in C-C-34-4 compared to C-C-34-11. However, note that these samples are about 10 cm far from the interface with the bentonite and they do not necessarily represent what happens right at the interface.

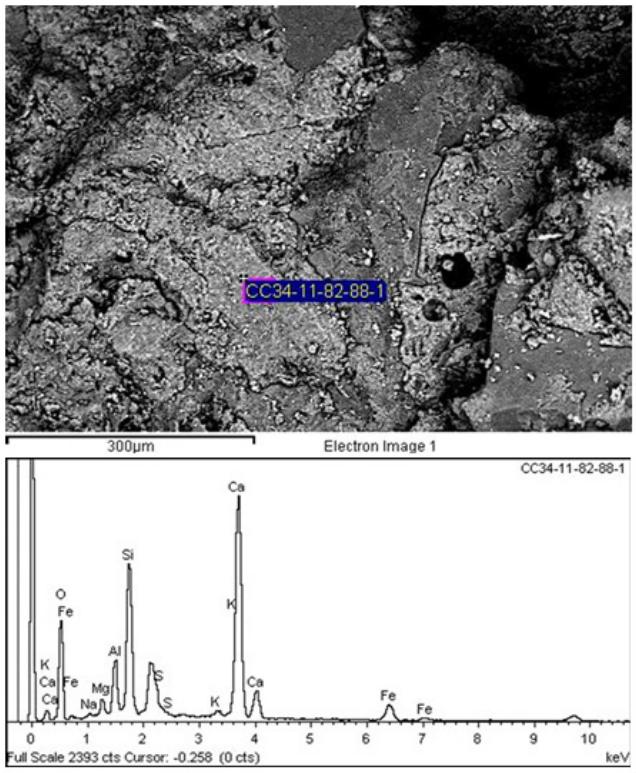

Element	Atomic%
O K	73.8
Na K	0.3
Mg K	1.2
Al K	2.9
Si K	7.6
S K	0.4
K K	0.3
Ca K	11.9
Fe K	1.6
Ca/Si	1.6
Ca/Al	4.1

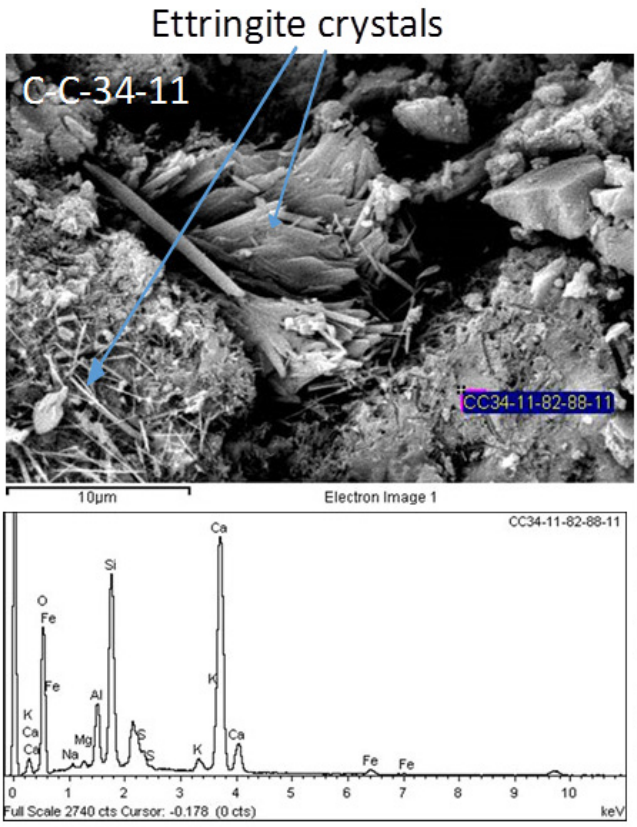

Element	Atomic%
O K	77.8
Na K	0.4
Mg K	0.3
Al K	2.5
Si K	7.4
S K	0.7
K K	0.4
Ca K	10.1
Fe K	0.4
Ca/Si	1.4
Ca/Al	4.0

Fig. 100: Concrete matrix and ettringite crystals in sample C-C-34-11.

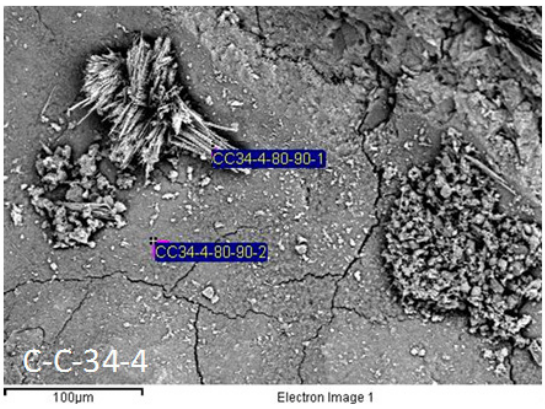

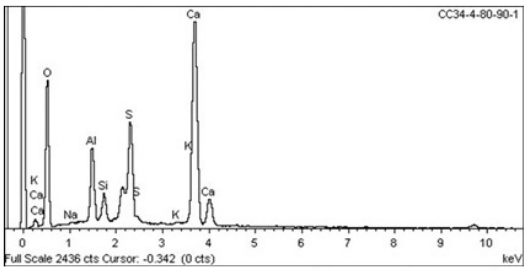

Element	Atomic%
O K	79.9
Na K	0.8
Mg K	0.9
Al K	1.2
Si K	6.2
S K	0.6
K K	0.4
Ca K	9.7
Fe K	0.3
Ca/Si	1.6
Ca/Al	7.8

Element	Atomic%
O K	81.38
Na K	0.16
Al K	3.22
Si K	1.17
S K	4.39
K K	0.07
Ca K	9.6
Ca/Si	8.20513
Ca/Al	2.98137

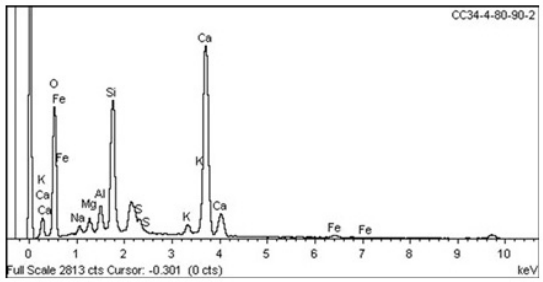

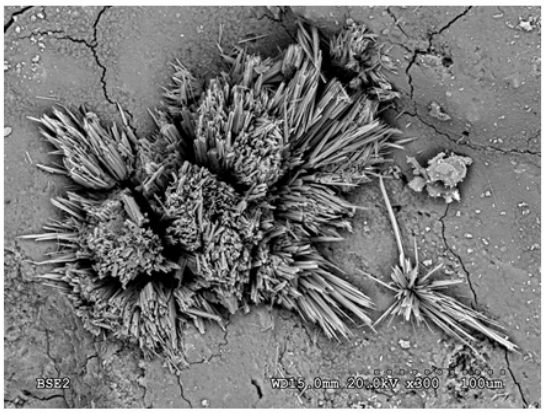

Element	Atomic%
O K	71.1
Na K	0.5
Mg K	1.5
Al K	3.5
Si K	10.2
S K	0.7
K K	2.1
Ca K	7.7
Ti K	0.4
Fe K	2.4
Ca/Si	0.8
Ca/Al	2.2

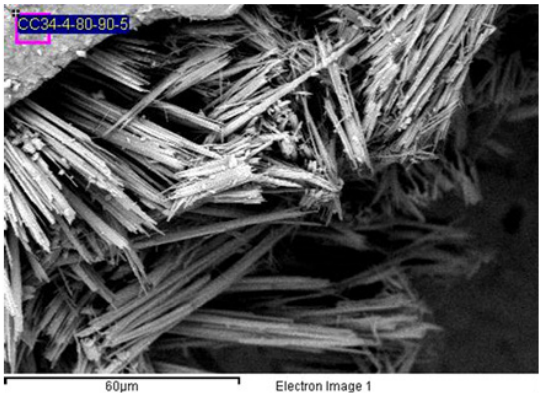

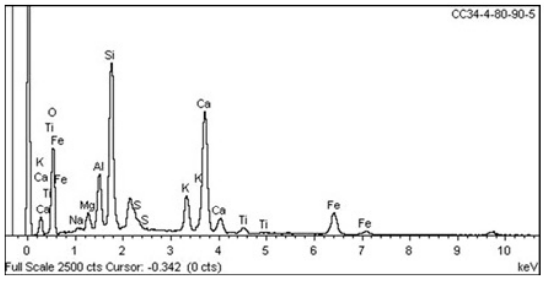

Fig. 101: Needle-fibrous morphologies found in sample C-C-34-4. Chemical analysis of ettringite and concrete matrix near the dummy-bentonite-concrete contact from sample C-C-34-4.

SEM analysis of the concrete/bentonite interface

Microstructure and morphology were studied in fresh pieces of the concrete/bentonite interface of different samples by various partners. Chemical composition of mineral phases was determined by EDX.

All studies agree on the fact that just at the interface there is an accumulation of very small crystals (Fig. 102) whose analysis indicates are calcite crystals. Precipitation of ettringite just at the interface or on the bentonite side has been observed as well. EDX profiles indicate an increase of Mg in both the concrete and the bentonite side. Further details are given below.

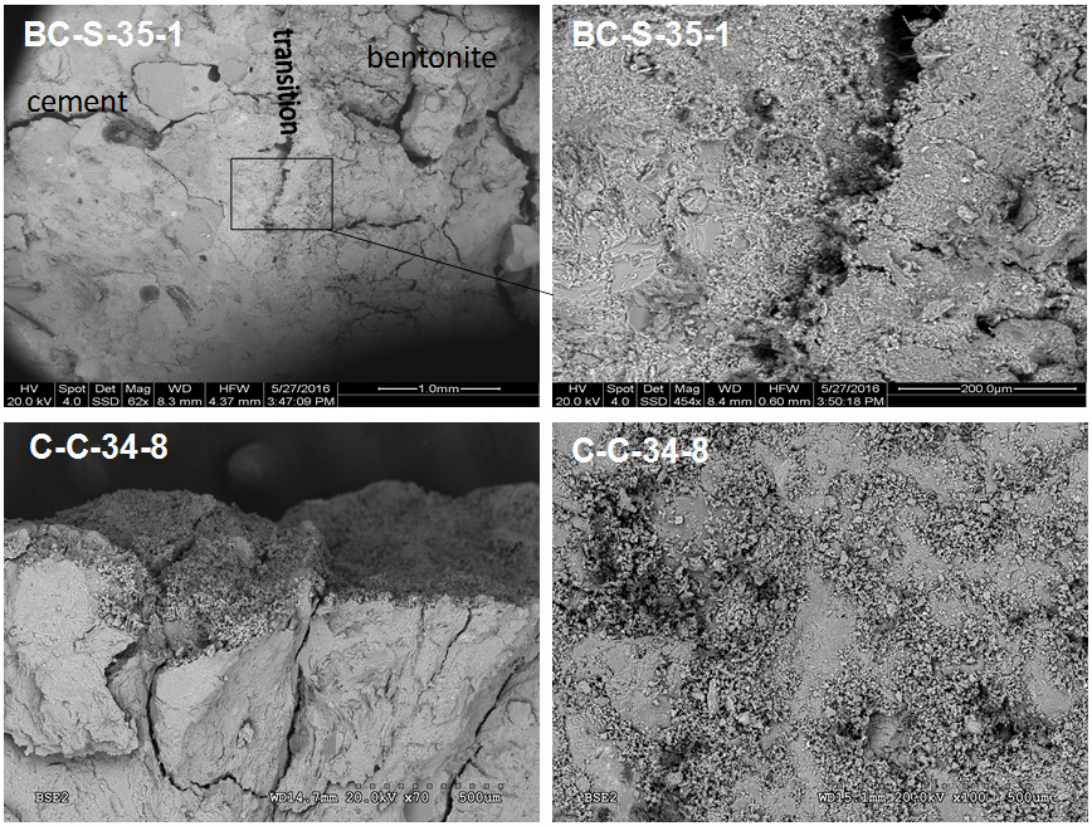

Fig. 102: SEM images of the concrete/bentonite in samples BC-S-35-1 (BGR) and C-C-34-8 (UAM) showing the accumulation of tiny particles just at the interface.

Fig. 103 shows an image of the concrete side of sample BC-C-35-2, in which acicular ettringite, C-S-H gel and silica have been analysed. The silica presents traces of dissolution and ettringite is dispersed over the matrix. In Fig. 104 portlandite crystals inside the cement matrix of sample C-C-34-10 can be observed.

SEM images also show ettringite occurring in various forms, as spherical clusters of small needle crystals (Fig. 105A), as large needle-like crystals, ranging from 10 to 100 µm length and thicknesses in the range between 10 to 80 nm (Fig. 105B), as well as massive coalescent needle-like crystals (Fig. 105C), always filling voids partially or totally (Fig. 105, Fig. 106 and Fig. 107), and with the needle-fibres projecting from the pore walls. The large acicular crystals observed filling pores are related to direct precipitation from solutions with high

contents in sulphate and high calcium availability. These crystals are always found in the concrete closest to the bentonite (first 2-3 cm) or just at the bentonite side of the interface. The differences in morphology are attributed to differences in the degree of supersaturation of the solutions from which the ettringite precipitates. Higher supersaturation should produce more massive crystals. SEM studies have not shown cracks associated with the secondary ettringite in any of the samples investigated.

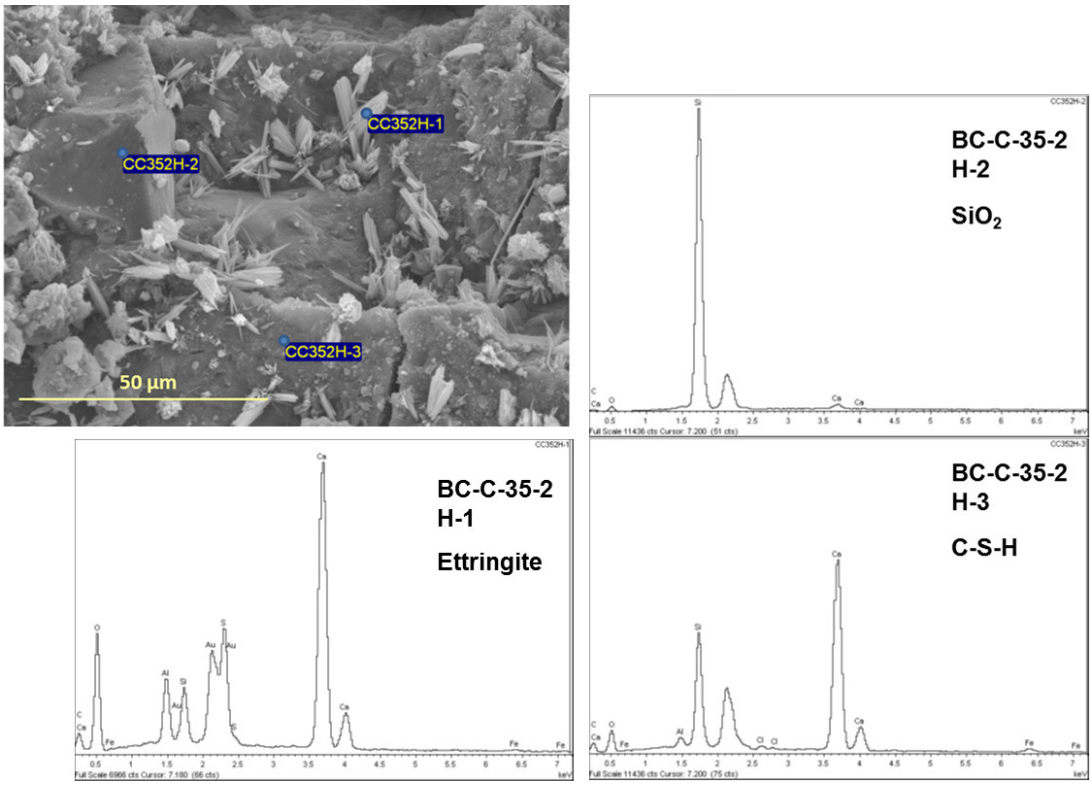

Fig. 103: SEM image and EDX analysis of sample BC-C-35-2 (Ciemat) showing the typical aspect and mineral phases in the concrete. The spots of the analyses are in blue.

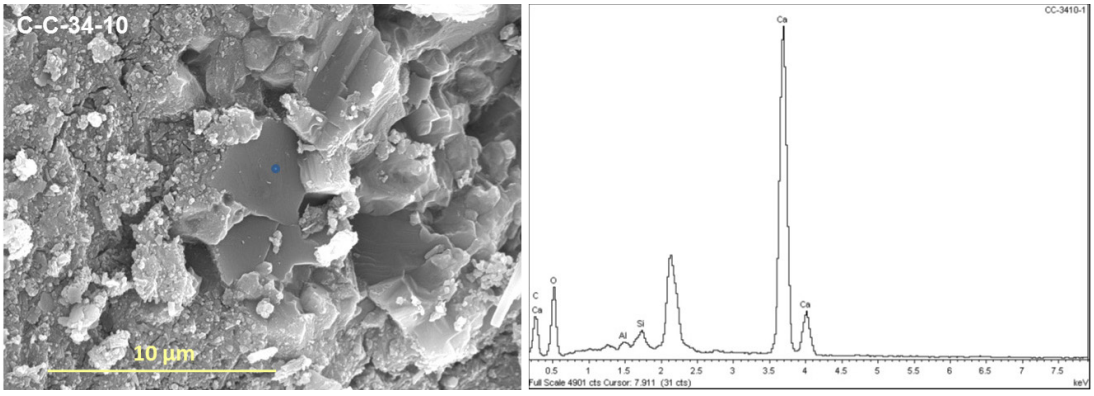

Fig. 104: SEM image and EDX analysis of sample C-C-34-10 (Ciemat) showing portlandite crystals in the concrete matrix. The spot of the analyses is in blue.

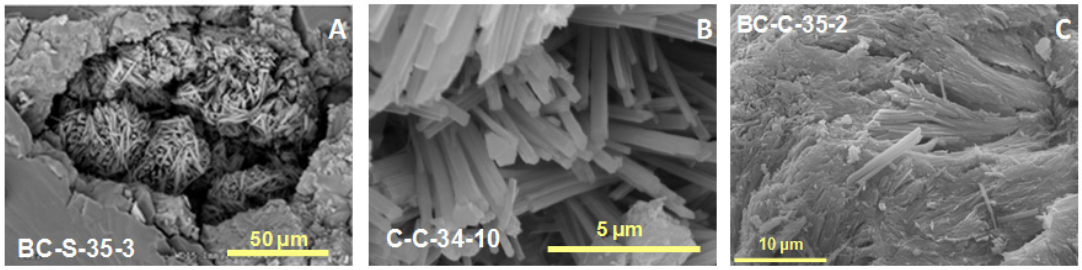

Fig. 105: SEM images of different samples showing ettringite occurring in various forms: A. As spherical clusters of small needle-like crystals (UAM); B. As fibrous needle-like crystals (Ciemat); C. As massive coalescent morphology (Ciemat). All of them appear to be filling voids.

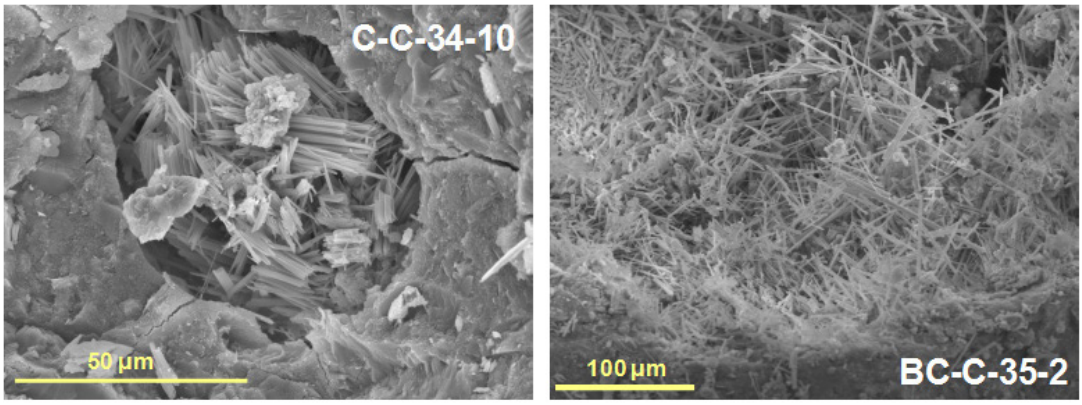

Fig. 106: SEM images of acicular crystals of non-expansive ettringite growth inside pores in samples C-C-34-10 and BC-C-35-2 (Ciemat).

Sample BC-S-35-3 has a very nicely conserved concrete/bentonite interface in which the ettringite morphology is easily observed in pores of the concrete face in direct contact with bentonite. Fig. 107 shows the aspect of the ettringite in the pores of the concrete sample, with the corresponding analysis. Additional analyses show a high concentration of Mg in the cement matrix.

Fig. 108 shows a BSE-SEM image of four composed areas containing the interface of the sample BC-S-35-3. Ellipsoidal pores with ettringite are visible and also small particles of bright aggregates concentrated near the interface. A chemical profile was made along the interface avoiding aggregates and ettringite (Fig. 109). A 0.5 mm-rim of concrete, corresponding to the bright parts of the picture, has an anomalous calcium concentration, presumably due to non- hydrated cement paste or fine-grained calcium carbonate. Sulphur content is not high at the concrete interface, while magnesium surpasses the aluminium content. This fact indicates Mg-silicates precipitate in the bentonite; in agreement with the presence of trioctahedral sheet silicates identified by XRD (see section 6.3.1). The scarcity or absence of gypsum agrees with the presence of ettringite detected at the interface by XRD.

Further analyses on this sample have shown composition characteristics of C-A-S-H minerals mixed with carbonates in the bentonite face in contact with concrete (Table C-7 of the Appendix C, part C.4). Carbonates are also present together with ettringite at the interface. In

this context, some ettringite in the bentonite interface appears as skeletal crystals with high contents of calcium and carbon elements (analysis 14 in Table C-7 of the Appendix C, part C.4). So far, dissolution of ettringite and precipitation of calcite is a process to be considered in further studies.

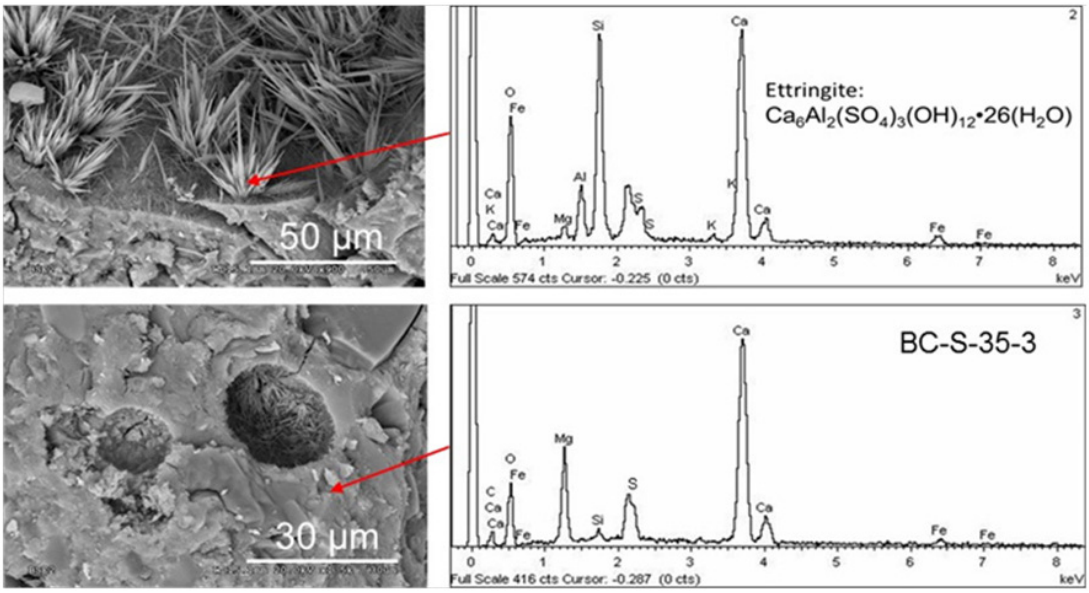

Fig. 107: SEM images of concrete scraped from the bentonite surface in the sample BC-S-35-3 (UAM). Ettringite precipitation in the concrete pores can be observed. EDX analysis of the concrete paste around the pores (red arrow) shows significant concentration of Mg in addition to Ca.

The morphological aspect of sample C-C-34-8 at the bentonite interface is shown in Fig. 110. The deposits at the interface are a mixture of crystal aggregates which can be described as complex C-S-H, sulphate, and carbonate mixtures (Tab. C-8 of the Appendix C, part C.4). Elongated prismatic crystals correspond to ettringite but the presence of gypsum has been detected by XRD as well. The presence of these mixtures altogether in the interface rim may indicate the alteration of the original disposition of these crystals at the interface. Chemical analyses on the bentonite surface in contact with the concrete (details the preparation of samples for SEM-EDX and analysis, 5, 9, 10, 11 in Tab. C-8 of the Appendix C, part C.4) show a Mg-Si enrichment such as previously detected in sample BC-S-35-3.

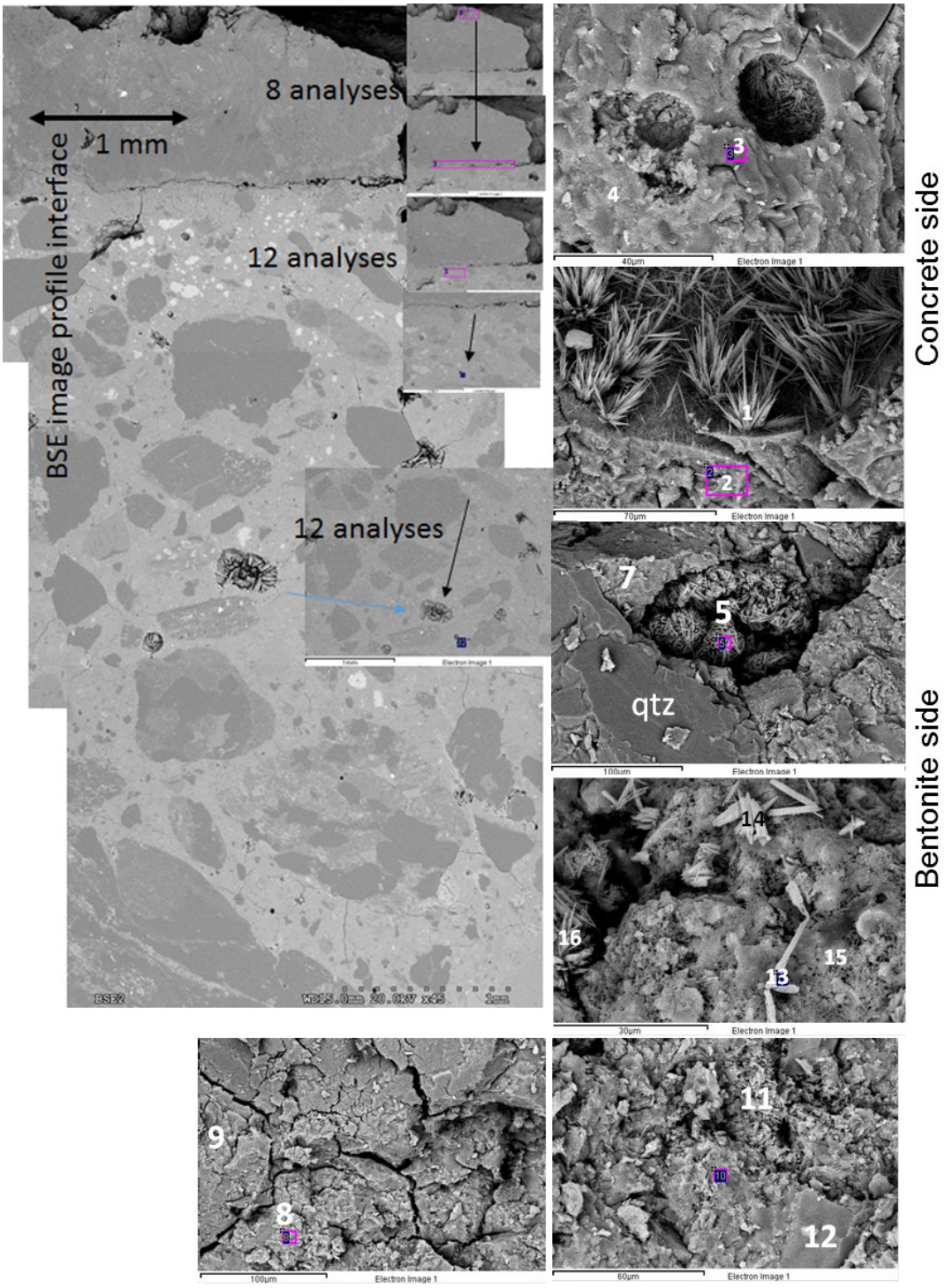

Fig. 108: Textural aspects of the BC-S-35-3 concrete/bentonite interface (UAM). Numbers in the pictures are the points on which punctual analyses were made.

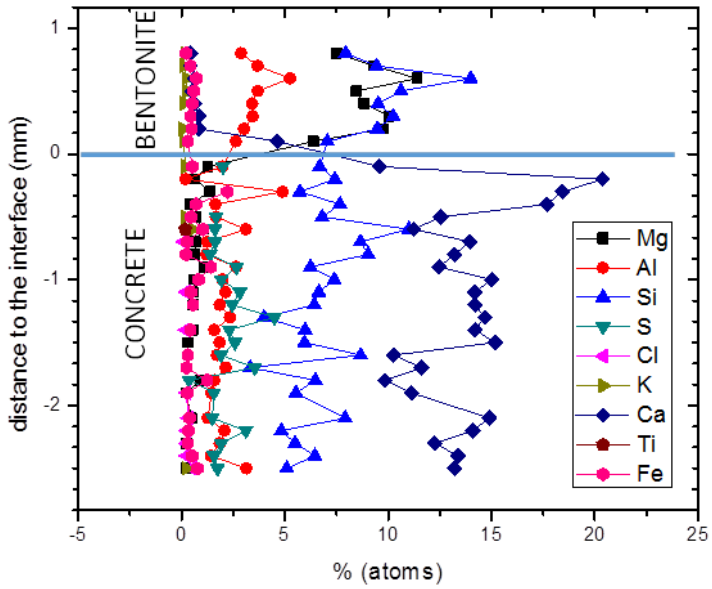

Fig. 109: Chemical profile of sample BC-S-35-3 along the interface (UAM).

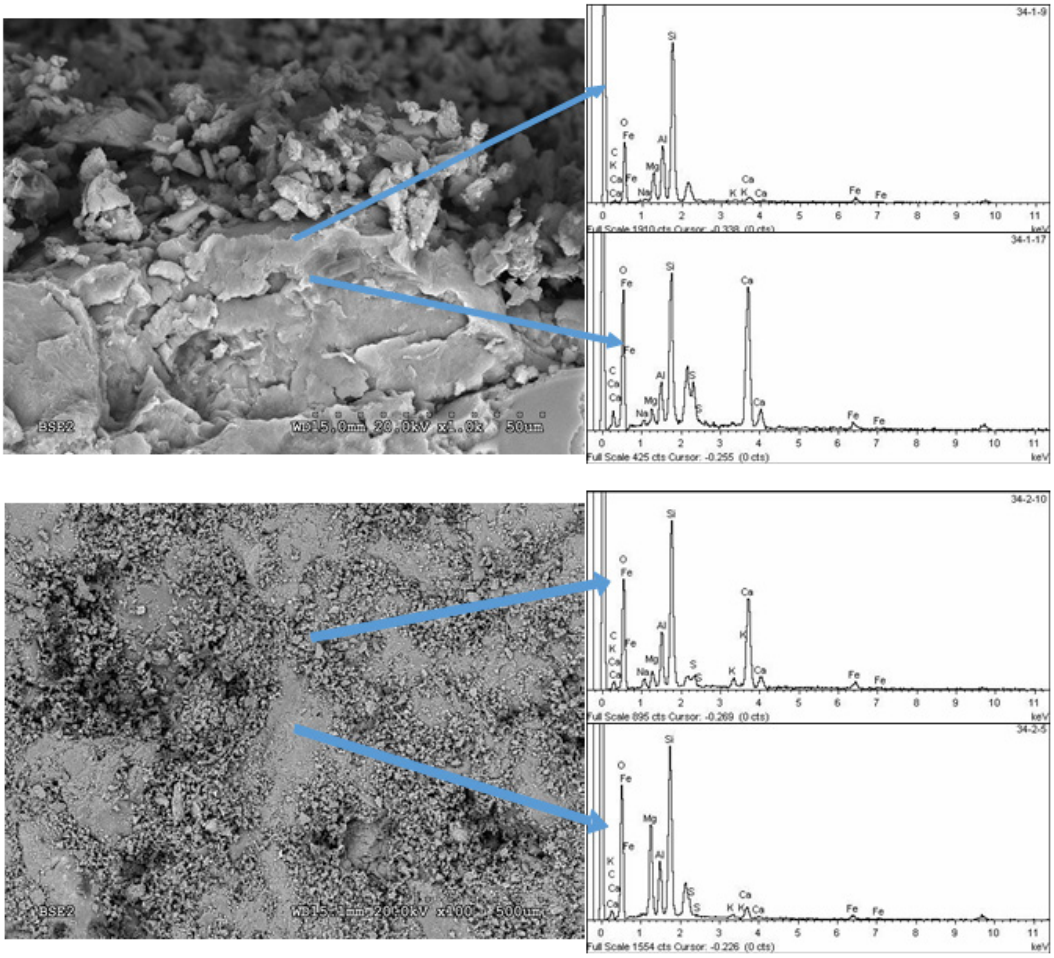

Fig. 110: Morphological aspect of sample C-C-34-8 (UAM).

SEM studies on sample C-C-34-10 bring the presence of tiny polycrystalline aggregates facing a layered crust rim of bentonite (Fig. 111) to light. Sulphates are less frequently found compared to their presence in samples BC-C-35-3 or C-C-34-8. Mg enrichment is clearly detected in the layered bentonite where calcium decreases to very small concentrations. Tab. C-9 of the Appendix C (part C.4) shows the analysis numbered in the photographs. The concrete face of sample 34-10 shows a compact matrix in which high contents of calcium are present. Ettringite is present and fills ellipsoidal pores in which it is mixed with carbonates and silicates. This mineral was not observed, in this case, at the interface contact.

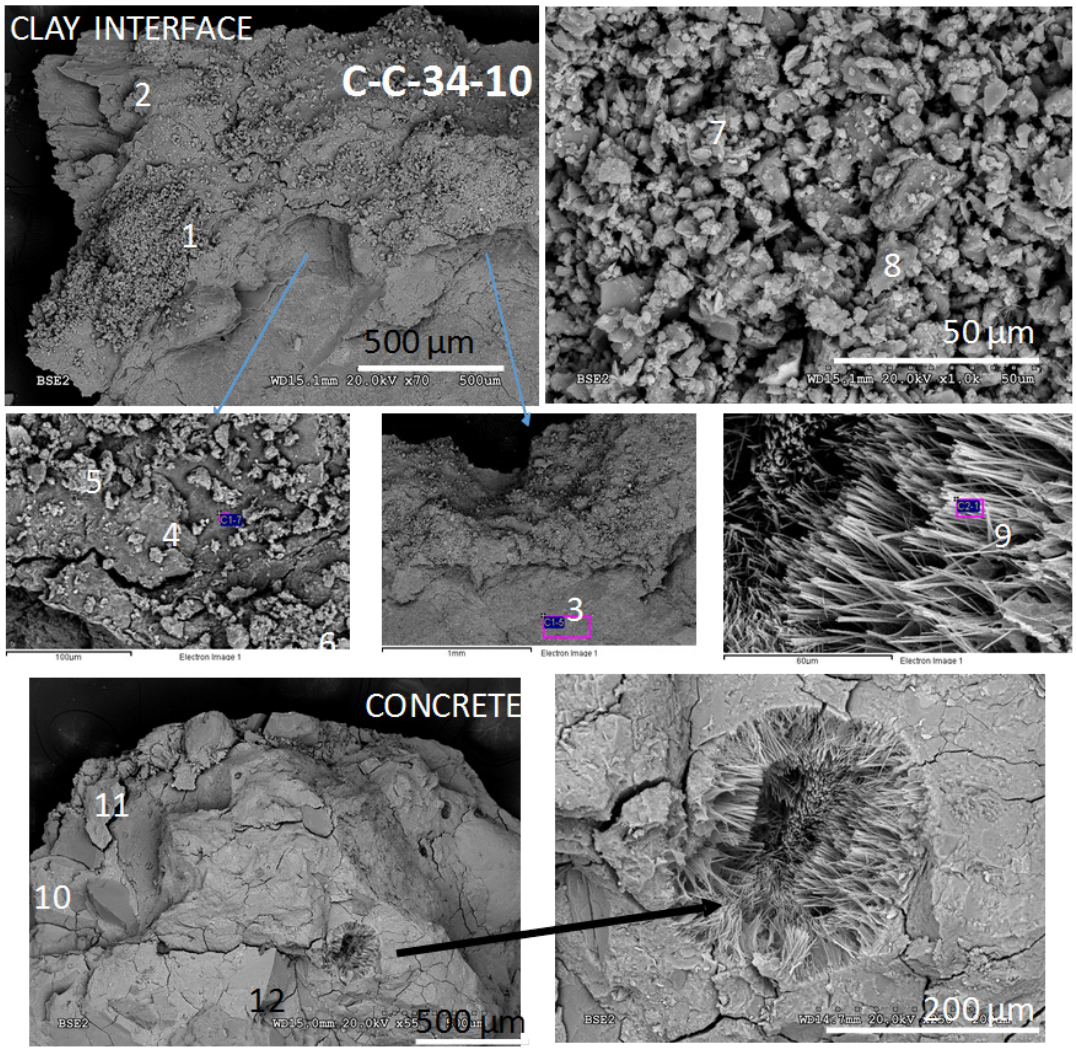

Fig. 111: Concrete/bentonite interface in sample C-C-34-10 (UAM).

The C-C-34-10 concrete/bentonite interface was re-examined in more detail for anomalies of magnesium which were detected in the bentonite surface (for example, analysis 2 in Tab. C-9 of the Appendix C (part C.4). Discrete bentonite aggregate interface layers were scraped from the concrete (Fig. 112). The EDX microanalysis shows well-differentiated compositions of magnesium or calcic silico-aluminate minerals. Aggregates with tabular compact form have a high content in Mg along with absence of Ca in the composition, while laminated clay

aggregates with closer morphology to the initial montmorillonite reveal a chemical composition enriched in Ca (Fig. 112).

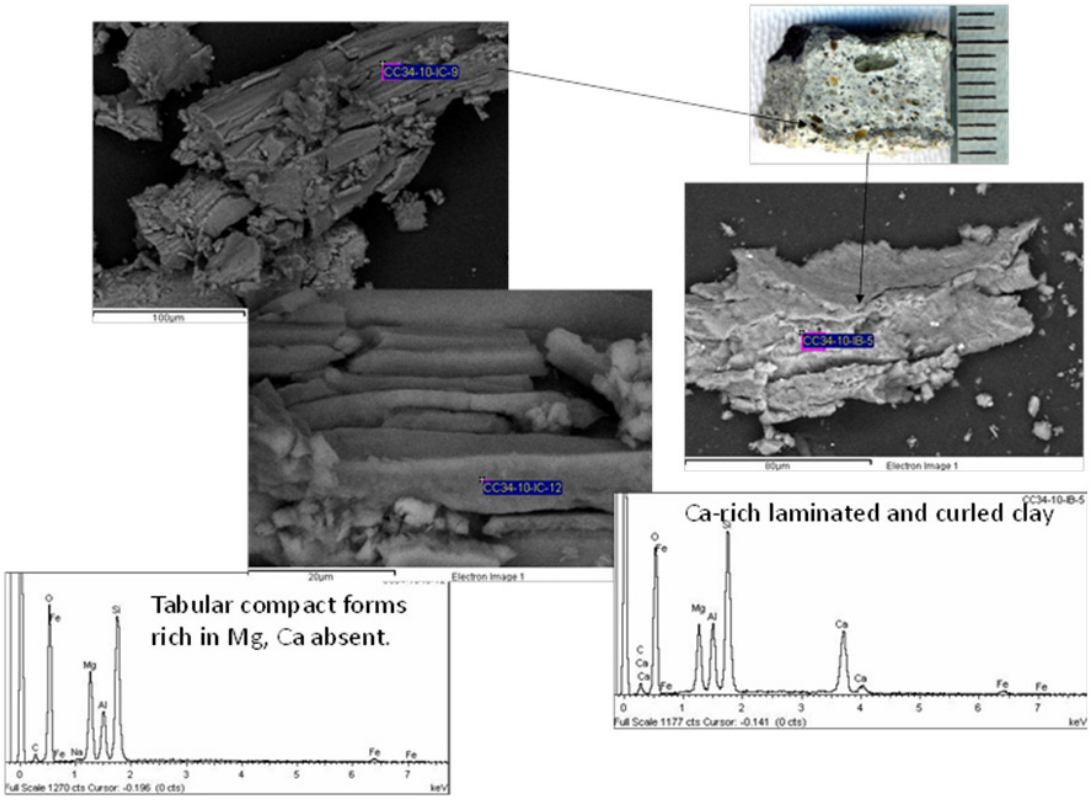

Fig. 112: Morphology of tabular Mg silico-aluminates (left) and laminated clay aggregates rich in Ca (right). Pink rectangles show the area covered by the EDX analysis shown for each SEM backscattered electrons image. Both taken in sample C-C-34-10 close to the interface (UAM).

A fresh fracture section of C-C-34-12 concrete was obtained near the interface but not in direct contact with bentonite. The composition of cement paste was evaluated in a chemical profile (Fig. 113). There was a relatively homogeneous composition with a slight trend of magnesium increase towards the interface region. Calcium and magnesium are visibly anti-correlated, where magnesium is linked to the presence of clinochlore in concrete. The anomalous magnesium or calcium increase is found in the very interface and they are not related to variations of clinochlore in concrete.

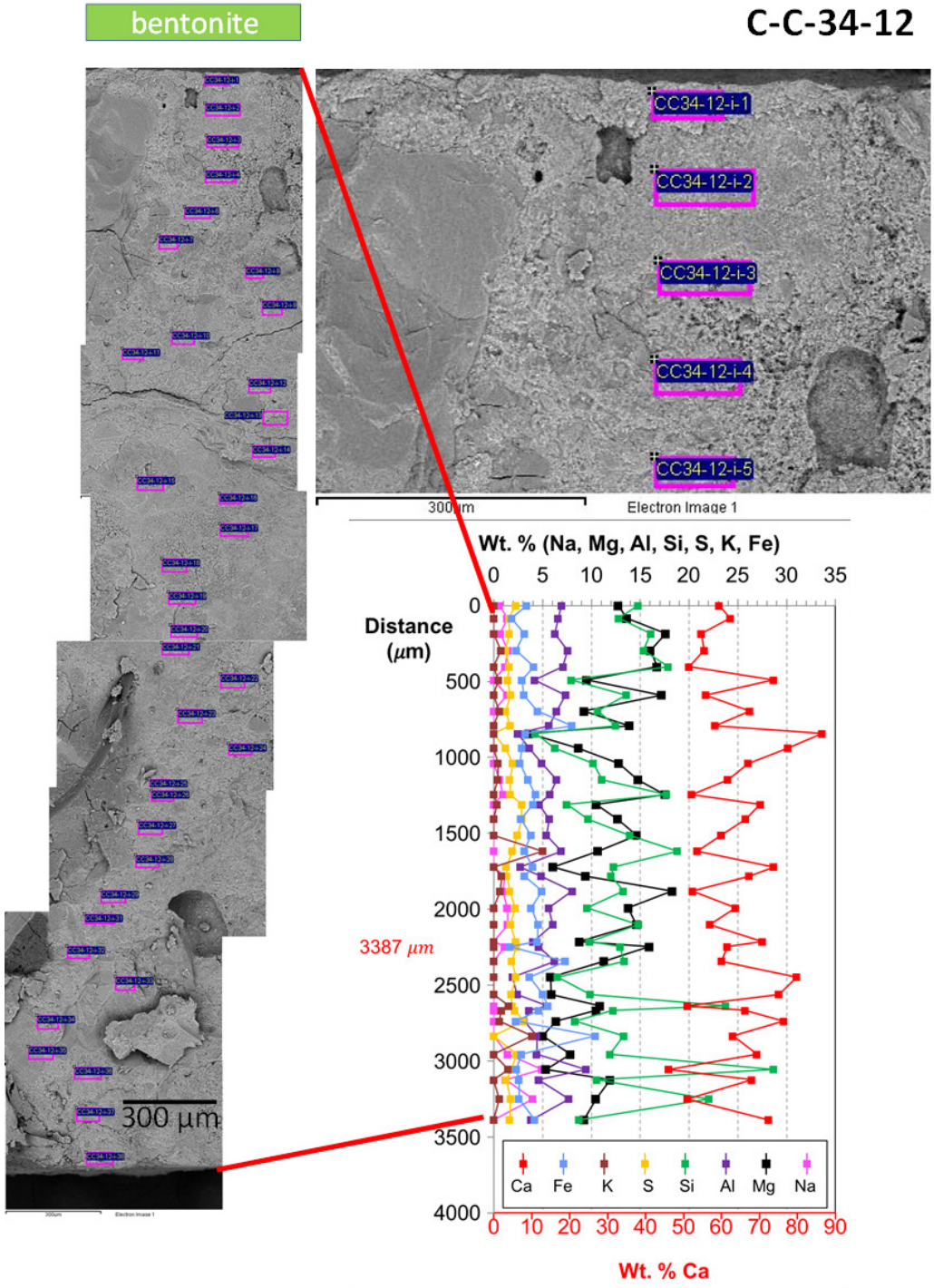

Fig. 113: Fresh fracture section of C-C-34-12 in BSE image. Chemical profile of the cement paste. Elements are expressed in weight % excluding oxygen.

TEM analysis of the concrete/bentonite interface

Ciemat carried out a deeper mineralogical study of sample C-C-34-12 by TEM. Sample C-C-34-12 was dropped onto a carbon-coated copper grid. TEM plus energy dispersive microanalysis (ED) or diffraction patterns (symmetry and cell parameters) were used to identify crystals in the interface.

Several feldspar particles were analysed, which are typical accessory minerals of the FEBEX bentonite (up to a 2% wt.). Differences in the chemical composition of the plagioclases found in the interface ranged from albite to anorthite. A micrograph of an andesine particle is shown in Fig. 114. Andesine is a member of the plagioclase solid solution series. $Na_{0.7\text{-}0.5}Ca_{0.3\text{-}0.5}Al_{1.3\text{-}1.5}Si_{2.7\text{-}2.5}O_8$. Its chemical formula ranges from 30% to 50% of anorthite. In this case, the anorthite content is close to 40%.

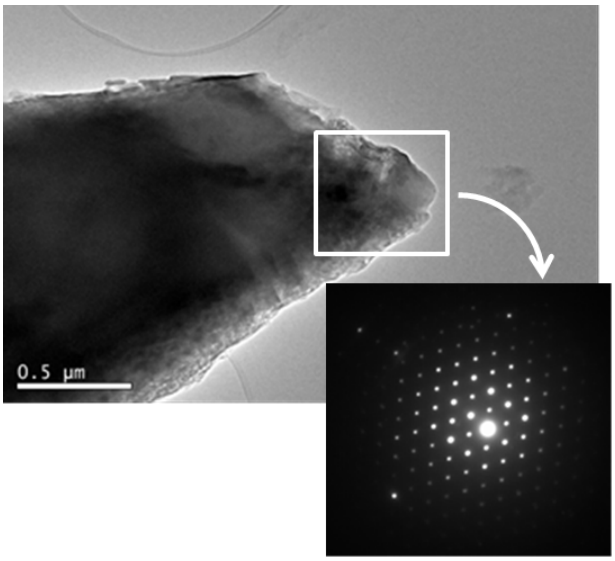

Element	Atomic %
Na	3.47
Mg	0.13
Al	9.06
Si	21.95
K	0.59
Ca	2.01
Fe	0.45
O	62.34

Fig. 114: (Left) Transmission Electron Micrograph of an andesine particle (plagioclase) and spot diffraction pattern of the andesine particle (COD reference # 900-1032). (Right) EDS analysis of the particle.

TEM-SAED supports the evidence (discussed in section 6.3.1) of a significant calcium carbonate precipitation in the first millimetres of the bentonite barrier. Besides calcite, aragonite and vaterite were detected in the interface (Fig. 115).

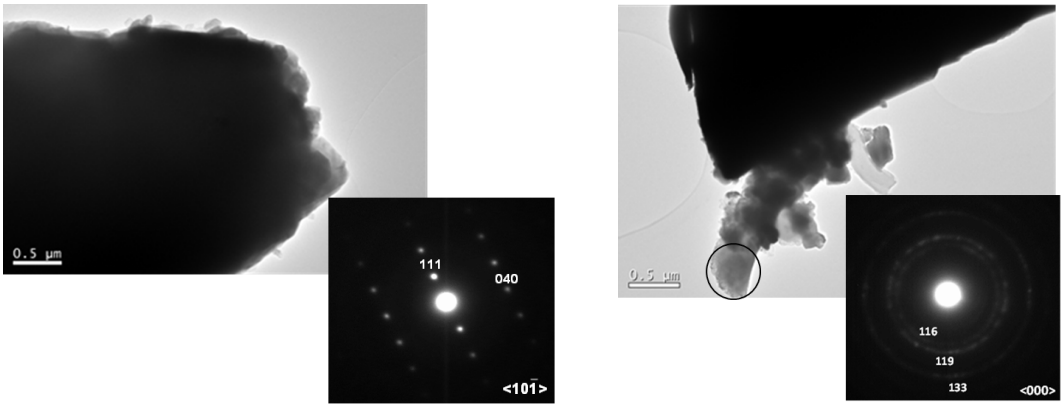

Fig. 115: (Left) Transmission Electron micrograph of one of the aragonite particles found in the bentonite sample collected at the interface, and spot diffraction pattern of a single aragonite particle (COD reference #900-0227). (Right) Transmission Electron micrograph of one of the vaterite particles found in the bentonite sample collected at the interface, and ring diffraction pattern of circled area in the TEM micrograph (COD reference # 901-3566).

The calcite morphology is illustrated in Fig. 116a, where calcite formed by an agglomeration of individual nanocrystals, can be observed in a transmission electron micrograph. The individual crystals are hexagons with sides of 40 to 150 nm showing hexagonal morphology and edges forming angles of $\approx 130^0$. Crystal borders are straight. Different dissolution behaviours were observed as a function of particle size. Micrometric calcium carbonate particles exhibit dissolution features (Fig. 116b), whereas in nanometre particles, crystal growth processes were observed. These observations point to the occurrence of dissolution and re-precipitation processes involving primary calcite and aragonite. As observed in Fig. 116a, nanometre particles of secondary calcium carbonate tend to coagulate in order to form micrometric-size particles.

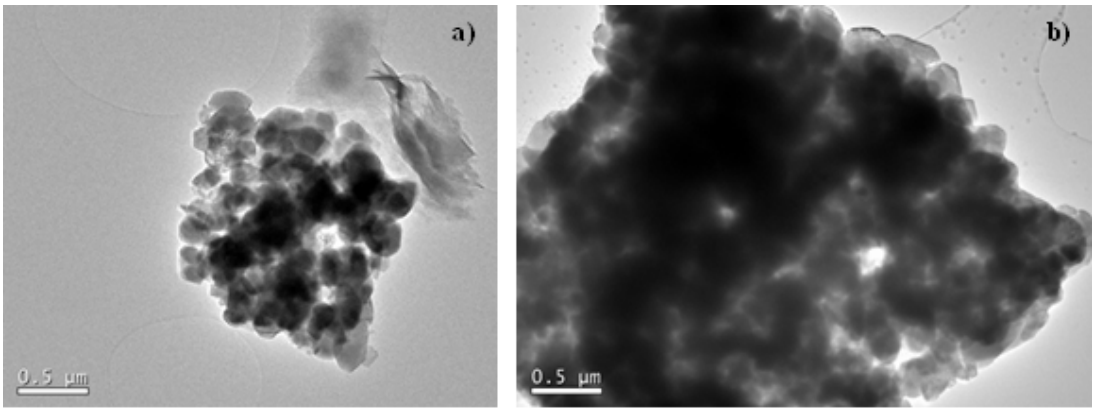

Fig. 116: Transmission Electron micrographs of two calcite particles of different sizes: a) agglomeration of neo-formed calcite nanoparticles; b) primary calcite particle exhibiting dissolution features

Bentonite particles from the interface exhibit the typical fringes found in smectitic particles (Fig. 117). Ring diffraction patterns obtained for bentonite particles from the interface are in good agreement with XRD patterns for calcium montmorillonite.

EDS analyses were carried out in montmorillonite particles in order to detect variations in the chemical composition of bentonite due to the influence of concrete leachates. No significant changes were observed. Slight differences in the chemical composition of the montmorillonite particles were found in all cases. Only minor differences in the calcium and potassium contents were detected. Tab. 6-4 shows the EDS analysis obtained for the two bentonite particles shown in Fig. 118.

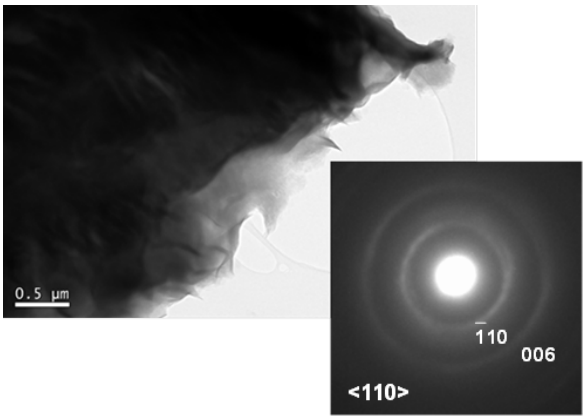

Fig. 117: Transmission electron micrograph of a montmorillonite particle collected in the concrete/bentonite interface (COD reference #110-1055).

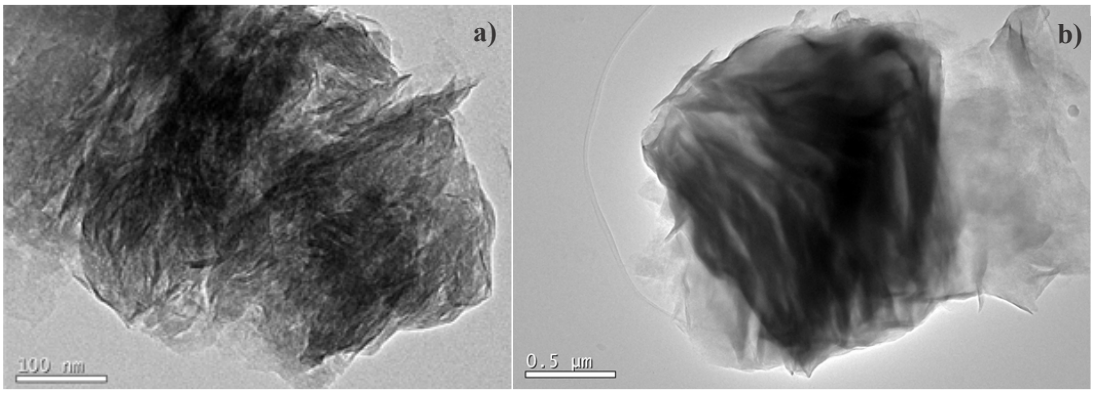

Fig. 118: Transmission electron micrographs of the two montmorillonite particles whose EDS analysis are shown in Tab. 6-4.

Tab. 6-4: EDS analysis of the two montmorillonite particles shown in Fig. 118.

	Montmorillonite particle Fig. 118a	Montmorillonite particle Fig. 118b
Element	**Atomic %**	**Atomic %**
Na	0.48	0.60
Mg	3.00	2.70
Al	8.13	9.07
Si	22.33	22.26
K	1.63	0.57
Ca	0.30	0.50
Fe	1.17	---
Ti	---	0.04
O	62.96	64.86

6.3.4 Infrared spectroscopy (Ciemat, BGR)

Analysis on samples C-C-34-10 and 12 (Ciemat)

Montmorillonite displayed four characteristic absorption features related to adsorbed water (OH stretching 3500 and 1645 cm^{-1}) and the vibration of the silicate group (Si-O stretching 1115 cm^{-1} and O-Si-O bending 460 cm^{-1}).

FTIR spectra confirm the presence of Mg-rich phases in samples from the interface (Fig. 146). Either brucite or trioctahedral smectites (i.e. saponite, stevensite), as well as poorly ordered M-S-H phases (Martín de Vidales et al. 1991; Nied et al. 2016) exhibited a band centred near 3698 cm^{-1}, corresponding to a characteristic OH vibration of the $Mg(OH)_2$ group.

Additionally, OH bending modes at 632, 602 and 560 cm^{-1} were also found. These absorption features resemble a chrysotile spectrum in the OH bending region. The appearance of another band centred at 660 cm^{-1} could indicate the possible formation of other Mg trioctahedral sheet silicates at the interface (Tonelli et al. 2016).

According to Fig. 119 and Fig. 120, concrete carbonation tends to intensify towards the interface, whereas in the first mm of bentonite, calcite depletion is likely to occur, as demonstrated in sample C-C-34-10. Three sharp carbonate-related bands were observed at 1420, 875 and 713 cm^{-1} in samples collected from the interface and the first millimetres of concrete.

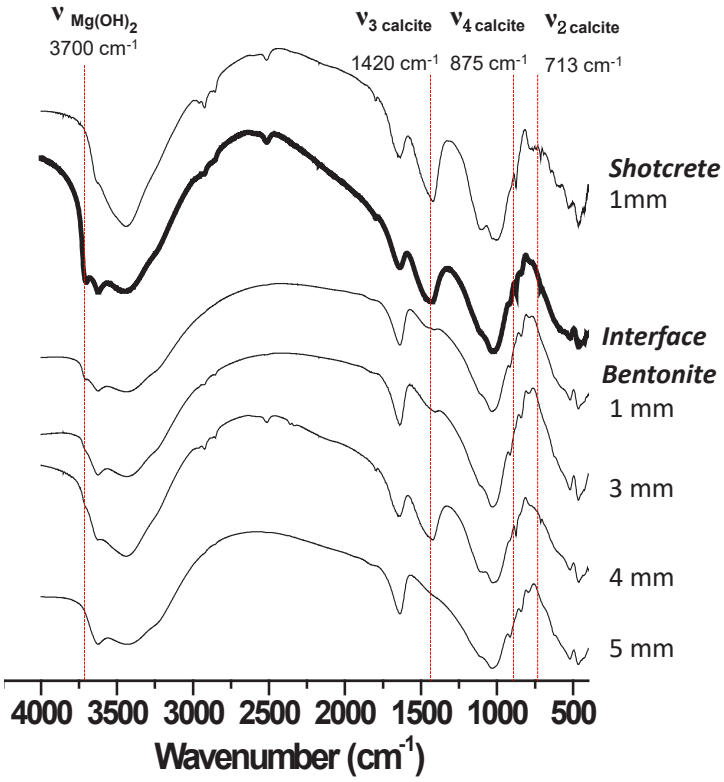

Fig. 119: FTIR spectra in the 4000-400cm^{-1} region corresponding to the C-C-34-12 concrete/bentonite interface.

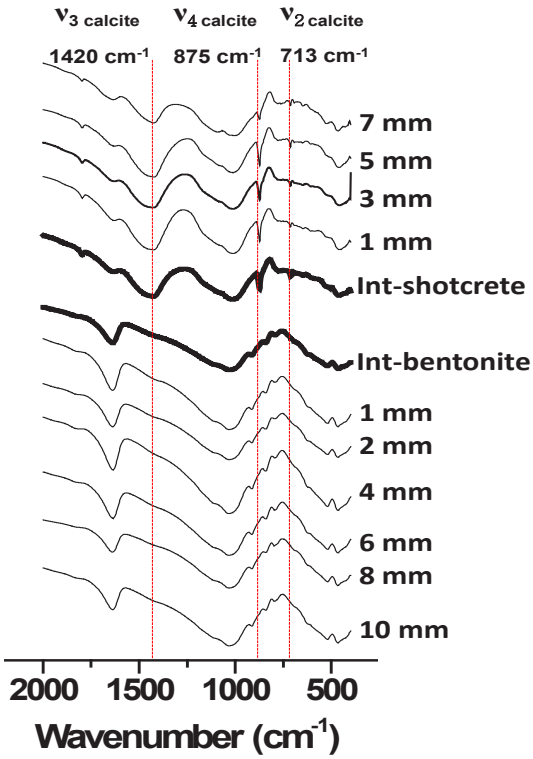

Fig. 120: FTIR spectra of samples collected in the vicinity of the interface in the C-C-34-10 sample.

Analysis on sample BC-S-35-1b (BGR)

Sample BC-S-35-1b was investigated with IR (Fig. 121). The spectrum of the concrete side is dominated by carbonates and silicates which were not characterised or discussed further. The contact between the cement and the bentonite, on the other hand, was particularly interesting. The contact samples (1 mm) were compared with the reference (FEB Ref. in the Fig. 121). A slight increase of the carbonate content and a new band at about 3698 cm^{-1} were observed. This band can be attributed either to brucite ($Mg(OH)_2$) or kaolinite/chrysotile (Madejova et al. 2017) – the alkaline Mg-medium probably leads to discarding kaolinite but it has to be assessed with further analyses. Brucite would also explain the observed MgO increase in the chemical analysis (section 6.4.3). Interestingly, this band corresponding to brucite or kaolinite/ chrysotile was not observed in the cement which indicates a separate reaction between cement and smectite.

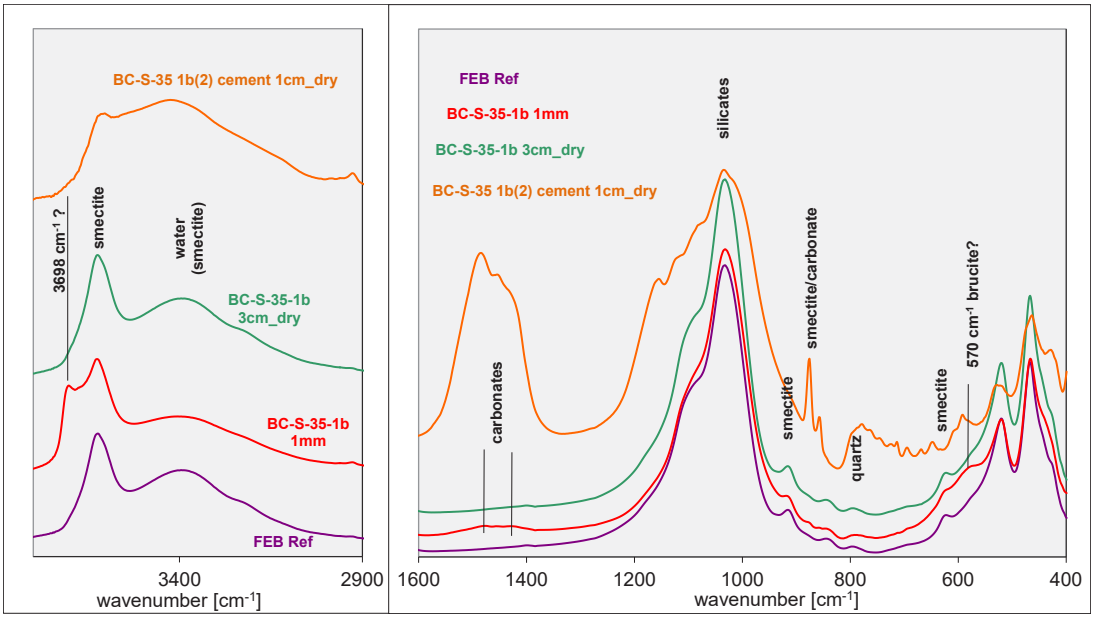

Fig. 121: IR spectra of sample BC-S-35-1.

6.4 Geochemical measurements

6.4.1 Soluble ions by aqueous leaching (UAM, Ciemat)

Bulk concrete

The main ions representing soluble salts in bulk concrete samples C-C-34-4 to 11 have been plotted in spatial (x,h) coordinates in Fig. 122. The data are compiled in Appendix B (part B.3, Tab. B-7). Note that the samples that represent the concrete are at a distance ranging from 10 cm to 100 cm from the bentonite.

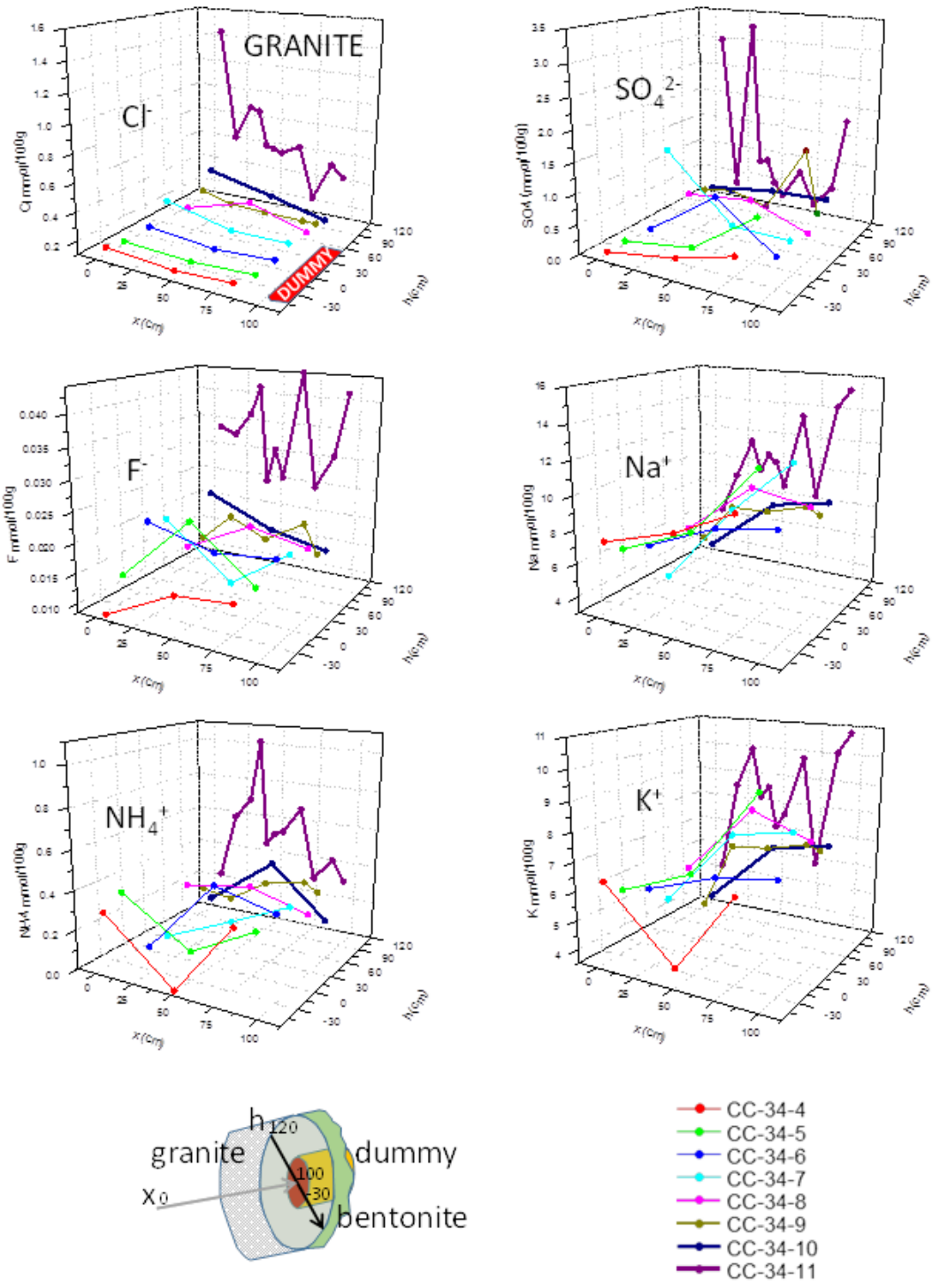

Fig. 122: 3D-representation of the aqueous extractable soluble ions as a function of the distance to the bentonite and the dummy front (higher x indicates proximity to the bentonite in agreement with the core distance marks) and the distance from the axis of the gallery following the line where the samples were taken (higher h indicates proximity to the granite).

In general, the concentration of soluble salts in the bulk concrete is small and increases near the granite interface (core C-C-34-11). No clear trends are observed towards the bentonite interface, except for chloride, that seems to decrease towards the bentonite. Fluoride concentration is high close to the granite and decreases towards the axis of the gallery. Sulphates exhibit erratic variations and have been represented with ettringite (Fig. 123). The higher content of sulphate correlates with increasing contents of ettringite semi-quantified by XRD (previous section 6.3.1). However, in most of the samples with low sulphate contents there was no relationship with the ettringite determined. Local variations of pH could possibly explain local high contents of sulphate related to ettringite dissolution.

Regarding cations, an increase of soluble sodium is observed close to the bentonite interface. The trend is roughly followed by potassium. In contrast, ammonium is concentrated near the granite. A hypothesis for the increase of soluble salts across the granite interface may be related to a higher porosity and permeability in this EDZ zone in which soluble salts can easily migrate.

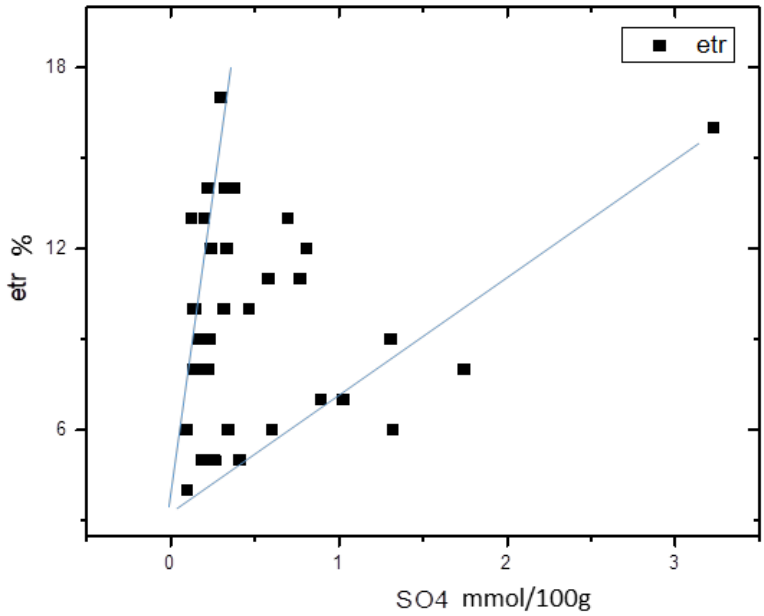

Fig. 123: Scatter plot of ettringite versus soluble sulphate content.

Concrete/bentonite interface

The complete set of results of aqueous extracts concentrations in the concrete/bentonite samples is presented in Appendix C (part C.1, Tab. C-1). Fig. 124, Fig. 126, Fig. 127 and Fig. 128 show the general trends of soluble salts in the concrete/bentonite interface. Every graph includes the reference values of the as-received material to compare. In general, the concentration of soluble salts in bentonite is similar or lower than the reference values. However, an inhomogeneous distribution of salts is observed regarding the bentonite front at the interface level (e.g. Fig. 124 and Fig. 126). The samples closest to the granite have lower saline content than those close to the dummy, which indicates a leaching process from the granite towards the dummy. This general trend agrees with the results presented by Villar (2017) in other sections of the experiment. The trends observed in the concrete side of the

interface are similar although additional analyses should be made covering more points to confirm the trend.

Fig. 124 (up) shows the plot of the concentration of chloride in the concrete and the bentonite versus the distance to the interface. The most remarkable fact is the general depletion in the bentonite with respect to the reference values, which seems to point to leaching processes in all the samples. Furthermore, apparently the samples of bentonite closest to the granite seem to have suffered more leaching than the samples in the inner part of the barrier (Fig. 124 – down), which is quite evident at 4 cm from the interface but is not so clear just in the first centimetre, where that distribution occurs in the top half of the barrier but not in the lower half. Further analysis in other locations is required to confirm this inhomogeneous trend at the interface level.

Chloride concentration in the concrete is higher than the reference value due to diffusion of this ion from the bentonite. Chloride penetrates into the concrete more than 5 cm and seems to decrease in the concrete plug toward the interface, which agrees with the results presented in section 6.4.5.5. The chloride diffusing into the concrete plug tends to precipitate as a Friedel's salt, that has been found in some of the samples, specifically in the lower half, again pointing to some heterogeneity in the plug. Fig. 125 shows the 1:1 relationship Cl:Ca that should result in Friedel's salt formation (e.g. sample C-C-34-12, see also section 6.3.3).

Fig. 126 (up) shows the plot of the concentration of sulphate in the concrete and the bentonite versus the distance to the interface. There is a general depletion of sulphate both in concrete and bentonite with respect to the reference values, which seems to point to leaching processes in almost all the samples, as in the case of chloride. Soluble sulphates increases close to the interface on the concrete side and so the formation of secondary ettringite could be favoured (see section 6.3.1). Furthermore, as in the case of chloride, the samples of bentonite closest to the granite seem to have suffered more leaching than the samples in the inner part of the barrier (Fig. 126 – down). However, the sulphate distribution is not homogeneous and higher concentrations are found in the lower half of the plug, especially at the interface (first cm) level. A downward advective gradient from the top to the bottom of the gallery could exist, transporting ions through the granite matrix near the bentonite.

Fig. 127 shows the distribution of fluoride in the concrete and the bentonite as a function of distance to the interface. In all the samples analysed, either of bentonite or concrete, an increase of fluoride is observed. Grimsel groundwater has relatively high concentration of fluoride (Garralón et al. 2018 and Tab. 3-1 of this report) and the hydration of the barriers with Grimsel groundwater provides fluoride to the materials. As in the case of chloride and sulphate, the distribution is not homogeneous and a pattern of distribution has not been found. A possible explanation for that inhomogeneous distribution of ions (top vs bottom) may be that any of the analysed ions can have natural sinks or sources as calcium salts dissolve or precipitate in distinct alkaline media. pH at the bentonite-concrete interface is heterogeneous (5.4.2 section) and for example sulphate can be more soluble if pH decreases below the ettringite precipitation threshold value (≈12).

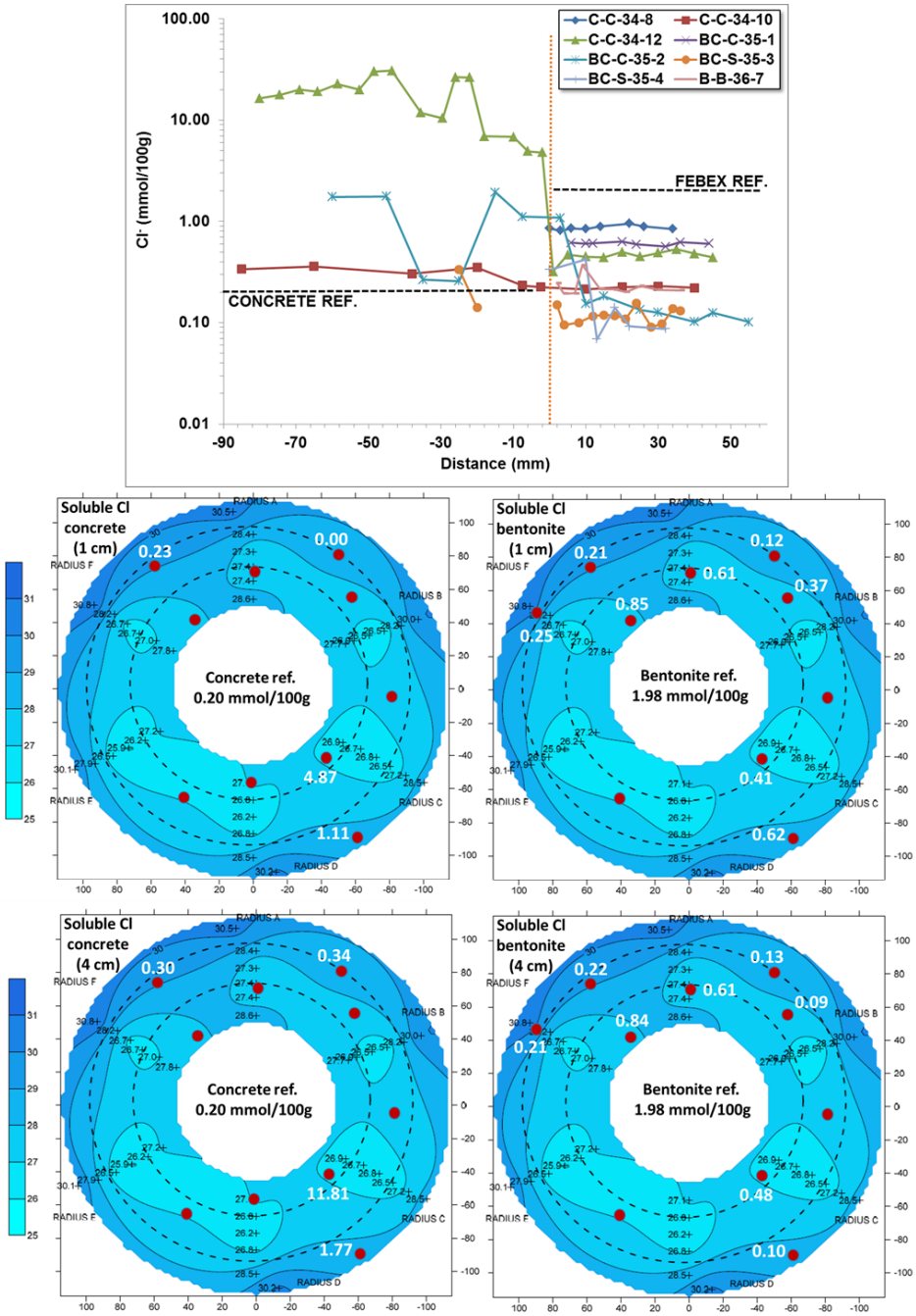

Fig. 124: Soluble chloride distribution in samples of the concrete/bentonite interface. (Up) Soluble chloride as a function of the distance to the concrete/bentonite interface (0 in the graph). Positive values of distance correpond to the bentonite side and negative values to the concrete side. (Down) Soluble chloride data (average of measurements in the first centimeter and in the fourth centimeter from the interface) are overlapped with the contour map for water content in section 37 taken from NAB16-012 (Villar et al. 2016) to observe the distribution in the plug related to the water content (%) and the granite and the dummy limits.

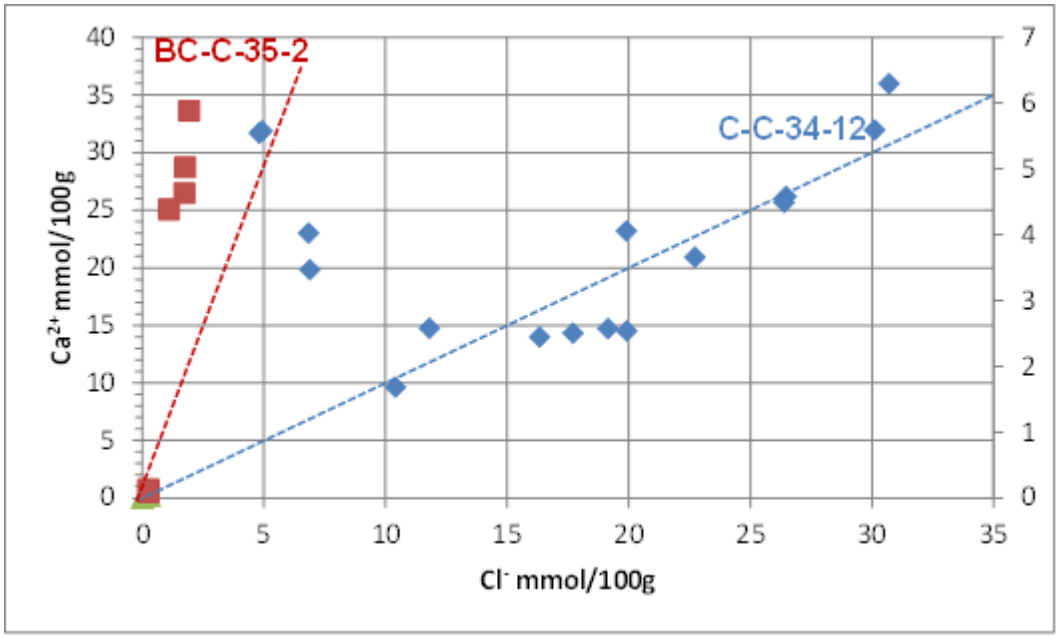

Fig. 125: Relationship between soluble chloride and calcium ions of the concrete in samples C-C-34-12 and BC-C-35-2

Na^+ measured in aqueous extracts from bentonite samples are, in all cases, much lower than the ones measured for the reference FEBEX. A decrease of Na^+ is also observed in the concrete, except for sample C-C-34-12, indicating a leaching of alkalis. This agrees with the measurements made on cores of concrete C-C-32-1 and 3 (see chapter 5) that showed a decrease of the alkali content. Na^+ from the bentonite may diffuse towards the concrete plug (e.g. C-C-34-12), but also towards the host formation and hotter zones of the bentonite barrier. Soluble K^+ tends to be lower than the reference value on the concrete side indicating, as in the case of Na^+, a leaching of this alkali. An increase of K^+ in the first 2 mm of the bentonite at the interface, reveals migration of that ion into the bentonite

Ca^{2+} in the concrete is below the reference value which may be associated mainly to portlandite dissolution (section 6.3.1) and subsequent dissolution/precipitation of calcite and gypsum. Part of that Ca^{2+} can migrate into the bentonite side, explaining the slight enrichment in the bentonite when compared to the reference value. Soluble Mg^{2+} gets accumulated in the first 2 cm from the interface in concrete (Fig. 128). In bentonite, however, Mg^{2+} measured in aqueous extracts is negligible, as precipitation of Mg silicates occurs, favoured by the solution chemistry at the interface: high ionic strength, alkaline pH and high SiO_2(aq) concentration in bentonite porewater (Tab. 3-1). Diagrams made with the HYDRA/MEDUSA, chemical equilibrium database and plotting software (Puigdomenech 2015) (Fig. 129), indicates that considering the conditions of the spill water analysed near the sample C-C-34-12 magnesium should precipitate as silicates.

Data from core C-C-34-12 are particularly noticeable since soluble ion content is higher than in the rest of cores. This core was very close to the water spill mentioned in section 3.2, which indeed has a high saline content and is located in the lower half of the plug. A possible explanation is the shotcreting procedure of the first millimetres that allowed certain rebound material to accumulate in the lower part making it more porous and permeable and hence facilitate the soluble salt migration.

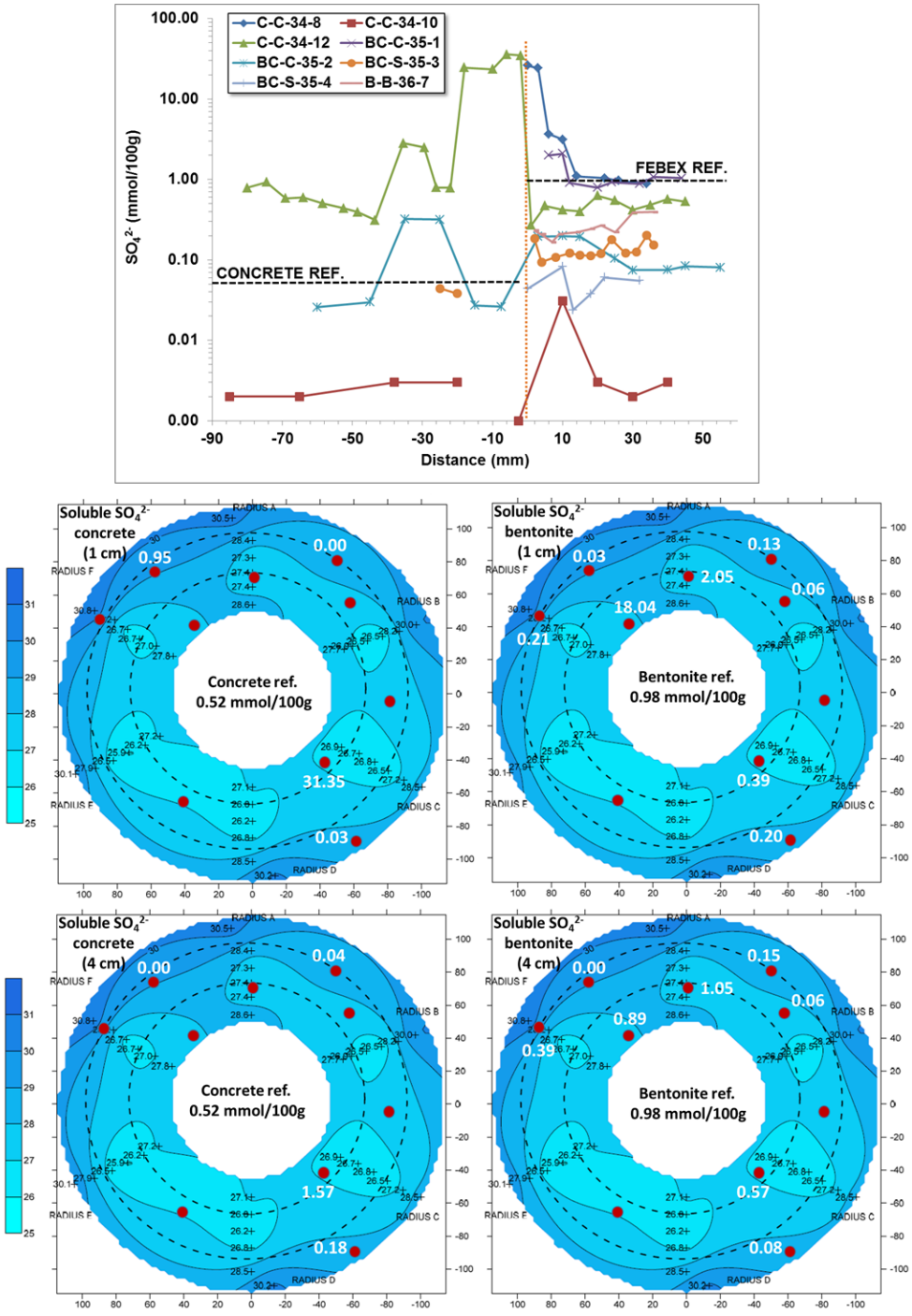

Fig. 126: Soluble sulphate distribution in samples of the concrete/bentonite interface. (Up) Soluble sulphate as a function of the distance to the concrete/bentonite interface (0 in the graph). Positive values of distance correpond to the bentonite side and negative values to the concrete side. (Down) Soluble sulphate data (average of measurements in the first centimeter and in the fourth centimeter from the interface) are overlapped with the contour map for water content in section 37 taken from NAB16-012 (Villar et al. 2016) to observe the distribution in the plug related to the water content (%) and the granite and the dummy interfaces.

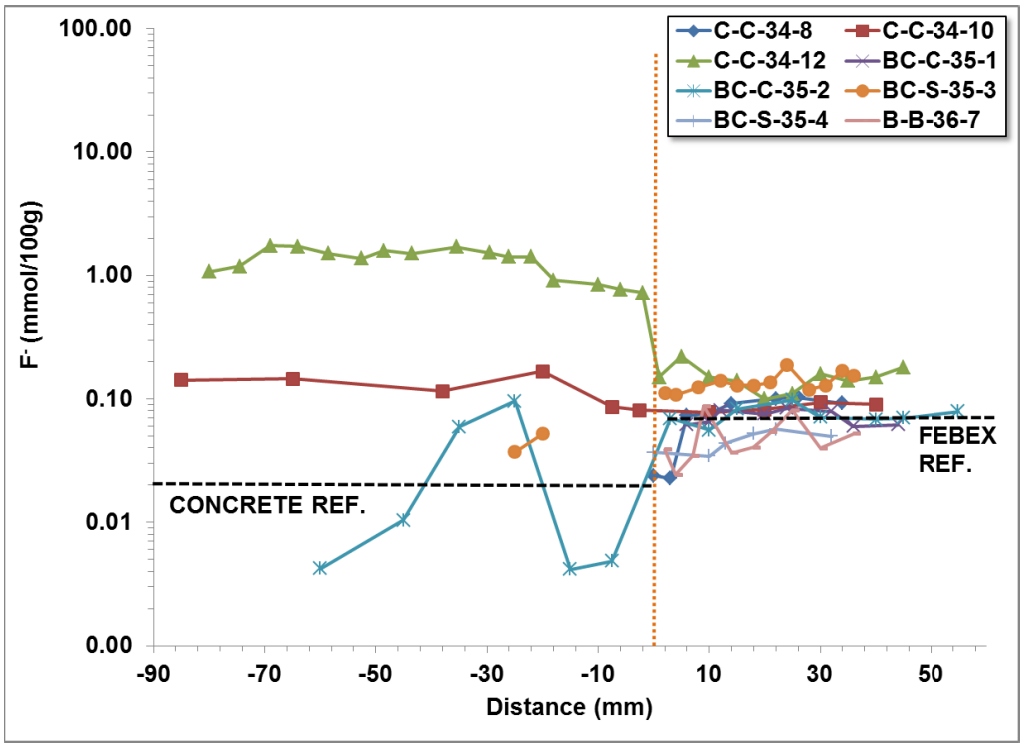

Fig. 127: Soluble fluoride distribution in samples of the concrete/bentonite interface.

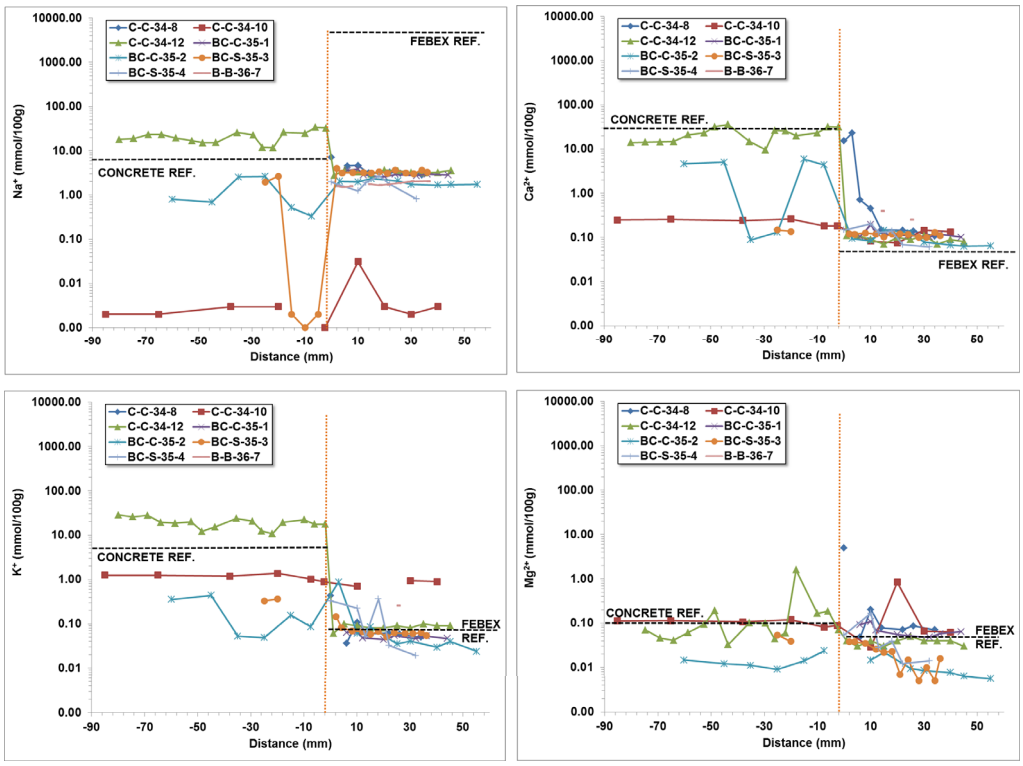

Fig. 128: Soluble cations distribution in samples of the concrete/bentonite interface.

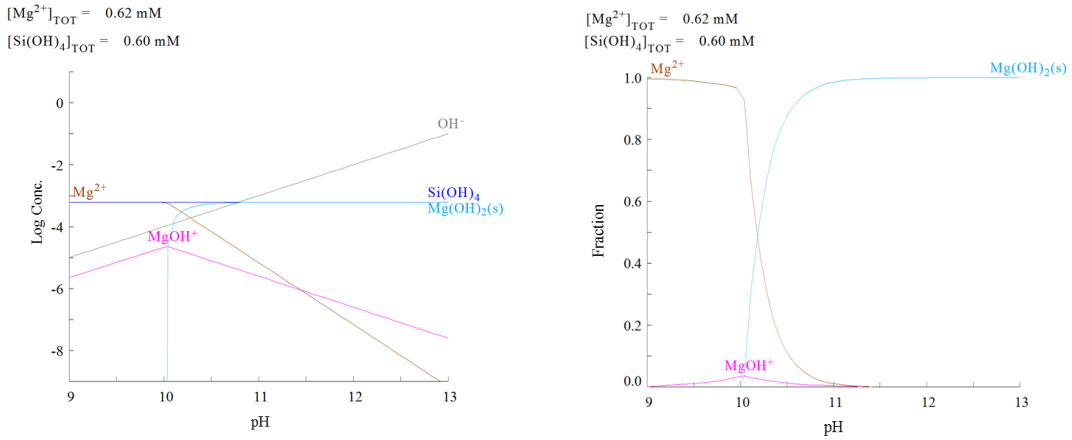

Fig. 129: Chemical diagrams showing stable forms of magnesium considering the chemistry of the spill water analysed in the vicinity of sample C-C-34-12 (Tab. 3-1).

6.4.2 Cation exchange capacity and exchangeable cations (Ciemat, BGR, Obayashi)

Cation exchange capacity (CEC) was measured by Ciemat in samples C-C-34-10, BC-C-35-2 and BC-S-35-3 and by BGR in samples BC-S-35-1a and b. Exchangeable cations (EC) were analysed by Ciemat (samples C-C-34-8, 10 and 12, BC-C-35-1 and 2 and BC-S-35-3 and 4), BGR (BC-S-35-1a and b) and Obayashi (C-C-32-6).

Results on CEC are shown in Fig. 130 (whole data in Appendix C, part C.2, Tabs. C-2,C-3 and C-5). The average cation exchange capacity is 85.9 ± 4.1 and it remains quite stable along the first 40 mm from the interface in the samples analysed.

BGR found a significant drop of the CEC at the contact (25 – 50 %). At 1 cm distance a CEC drop of 10 % was still found. The justification is that it cannot be explained by a higher pH because elevated pH increases the CEC. The CEC decrease, therefore, indicates a reaction of the smectite which nevertheless is still smectite structurally. The XRD analysis after ethylene-glycol intercalation showed that sample BC-S-35 1b 1mm has still the same expendability to 16.9 Å as the reference sample (see section 6.3.1.3, Fig. 92), however, the peaks of the basal series were broadened.

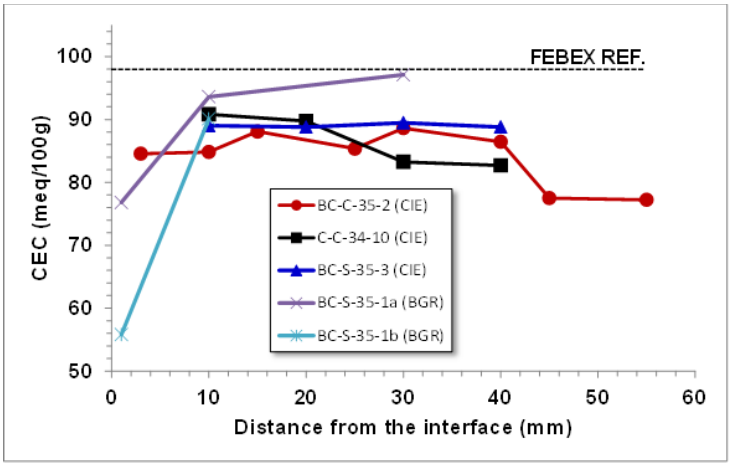

Fig. 130: Profile of cation exchange capacity of three samples at two opposite locations in the plug.

Integrated results of exchangeable cations are presented in Fig. 131. The results of the exchangeable cation measurement are shown in Appendix C (part C.2, Tabs. C-3 to C-5). Na, K, Ca and Mg were the exchangeable cations measured by all partners.

A heterogeneous distribution of the exchangeable cations is observed in the bentonite in contact with the concrete plug. Three groups of samples can be distinguished (Fig. 131):

- Bentonite with the highest Ca and Mg content and the lowest Na and K content. It is a sample located in the outer ring of bentonite, close to the granite (C-C-34-10).
- Bentonite with a very high Ca and Na and the lowest Mg in the exchange complex compared to the reference FEBEX. Those samples were taken in bentonite ring closest to the granite at the right side of the gallery (BC-C-35-2, BC-S-35-3 and BC-S-35-4).
- Bentonite with the exchange complex very similar to that of the original FEBEX bentonite, but still with higher calcium and lower magnesium. Those are located towards the dummy, in the second bentonite ring and inner (BC-C-35-1, BC-S-35-1a and b, C-C-34-8, C-C-34-12).

The generalised increase of exchangeable calcium can be explained by the excess of dissolved Ca^{2+} from the alkaline concrete porewater entering in the interlayer of montmorillonite and displacing Mg^{2+}. The magnesium migrates towards the concrete, precipitating at high pH as magnesium silicate or silica-aluminate. The porewater conditions at the interface are favourable for the formation of Mg-rich precipitates (previous section 6.4.1).

Then, at the experiment scale the influence of the concrete Ca^{2+} leaching promotes calcium increases up to 63% in the exchange complex compared to the reference FEBEX value in areas close to the granite. Values decrease to values closer to the reference, although still around 20% higher, towards the internal part of the barrier (Fig. 132). The opposite occurs with Mg, that decreases up to 71% in those areas close to the granite, and increases towards the inner part of the barrier, although values remain lower than the reference value (around 6% lower) (Fig. 132). This trend is maintained up to 4 cm from the interface, which is the depth covered by this study. Villar (2017) found similar patterns in the bentonite samples analysed in the dismantling section closest to the concrete plug (section 36). Na^{+} maintains values quite close to the reference values in all samples and variation of K^{+} ranges from

values similar to the reference up to 88% of difference, without a clear pattern in the spatial distribution. K^+ increase supports the assumption of a certain release from concrete to bentonite (Fig. 133).

A detailed exchangeable cations study was performed on the bentonite for most of the samples. As a general trend, at the interface scale, a homogeneous distribution in exchangeable cations is observed (Fig. 134), except for the first millimetres. Taking into account the above-mentioned differences (higher Ca and lower Mg) with respect to the FEBEX reference value, a slight decrease of Ca and Na is observed just at the interface together with a slight increase of Mg and K, which remains limited to the first millimetres from the interface with the concrete. As discussed in Fernández et al. (2017), laboratory experiments indicate that this increase in exchangeable Mg^{2+} could be caused by dissolution of the magnesium mineral phases in the extraction solution for determination of exchangeable cations rather than a real increase of exchangeable Mg^{2+}. Nevertheless, the CEC data in the present study, which remain almost constant along the whole length of bentonite analysed (36 mm from the interface), do not confirm that observation. Further analysis are necessary to confirm or disprove this possibility.

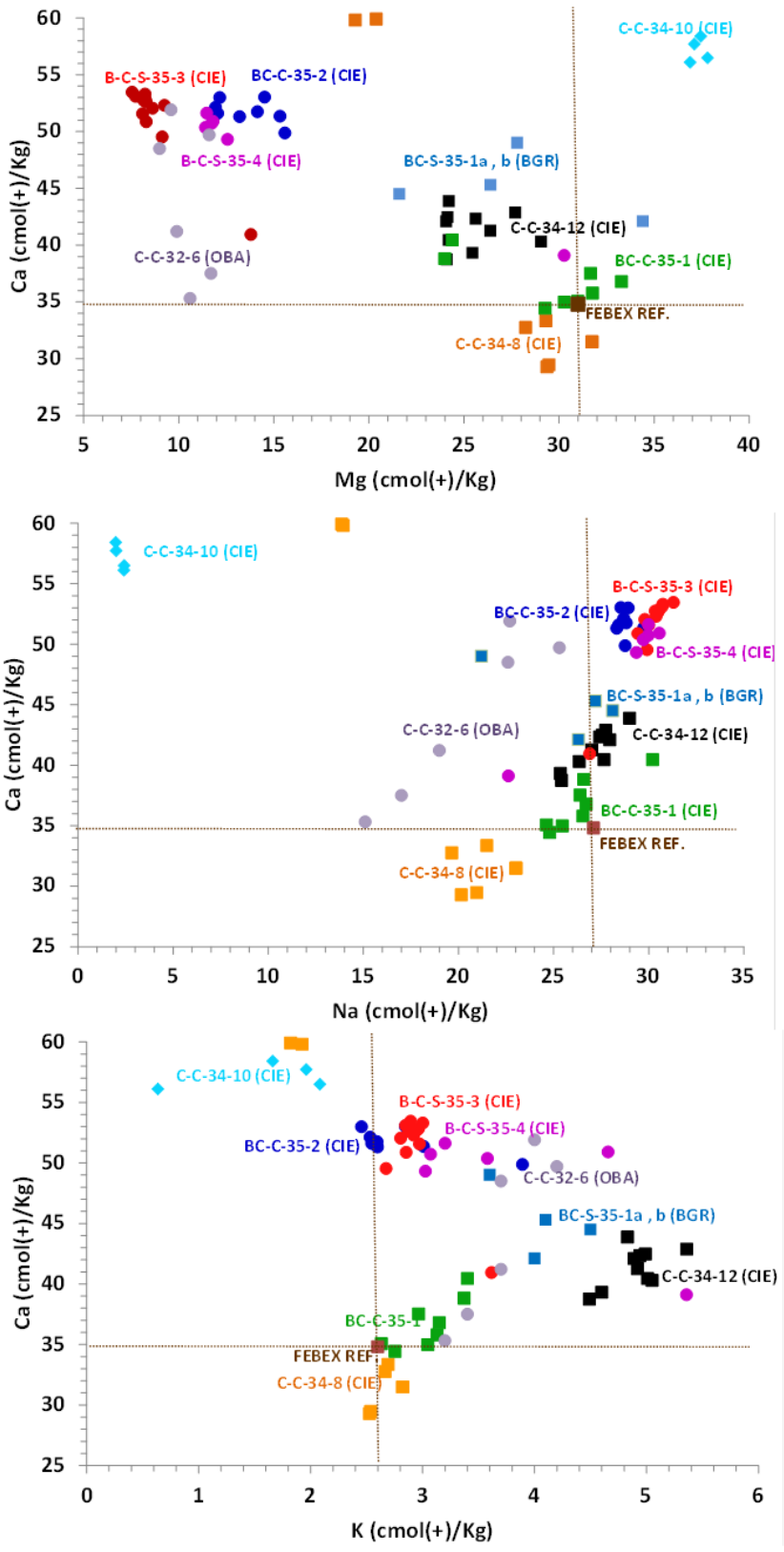

Fig. 131: Exchangeable Mg vs Ca in the bentonite samples contacting the concrete plug.

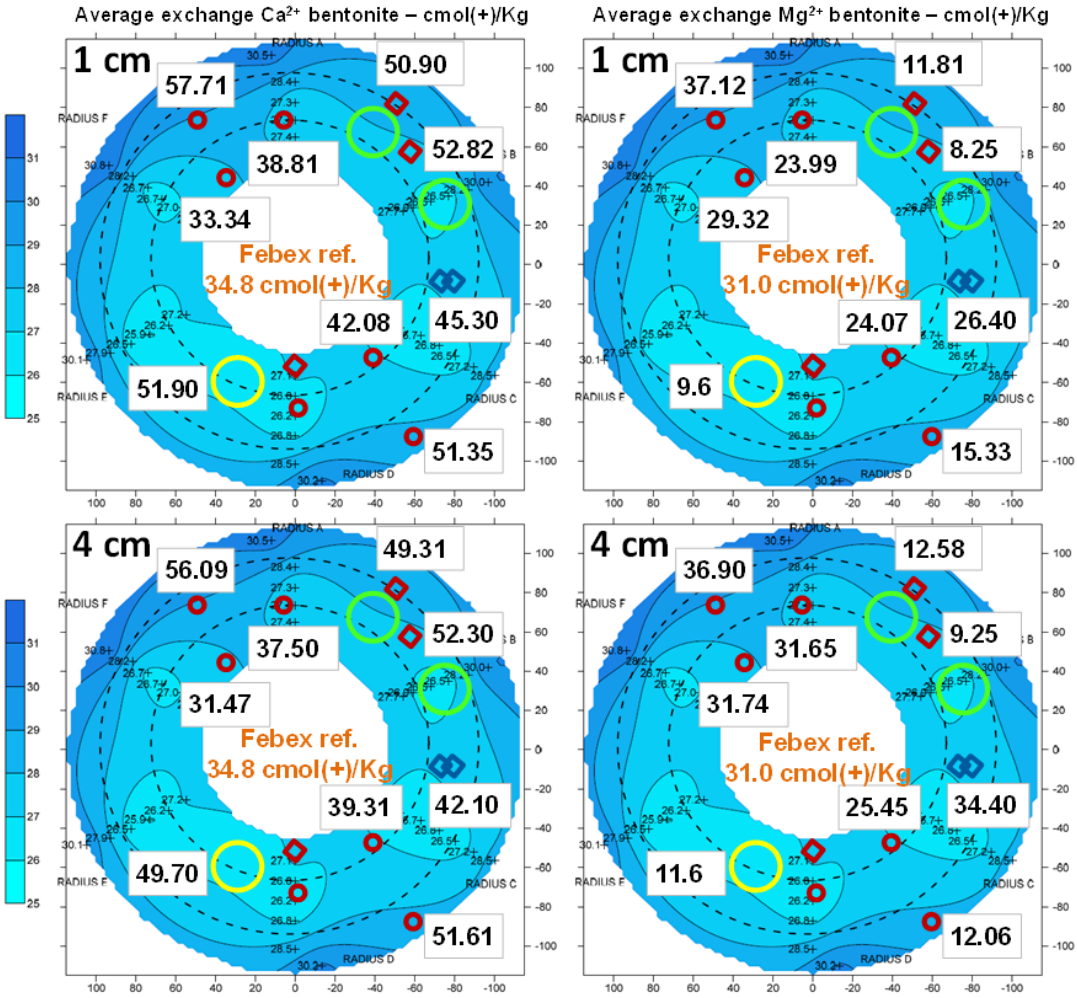

Fig. 132: Exchangeable Ca^{2+} (left) and Mg^{2+} (right) values in selected bentonite samples at two distances (1 cm and 4 cm) from the concrete are overlapped with the contour map for water content in section 37 taken from NAB16-012 (Villar et al. 2016).

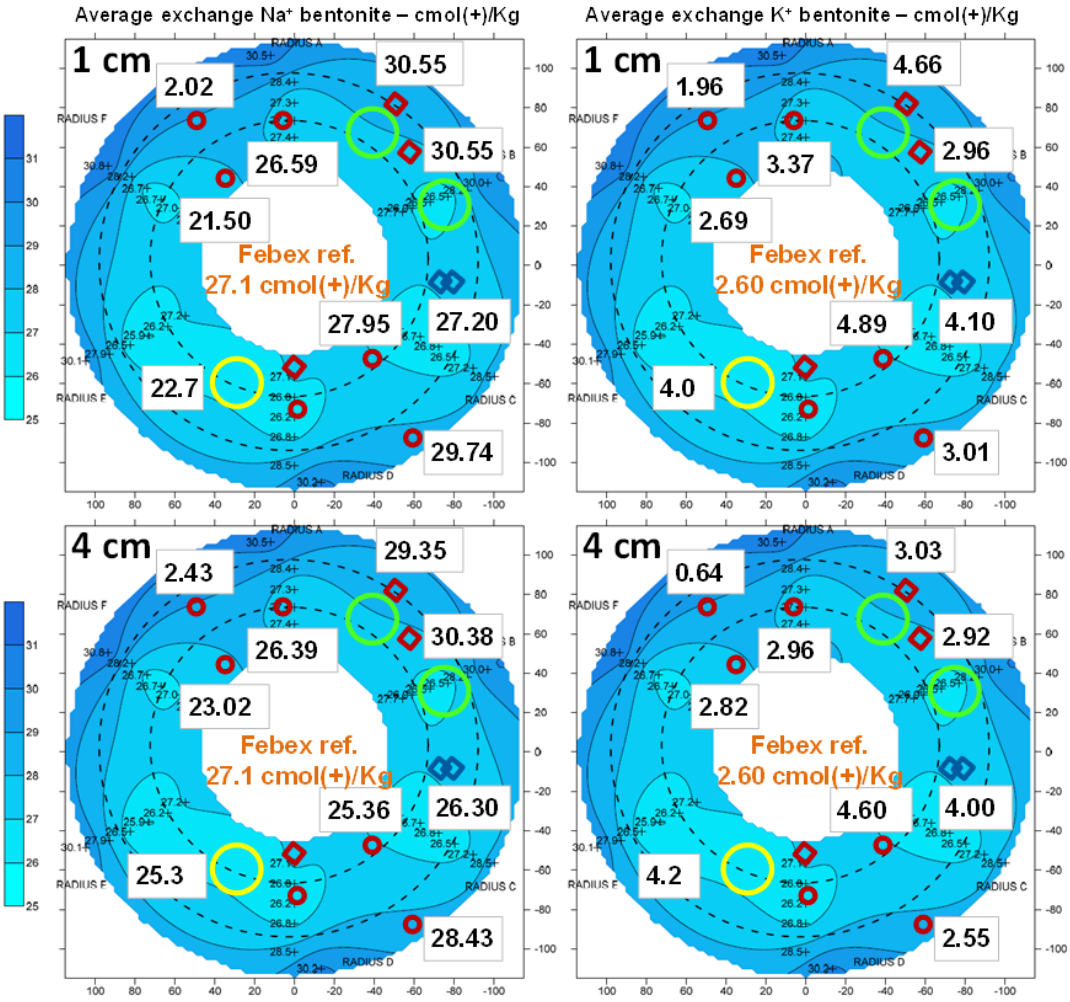

Fig. 133: Exchangeable Ca^{2+} (left) and Mg^{2+} (right) values in selected bentonite samples at two distances (1 cm and 4 cm) from the concrete are overlapped with the contour map for water content in section 37 taken from NAB16-012 (Villar et al. 2016). FEBEX ref. Values can be found in Huertas et al. 2006.

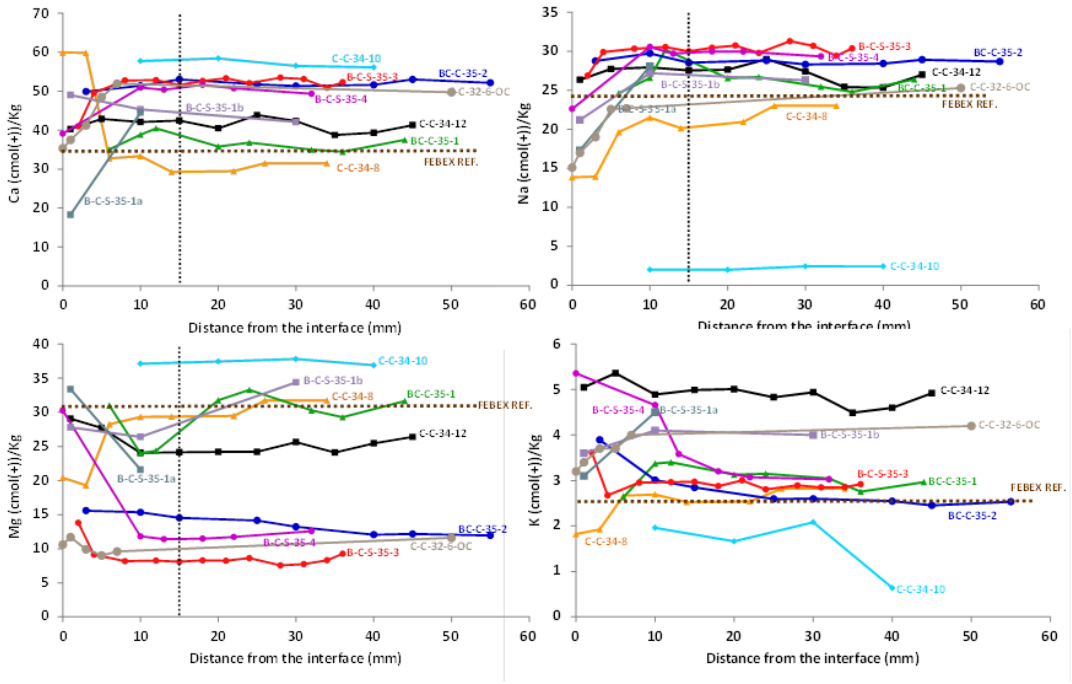

Fig. 134: Exchangeable cations in the bentonite exchange complex as a function of the distance to the concrete plug.

6.4.3 Chemical analysis by XRF (BGR)

Tab. 6-5 shows the chemical analysis of samples BC-S-35-1a and b. The most striking change in the bentonite samples is the increase of the MgO content near the contact to the concrete interface surface, as well as an increase of C and S (marked in yellow in Tab. 6-5). Contact samples from the "b-series" were investigated with XRD-Rietveld, STA (section 6.3.1.3) and IR (section 6.3.4).

Tab. 6-5: Chemical composition and loss of water upon drying at 60 °C of samples BC-S-35-1a and b taken from section 35.

	distance	water (60°C)	SiO_2	TiO_2	Al_2O_3	Fe_2O_3	MnO	MgO	CaO	Na_2O	K_2O	P_2O_5	(SO_3)	LOI	Sum	C_{total}	C_{org}	C_{carb}	S_{total}
		[mass%]	[mass%]	[mass%]	[mass%]	[mass%]	[mass%]	[mass%]	[mass%]	[mass%]	[mass%]	[mass%]	[mass%]	[mass%]	[mass%]	[mass%]	[mass%]	[mass%]	[mass%]
REF ABM			55.2		17.2	3.1		4.4	1.8	1.1	1.0	0.0	0.1	16.0	100.0	0.1	0.0	0.1	0.0
REF FEB AVG.			54.8	0.2	17.2	3.3	0.0	4.4	1.9	1.1	1.0	0.0	0.0	15.7	99.9	0.1	0.1	0.1	0.0
BC-S-35-1b	1 mm	14.3	51.5	0.2	15.9	2.9	0.1	7.5	2.9	1.0	1.0	0.0	0.5	16.4	99.9	0.4	0.1	0.3	0.2
BC-S-35-1b	1 cm	16.8	55.0	0.2	17.3	3.3	0.0	4.4	2.2	1.2	1.2	0.0	0.0	15.0	99.9	0.2	0.1	0.1	0.0
BC-S-35-1b	3 cm	17.2	55.6	0.2	17.2	3.1	0.0	4.4	1.9	1.1	1.0	0.0	0.0	15.3	99.9	0.2	0.1	0.1	0.0
BC-S-35-1a	1 mm	12.6	50.5	0.2	15.2	3.1	0.1	10.8	2.1	1.1	1.1	0.0	0.1	15.5	99.9	0.4	0.1	0.3	0.1
BC-S-35-1a	1 cm	16.7	54.5	0.2	16.9	3.2	0.0	4.7	2.4	1.3	1.1	0.0	0.0	15.5	99.9	0.3	0.1	0.2	0.0
BC-S-35-1b (2) Z	3 cm	6.7	46.8	0.3	10.1	3.2	0.0	1.5	17.5	1.9	1.8	0.1	2.0	14.5	99.9	2.7	0.3	2.4	0.8

6.4.4 Carbonates and stable isotope analysis (UAM)

The calcimetry method was chosen to quantify the carbonate content. It offers more reliability in this case because it is not biased by the presence of C-S-H minerals.

Bulk concrete

The carbonate content in the bulk concrete shows a wide range from 8 to 25 wt. % (Appendix B - part B.5, Tab. B-10). Nevertheless, there is a high variability of the carbonate content related to initial heterogeneities in concrete composition, the extent of ettringite or C-S-H formation during the curing stage, or carbonation during ageing. In general, the carbonate content increases towards the granite interface.

The values of $\delta^{13}C$ show a clear difference depending on what experiment boundary they are close to (Fig. 135); and this despite the high variability in calcite content. The dummy- and bentonite-affected zones exhibit the more positive values and the granite or the zone located far from the bentonite and dummy front show the more negative delta values. The observed distribution near the bentonite may indicate a zone of carbonate dissolution in which the light ^{12}C carbon is selectively dissolved. The opposite can be argued near the granite in which light ^{12}C (atmospheric related) carbonates coming from the granite are precipitating. $\delta^{18}O$ shows roughly the same distribution as C although in the bottom zones lighter delta values are displayed.

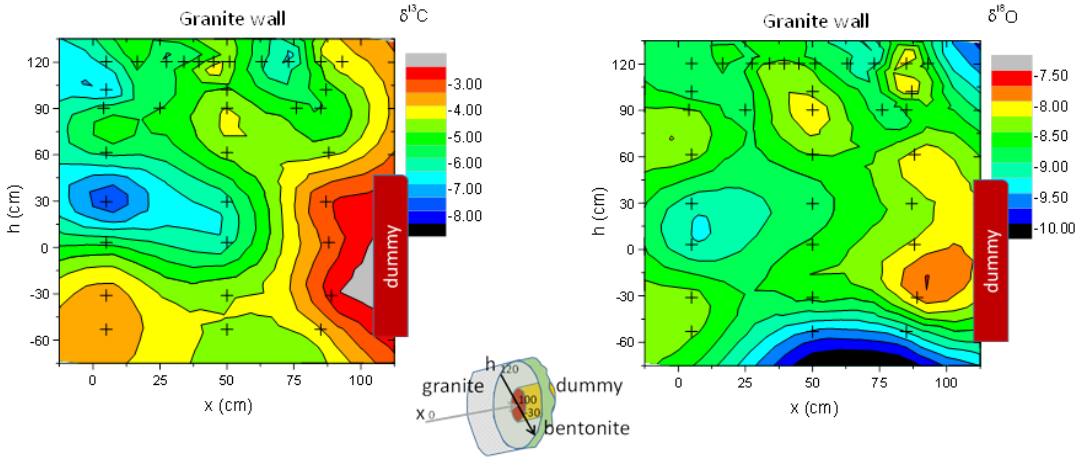

Fig. 135: Distribution map of $\delta^{13}C$ and $\delta^{18}O$ stable isotopes as function of the distance to the bentonite and the dummy front (increasing-x) and the length (h) measured in the diagonal line where the samples were taken (see intermediate picture).

Concrete/bentonite interface

Calcite is more concentrated in concrete than in bentonite, in which 1-2 mm away from the interface calcite contents are similar to its original content in bentonite. In fact, the bentonite calcite content is frequently below the original values. There was no obvious dependence of carbonate concentration at the interface and the position of the core or sample, e.g. C-C-34-8 and C-C-34-10 (+z) and BC-C-35-2 (-z) are samples with the highest calcite concentrations.

Tab. C-6 in Appendix C (part C.3) shows the carbonate content determined by calcimetry, values of $\delta^{13}C$ and $\delta^{18}O$ stable isotopes, specific surface area measured by BET N_2 isotherm and % of <2µm fraction extracted in distilled water. The yield of extraction is close to 20 % and only BC-C-35-1 has very low values. This is the interface with the highest concentration in C-A-S-H minerals which presumably affected the aggregation of clay particles.

Results of $\delta^{13}C$ show more negative values in concrete towards the interface, and the same trend on the bentonite side, indicating a clear redistribution of carbonates. Although more detailed data are necessary to know how carbonates redistribute, the present data confirm that carbonates concentration is governed by calcite dissolution in concrete and bentonite, and probably by dissolution/precipitation processes from other sources such as the granite groundwater. Highly negative values at the interface are present in all the analysed interface samples and it is interpreted as the precipitation of light C dissolved in the proximity of the interface. The analysis of $\delta^{18}O$ data is more complex since the original source can be attributed to either carbonates or pore water, but the overall trend, as for $\delta^{13}C$, shows more negative values towards the interface (Fig. 136).

C-C-34-8 and BC-C-35-1 show the highest concentration of gypsum at the concrete interface. These samples show a less negative trend for heavy oxygen or carbon. The complex relation of the sparingly soluble salts near the interface involving sulphates, carbonates, and the precipitation of other calcium minerals such as C-A-S-H, should change the carbonate dynamics and also the distribution of the isotopic signature. These results have to be studied and interpreted further.

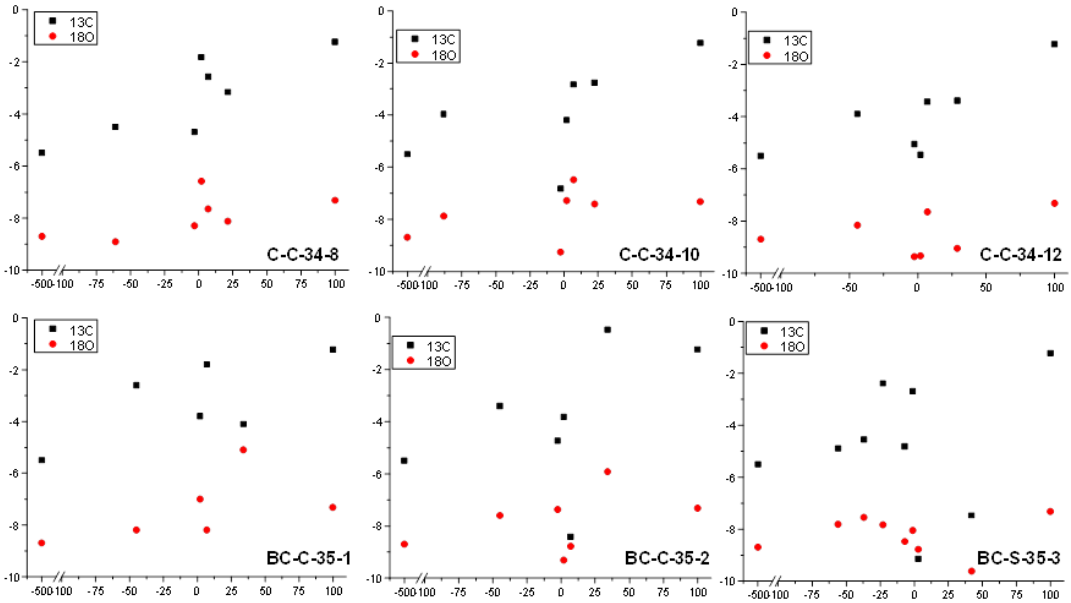

Fig. 136: Isotopic data of $\delta^{13}C$ and $\delta^{18}O$ in concrete and bentonite for samples C-C-34-8, 10 and 12, BC-C-35-1 and 2 and BC-S-35-3. X-axis is mm.

6.4.5 Elemental mapping of polished sections (UAM, UniBern, Obayashi, Sandia)

Results of elemental profiles and mapping, analysing the concrete/bentonite interface on polished sections by SEM-EDX (UAM, UniBern and Sandia), EPMA (Obayashi) and XRF (Sandia) are presented in this section. Additional data focused just on the 3 centimeters of concrete closest to the bentonite in samples C-C-32-1 and 3 are presented (CSIC).

6.4.5.1 Results on samples C-C-34-10 and 12, BC-C-35-1 and 2, and BC-S-35-3 (UAM)

C-C-34-10, C-C-34-12 and BC-S-35-3 were selected for their qualities to perform EDX elemental profiles and mappings. Appendix C (part C.4) details the preparation of samples for SEM-EDX analysis. Fig. 137 shows the aspect of the polished sections analysed. Bentonite exhibits a < 1mm dark rim either when it is polished dry or embedded in resin. Concrete, on the other hand, seems to brighten to pale grey after another dark rim of millimetre dimensions in contact with bentonite. An orange colour appears in sample C-C-34-12 but it is not observed in the other specimens.

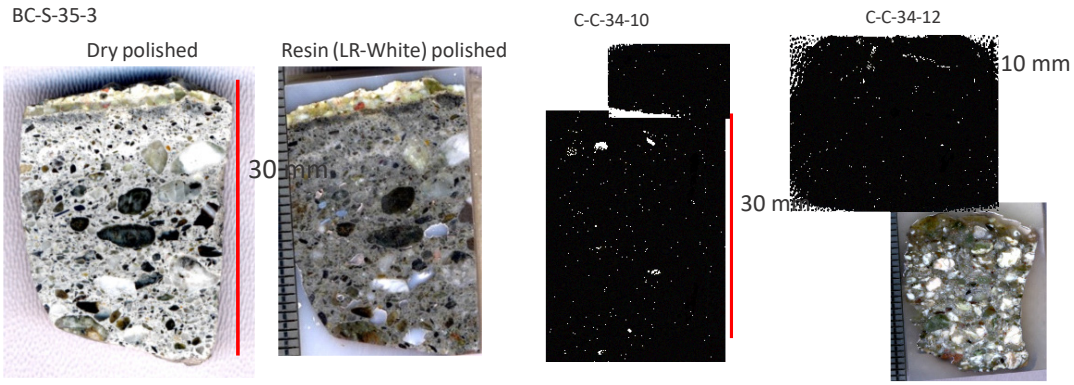

Fig. 137: Pictures showing the polished sections of samples C-C-34-10, C-C-34-12 and BC-S-35-selected for elemental mapping or chemical profiles analyses.

The elemental maps in sample BC-S-35-3 show that the ettringite observed in concrete and the different morphologies rich in Mg detected in bentonite are not just anomalies detected punctually in selected zones since net fronts of sulphate and magnesium are visible at millimetre scale (Fig. 138).

An enriched thickness ~5 mm of sulfur (in grey colour) is detected on the concrete side in the elemental map of sample BC-S-35-3. The polished section considers mostly concrete and a few millimetres of bentonite (Fig. 138). Both materials were well soldered in this sample. An enrichment in Mg (in purple colour) is also observed on the bentonite side in sample BC-S-35-3, but also in sample C-C-34-12 (Fig. 139) where an area of at least 3 mm from the interface with concrete, enriched in Mg, is observed. This is consistent with the semi-quantification of 10-15 % of trioctahedral sheet silicates in a 4 mm section around the concrete–bentonite interface (see section 6.3.3) in sample C-C-34-12.

The compositional profiles performed in samples C-C-34-10 and C-C-34-12 show in detail (Fig. 140) the extension and amount (in weight percentage) of the enrichment in Mg that

extends up to 4-5 mm in bentonite from the interface with concrete. In both chemical profiles, Mg displays two peaks decreasing the concentration with distance to the concrete interface. In general, elemental chemical profiles are very homogeneous and constant in the bentonite 5 mm away from the concrete.

Fig. 140 shows that the increase in Mg concentration at the interface is not quantitatively comparable between both samples but confirms net trends of redistribution of elements.

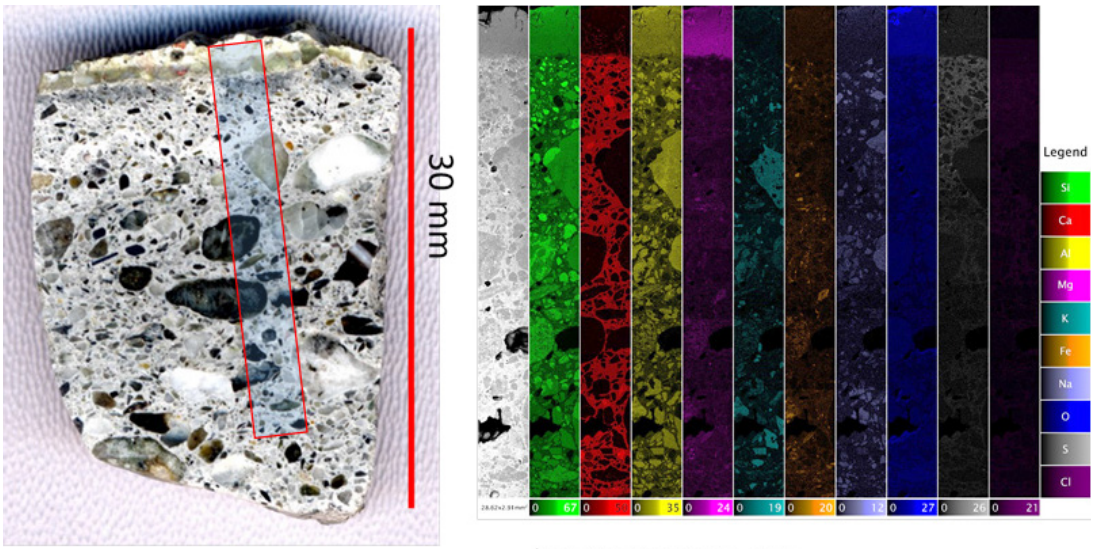

Fig. 138: Elemental map on a polished section of concrete in sample BC-S-35-3. Approximately 3 mm of cemented bentonite are included at the top of the sample.

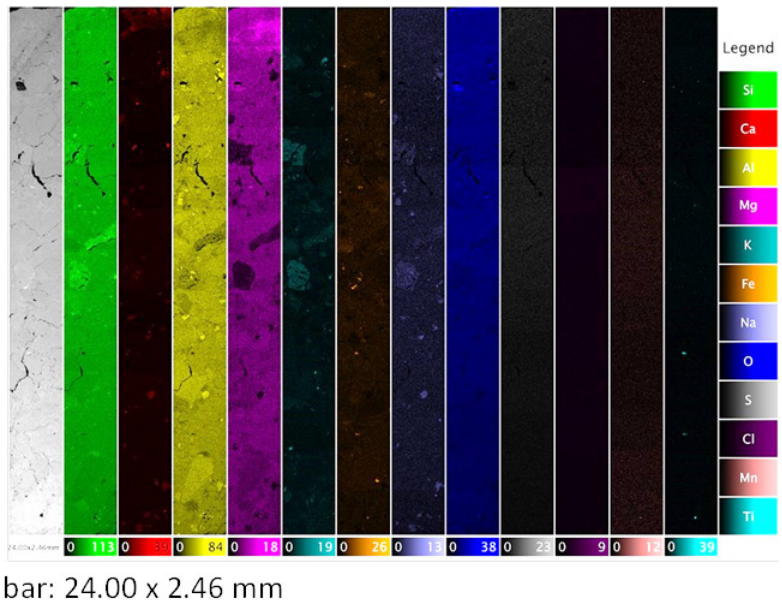

Fig. 139: Elemental map on a polished section of bentonite in sample C-C-34-12. The interface with concrete is at the top of the image.

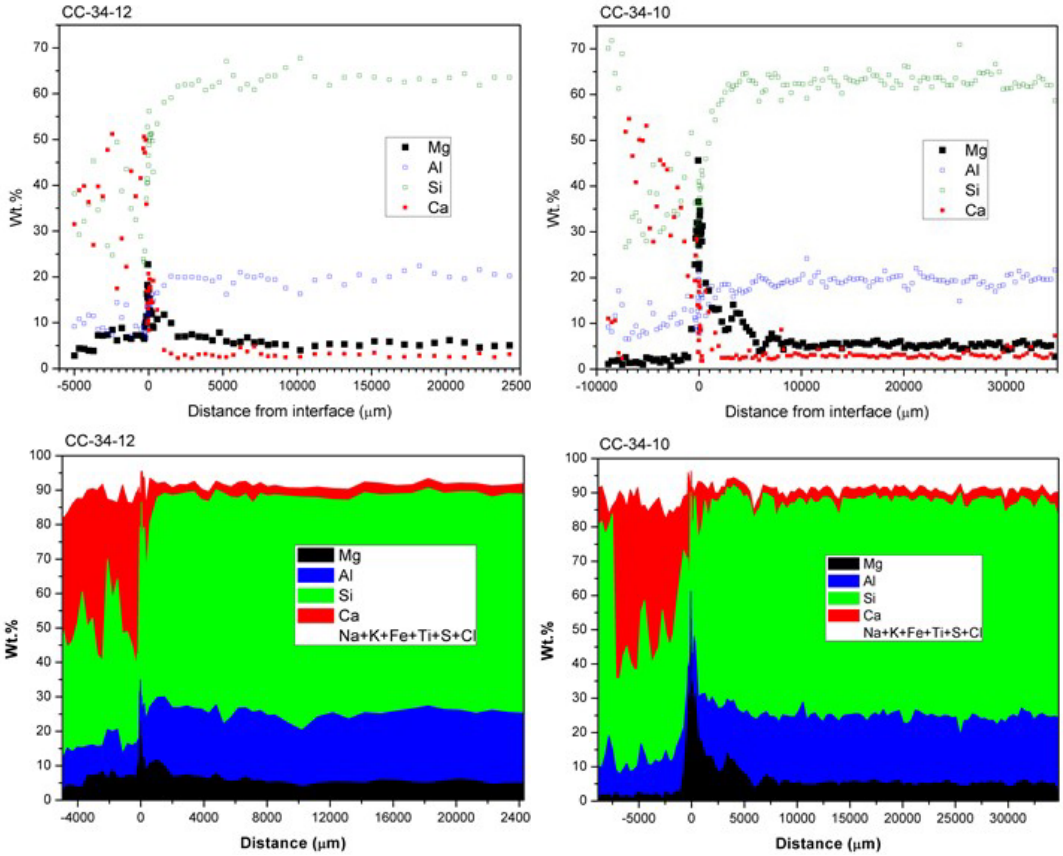

Fig. 140: Chemical profiles of compositions (in wt. %) obtained by EDX analyses on samples C-C-34-12 and C-C-34-10. Only Mg (black), Al (blue), Si (green) and Ca (red) are represented in the scatter plots, while the sum of other elements detected (white) are represented in the area graphs.

6.4.5.2 Results on sample C-C-32-6 (UniBern)

The resin-impregnated and polished sample (Fig. 141) measures ca. 100x35 mm and covers a section across the entire quarter core C-C-32-6-OC-cb-III, including ca. 50 mm of concrete and 50 mm of bentonite on either side of the interface. The BE image overlays the centre of the reflected light micrograph and represents the area investigated by SEM. The concrete area in the light micrograph seen to the left of the BE image appears relatively homogeneous, whereas the entire bentonite does not reveal any zonation parallel to the interface. SEM EDX data show that the bulk chemistry of bentonite more than 4 mm away from the interface matches the reference material (next section). Shrinkage cracks visible in the BE image as well as in reflected light follow pre-existing structures in the bentonite. They originate from the sample preparation (freeze-drying) and were filled with resin during the impregnation. Below, the chemical and porosity distribution on the concrete side (left) is presented, followed by a study of the concrete/bentonite close to the interface, and finally the bentonite side (right) is examined.

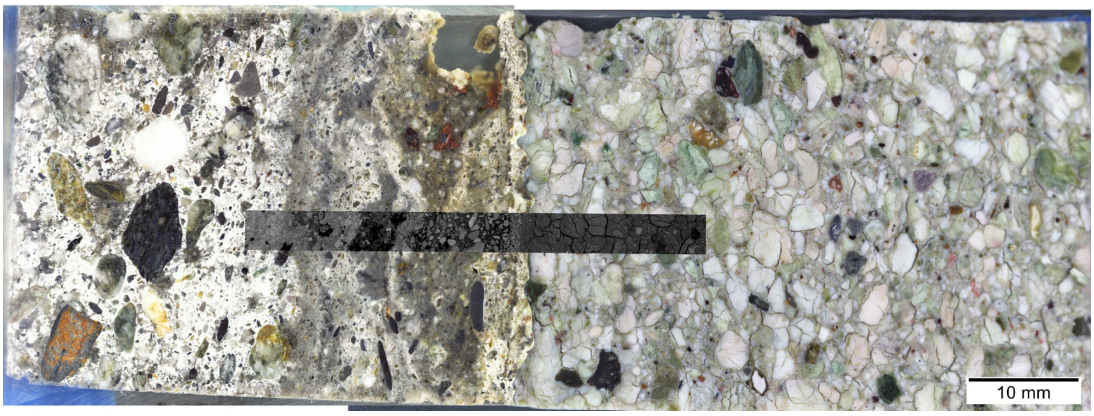

Fig. 141: Reflected light micrograph and SEM BE image (overlay in the centre) of concrete (left) and bentonite (right). Optical image is merged from to separate images for concrete and bentonite, and the interface line is therefore not a realistic representation.

The BE close-up of the *concrete side* (overlay in Fig. 142, top) reveals layering parallel to the interface. The layers differ in content and grain size (sand with approx. 0.1-1 mm diameter), in porosity (black areas representing the impregnated resin), or in content of unhydrated clinker (light grey particles <0.1 mm). The segmented carbon EDX map (Fig. 142, lower part) shows the porosity impregnated by the resin in black. Layers are characterised by the occurrence of air voids, or by different amounts of capillary porosity.

The Ca and S maps (cement matrix only, with high concentrations in light grey, porosity and aggregates segmented in black) are strongly influenced by the inhomogeneous porosity distribution. The low-Ca-low-S layer close to the interface does not coincide with high porosity and therefore reflects real depletions within the cement matrix (further explored below). Very likely, the layered structure further away from the interface originates from the method of concrete application, and not from more distant concrete/bentonite interactions.

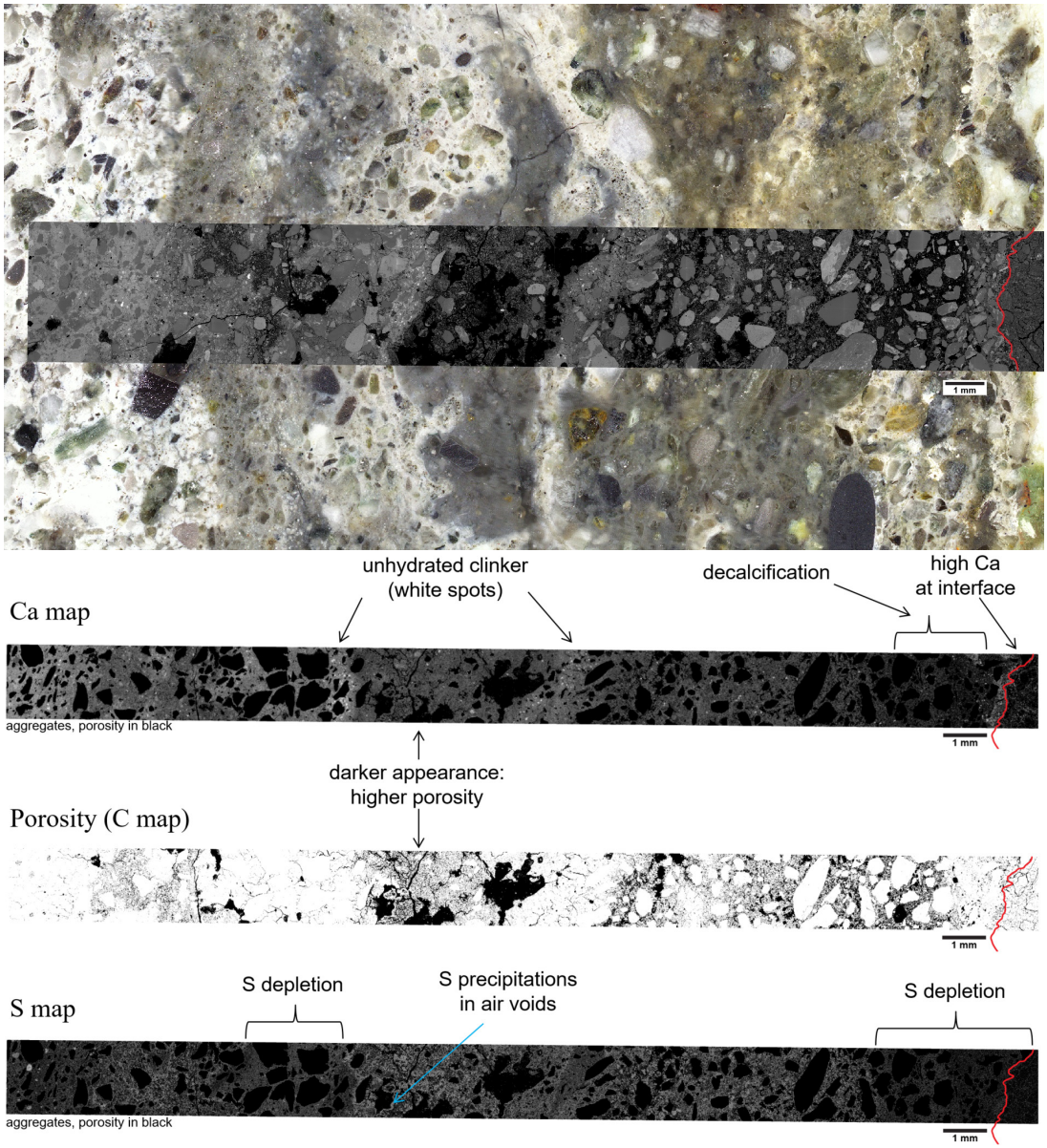

Fig. 142: Top: reflected light micrograph and SEM BE image (overlay in the centre) of shotcrete. Below: Ca and S EDX maps of cement matrix only (with high concentrations in light grey, porosity and aggregates segmented in black), and the segmented C EDX map (porosity in black, cement matrix and aggregates in white). Interface marked in red.

Fig. 143 shows element distributions in the concrete/bentonite matrices in the *interfacial region*. Ca is enriched in the cement right at the interface (approx. 200 µm), followed by a 3 mm thick layer depleted in Ca and S. Mg and Si are enriched in the area 1 mm from the interface.

Ca and Mg are enriched in the bentonite approximately 1.5 mm from the interface. The spotty Ca enrichments do not occur within bentonite grains with a white appearance in reflected light

microscopy. Considering Fe migration from corroding steel into FEBEX bentonite, Fe did not either enter the white domains (Wersin & Kober 2017). In contrast, Mg is more evenly enriched in bentonite close to the concrete: especially the first 200 µm from the interface show a layer with continuously higher Mg concentration. Further away, the Mg enrichments appear to be more affected by the heterogeneous bentonite structure.

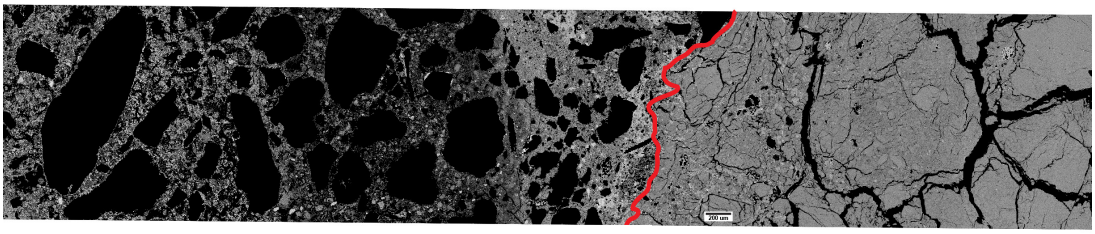

BE

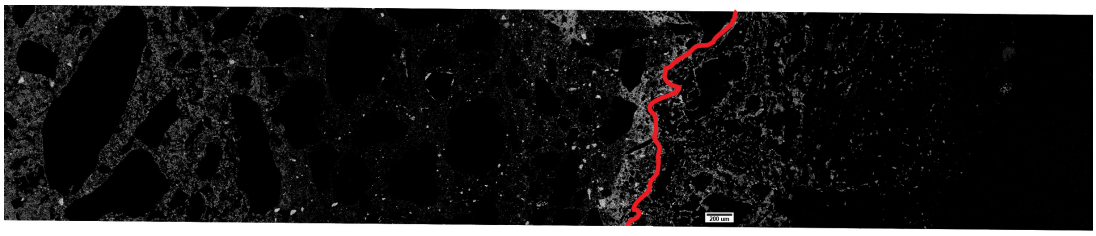

Ca

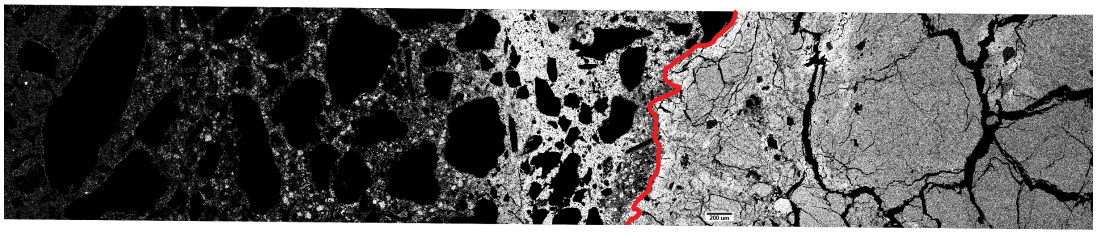

Mg

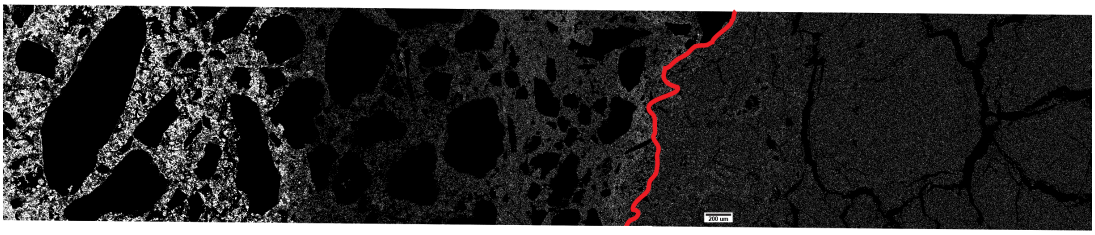

S

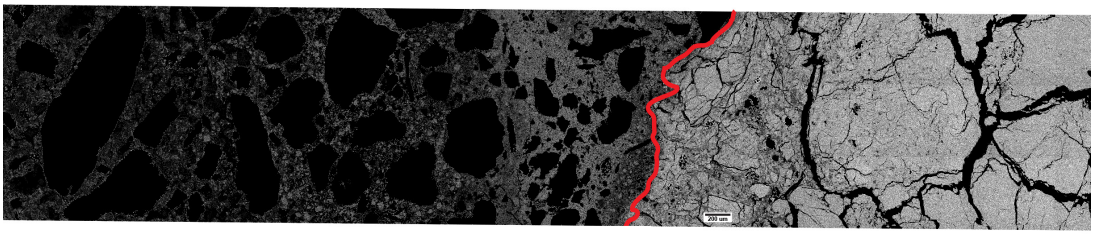

Si

Fig. 143: SEM BE image and corresponding EDX element maps of shotcrete matrix (left) and bentonite matrix (right). Porosity, aggregates, and accessory minerals are segmented in black. The interface is shown in red.

No layered structures parallel to the interface occur in the bentonite between 1.5 and 10 mm from the interface (Fig. 144). Chemical inhomogeneities seem to be controlled by the inhomogeneous structure of the bentonite, which is not fully understood at the current state. Minor variations in the content of clay minerals and amounts of submicron accessories (e.g., amorphous quartz) might explain domains with small differences in Al or K concentrations (Wersin & Kober 2017).

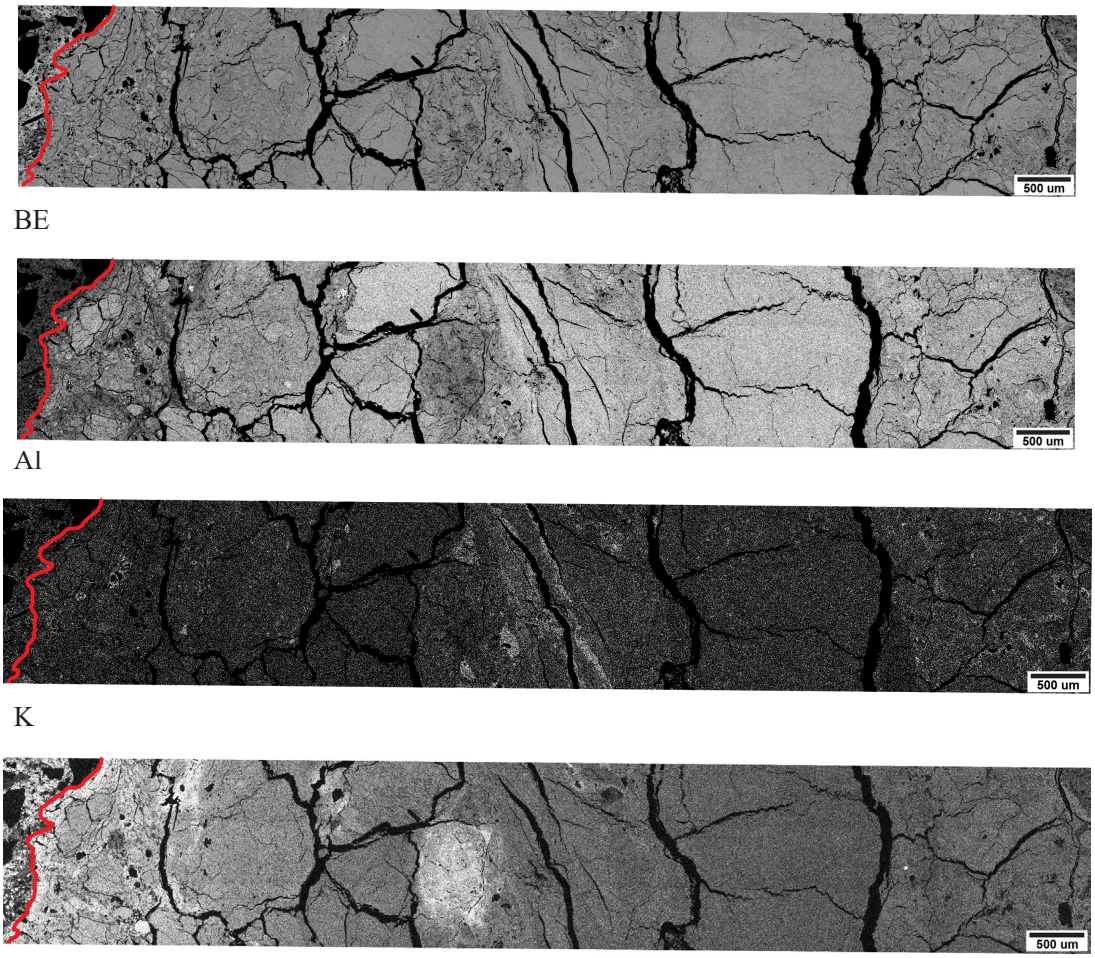

Fig. 144: SEM BE image and corresponding EDX element maps of the bentonite matrix. Porosity and accessory minerals are segmented in black. The interface is shown in red.

SEM-EDX bulk quantification of interaction layers in bentonite

The presence of multimineral aggregates makes a chemical quantification of the cement matrix in layers parallel to the interface extremely difficult. In the bentonite however, this approach quantifies the chemical inhomogeneities parallel to the interface that have been described qualitatively above.

Fig. 145 shows that the main bentonite chemistry measured more than 4 mm from the interface coincides with XRF data of the reference material (Svensson et al. 2011). Deviations in minor elements are due to the systematic error of the standardless EDX quantification approach. The Mg hump at 3-4 mm coincides with a Mg cluster (see Fig. 145) that leads to a larger lateral variability indicated by the larger range bar (an undefined Mg-silicate, possibly fine-grained diopside, also present in the reference material). Due to the relative quantification method, enrichments in Mg and Ca have to be compensated by the other major elements Si and Al, as the sum equals 100%. Such an artefact is prevented by normalising all elements to Al, which is supposed to be mainly present in clay minerals and thus quite homogeneously distributed. The resulting Fig. 146 shows a significant enrichment of Mg and Ca at the interface relative to clay, whereas the Si enrichment is in the range of the Si variability parallel to the interface. Of the minor elements, only the S enrichment is significant.

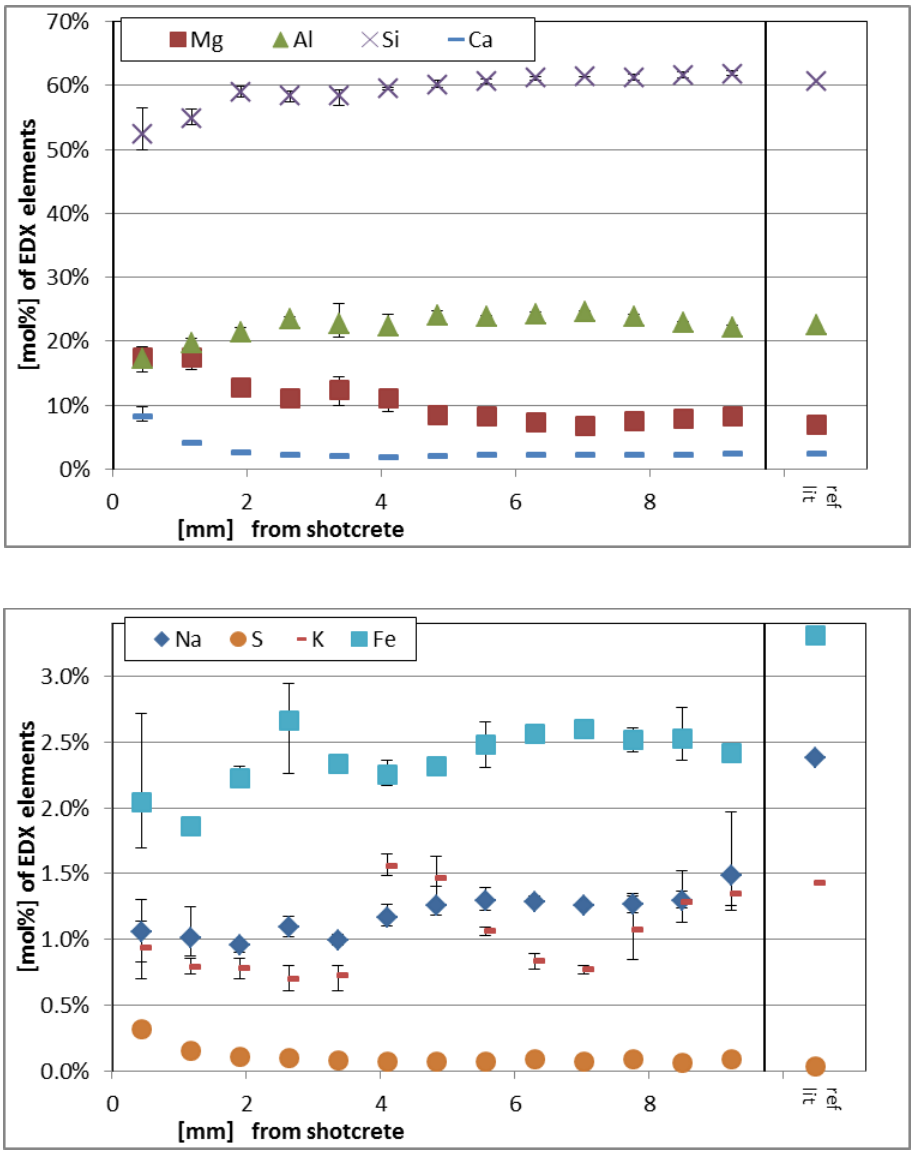

Fig. 145: SEM-EDX quantification of bentonite bulk chemistry in layers parallel to the interface, compared to XRF reference data (on right side). The bars show the range of three area-integrated measurements parallel to the interface.

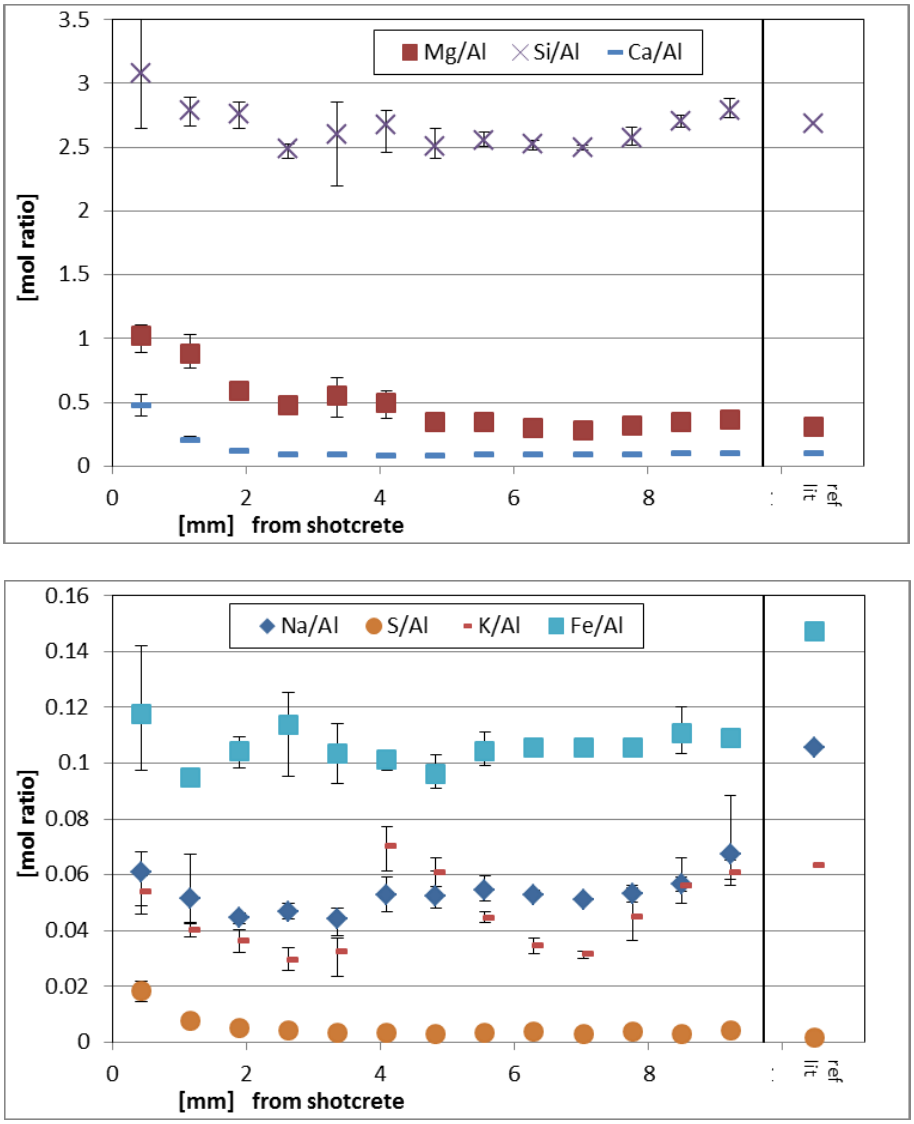

Fig. 146: SEM-EDX quantification of bentonite bulk chemistry in layers parallel to the interface plotted as Al ratios, and compared to XRF reference data (on the right side). The bars indicate the range of three measurements parallel to the interface.

Chemical line profiles across the hydrated cement and bentonite matrix

X-ray counts corresponding to the energy range of an element can be summed along lines exactly parallel to the irregular interface. Counts from concrete aggregates, unhydrated clinker, bentonite accessory minerals (>1 µm), and any porosity (>1 µm) are discarded. This approach reveals no quantitative element profiles, but relative distributions of the single elements in the cement and clay matrices at high spatial resolution (3 µm), mostly independent of one another.

The cement matrix <5 mm at the interface is significantly depleted in Ca, except for a thin crust in contact with the bentonite. At larger distance, variations in Ca are caused by the

layered shotcrete structure originating from the layerwise application. In contrast, Ca is strongly enriched in the bentonite close to the concrete. Mg is enriched in both cement and bentonite close to the interface. High Mg concentrations at ca. 4 mm distance in bentonite originate from a Mg cluster (Fig. 148) interpreted as an inhomogeneity already present in the reference material. The decalcified cement layer also shows S depletion, and the bentonite is weakly enriched in S towards the cement. The Al distribution in cement shows numerous small-scale enrichments across the entire profile. Al and Si in bentonite, the main constituents in smectite, show a pattern inverse to Mg (Fig. 147 and Fig. 148): both are depleted towards the interface, indicating most likely an absolute decrease of smectite. The Mg hump at 4 mm corresponds to low Al, but not with low Si. This can be explained by the presence of diopside ($MgCaSi_2O_6$) at the expense of smectite. Si is enriched in the cement at the interface, but shows an irregular pattern further away, similar to Ca, Fe, and K (Fig. 147 and Fig. 148). This might indicate different contents of submicron porosity in the cement matrix. Inhomogeneous Fe and K profiles in bentonite reflect inhomogeneities in the reference material. The small decrease of Na in the bentonite towards the cement might be caused by an alteration of the smectite exchanger population to more Ca and Mg.

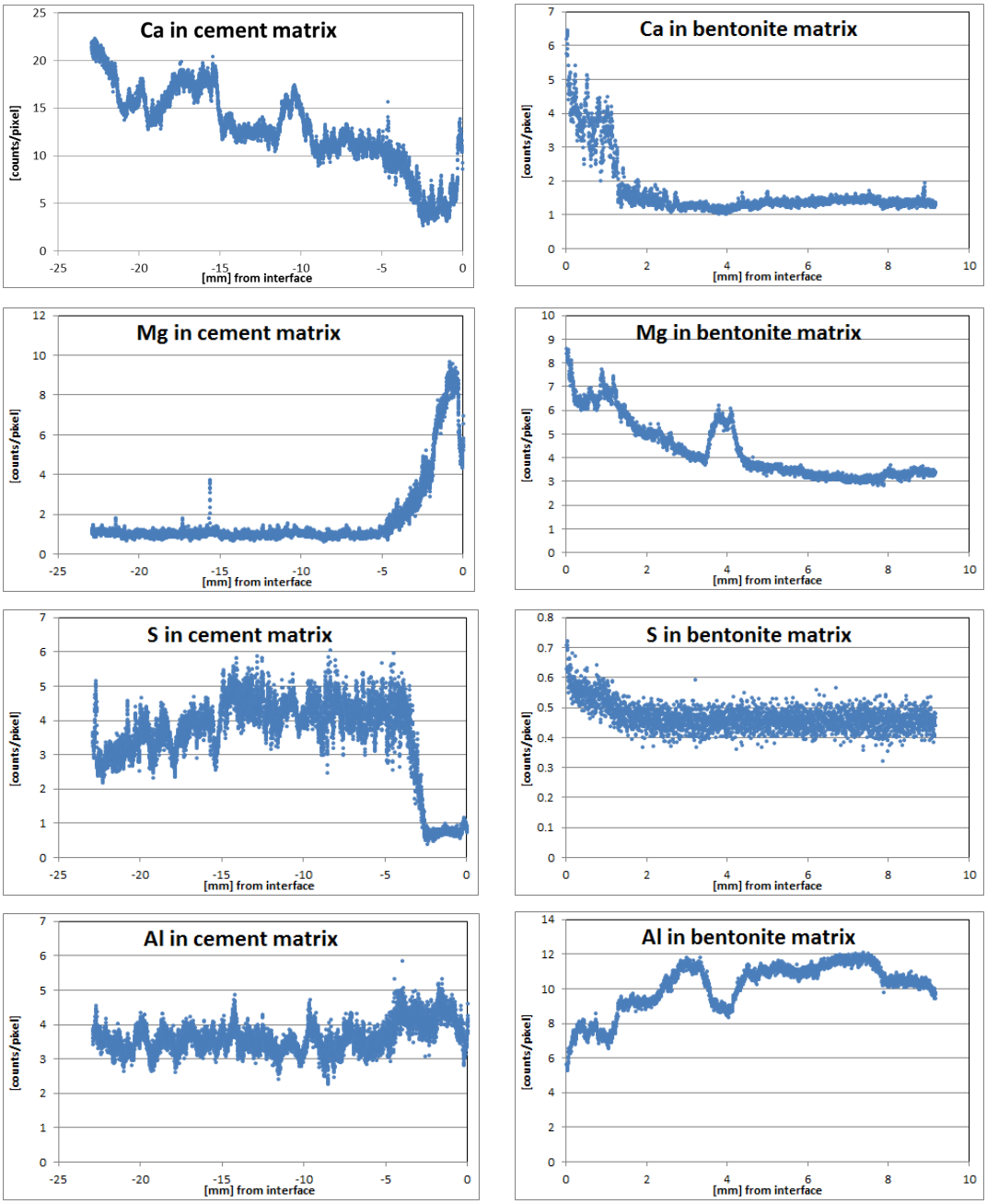

Fig. 147: SEM-EDX counts of cement/bentonite matrices in 3 µm thick layers parallel to the interface.

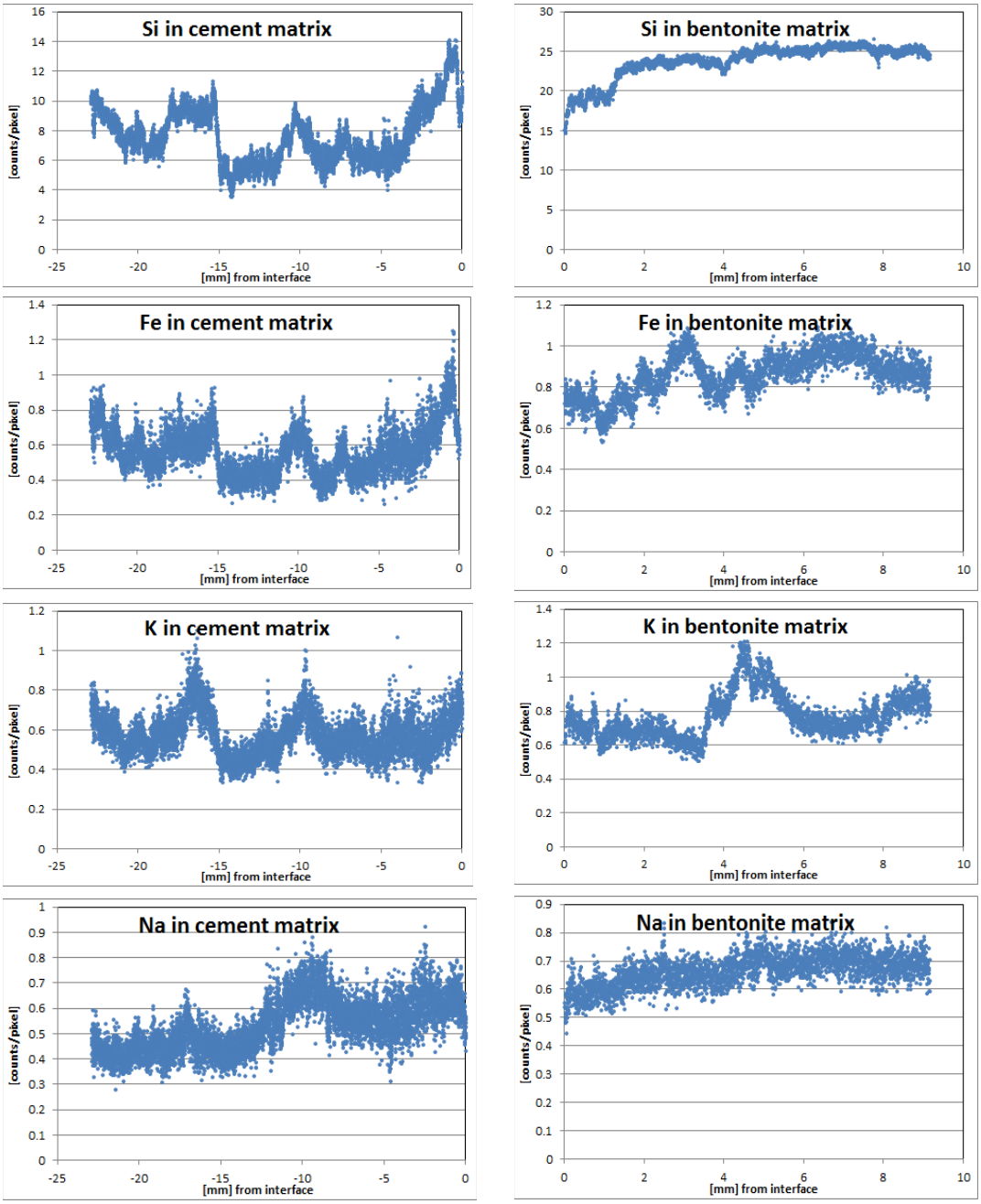

Fig. 148: SEM-EDX counts of cement/bentonite matrices in 3 µm thick layers parallel to the interface.

Discussion

The large pH gradient between the concrete and the bentonite leads to the diffusion of a high-pH front into the bentonite. It is buffered by dissolution of primarily accessory minerals, but probably also by smectite at a lower reaction rate, as well as by precipitation of secondary phases (mostly hydrates). On the cement side, the pH evolution is unclear and may be complex: as long as portlandite is present, no significant drop in pH below 12.5 can be

expected, at the condition that dissolved Ca is relatively high. Ca diffuses into the bentonite following the Ca gradient, where presumably calcite precipitates with carbonate deriving from minor calcite present in bentonite and from the infiltrating fracture water from the surrounding granite. A decrease in Ca activity and/or in pH destabilises portlandite, C-S-H (Ca-Si-hydrate), and ettringite. These processes cause the Ca depletion in the cement and the enrichment in the bentonite at the interface, commonly observed at most cement-clay interfaces.

The elevated pH in the bentonite increases the stability of Mg hydrates like brucite, hydrotalcite, or M-S-H (Mg-Si-hydrate). Such phases are expected to precipitate at the interface, which leads to a Mg-sink and a sustained Mg-gradient and thus Mg diffusion from the bentonite towards the interface and partly into the cement (see previous section 6.3 on mineralogy). Mg is readily available from the smectite exchanger sites, exchanging mainly for the incoming Ca from the cement. The large volume of anion-restricted porosity in the bentonite provides a fast pathway for diffusion ("surface diffusion", Gimmi & Kosakowski 2011), and the bentonite volume affected by the Ca-Mg exchange is expected to exceed the area investigated. This process is suggested by other experimental studies (Fernández et al. 2009; Dolder et al. 2016), as well as by reactive transport models considering diffusion in the anion-restricted porosity (Jenni et al. 2017).

The decrease in Ca activity and/or in pH in the cement at the interface destabilises ettringite (and possibly monosulphate). The mobile sulphate species migrate away from this layer, either deeper into the cement – where they re-precipitate, or into the bentonite. The only faint S enrichment observed in the bentonite at the interface might indicate that rather a low Ca activity, and not a low pH, may destabilise ettringite in the cement at the interfaces. Ca is available in the bentonite close to the interface.

The Si-depletion in the bentonite at the interface might derive from dissolution of accessory minerals (preferentially cristobalite) and/or smectite. The Al-depletion in concert with Si-depletion in the bentonite might also indicate smectite dissolution. How and in which form Si enriches in the cement at the interface is unclear.

Although the carbon content in FEBEX bentonite is lower than in most other bentonites, diffusion of carbon species from bentonite into cement and subsequent carbonation is to be expected. Due to the sample impregnation with organic resin and the poorly resolved elemental information for C of the EDX analysis, the current study does not reveal any carbon-related information – this would have to be complemented by spectroscopic methods.

Additional details, such as the thin cement layer at the very interface unaffected by Ca depletion and Mg enrichment, emphasise that the interface is a very dynamic system with strong gradients and changes in geochemical conditions during its evolution. The mechanisms, active at different stages, leave their footprints, which overlap and lead to the complex appearance of such interfaces.

6.4.5.3 Results on sample C-C-32-6 (Obayashi)

The picture of the polished surface of the sample C-C-32-6 is shown in Fig. 149. On the left, an image of the interface can be observed and on the right-hand side the dimensions of the sample are depicted. The maps of elements and the plots of the line-averaged values of Si, Al, Ca, and Mg are shown in Fig. 150; those of Fe, S, Na and K in Fig. 151.

For the bentonite part, Si, Al, Na and K show depleted values close to the interface. Fe and S are almost constant in the bentonite part. Ca and Mg show an increase near the interface. Especially the increase of Mg was quite large.

For the concrete part, Si and Ca show a large depletion between 40 mm and 70 mm. A distinction can be made between two regions: the profile within 3 mm from the interface (between 40 mm and 43 mm) and the profile between 43 mm and 70 mm. In the 3 mm from the interface, Si, Al, Ca, Mg, Na and K show an upward spike, while S exhibits depletion.

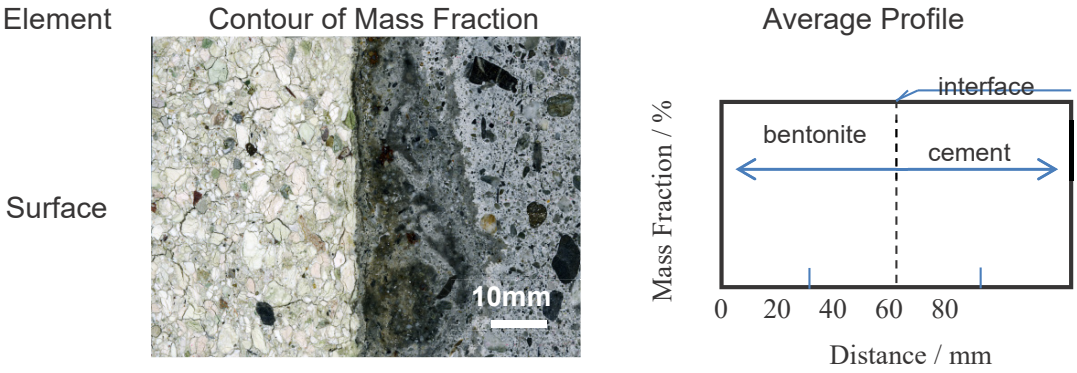

Fig. 149: Polished surface of the sample C-C-32-6 at the interface.

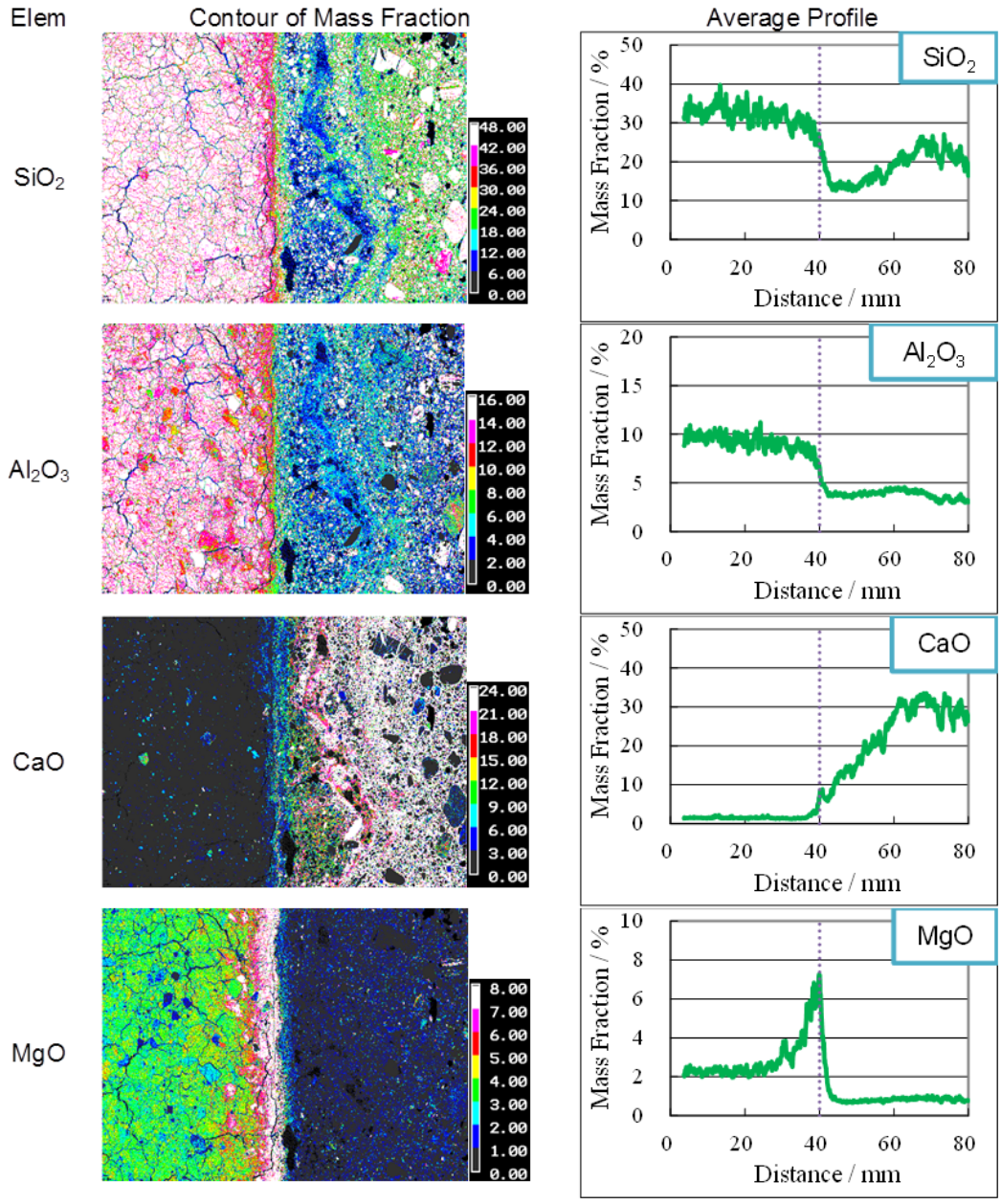

Fig. 150: Element maps and line-averaged profiles of Si, Al, Ca and Mg.

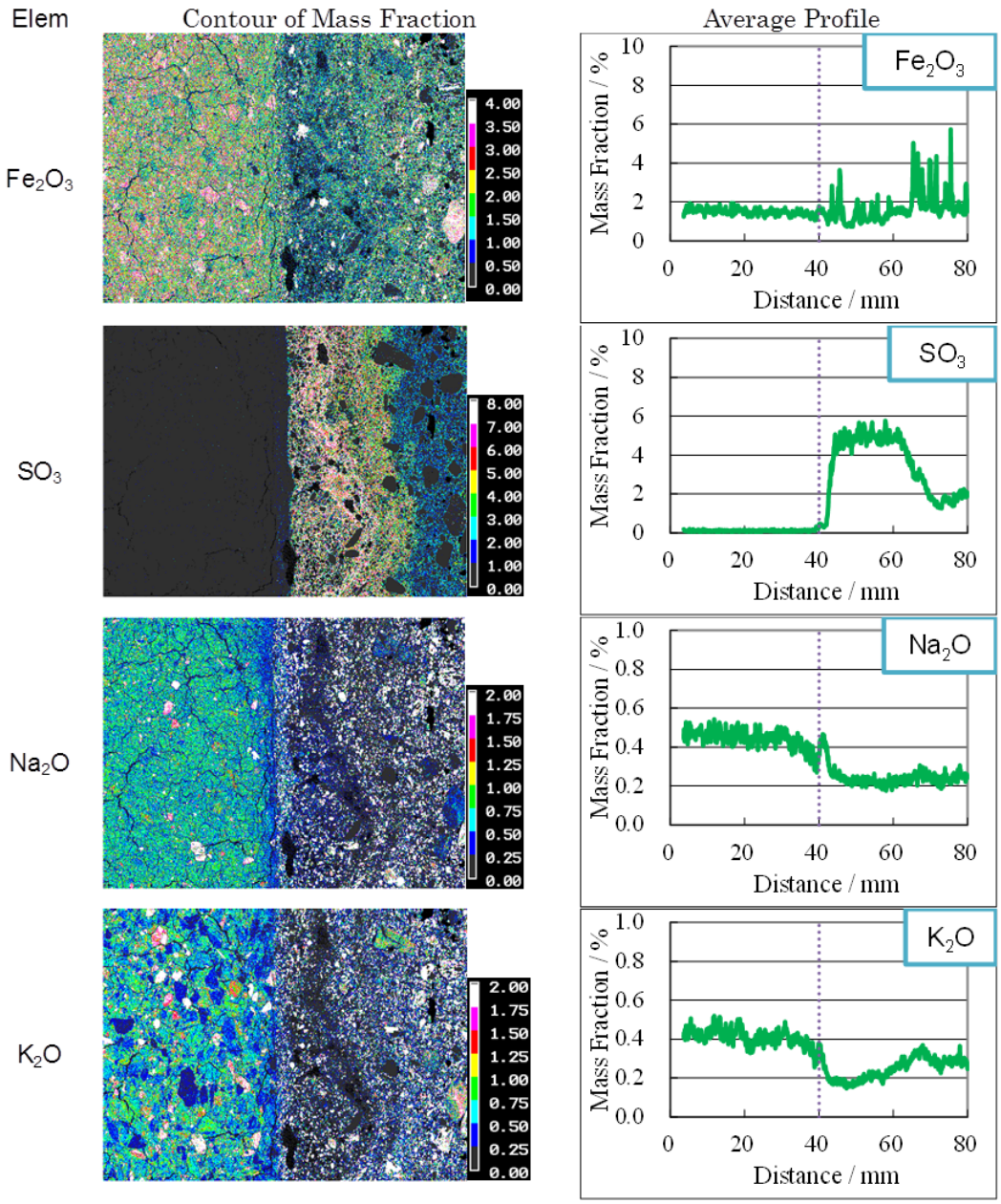

Fig. 151: Element maps and line-averaged profiles of Fe, S, Na and K.

6.4.5.4 Results on sample C-C-32-6 (Sandia)

Fig. 152 shows a BSEI micrograph and an EDS line scan of Ca across the concrete/bentonite interface. The BSEI analysis shows the granular texture of concrete with angular grains having a fairly wide size range embedded in a fine-grained matrix. The bentonite region shows cracks resembling the craquelure pattern observed in the CT imaging analysis (see section 6.2.5) along with some minor accessory grains. The purpose of the line scan and X-ray maps is to probe for elemental distributions indicative of a reactive front or mineral phase alteration along the interface region.

Ca is a ubiquitous component in many of both FEBEX bentonite and concrete phases and its overall distribution should serve as an indicator of alteration at the interface as shown in Fig. 152. The peak Ca counts observed along the line scan transect (Fig. 152) are for a grain which is presumably portlandite based on the detection of elevated Ca and O only in X-ray maps.

Based on various EDS X-ray maps and line scans, there is no indication of pervasive alteration or mineralization in the analysed interface regions. Notice that on both sides of the Ca peak in Fig. 152, elemental counts decreased to nominal levels that are comparable to both sides of the interface. This indicates little or low levels of alteration within the interface region. Other elemental profiles also show a similar behaviour across the concrete/bentonite interface. Likewise, analysis of textures using BSEI and EDS at the micron level also indicates little or no alteration along the interface.

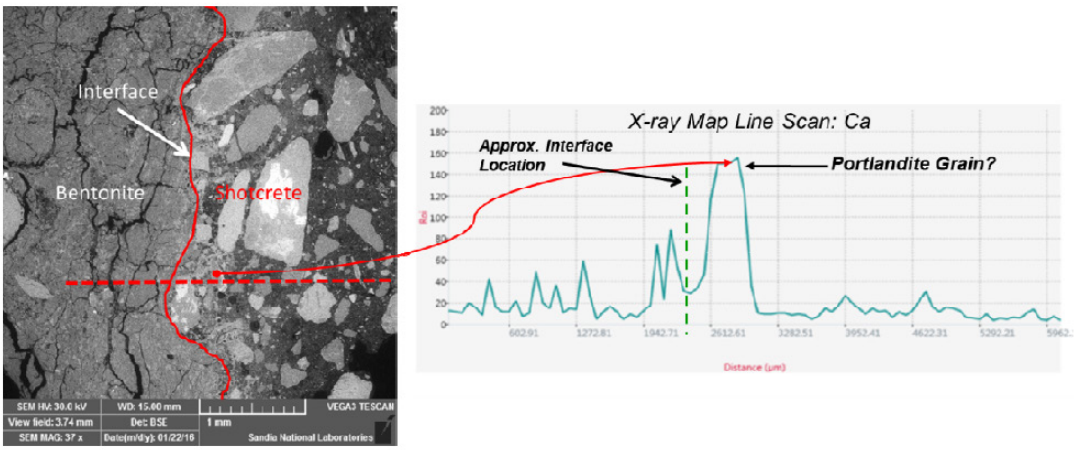

Fig. 152: BSEI with Ca element profile line scan retrieved from X-ray map of the concrete/bentonite interface region. The horizontal red-dashed line in the BSEI is an approximate position of the line scan.

Compositional analysis using micro–X-ray Fluorescence (XRF) was conducted on polished thin section of sample C-C-32-6. Micro-XRF allows for micron-scale compositional analysis but covering a larger scan area. Fig. 153 shows the energy spectrum of elements detected in the sample for which maps were generated. Fig. 154 shows micro-XRF maps for Ca and S indicating slight or virtually no alteration in the bentonite side. This observation is consistent with the SEM/EDS X-ray map analyses described previously. These Ca and S compositional maps in Fig. 154 also suggest the existence of an apparent millimeter-scale depletion zone in concrete close to the interface. The depletion zone is demarcated by some gradation from the bulk concrete towards the bentonite interface which is depicted by the Ca map. The depletion zone does not appear to traverse the bentonite side suggesting a reaction zone confined mainly to the concrete side. Further evaluation µ-XRF data maps for Ca, Si, and S using line scans appears to indicate millimeter-scale separation of depletion features within these zones (Birkholzer et al. 2017). The more detailed line scan transects show wide variations in Ca within the bulk concrete but a common feature is the appearance of a thin Ca-rich band paralell to the interface. This Ca-rich band is interpreted as leached out material from shotcrete. These observations are still part of ongoing work and are very preliminary needing further analysis of micro-XRF map data to assess spatial compositional heterogeneities.

All these observations regarding the spatial extent of reaction between concrete and bentonite are consistent with those of other investigators in the FEBEX-DP project (Turrero et al. 2016) working with similar samples. The use of micro-XRF has the advantage of minimal sample preparation and scanning sample areas from mm^2 to cm^2 at a high spatial resolution for a wide range of elements. This technique is more flexible and better suited for the specimen sizes collected from the dismantling phase activities where other microscopic techniques (e.g., SEM/EDS), although useful, would otherwise be much more laborious.

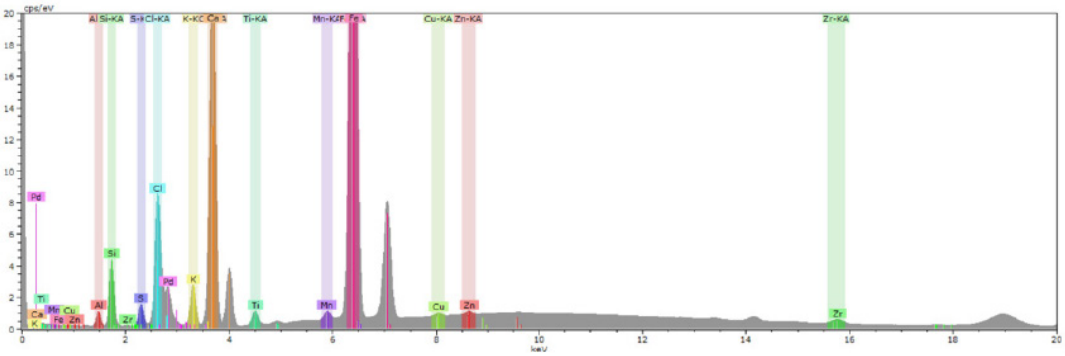

Fig. 153: Micro-XRF energy spectrum of elements detected in the concrete/bentonite thin section sample of Fig. 154.

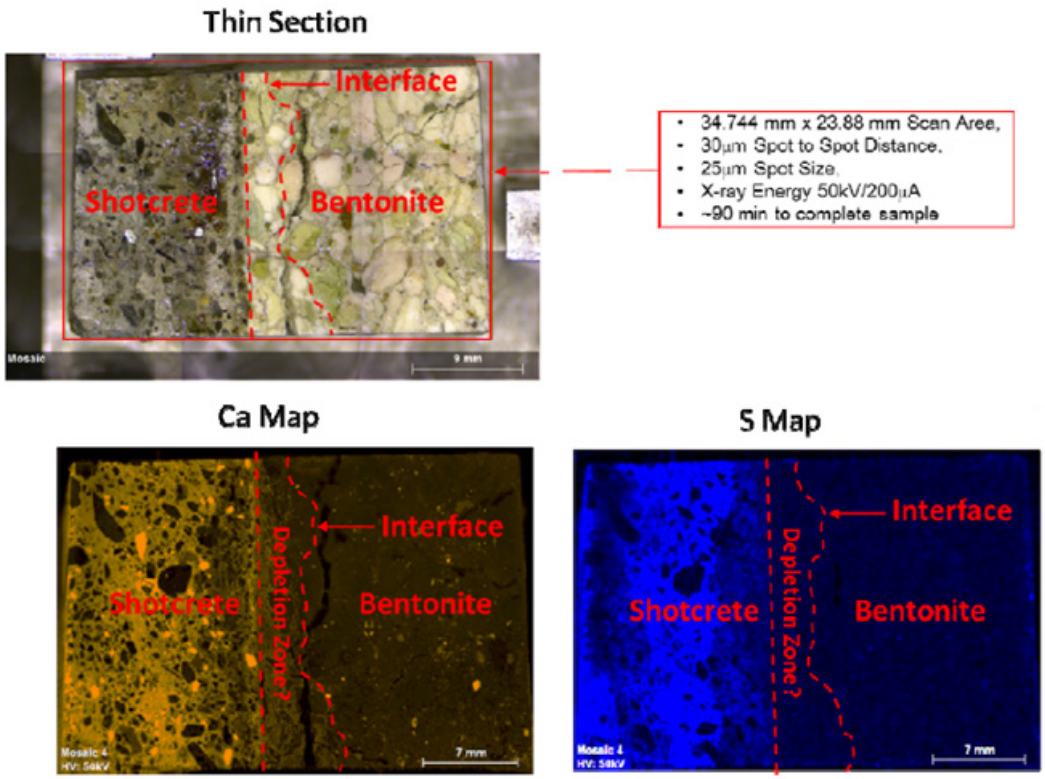

Fig. 154: Micro-XRF maps for Ca and S at the concrete/bentonite interface. An apparent depletion zone close to the concrete/bentonite interface is delineated by red-dashed lines.

6.4.5.5 Results on samples C-C-32-1 and C-C-32-3 (CSIC)

This part is just focused on the 3 cm of concrete contacting the bentonite (e.g. Fig. 155) and does not present any result on bentonite itself. Polished samples were prepared for a first observation of a piece of concrete with a stereo microscope. Fig. 155 (left) shows the bentonite (yellow) clearly differentiated from the concrete cement paste (white grey) mixed with aggregates (white and black) of different sizes. At the interface between both materials a thin white line more or less homogenously distributed along the interface is observed. Fig. 155 (right) depicts another picture in which again a white line with crystalline appearance (<1 cm) is observed.

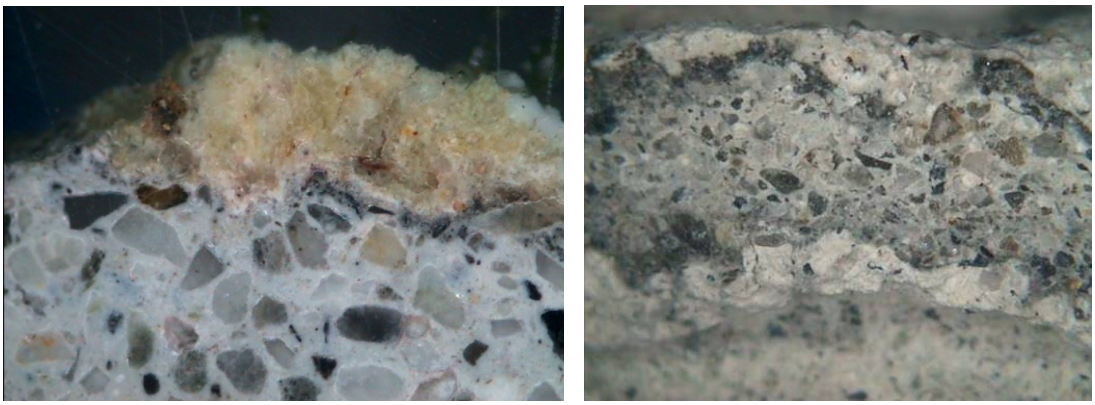

Fig. 155: Stereomicrocopic images showing an example of the concrete/bentonite interface from a fragment of 2 cm of concrete (depth from the bentonite) with some bentonite adhered.

SEM images and analyses of sections 1 and 2 of cores C-C-32-1 and 2 in those zones close to the bentonite are presented and discussed below. Detailed analyses from the interface (0 cm) up to 3 cm deep in the concrete were made, dividing the study in three sections: 0-2 mm, 0-10 mm and 10-30 mm from the interface.

Concrete at 0-2 mm from the interface with bentonite

Fig. 156 shows that the cement paste close to the bentonite is less dense than the cement paste of the core C-C-32-2 (reference). Microcracks running inside the cement paste are observed as well as crystal formation. The solid crystalline phase observed in the picture of the right side of Fig. 156 has been identified by EDS as Friedel's salt, that was also recognised by XRD (Fig. 46), confirming the diffusion of Cl from bentonite (details in section 6.4.1). The Friedel's salt does not induce microcracking and has continuity with the C-S-H phase of the cement paste.

The elemental compositions of all analyses performed in different points (green colour spots in the pictures) are represented in Fig. 156 (bottom). Bentonite containing mainly Si, Mg and variable Ca, as well as areas with high Ca content, probably associated to calcite, can be observed. The C-S-H shows large variability of Si and Ca content, mainly in the region closest to the bentonite. High contents of SO_3 and Al, the presence of Friedel's salts and ettringite are observed in different locations.

Concrete at 0-10 mm from the interface with bentonite

The SEM images of cement paste at 0-10 mm from the bentonite can be seen in Fig. 157 and Fig. 158, corresponding to cores C-C-32-1 and 3, respectively. The increase in microcracks is evident (Fig. 157A and B), together with the formation of new crystals that grow inside the concrete, as observed in Fig. 158A. Alteration of C-S-H is evident in the first cm of the concrete close to the bentonite. Low density C-S-H can be observed in Fig. 157C and Fig. 158B and C.

The elemental oxide distribution of cores C-C-32-1 and 3 (Fig. 157, Fig. 158) shows a C-S-H with zones richer in Al, S and other elements, similar to the oxide distribution in the cement paste of core C-C-32-2. Furthermore, the formation of new massive phases growing inside the cement paste (e.g. Fig. 158) corresponds to ettringite.

Different shapes and compositions of the C-S-H (dark-grey and white-grey zones in the figures) are demonstrated in the oxide analysis presented in Fig. 159. The dark-grey zone shows higher variability than the white-grey zone, but general conclusions are: 1) both zones (dark-grey and white-grey) show slight decalcification with respect to the C-S-H gels of C-C-32-2 concrete, 2) the dark-grey zone has a composition similar to the C-S-H gels of the concrete with no water interaction than the light-grey zone, 3) the white-grey zones have higher sulphate and alumina contents and remarkable lower silica contents. In fact, the composition of the white-grey zone is approaching that of ettringite.

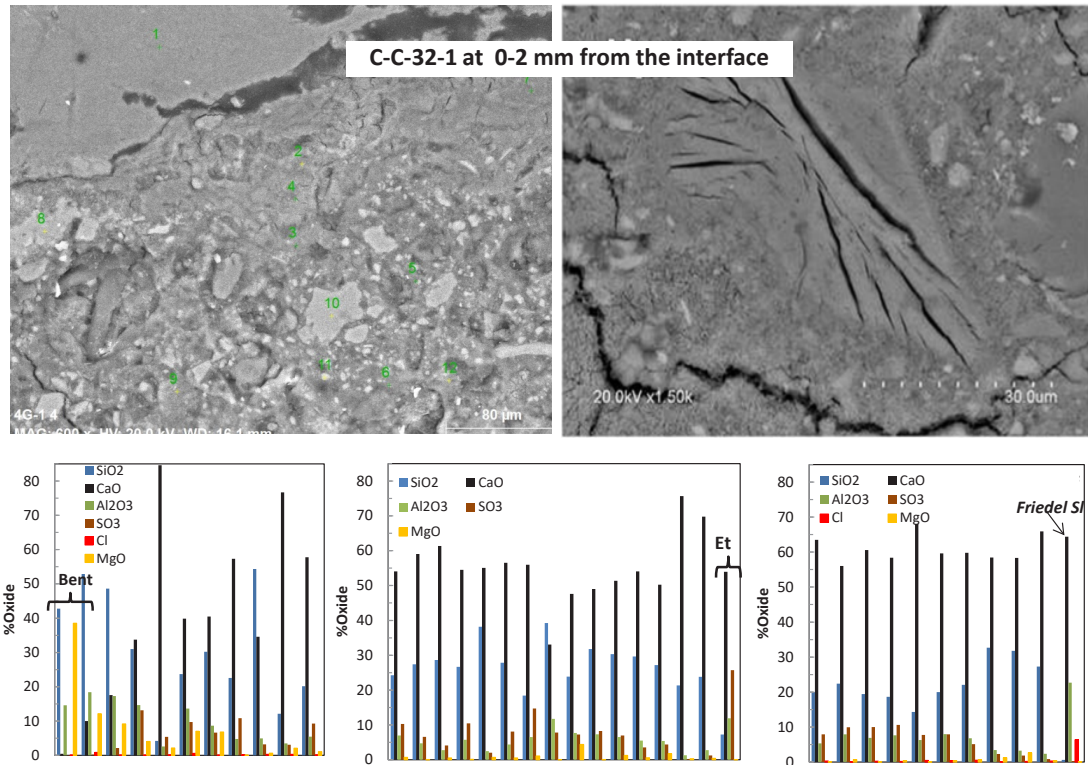

Fig. 156: BSEM images of samples of concrete from section 1 of core C-C-32-1 close to the interface with bentonite (0-2 mm). Analysis (% oxides) of C-S-H, Friedel's salt and ettringite in cement paste are shown below. Analyses correspond to green spots in the pictures.

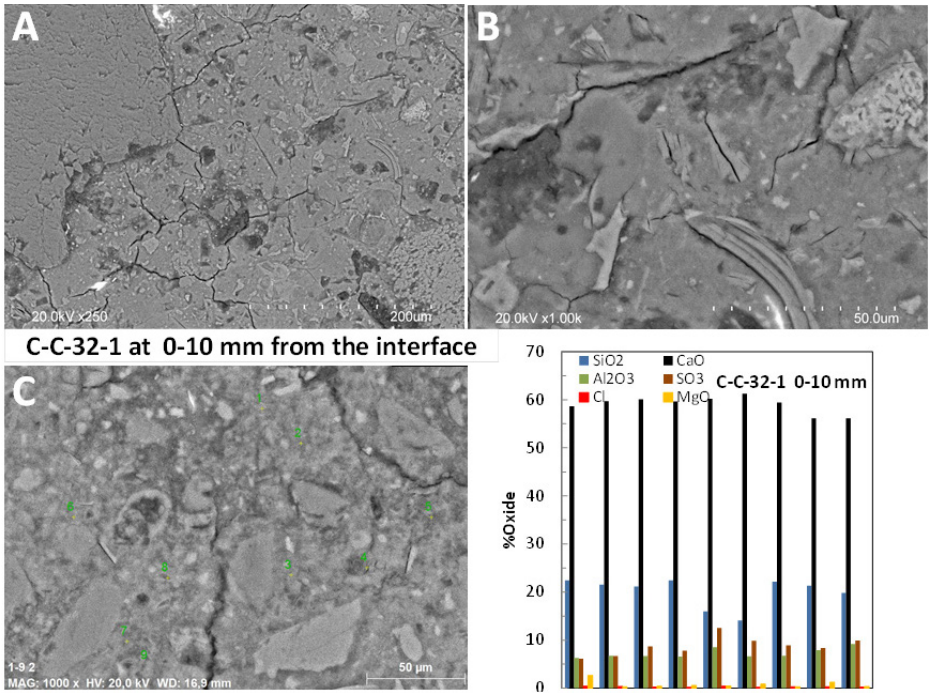

Fig. 157: BSEM images of samples of concrete from section 1 of core C-C-32-1 close to the interface with bentonite (0-10 mm). Analysis (% oxides) of C-S-H and ettringite in cement paste are shown below. Analyses correspond to green spots in the pictures.

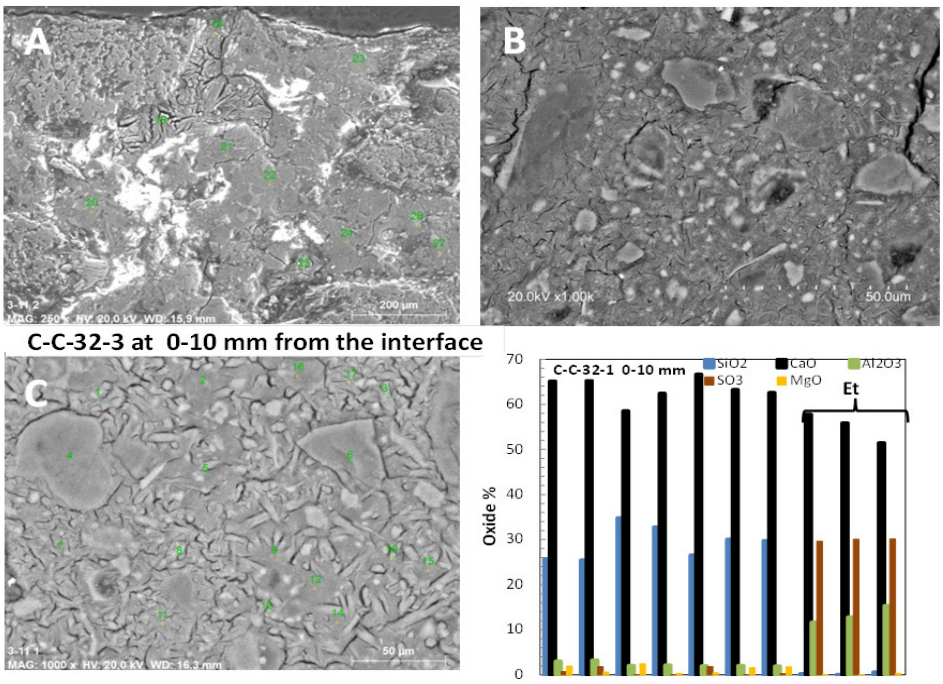

Fig. 158: BSEM images of samples of concrete from section 1 of core C-C-32-3 close to the interface with bentonite (0-10 mm). Analysis (% oxides) of C-S-H and ettringite in cement paste are shown in the bottom right. Analyses correspond to green spots in the pictures.

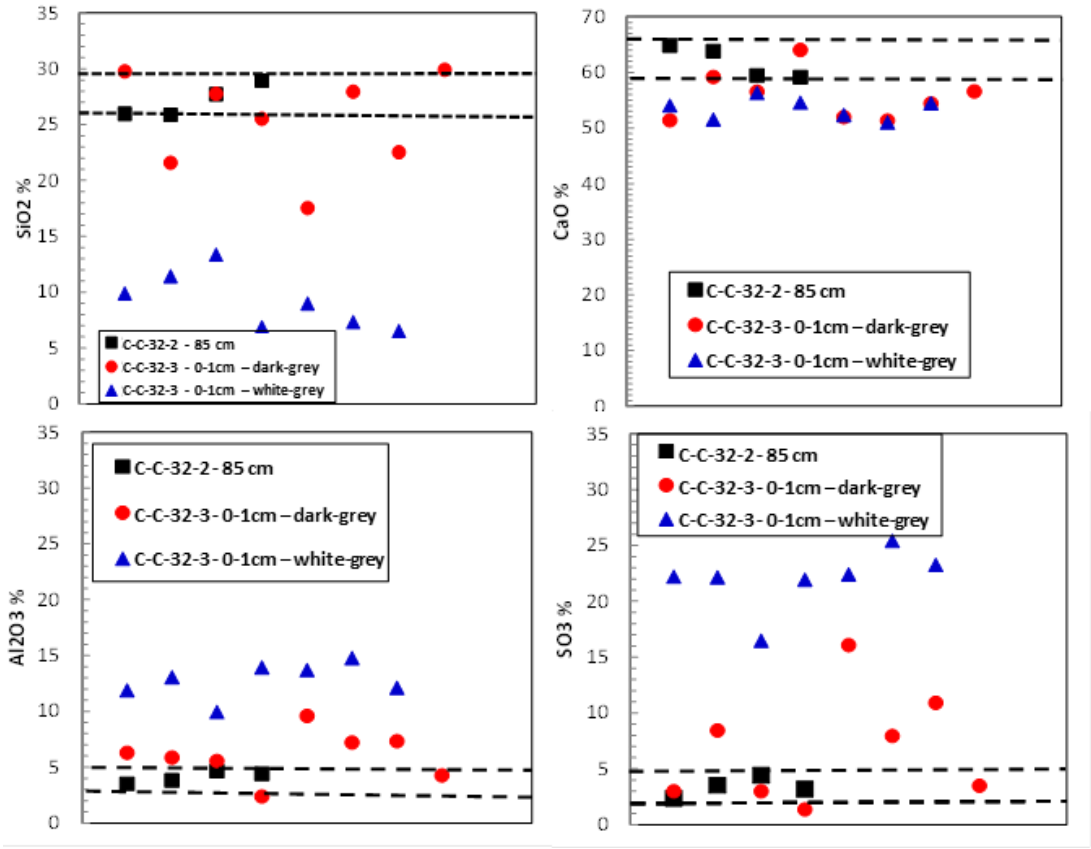

Fig. 159: % of oxide distribution in cement paste of the concrete plug near the bentonite barrier (<1cm) for cores C-C-32-2 and C-C-32-3 (dark-grey and white-grey zones).

The progressive alteration of C-S-H is detected after analysing the changes occurring in the concrete plug at different distances from the bentonite, as shown in Fig. 160. From this figure the following can be deduced: 1) the SiO_2 and CaO content progressively decrease with distance from bentonite, so that a decrease in C/S ratio is taking place, 2) incorporation of Mg in the cement paste can also occur by incorporation in C-S-H but just at the interface, 3) Al and SO_3 progressively increase with distance from bentonite, and 4) at 3 cm from the bentonite the alteration of C-S-H is not relevant.

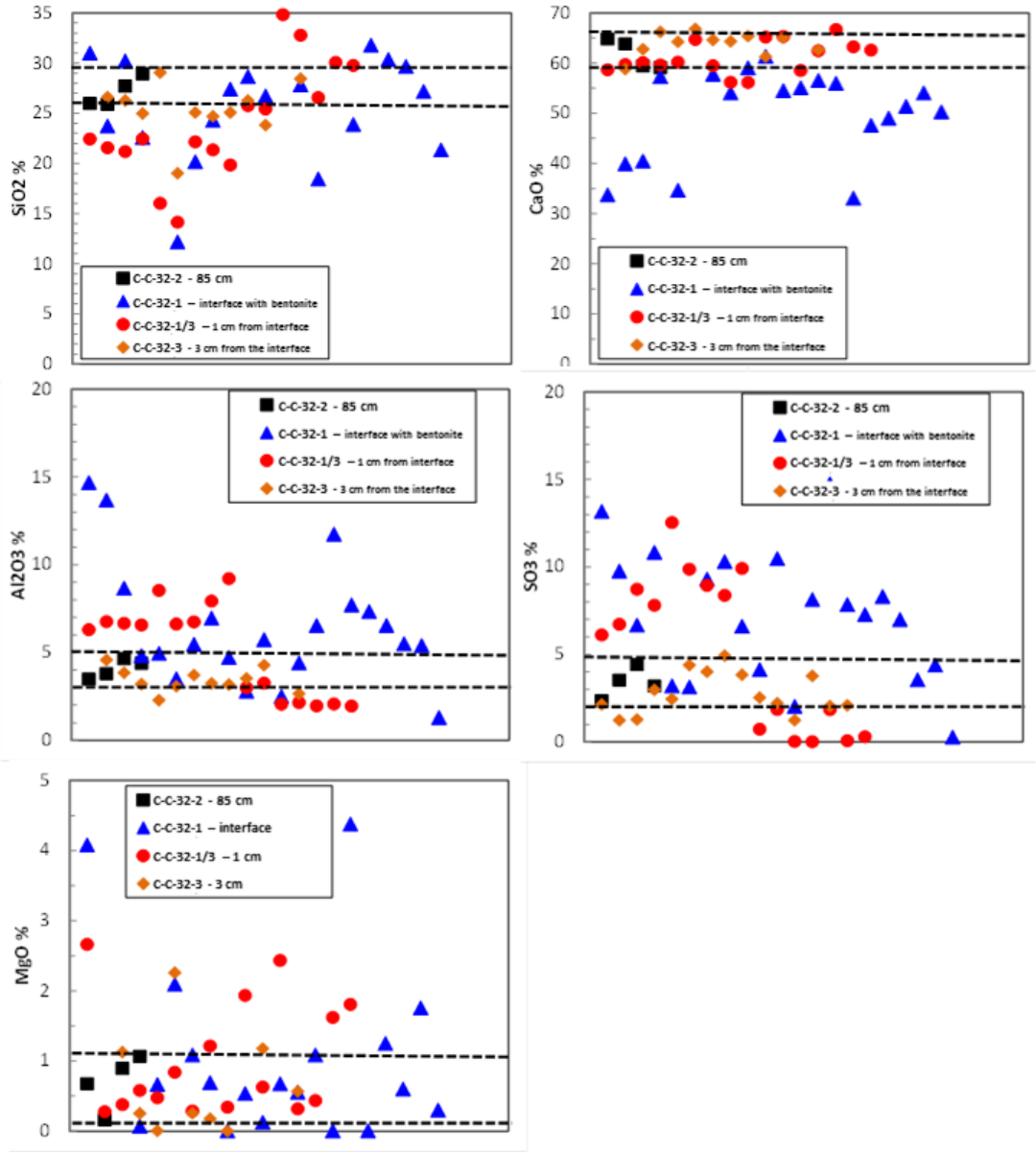

Fig. 160: % of oxide distribution in cement paste of the concrete plug at different distances from the bentonite.

A mapping of the concrete's elemental distribution in the 0-10 mm zone from the bentonite interface is presented in Fig. 161. The rich content of Mg, Si and Ca from bentonite is observed in the upper part of the figure. Accumulation of SO_3 at the interface attributed to ettringite formation near the bentonite barrier is clear from the S mapping. Many ettringite nodules are observed but a clear increase in the S content is detected near the bentonite barrier. Although small ettringite nodules can be detected, this zone shows massive ettringite formation. Deeper into the cement paste, up to 7 mm in the mapping, the S-rich nodules confirm the distribution of ettringite. Si appears dispersed in the cement paste that is rich in Ca, as elemental analyses have confirmed. Mg is mainly present in the bentonite, although in local points of the cement paste it is also observed. It should be noted that some aggregates

also contain Mg which may interfere in the observation and distribution of this element in cement paste.

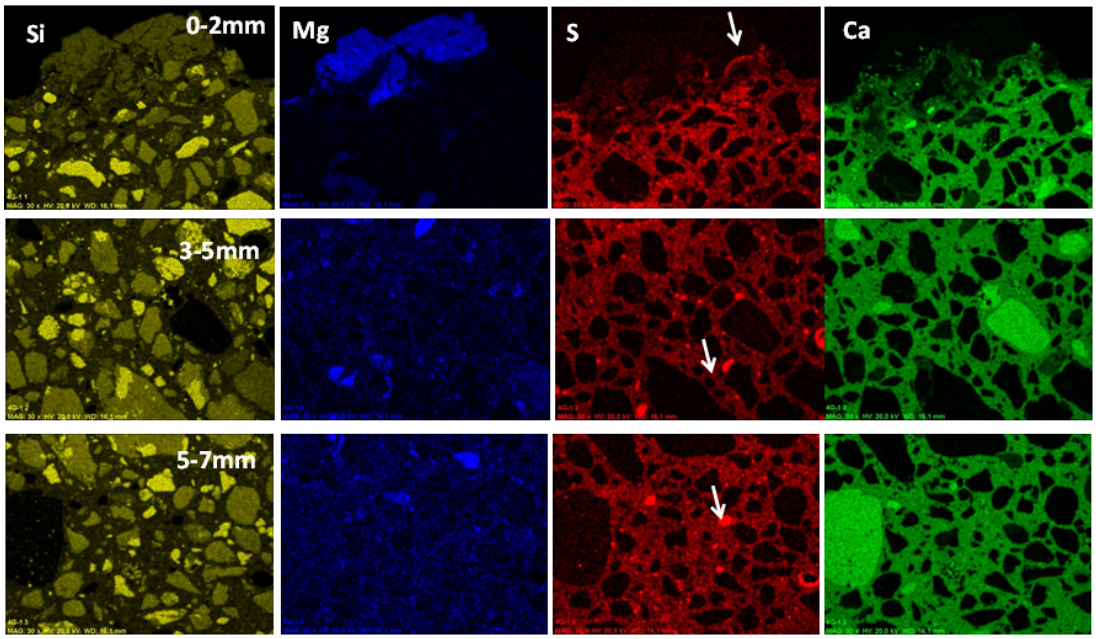

Fig. 161: Mapping of main elements analysed in the concrete from section 1 of core C-C-32-1 close to the interface with the bentonite (0-10 mm).

Concrete at 10-30 mm from the interface with bentonite

Polished samples at distances of 10-30 mm from the interfaces show steel fibres inside the concrete (Fig. 162). The brown colour precipitated at the steel fibre-concrete interface is iron oxide formed by corrosion of the steel fibres as a consequence of the chlorides that have diffused inside the concrete. No microcracks have been found associated to the expansive volume of this iron oxide.

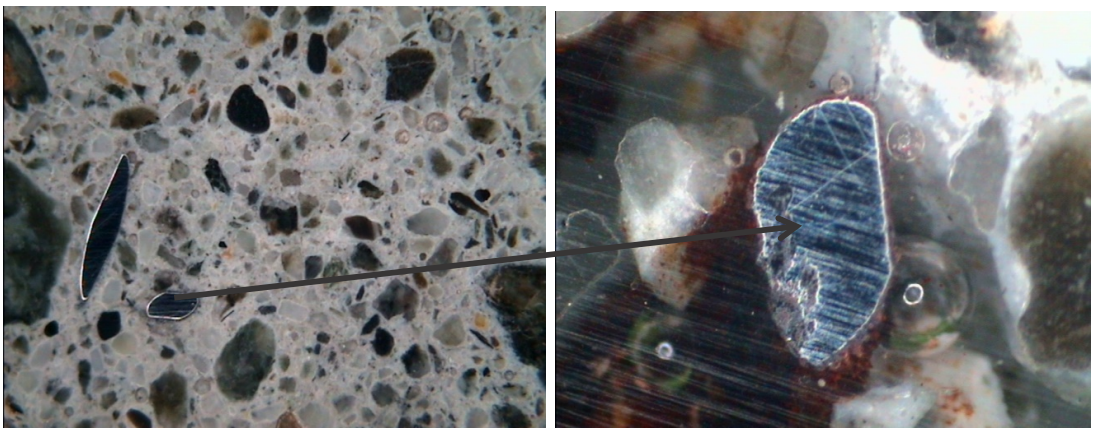

Fig. 162: Stereomicroscopic image of concrete at 1-3 cm from the bentonite. Steel fiber.

The steel fibre-cement paste interface is shown clearly in Fig. 163A. Microcracking is randomly distributed inside the cement paste. The presence of polypropylene fibres is observed in Fig. 163B. The polypropylene fibres-cement paste interface is not as clearly observed as steel fibres' contact. This is mainly due to the hydrophobic treatment usually applied to this type of fibres to favour the homogenous distribution inside the concrete. Some microcracks grow from this type of fibre towards the cement paste. Fig. 163C depicts the typical nodules of ettringite filling air pores. At these distances the cement paste has recovered its initial density and aspect compared to that of core C-C-32-2, used as reference.

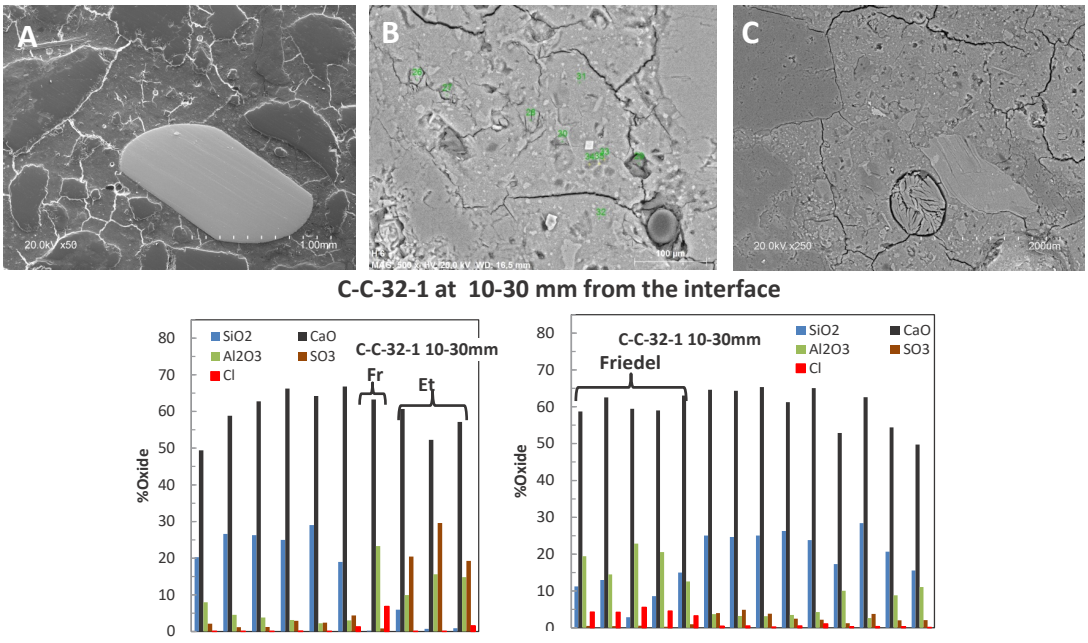

Fig. 163: BSEM images of samples of concrete from section 1 of core C-C-32-1 close to the interface with the bentonite (10-30 mm). Analysis (% oxides) of C-S-H, Friedel's salt and ettringite in cement paste are shown below. Analyses correspond to green spots in the pictures.

In the elemental distribution in this region (Fig. 163 bottom) the presence of ettringite in the nodules and Friedel's salts in some local zones stands out, both are also detected by XRD (Fig. 46). The C-S-H shows quite a homogenous distribution in Si and Ca and also contains minor proportions of Al and S (less than 5%).

A mapping of elemental distribution of the concrete 10-30 mm from the bentonite interface is presented in Fig. 164. The Ca (green) and Si (yellow) are very homogenously distributed in the cement paste, although aggregates that contain Si disturb the observation of this element in the cement paste. Mg (blue) is present in some local parts and in some aggregates. Concerning S, although it is visible everywhere in the cement paste it is enriched in some clear local zones (red) that typically correspond to ettringite filling nodules in this concrete. These nodules are initially present in the concrete and are not a consequence of concrete ageing in the Grimsel environment.

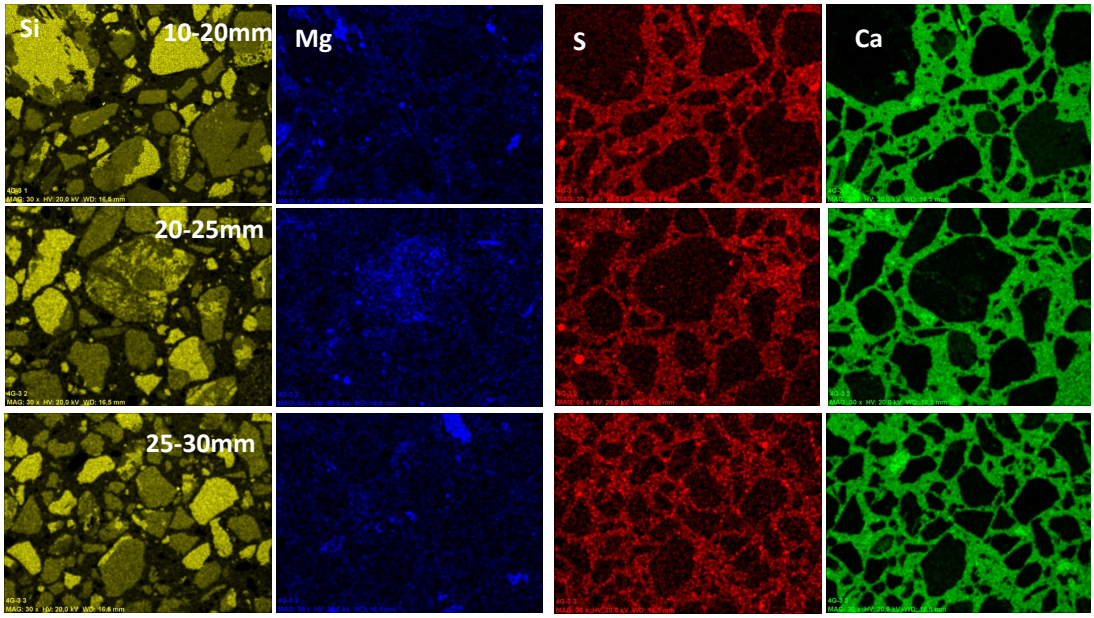

Fig. 164: Mapping of the main elements analysed in the concrete from section 1 of core C-C-32-1 close to the interface with bentonite (10-30 mm).

6.5 Discussion of the concrete/bentonite analysis (all)

Both concrete and bentonite are materials considered for designing deep geological repositories to store high level radioactive waste. A number of in-situ tests in different geological formations have been performed (Gaboreau et al. 2012; Gaboreau et al. 2011; Jenni et al. 2014; Techer et al. 2012; Tinseau et al. 2006; Dauzères et al. 2016; Moyce et al. 2014; Watson et al. 2012) to test these barriers under the most realistic conditions. In-situ experiments can then offer information and constraints for modelling tasks which allow assessing the performance of the barrier system.

Dismantling of the long-term FEBEX experiment has provided a unique opportunity of studying the concrete/bentonite interface of an in-situ experiment after 13 years of interaction. The objective was obtaining evidence on those processes that could affect the performance of the engineered barrier system. The results of the characterisation of the concrete/bentonite interaction by different institutions (Autonomous University of Madrid (UAM, Spain), the Federal Institute for Geosciences and Natural Resources (BGR, Germany), Obayashi (Japan), Sandia National Laboratory (U.S. Department of Energy, USA), the Spanish National Research Council (Eduardo Torroja Institute, CSIC-IETcc, Spain), the Spanish Research Centre for Energy Environment and Technology (Ciemat, Spain) and the University of Bern (Switzerland)) are presented in this chapter. This section summarises and discusses the evidence of perturbations that occurred in the barrier system through interaction with concrete. It provides some considerations on sampling methods and macroscopic observations, and presents the main findings at the scale of the interface.

6.5.1 Sampling considerations and macroscopic observations

The sampling of the concrete plug-bentonite interface has allowed to nicely picture the processes occurring at the interface. Overcores (Mäder et al. 2016) gave the best preserved concrete/bentonite interface and were very useful for image-based analysis techniques (e.g. CT, EPMA, XRF or SEM-EDX). Furthermore, overcores allowed a precise macroscopic description of the main features, which in fact is very valuable for further interpretation. Samples taken by dry drilling and hand-picked samples did not have such nicely preserved interfaces in most cases, but were very useful for physical, chemical and mineralogical investigations. It is worth to mention that the dry drilled and hand-picked samples with the best preserved interfaces allowed to add information for elemental mapping and microstructural analysis, at least in three distinct locations with respect to the overcore. Moreover, it gave quite a complete picture of what is occurring at the interface level in relation to other components or interfaces (e.g. granite or dummy). Furthermore, those samples could be analysed almost immediately after collection, considered important for avoiding further perturbations (e.g. homogeneization of chemical gradients). The sum of overcore, drill cores and hand-picked samples provided a good distribution of samples covering a large part of the plug. It has been shown to be a major challenge to observe the influence in the proximity of granite or the dummy/liner at the interface level. Finally, the analysis of the concrete and the interface have also revealed heterogeneities depending on the position of the samples, observing differences between the upper and the lower half of the concrete plug.

It should be noted also that being present for sampling when experiments are dismantled is important. This allowed observation on a large scale to assess the homogeneity of the experiment at any level before analysis. It also permitted taking decisions on an ad-hoc basis, as was the case, for example, of the water outflow close to sample CC-34-12. As a consequence of this leaking, it was impossible to take the sample initially planned (CC-34-04) because it crumbled too easily, so that the mentioned CC-34-12 sample, very close to the other but in an “unaltered” zone, was taken. Furthermore, the water leaking was sampled and allowed obtaining the chemical composition for comparison with granite water and pore water of the bentonite. This was interesting to understand geochemical processes and for future modelling purposes. The same situation occurred when trying to obtain samples in areas close to the granite. In those zones concrete was also altered and easily disaggregated.

At a smaller scale, from the macroscopic observations of the overcores (UniBern), it can be seen that the concrete has a layered aspect. This is a consequence of the application method (shotcreting technique). The concrete contains steel fibres randomly distributed. There is a faint brownish discoloration of the concrete part next to the bentonite assumed to be related to the presence of bentonite and the resultant geochemical interactions. There is also a very faint lighter-coloured zone, ca. 12 mm wide, of the bentonite adjacent to the concrete. A very thin (<1 mm) light-coloured irregular skin is observed just at the interface on the bentonite side. The interface itself appears to be physically very well preserved in the overcores, without any obvious fractures or joints. These first observations related to the extension of the alteration in the concrete/bentonite interaction zone, fit fairly well with that obtained from the detailed analysis of concrete and bentonite.

6.5.2 Physical properties and microstructure

Water content and dry density were measured in bentonite at different distances from the granite wall. The water content was always above the original one and the dry density was lower. A detailed discussion on data was reported in NAB16-17 (Villar 2017). The water

content decreases from the granite towards the inner part of the barrier whereas the dry density increases. However, there is a slight increase of water content and decrease of dry density in those samples close to the dummy (central axis of the gallery). A water spill occurred during dry drilling of cores to obtain samples of the concrete/bentonite interface. The spill was located almost at the contact with the dummy, wich could explain the slight increase of water content and decrease of dry density just in those points closest to the dummy.

The swelling strain values measured in bentonite close to the concrete are a 1% lower than the values expected for the reference sample with the same initial state in terms of dry density and water content. However, for the rest of the samples tested, not affected by interfaces, the decrease in swelling capacity with respect to the theoretical one was even higher. A detailed discussion on data was reported in NAB16-24 (Villar et al. 2018). Hence, it is considered that the concrete interface had no effect on the swelling capacity of the bentonite.

The pore size distribution of the bentonite measured by CIEMAT with the MIP technique indicated a bimodal distribution quite typical of the FEBEX bentonite (Villar 2017), as well as the percentage of each type of pores: 27 ± 9 % macropores, 21 ± 1 % mesopores, and 53 ± 8 % micropores. The macropores' size increases towards the granite and also in the vicinity of the concrete interface, from 21 ± 3 μm (1-5 cm from the concrete) to 71 ± 30 μm just at the interface. These values are higher than those of untreated bentonite (17 ± 3 μm). The mesopores size is 13 ± 3 nm in any position, and is also higher than the untreated bentonite (9 ± 2 nm). Computerized tomography was used by Sandia Lab and UniBern to study the microstructure and the pore network on the undisturbed C-C-32-6 sample. This technique covers a larger scale than MIP and the analyses showed the common occurrence of microcracks in bentonite and pores (no cracks) in concrete. In bentonite, gaping cracks and pores tend to form near or at the concrete/bentonite interface, whereas in other cases these are found at the interface of dissimilar materials. Crack formation is not only restricted to areas close to material interfaces but are also common to bulk bentonite regions. The cracks have nominal apertures ranging from a few hundred microns up to about a millimetre for large cracks. Connected crack lengths can extend to length distances exceeding 1000 microns, in some cases evolving to or terminating into large pores. The network of fractures could be artefacts due to sample storage. Dehydration may not necessarily be significant, but unloading and some minor shrinkage does result in these obvious features. The observations agree fairly well with the data obtained by MIP, since a noticeable percentage of macropores is found, up to 38% in some cases in samples close to the interface. The increase of pore sizes with respect to the original can be due to the increase of water content but also to the unloading and shrinkage phenomena in the case of the interface.

Specific surface area measured by UAM and CIEMAT (BET method) in the bentonite was slightly lower than the FEBEX reference value but increases at 1-2 mm from the interface. The mineralogy showed the precipitation of M-S-H and calcite just at the interface that are probably related to this increase in specific surface area.

The pore size distribution of the concrete side of the samples measured by CIEMAT (MIP) is bimodal as well, with a population of macropores, corresponding to inter-aggregate pores (> 50 nm), and a population of mesopores (2.5-50 nm), corresponding to intra-aggregate pores, which would include small (gel) capillaries (2.5-10 nm). The samples to distances > 20 mm from the interface with the bentonite has a mode 9 ± 3 nm which would correspond to the typical sizes of the space between the C-S-H particles (gel capillaries), while in the other samples the mode is 43 ± 6 nm, quite close to the mode of macropores. Computerized tomography analysis indicated that the concrete texture tends to be more regular than bentonite texture with granular material embedded in a fine-grained matrix with dark spots

interpreted as circular shaped pores/voids having a wide size range. The shapes and sizes of these pores/voids, which are quite irregularly distributed, as well as the apparent lack of secondary solid precipitation suggests these are the result of entrapped air during the concrete emplacement. These voids, which may have some tens of microns were also observed by SEM in some of the samples analysed and would correspond to macropores quantified by MIP.

Minimum specific surface area values are approximately 2 mm before the interface and tend to increase at the interface. This result would agree with the presence of pores around 9 nm in the zones closest to the interface, which usually correspond to the typical sizes of the space between the C-S-H particles.

Morphological and structural changes in smectite were checked on sample C-C-32-6 using Atomic Force Microscopy and no changes in the smectite crystal sizes have occurred. However, since measurements were made on one single sample, further analyses are recommended to assess it.

6.5.3 Geochemical evolution of the concrete/bentonite interface

Pore water composition

The analyses of the soluble salt content of both concrete and bentonite were performed by aqueous extracts by CIEMAT on samples at different locations in the plug. Therefore, CSIC and UAM made some analysis of concrete samples close to the granite and/or to the bentonite barrier. Overall, there is a decrease in the ionic content of the bentonite when compared to the FEBEX reference although the decrease is greater in the external parts of the barrier, i.e. closer to the granite. This decrease is especially significant in the case of the chloride content, which becomes an order of magnitude lower in the first 5 cm of bentonite analysed close to the concrete. Ion concentration at this stage in this bentonite section is mainly governed by hydration and the granite boundary has become the preferred pathway for leaching and soluble salt transport. The ionic concentration in the concrete is dominated by diffusion towards less concentrated areas. Thus, chloride diffuses into the concrete plug and Friedel's salt precipitates on the concrete side of the interface; XRD, SEM and chemical analyses support the presence of this salt in the concrete. However, such low chloride content in the bentonite could only be explained if there has been a migration of salts towards the heater located 1.9 m from the interface, already suggested by Villar (2017) from the analyses of section 36, which is the first section of bentonite in contact with the plug.

Near the liner-dummy ionic contents are closer to those of the reference bentonite or even sometimes higher, as in the case of sulphate. This may be due to the influence of the liner-dummy boundary and to a concrete-leaching process. The results of mineralogy (XRD, TG and SEM-EDX) have shown that the sulphate accumulates on the interface in the form of secondary ettringite that is also found filling air voids in the concrete (≈ 5 mm). CSIC studies conclude that in the concrete close to the granite there is more ettringite than ususally expected in a conventional OPC.

Na^+ measured in aqueous extracts either on bentonite or concrete samples is lower than the value measured for the reference FEBEX bentonite or the reference concrete. Analyses of soluble ions in concrete made by CSIC and presented in chapter 5 showed some leaching of Na^+, as well as K^+, in the concrete closer to the bentonite that may diffuse towards the bentonite. Then, in the bentonite Na^+ may diffuse towards the host formation and hotter zones

of the bentonite barrier. K^+ increases significantly in the first 2 mm of the bentonite, which seems to support the assumption of a certain release from concrete to bentonite. Again, this effect seems to be more pronounced in the outer zones of the barrier. The alkalis leachate is associated with a decrease in pH. This may be related to portlandite dissolution (pH<12.5) in the concrete, which has been pointed out by CSIC through different microstructural analysis; e.g. TG at different distances from the bentonite shows the disappearance of the portlandite in the ≈ 2 mm of concrete closest to the bentonite. Thus, Ca^{2+} from portlandite diffuses towards the bentonite, where an increase in concentration is observed in the first centimeters compared to the FEBEX original. The higher Ca^{2+} close to the interface might also be related to dissolution/precipitation of calcite and gypsum, both detected in the mineralogy analysis. Soluble Mg^{2+} gets accumulated in the first 2 cm from the interface in concrete. In bentonite, however, Mg^{2+} measured in aqueous extracts is negligible, as precipitation of Mg silicates occurs, favoured by the solution chemistry at the interface (pH>10), proven by TG and FT-IR analysis.

Variations in the exchangeable cations of the montmorillonite

Results of exchangeable cations indicate a heterogeneous distribution in the bentonite close to the concrete plug. Na values in the samples analysed are maintained quite close to (or slightly higher than) the reference values in all samples, although a drop just at the interface occurs, sometimes below the reference FEBEX value (Fig. 134). The small decrease of sodium in the exchange complex is also detected in the chemical profiles obtained by SEM-EDX by UniBern. Variation of K range from values similar to the reference up to 88% of difference, without a clear pattern in the spatial distribution. K increase seems to support the assumption of a certain release from concrete to bentonite.

The excess of dissolved Ca^{2+} from the alkaline concrete porewater enters the interlayer of montmorillonite as an exchangeable ion, displacing Mg^{2+} that migrates towards the concrete. That increase of calcium in exchangeable positions is also evident in the XRD and TEM analysis. The porewater conditions at the interface are favourable for the formation of Mg-rich precipitates, as proven by TG and FT-IR analysis. Considering the whole surface of bentonite contacting the plug, Ca increases up to 63% in the exchange complex compared to the reference FEBEX value in those zones close to the granite, and then decreases to values closer to the reference (around 20% higher) towards the internal part of the barrier, towards the dummy. The opposite occurs with Mg that decreases up to 71% in those areas close to the granite, and increases towards the inner part of the barrier, although it has lower values than the reference (around 6% lower). This trend is maintained up to 4 cm from the interface, which is the furthest distance analysed in this report. However, analysis of bentonite from the middle part of section 36, presented in Villar 2017, also showed an overall increase in exchangeable calcium, sodium and potassium with respect to the reference bentonite and a decrease in magnesium. This result is consistent with the changes observed in the samples analysed in this report and with the findings for the section closest to the concrete plug dismantled in 2002 (Villar et al. 2006). At the interface scale, taking into account the above-mentioned differences (higher Ca and lower Mg) with respect to the FEBEX reference value, a slight decrease of Ca and Na is observed just at the interface along with a slight increase of Mg and K, limited to the first centimetre away from the concrete interface.

Decalcification

Chemical profiles based on SEM-EDX, EPMA, μ-XRF and soluble salts show that the concrete matrix ≈ 15 mm from the interface is significantly depleted in calcium compared to

the original calcium in the concrete, except a thin layer in contact with the bentonite (≈ 200 μm) where calcium accumulates. More distant, variations in Ca are caused by the layered concrete structure originating from the layerwise application. As already mentioned, there is a Na^+ and K^+ release from the concrete followed by a decrease of pH (pH<12.5). As the pH at the interface decreases, dissolution of portlandite in the 2 mm closest to the interface occurs, especially in the outer ring of the barrier, closest to the granite, and also in the zones close to the dummy. CSIC observed also evidences of a slight C-S-H decalcification just at the interface. A similar decalcification process was described by Dauzères et al. (2010) in cement, with a decrease in the Ca/Si ratio in C-S-H phases.

The chemical profiles also show sulphate depletion in the ≈ 10 mm of concrete from the interface. As stated by UniBern, the decrease in Ca activity and pH in the concrete destabilises ettringite, which is an additional source of calcium. XRD analysis by different partners showed that on the bentonite side some dissolution of smectite occurred, so availability of Si and Al and its migration towards the concrete supports the formation of C-A-S-H, detected in samples analysed by UAM (XRD), and the precipitation of ettringite. Next, the sulphate reprecipitates as secondary ettringite filling voids (e.g. Fig. 111, bottom right) that was found in the XRD, SEM and TG analyses. Precipitation of secondary ettringite occurs in the first 10 mm of concrete close to the interface and is always found when gypsum is not detected. Gypsum has been detected only in the upper part of the plug. Ettringite occurs in various forms, as spherical clusters of small needle crystals, as large needle-like crystals, ranging from 10 to 100 μm length and thickness in the range between 10 to 80 nm, and as massive coalescent needle-like crystals, always filling voids partially or totally. The large acicular crystals observed filling pores are related to direct precipitation from solutions with high contents in sulphate and high calcium availability. These crystals are always found in the concrete closest to the bentonite (1 cm) or just at the bentonite side of the interface. The differences in morphology are attributed to differences in the degree of supersaturation of the solutions from which the ettringite precipitates. Higher supersaturation should produce more massive crystals, as those mentioned filling pores completely. Some cracks observed in the first millimetres of the concrete are associated to that massive ettringite. The precipitation of secondary ettringite was also observed in short-term laboratory experiments (i.e., Fernández et al. 2009).

Carbonation

XRD, SEM, TEM, TG and FT-IR demonstrate a carbonation process that tends to intensify towards the interface; the closer to the interface the greater the intensity of the calcite peaks. CT analysis by UniBern also shows an accumulation of very thin particles at the interface of a phase with higher X-ray attenuation attributed to calcium carbonates. The availability of calcium either by the decalcification of the concrete or by the dissolution of carbonates present in the bentonite promotes the precipitation of calcite at the interface. A thin layer in between bentonite and concrete acts as preferred new calcite precipitation site, which is not observed in the bentonite or in the concrete matrix.

That thin layer is an accumulation of very small crystals of calcite, found in relatively high contents. Temperatures of decarbonation in TG analysis are typical of fine-grained carbonates, and TEM/SEM analysis show the presence of nano- to micrometric calcium carbonate particles, mainly calcite and aragonite, exhibiting dissolution features, as well as nanometre particles crystal growth. This evidence points to the occurrence of dissolution and re-precipitation processes involving primary calcite and aragonite. Nanometre particles of secondary calcium carbonate tend to coagulate in order to form micrometric-size particles. Isotopes have demonstrated that carbonate for calcite precipitation derives from minor calcite

present in bentonite and from the infiltrating fracture water from the surrounding granite. Dissolution and precipitation processes of carbonates and sulphates linked to ion diffusion and reactions across the interface are also described in laboratory experiments (Cuevas et al. 2016).

Mg perturbation

Magnesium is displaced in the exchange complex of montmorillonite by calcium coming from the decalcification of concrete. The pH > 10 favours the formation of Mg-phases which were detected in bentonite close to concrete; the first 200 µm from the interface shows a layer with continuously high Mg concentration (SEM-EDX, EPMA). The further away from the interface the lower Mg content becomes. Al and Si in bentonite, which are the main constituents in smectite, show a pattern inverse to Mg: both are depleted towards the interface, most likely indicating a decreasing montmorillonite content.

XRD analyses indicate that montmorillonite still has the same expandability (16.9Å) as the original FEBEX, although the peaks of the basal series are broadened. Partial transformation of dioctahedral smectite to a trioctahedral Mg-sheet silicate is detected, and thermal analysis indicates a differentiated maximum of water loss near 490 ºC in bentonite at the interface in agreement with the presence of M-S-H with 0.8-1.3 Mg/Si. Those changes are observed over the whole bentonite surface following the same trends as exchangeable cations, since Mg involved in these processes comes from the exchange complex (Fig. 165). Infrared spectra confirm the presence of Mg-rich phases in samples from the interface, either brucite or trioctahedral smectites (i.e. saponite, stevensite), as well as poorly ordered M-S-H phases. M-S-H phases were observed by other authors as reaction products of interaction between cements and clays (Dauzères et al. 2010; Jenni et al. 2014; Roosz et al. 2015) and the Mg perturbation has also been observed in laboratory experiments by different authors (Dauzères et al. 2010; Fernández et al. 2006; Sanchez et al. 2006). The accumulation of Mg in contact with concrete is able to buffer the alkaline front from concrete. C-(A)-S-H are abundant in the first 1-2 mm as well. The precipitation of C-A-S-H, M-S-H and calcite minerals are interpreted as responsible for the increase of the BET surface observed towards the interface.

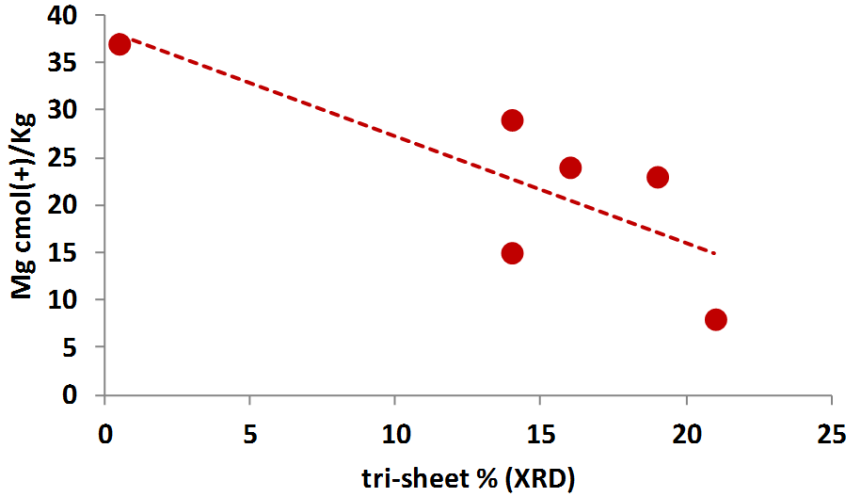

Fig. 165: Relationship between Mg from the exchange complex and trioctahedral M-S-H 2:1 sheet silicate phase (XRD) at the concrete bentonite interface.

6.5.4 Comparison to other cement-claystone interfaces (UniBern)

Several studies investigated interfaces between shotcrete (OPC based) and Opalinus Clay and between a shotcrete-type concrete (ESDRED, low-alkali cement) and Opalinus Clay (OPA) (e.g., Jenni et al. 2014,Jenni & Mäder 2014, Mäder et al. 2017). The main differences between OPA and FEBEX bentonite are:

- OPA contains a variety of sheet silicates (kaolinite, smectite, illite/smectite mixed layers, chlorite), whereas smectite is the major constituent of FEBEX bentonite. This leads to a higher cation exchange capacity, a larger anion restricted porosity, and a higher swelling pressure of the bentonite. In contrast, the free porosity portion (pore space not affected by electrostatics) is larger in OPA than in a highly-compacted bentonite. Reactivity of all clay minerals is small at the time-scale of the experiments.
- Calcite and quartz are present in both materials, but in smaller amounts in bentonite.
- Cristobalite is found in the FEBEX bentonite, and is more reactive than quartz, especially at elevated pH.
- Dolomite is expected to dissolve in OPA during its interaction with cement, but is not present in the bentonite.
- One third of the exchanger sites in the bentonite are occupied by Mg^{2+}. This leads to a large amount of mobile and readily available Mg^{2+}.
- The relatively high pyrite content (ca. 1 wt%) in OPA might partially dissolve under oxidising conditions, whereas pyrite content is rather low in the bentonite.

The similarities of the two clay materials prompt a comparison of the different interfaces. EDX element maps shown below are taken from Jenni & Mäder (2014, CI Experiment, Mont Terri Rock Laboratory), Mäder et al. (2017), and Jenni & Mäder (2016, FE Experiment, Mont Terri Rock Laboratory).

All cements show an obvious depletion in Ca within 1-2 mm from the interface (Fig. 166). Two of the three interfaces show a Ca-enrichment in the clay at the interface. Mg is enriched at the interface in both cement and clay (Fig. 167). A second sample from the FE Experiment (Mont Terri) shows no Mg enrichment in the cement and indicates a high lateral variability at the interface in this experiment, where the concrete was applied onto the surface of a rough tunnel wall. Furthermore, large air voids in the concrete are frequent close to the interface. S is depleted in the cement in all samples at the interface. In the FE sample, the depleted layer is thinner and followed by a strong enrichment. Sulphur enrichment in the cement detached from the interface is commonly observed in ordinary Portland cement-OPA samples, but it is less obvious in samples containing low-alkali (“low-pH”) cements (Fig. 168).

The redistribution of the main elements influenced by cement-clay interaction is similar in all shown interfaces, regardless of the type of clay, the type of cement or the method of concrete application (shotcreting in case of FEBEX and FE samples, casting in case of CI samples). This implies the presence of similar main interaction mechanisms, as those described above.

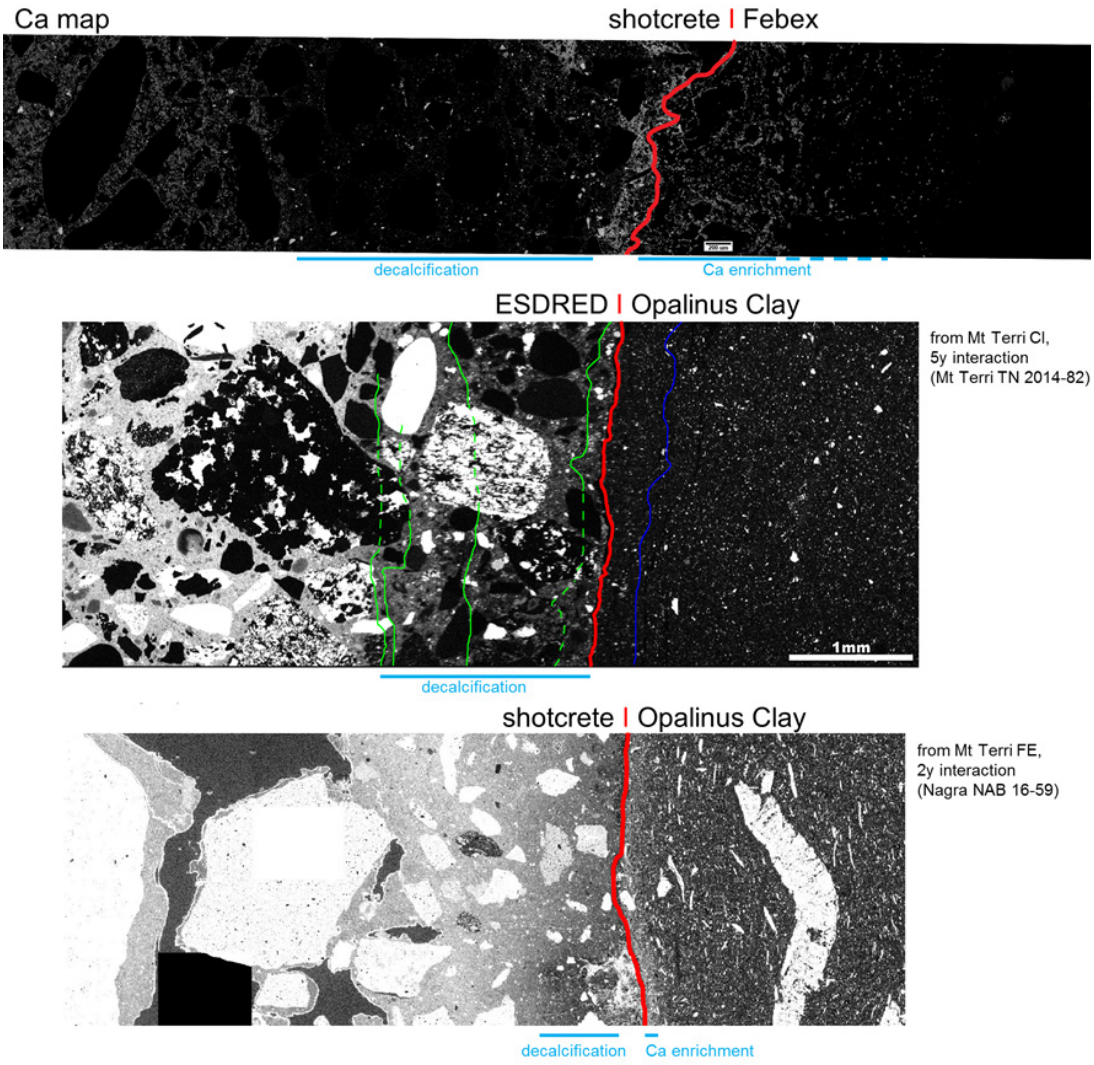

Fig. 166: Comparison of Ca-EDX maps of the concrete-FEBEX bentonite interface with other cement-claystone interfaces, shown at equal magnification. High concentrations in light grey (same grey levels do not represent the same concentrations in the different maps), non-matrix phases segmented in black in the FEBEX interface only, whereas their true concentrations are shown in the other maps.

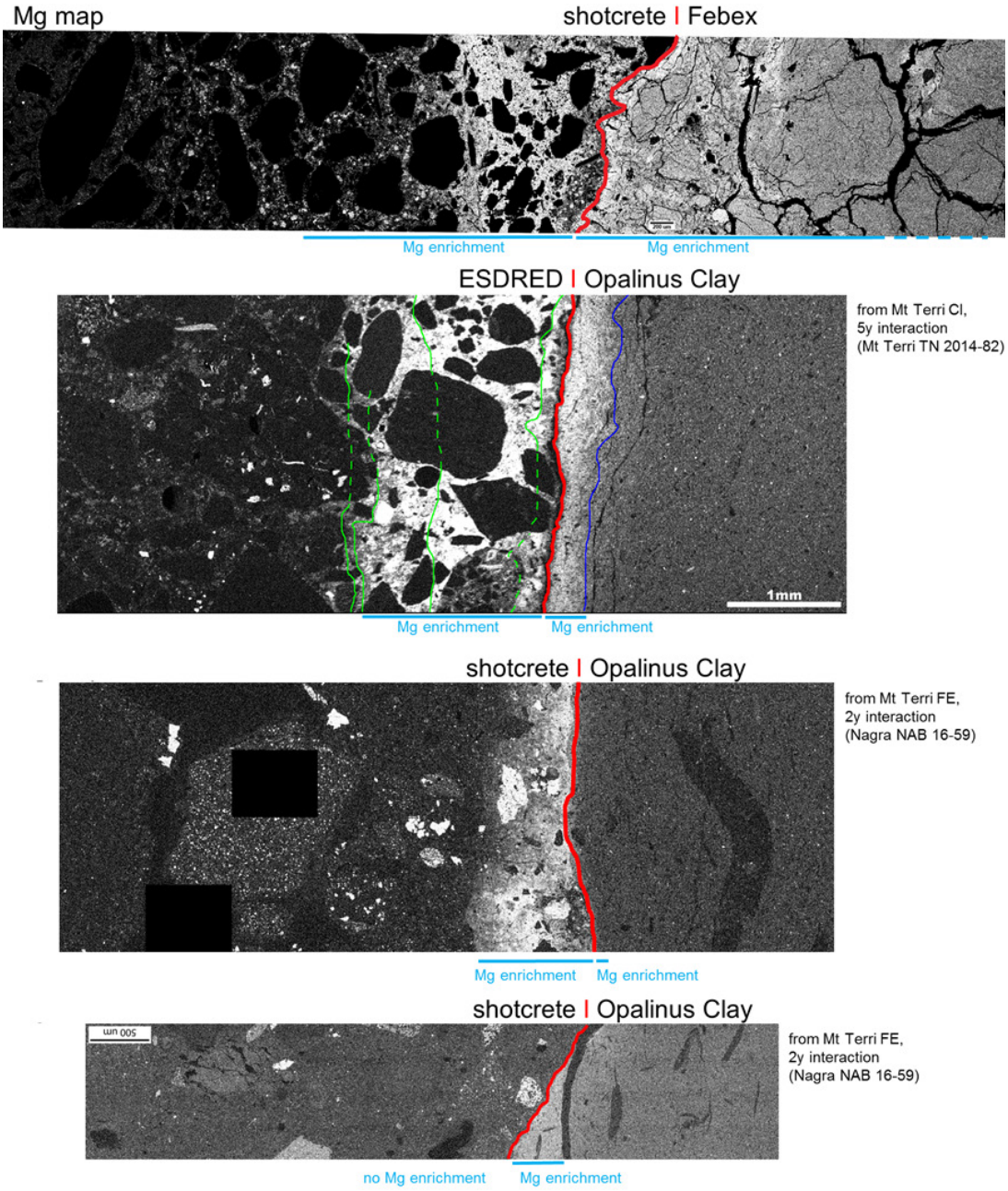

Fig. 167: Comparison of Mg-EDX map of the concrete-FEBEX bentonite interface with other cement-claystone interfaces at equal magnification. High concentrations in light grey (same grey levels do not represent the same concentrations in the different maps), non-matrix phases segmented in black in the FEBEX interface only, whereas their true concentrations are shown in the other maps.

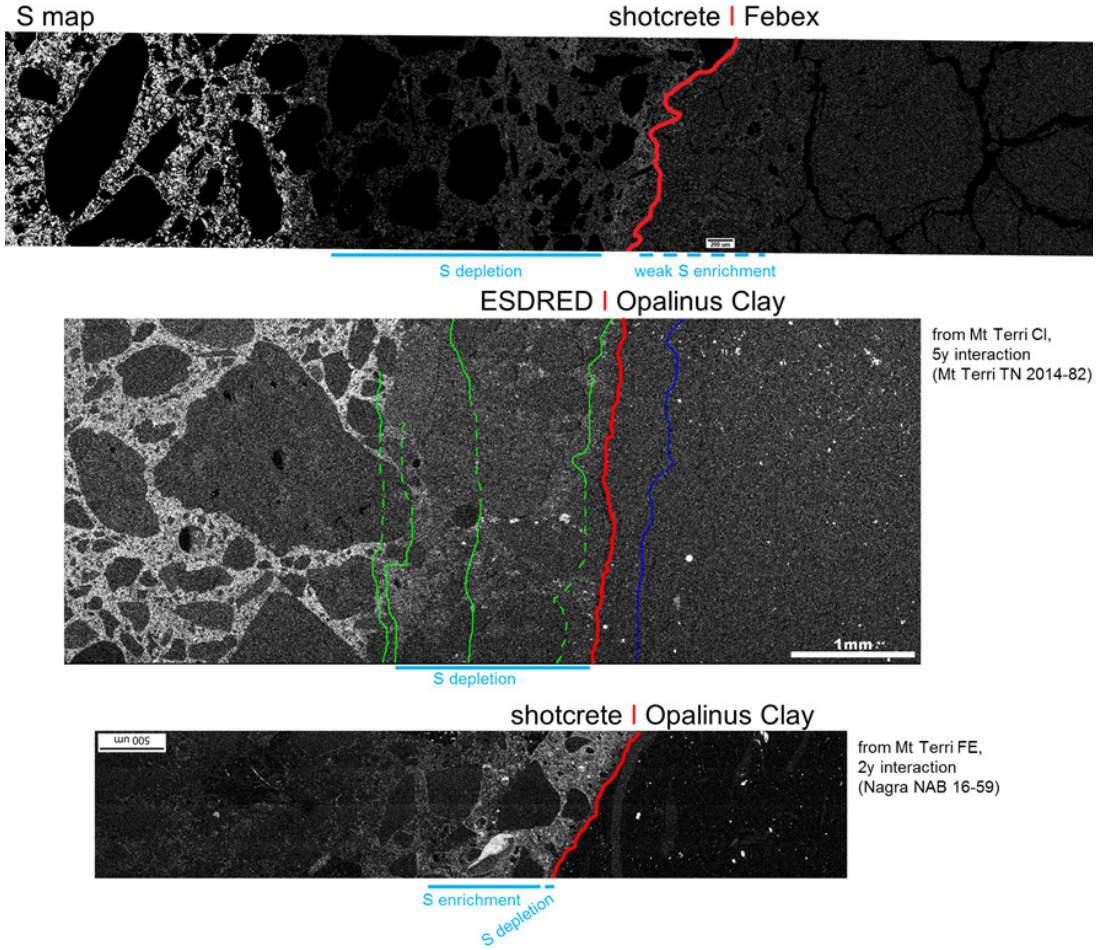

Fig. 168: Comparison of sulphur EDX map of the concrete-FEBEX bentonite interface with other cement-claystone interfaces at equal magnification. High concentrations in light grey (same grey levels do not represent the same concentrations in the different maps), non-matrix phases segmented in black in the FEBEX interface only, whereas their true concentrations are shown in the other maps

7 Conclusions

Concrete ageing, concrete/bentonite and concrete/rock interaction have been studied as part of the FEBEX-DP project from samples collected during the dismantling phase carried out in 2015. Seven organizations were part of the investigations and the joint results lead to a coherent description of the processes that ocurred during 13 years of operation of the in-situ experiment and the extension of the alteration.

The number of samples collected allowed investigating a representative distribution of different parts of the concrete plug and the concrete/bentonite interface. Observations made in situ and macroscopic observations from overcores were very useful to understand both the heterogeneity of the plug itself and of the concrete/bentonite interface. The concrete plug was constructed in two sections. The first section (1 m) showed a layered and heterogeneous texture. The way of construction, including a first shotcreting layer with a w/c ratio higher than the rest, influenced that aspect. Porous rubbly layers of rebound material were located at the base of the plug giving a more porous and permeable material. The second section (2 m) is massive and homogeneous. Layers are characterised by the occurrence of air voids, or by different amounts of capillary porosity.

Concerning the concrete/bentonite interface sample there is a faint brownish discoloration of the concrete part next to the bentonite assumed to be related to the presence of bentonite and the resultant geochemical interactions. There is also a very faint lighter-coloured zone, ca. 12 mm wide, of the bentonite adjacent to the concrete. A very thin (<1 mm) light-coloured irregular skin is observed just at the interface on the bentonite side. The interface itself appears to be physically very well preserved in the overcores, without any obvious fractures or joints. The entire bentonite shows inhomogeneities considered as pre-existing inhomogeneities in the pristine bentonite.

Concrete plug

The whole set of analyses made on the concrete plug suggests differences between plug sections 1 and 2 and also differences related to the location: proximity to the bentonite and/or to the granite. The compressive strength of section 2 was higher than in section 1, this difference was observed after 28 days and also after 13 years and agrees with higher binder content of section 2. Focusing on section 1, the compressive strength of samples located in the middle and base of the plug was lower compared to the upper part of the plug. The elastic modulus is similar in both sections. The total and accessible porosity in section 1 was higher than in section 2, but concentrating on section 1, the vicinity of the bentonite and granite interaction implies an increased total porosity. Water absorption is higher in section 1 than in section 2, which agrees with the higher quality of section 2.

The main precipitation and dissolution processes in the concrete have been located near the granite and bentonite boundaries, which promote leaching processes in the concrete matrix and dissolution of the portlandite with the resultant release of calcium. Pore solution pH values near or even below 12.5 have been measured in the corresponding affected concrete in section 1, while section 2 remained largely unaffected. The analysis of the soluble ions shows that the lower Ca and alkaline content (Na and K) is linked to a pH decrease. An increased concentration of Mg was observed in SEM-EDS mapping of section 1 in zones near the granite and bentonite boundaries. Conservative anions as chloride show the highest concentrations near the granite boundary, but have been detected as far as 5 cm from the interface. Sulphate decreases near the bentonite in section 1. Precipitation of ettringite and

calcite occurs near bentonite in section 1, and although ettringite has slightly lower concentrations at the top part of the section, near the bentonite or the granite, it is rather randomly distributed. The CaO and SiO_2 distribution and ratio as a function of distance away from the bentonite become more homogeneous and decrease, suggesting a decreasing C/S ratio. Despite the leaching, significant damage in the cementitious cement paste matrix has not been observed at 1 cm from the bentonite or 15 cm from the host-rock (closest sample to the granite).

Concrete/bentonite interaction

As a general trend, the bentonite water content decreases from the granite towards the inner part of the barrier whereas the dry density increases. The swelling strain values measured in bentonite close to the concrete are 1% lower than the values expected for the reference sample with the same initial state in terms of dry density and water content. Consequently, it is concluded that the concrete interface had no effect on the swelling capacity of the bentonite.

The bimodal distribution obtained by MIP in all the bentonite samples is quite typical of the FEBEX bentonite, as well as the percentage of each type of pores. The percentage and size of macropores increase towards the granite and also in the vicinity of the concrete interface. As the distance to the interface increases, the macropores mode decreases. CT-analysis shows the common occurrence of microcracks in bentonite and pores in concrete. The observations agree fairly well with the data obtained by MIP, since a noticeable percentage of macropores is found, up to 38% in some samples close to the interface.

The pore size distribution of the concrete side is bimodal as well. The samples at distances > 20 mm from the interface with bentonite have a mode 9 ± 3 nm while in the rest of samples the mode is 43 ± 6 nm, quite close to the mode of macropores. CT-analysis indicates that the concrete texture tends to be more regular than the bentonite one with granular material embedded in a fine-grained matrix with dark spots interpreted as circular shaped pores/voids having a wide size range.

The granite boundary and presumably liner-dummy boundary have become preferred pathways for soluble salt transport. A significant decrease in the main components, sulphates and chlorides, is observed in bentonite close to the interface with respect to the original FEBEX bentonite. Ion concentration at this stage in this bentonite section is mainly governed by temperature and hydration (Villar 2017), while the ionic concentration in the concrete is dominated by diffusion towards less concentrated areas. Chloride diffuses into the concrete plug forming Friedel's salt and sulphate accumulates at the concrete side of the interface in the form of ettringite/gypsum. Precipitation of secondary ettringite occurs in the first 10 mm of concrete close to the interface and is always found when gypsum is not detected. There is a certain release of Na^+ and K^+ from concrete to bentonite. Decalcification occurs in the concrete close to the interface with the bentonite and also close to the granite. The Ca depletion in the concrete is caused by dissolution of ettringite and/or portlandite, which decreases the Ca/Si ratio in C-S-H phases and provides a source of Ca for the precipitation of carbonates. There is an accumulation of very small crystals whose analysis indicates calcite, found in relatively high contents as a very continuous layer at the interface. Isotopes have demonstrated that carbonate for calcite precipitation derives from minor calcite present in bentonite and from the infiltrating fracture water from the surrounding granite. Based on infrared spectroscopy concrete carbonation tends to intensify towards the interface.

The excess of dissolved Ca^{2+} from the alkaline concrete porewater enters the interlayer of montmorillonite as an exchangeable ion, displacing Mg^{2+} that migrates towards the concrete.

Soluble Mg^{2+} gets accumulated in the first 2 mm from the interface in concrete. In bentonite, however, Mg^{2+} measured in aqueous extracts is negligible, as precipitation of Mg silicates occurs, favoured by the solution chemistry at the interface. The further away from the interface the lower Mg content becomes. Al and Si in bentonite, which are the main constituents in smectite, show a pattern inverse to Mg: both are depleted towards the interface, indicating most likely decreasing montmorillonite content. Partial transformation of dioctahedral smectite to a trioctahedral Mg-sheet silicate is detected by XRD, and thermal analysis indicates a differentiated maximum of water loss near 490 ºC in the bentonite at the interface in agreement with the presence of M-S-H with 0.8-1.3 Mg/Si. Those changes are observed over the whole bentonite surface following the same trends as the exchangeable cations. Infrared spectra confirm the presence of Mg-rich phases in samples from the interface, either brucite or trioctahedral smectites (i.e. saponite, stevensite), as well as poorly ordered M-S-H phases. The accumulation of Mg in contact with concrete is able to buffer the alkaline front from concrete. C-(A)-S-H are abundant in the first 1-2 mm as well. The precipitation of C-A-S-H minerals, as well as calcite and M-S-H at the interface are interpreted as responsible for the increase of the BET surface observed towards the interface.

Concrete/rock interaction

To investigate the internal structure and mineralogy of the concrete and granite at the interface level two concrete/rock samples were taken, one from the remains of a concrete/rock sample after the dismantling of heater #1 in 2002, and another from the dismantling of heater #2 in 2015. The study compares both samples by using XRD-CT analyses.

The concrete/rock interface sample from the dismantling of heater #1 of the FEBEX experiment exhibits a space attributed to shrinkage by exposition to air for 13 years. The micro-XRD analysis showed the presence of calcite and clay minerals, specifically illite, which may be the product of the alkaline interaction of concrete and granite before the first dismantling.

The concrete/rock interface sample from the dismantling of heater #2 of the FEBEX experiment does not have the space between concrete and granite. However, high porosity is observed in the concrete, what may be due to the shotcreting technique and the rebound material when applying it. Calcite is found on the concrete side but illite is not present.

Implications for repository and open questions

The findings of FEBEX experiment are consistent with those from other in-situ and laboratory experiments. Results indicate that despite the heterogeneity found there have been no discernible changes in concrete after 13 years of exposition to granite or bentonite. Also, bentonite properties have not been significantly affected by the interaction with concrete. One of the important assessments of the work is that the accumulation of Mg in the concrete/bentonite contact is able to buffer the alkaline front from concrete. Further studies on the formation of carbonates and Mg-silicates, as well as detailed studies of changes in porosity at the interface level are part of the studies addressed in the collaborative project Cement-based materials, properties, evolution, barrier functions (Cebama, www.cebama.eu) funded by the European Commission (H2020).

As described above, several interactions between the concrete and bentonite have occurred. Whether the interactions between concrete and bentonite are detrimental to the long-term safety of the repository, can best be analysed by comparing the bentonite properties to the

long-term safety requirements. One of the most important requirements for the bentonite backfill is that the bentonite ensures a low hydraulic conductivity in order to provide a diffusive regime. Furthermore, a sufficient density and swelling pressure are required to prevent colloidal transport and to avoid canister sinking, respectively. As densities increase, microbial activity around the canister can be prevented as well.

Although cation exchange within the bentonite and the dissolution of montmorollonite due to the interaction with the cementitious water were observed close to the interface, no significant changes in dry density and swelling pressure could be measured. In other words, despite any mineralogical changes in the bentonite, no physical properties were changed. It can thus be concluded that under the given conditions of the FEBEX experiment, no loss of safety-relevant properties of the bentonite took place. The long-term evolution of the bentonite still needs to be assessed through reactive transport modelling. The process understanding and data acquired through this experiment are excellent input data to refine these models, which will then allow a final statement regarding, if any, impact of cement-clay interactions on the long-term safety of the repository.

8 Acknowledgements

UAM team acknowledges the work performed by Enrique Rodríguez Cañas (SEM-EDX); Noemí González, Paula Ciria and Eugenia Rodríguez (powder XRD); Ramón Redondo and Vanessa Peiro (Stable Isotopes) and Mª José Mata (TG-DSC), our support personel in the interdepartmental research service of UAM. Special thanks to prof. Javier González Yélamos for his aid and support during the hand-picked sampling at the GTS site.

UniBern wants to acknowledge the engineers from Aitemin involved in the planning stage to establish drilling locations that would not interfere with equipment, sensor components and other sampling activities. The field team included Urs Mäder (technical lead, sampling), Hans Abplanalp and Toni Baer (drilling team), Kai Detzner (documentation, technical support, sampling), and Florian Kober (FEBEX-DP project lead, general support). The analytical results presented here relied on samples carefully crafted by the rock preparation team of the Institute of Geological Sciences, UniBern. The X-ray CT facility at the University of Fribourg is directed by Anneleen Foubert and operated by Christof Neururer who also performed the CT scans.

The assistance of John Eric Bower for the X-ray CT analyses of bentonite/cement core material at Sandia National Laboratories (SNL) is very much appreciated. Mark Rodriguez, Marshall Reviere, and James Griego also at Sandia National Laboratories (SNL) conducted the micron-XRF analyses in this study. The assistance of Patrick D. Burton (Sandia National Laboratories – SNL) with the SEM/EDS system is also appreciated.

Obayashi wants to acknowledge Urs Mäder (technical advices) and Florian Kober (FEBEX-DP project lead, general and on-site support). The synchrotron radiation experiments were performed at SPring-8 with the approval of the Japan Synchrotron Radiation Research Institute (JASRI) as Proposal No. 2013B1594, 2014A1559, 2014B1010, 2014B1587, 2014B1606, 2014B1607, 2015A1002, 2015A1680, 2015A1711, 2015A1709, 2015B1569, 2015B1608, 2015B1623, 2016B1614, 2016A1532, 2016A1531, 2016B1598, 2017A1552, 2017A1009/BL No. 28B2).

Ciemat authors acknowledge the assistance of Ana Vicente, Alfonso Rodríguez and Juan Luis Baldonedo for the SEM and TEM analyses at Centro Nacional de Microscopía Avanzada (Universidad Complutense de Madrid). We also appreciate the willingness of the in-situ working team from Aitemin to take all the samples required extremely careful. The assistance, guidance and discussions of Florian Kober at every step of the FEBEX-DP project are deeply appreciated

9 List of References

Abós, H. & Martínez, V. (AITEMIN) (2015): Sample Log Book 34 to 62 FEBEX-DP. AN 15-578 September 2015.

Alonso, M.C., García Calvo, J.L., Petterson, S., Puigdomenech, I., Cuñado, M.,Vuorio, A.M., Weber, H., Ueda, H., Naito, M., Walker, C., Takeshi, Y., Cau-dit-Coumes, C. (2013): Round robin test for defining an accurate protocol to measure the pore fluid pH of low-pH cementitious materials. In: Bart, F., Cau-dit-Coumes, C., Frizon, F., Lorente, S. (Eds.), Cement-based Materials for Nuclear Waste Storage. Springer, pp. 251-259.

Bai, T.B. & Koster van Groos, A.F. (1998): Phase relations in the system MgO-NaCl-H2O: The dehydroxylation of brucite in the presence of NaCl-H2O fluids. American Mineralogist, 83, 205-212.

Bárcena, I., Fuentes-Cantillana, J.L. & García-Siñeriz, J.L. (2003): DISMANTLING OF HEATER No 1 AT THE FEBEX "IN SITU" TEST Description of operations. Project Deliverable D7. FEBEX project. 124pp.

Bárcena I. And García-Siñeriz, J.L. (2015a): FEBEX-DP (GTS): Full Dismantling Sampling Plan (In situ Experiment). NAB 15-14. 109pp.

Bárcena I. And García-Siñeriz, J.L. (2015b): FEBEX-DP (GTS): Full Dismantling Test Plan (In situ Experiment). NAB 15-15. 105pp.

Beyler, C.L. & Hirschler, M.M. (2002): Thermal Decomposition of Polymers. SFPE Handbook of Fire Protection Engineering 2, Section 1, Chapter 7, 111-131.

Birkholzer, J., Faybishenko, B., Zheng, L., Rutqvist, J., Reimus, P., Viswanathan, H., Jove Colon, C.F., Wang, Y. Kuhlman, K. McMahon, F.J. & Zavarin, M. (2017): International Collaboration Activities in Different Geologic Disposal Environments (SFWD-SFWST-2017-000013), Lawrence Berkeley National Laboratory (LBNL-2001063): Berkeley, CA USA. 236 pp.

Corte, A. & Higashi, A. (1964): Experimental research on desiccation cracks in soil, U.S. Army Cold Regions Research and Engineering Laboratory, CRREL-RR-66 Final Report, Alexandria, VA.

Cuevas, J., Ruiz, A.I., Fernández, R., Torres, E., Escribano, A., Regadío, M. & Turrero, M.J., (2016): Lime mortar-compacted bentonite–magnetite interfaces: An experimental study focused on the understanding of the EBS long-term performance for high-level nuclear waste isolation DGR concept. Applied Clay Science 124-125, 79-93.

Dauzères, A., Achiedo, G., Nied, D., Bernard, E., Alahrache, S. & Lothenbach, B. (2016): Magnesium perturbation in low-Ph concretes placed in clayey environment—solid characterizations and modelling. Cement and Concrete Research 79, 137-150.

Dauzères, A., Le Bescop, P., Sardini, P. & Cau Dit Coumes, C. (2010) : Physico-chemical investigation of clayey/cement-based materials interaction in the context of geological waste disposal: Experimental approach and results. Cement and Concrete Research 40, 1327-1340.

DeCarlo, K.F. & Shokri, N. (2014): Salinity effects on cracking morphology and dynamics in 3-D desiccating clays. Water Resources Research, 50(4): 3052-3072.

Dolder, F., Mäder, U., Jenni, A., Schwendener, N. (2014): Experimental characterization of cement–bentonite interaction using core infiltration techniques and 4D computed tomography. Physics and Chemistry of the Earth, Parts A/B/C, 70–71, 104–113.

Dolder, F., Mäder, U., Jenni, A., Münch, B. (2016): Alteration of MX-80 bentonite backfill material by high-Ph cementitious fluids under lithostatic conditions – an experimental approach using core infiltration techniques. In: Norris, S., Bruno, J., Van Geet, M. & Verhoef, E. (eds) Radioactive Waste Confinement: Clays in Natural and Engineered Barriers. Geological Society, London, Special Publications, 443.

Dohrmann, R. & Kaufhold, S. (2009): Three new, quick CEC methods for determining the amounts of exchangeable calcium cations in calcareous clays. Clays and Clay Minerals, 57(3), 338–352.

Dohrmann, R., Olsson, S., Kaufhold, S. & Sellin, P. (2013): Mineralogical investigations of the first package of the alternative buffer material test – II. Exchangeable cation population rearrangement. Clay Minerals, 48, 215–233.

Emmerich, K. (2011): Thermal analysis in the characterization and processing of industrial minerals. In: G.E. Christidis, Editor: Advances in the Characterization of Industrial Minerals. EMU notes in mineralogy, 9, 129-164.

Fernández, A.M., Baeyens, B., Bradbury, M. & Rivas, P. (2004): Analysis of the porewater chemical composition of a Spanish compacted bentonite used in an engineered barrier. Physics and Chemistry of the Earth, Parts A/B/C 29, 105-118.

Fernández, R., Cuevas, J., Sánchez, L., Vigil de la Villa, R. & Leguey, S. (2006): Reactivity of the cement-bentonite interface with alkaline solutions using transport cells. Appl. Geochem. 21, 977-992.

Fernández, R., González, L., Ruiz, A.I. & Cuevas, J. (2014): Nature of C-(A)-S-H Phases Formed in the Reaction Bentonite/Portlandite. Journal of Geochemistry 2014, 1-8.

Fernández, R., Isabel Ruiz, A. & Cuevas, J. (2016): Formation of C-A-S-H phases from the interaction between concrete or cement and bentonite. Clay Minerals 51, 223-235.

Fernández, R., Mäder, U., Rodríguez, M., Virgil de la Villa, R. & Cuevas, J. (2009): Alteration of compacted bentonite by diffusion of highly alkaline solutions. European Journal of Mineralogy 21, 725-735.

Fernández, R., Vigil de la Villa, R., Ruiz, A.I., García, R. & Cuevas, J. (2013b): Precipitation of chlorite-like structures during OPC porewater diffusion through compacted bentonite at 90°C. Applied Clay Science 83-84, 357-367.

Fernández, R., Torres, E., Ruíz, A.I., Cuevas, J., Alonso, M.C., García-Calvo, J.L., Rodríguez, E. & Turrero, M.J. (2017): Interaction processes at the concrete-bentonite interface after 13 years of FEBEX-Plug operation. Part II: Bentonite contact. Physsics and Chemistry of the Earth, 99, 49-63.

Fernández, A.M. & Villar, V. (2010): Geochemical behavior of a bentonite barrier in the laboratory after up to 8 years of heating and hydration. Applied Geochemistry, 25, 809-824.

Fernández, A.M. & Rivas, P. (2005): Analysis and distribution of waters in the compacted FEBEX bentonite: pore water chemistry and adsorbed water properties. In: Alonso & Ledesma (eds.) Advances in Understanding Engineered Clay Barriers. Taylor & Francis Group, London. pp. 257-275.

Ferrage, E., Lanson, B., Sakharov, B.A. & Drits, V.A. (2005): Investigation of smectite hydration properties by modeling experimental X-ray diffraction patterns: Part I. Montmorillonite hydration properties. American Mineralogist, 90, 1358-1374.

Fuentes-Cantillana, J.L., García-Siñeriz, J.L., Obis, J., Pérez, A. (AITEMIN); Alberdi, J., Barcala, J.M., Campos, R., Cuevas, J., Fernández, A.M., Gamero, E., García, M., Gómez, P., Hernández, A., Illera, A., Martín, P.L., Melón, A.M., Mingarro, M., Ortuno, F., Pardillo, J., Pelayo, M., Rivas, P., Rodríguez, V., Turrero, M.J., Villar, M.V. (CIEMAT); Caballero, E., Jiménez de Cisneros, C., Linares, J. (CSIC-Zaidín); Martínez, M.A. (SGS Tecnos, S.A.); Samper, J., Delgado, J., Juncosa, R., Molinero, J. (ULC); Alonso, E., Carrera, J., Gens, A., García-Molina, A.J., Guimera, J., Guimaraes, L.do N., Lloret, A., Martínez, L. (UPC-DIT); Elorza, F.J., Borregón, J.L. (UPM); Fariña, P. (DM Iberia, S.A.) & Farias, J. (Geocontrol, S.A.) were the technical editors of this report under the direction of Huertas, F. (Enresa). (1998): FEBEX Full-scale Engineered Barriers Experiment in Crystalline Host Rock. Pre-operational Stage Summary Report. Enresa Technical Report 1/98.

Fuentes-Cantillana, J.L. & García-Siñeriz, J.L. (1998): FEBEX Full-scale Engineered Barriers Experiment in Crystalline Host Rock. Final design and installation of the "in situ" test at Grimsel". Enresa Technical Report 12/98.

Fuentes-Cantillana, J.L., García-Siñeriz, J.L., Franco, J.J., Obis, J., Pérez, A. (AITEMIN); Jullien, F. (Andra); Alberdi, J., Barcala, J.M., Campos, R., Cuevas, J., Fernández, A.M., Gamero, E., García, M., Gómez, P., Hernández, A., Illera, A., Martín, P.L., Melón, A.M., Missana, T., Ortuno, F., Pardillo, J., Rivas, P., Turrero, M.J., Villar, M.V., Mingarro, M., Pelayo, M. (CIEMAT); Caballero, E., Cuadros, J., Huertas, F., Huertas, F.J., Jiménez de Cisneros, C., Linares, J. (CSIC-Zaidín); Bazargan-Sabet, B., Ghoreychi, M. (G.3S); Jockwer, N., Wieczorek, K. (GRS); Kickmaier, W., Marschall, P. (Nagra); Martínez, M.A. (SGS Tecnos, S.A.); Carretero, P., Dai, Z., Delgado, J., Juncosa, R., Molinero, J., Ruiz, A., Samper, J., Vázquez, A. (ULC); Alonso, E., Carrera, J., Gens, A., García-Molina, A. J., Guimera, J., Guimaraes, L.do N., Lloret, A., Martínez, L., Olivella, S., Pintado, X., Sánchez, M. (UPC-DIT); Elorza, F.J., Borregón, J.L., Canamon, I., Rodriguez Pons-Esparver, R. (UPM); Fariña, P. (DM Iberia, S.A.) & Farias, J. (Geocontrol, S.A.) were the technical editors of this report under the direction of Huertas, (Enresa) (2000): FEBEX full-scale engineered barriers experiment for a deep geological repository for high level radioactive waste in crystalline host rock Final Report. Enresa, Technical Report 1/2000.

Gaboreau, S., Lerouge, C., Dewonck, S., Linard, Y., Bourbon, X., Fialips, C.I., Mazurier, A., Prêt, D., Borschneck, D., Montouillout, V., Gaucher, E.C. & Claret, F. (2012) : In-situ interaction of cement paste and shotcrete with claystones in a deep disposal context. American Journal of Science 312, 314-356.

Gaboreau, S., Prêt, D., Tinseau, E., Claret, F., Pellegrini, D. & Stammose, D. (2011) : 15 years of in situ cement–argillite interaction from Tournemire URL: Characterisation of the multi-scale spatial heterogeneities of pore space evolution. Applied Geochemistry 26, 2159-2171.

Garralón, A., Gómez. P., Peña, J., Buil, B., Turrero, M.J., Torres, E. & Sánchez, L. (2018): Hydrogeochemical characterization of the groundwater in the FEBEX gallery. NAB 16-14. 109pp.

García-Siñeriz, J.L., Abós, H., Martínez, V., De la Rosa, C., Mäder, U. & Kober, F. (2016): FEBEX DP: Dismantling of Heater 2 at the FEBEX "in Situ" Test. Description of Operations. Nagra Report NAB 16-11.

Gebrenegus, T., Ghezzehei, T.A. & Tuller, M. (2011): Physicochemical controls on initiation and evolution of desiccation cracks in sand–bentonite mixtures: X-ray CT imaging and stochastic modeling. Journal of contaminant hydrology, 126(1): 100-112.

Gebrenegus, T., Tuller, M. & Muhunthan, B. (2006): The Application of X-ray Computed Tomography for Characterization of Surface Crack Networks in Bentonite-Sand Mixtures, Advances in X-ray tomography for geomaterials. ISTE Ltd. London, UK, pp. 207-212.

Gimmi, T. & Kosakowski, G. (2011): How mobile are sorbed cations in clays and clay rocks? Environmental Science and Technology 45, 1443-1449.

Huertas F., Fariña P., Farias J. [et al.]. (2006): Febex Full-scale Engineered Barriers Experiment. Updated Final Report 1994-2004. ENRESA Publicación Técnica PT 05-0/2006. Madrid. 590 pp.

Jenni, A., Mäder, U., Lerouge, C., Gaboreau, S., & Schwyn, B. (2014): In situ interaction between different concretes and Opalinus Clay. Physics and Chemistry of the Earth, Parts A/B/C 70–71, 71-83.

Jenni, A. & Mäder, U. (2014): CI (cement clay interaction) experiment: SEM/EDX characterisation of concrete/Opalinus Clay interfaces from 2nd sampling campaign and comparison to state after 1st sampling. Unpublished Mont Terri Technical Note TN 2014-82, Mont Terri Project, St. Ursanne, Switzerland.

Jenni, A. & Mäder, U. (2016): Analysis of the shotcrete – Opalinus Clay interface from FE-experiment at Mont Terri URL. Nagra Working Report NAB 16-59, Nagra, Wettingen, Switzerland.

Jenni, A., Gimmi, T., Alt-Epping, P., Mäder, U. & Cloet, V. (2017): Interaction of ordinary Portland cement and Opalinus Clay: Dual porosity modelling compared to experimental data. Physics and Chemistry of the Earth (in press).

Jové Colón, C.F. (2016): International Collaboration Activities on Engineered Barrier Systems (FCRD-UFD-2016-000628), Sandia National Laboratories: Albuquerque, NM, SAND2016-8935 R. 26 pp.

Kajiwara, K., Hitomi, T. & Sugiyama, T. (2013): Development of the evaluation technic of mineral distributtion in concrete with non-destructive integrated CT-XRD method, abstract of 67th the annual meetings cement and concrete engineering, pp.82-83, in Japanese.

Lothenbach, B., Nied, D., L'Hôpital, E., Achiedo, G. & Dauzères, A. (2015): Magnesium and calcium silicate hydrates. Cement and Concrete Research 77, 60-68.

Kaufhold, S., Dohrmann, R., Sandén, T., Sellin, P. & Svensson, D. (2013): Mineralogical investigations of the alternative buffer material test – I. Alteration of bentonites. Clay Minerals, 48, 199–213.

Kober, F. & Van Meir, N. (2017): FEBEX-DP – Dismantling related supplementary documents. Nagra Arbeitsbericht NAB 16-068.

Kulander, B.R., Dean, S.L. & Ward, B.J. (1990): Fractured core analysis: interpretation, logging, and use of natural and induced fractures in core, AAPG Methods in Exploration No. 8. Published by the American Association of Petroleum Geologists (AAPGDatapages).

Mäder, U., Detzner, K., Kober, F., Abplanalp, H. & Baer, T. (2016): FEBEX-DP – Plug Overcoring and Concrete/bentonite Interface Sampling prior to Dismantling. Nagra Arbeitsbericht NAB 16-010.

Mäder, U., Jenni, A., Lerouge, C., Gaboreau, S., Miyoshi, S., Kimura, Y., Cloet, V., Fukaya, M., Claret, F., Otake, T., Shibata, M. & Lothenbach, B. (2017): 5-year chemico-physical evolution of concrete–claystone interfaces, Mont Terri rock laboratory (Switzerland). Swiss Journal of Geosciences, 1-21.

Madejova J., Gates W.P. & Petit S. (2017): IR Spectra of Clay Minerals. In: W.P. Gates, J.T. Kloprogge, J. Madejova, F. Bergaya, Editors: "Infrared and Raman Spectroscopies of Clay Minerals". Developments in Clay Science, Volume 8, 107-149.

Martín de Vidales, J.L., Pozo, M., Alia, J.M., Garcia-Navarro, F. & Rull, F. (1991) : Kerolite-stevensite mixed-layers from the Madrid basin, Central Spain. Clay Miner. 26, 329-342.

Martínez, V., Abós, H. & García-Siñeriz, J.-L. (2016): FEBEX/FEBEX-DP: Final sensors data report. Nagra Working Report NAB 16-19

Meier, L.P. & Kahr, G. (1999): Determination of the cation exchange capacity (CEC) of clay minerals using the complexes of Copper (II) ion with Triethylenetetramine and Tretraethylenepentamine. Clays and Clay Minerals, 47, 386 – 388.

Mindess, S., Young, J.F. & Darwin, D. (2002): "Concrete" ed. 2ª, ed. Prentice Hall Inc., Englewood Cliffs, NJ, USA, 2002.

Morris, P.H., Graham, J. & Williams, D.J. (1992): Cracking in drying soils. Canadian Geotechnical Journal, 29(2): 263-277.

Moyce, E.B.A., Rochelle, C., Morris, K., Milodowski, A.E., Chen, X., Thornton, S., Small, J.S. & Shaw, S. (2014): Rock alteration in alkaline cement waters over 15 years and its relevance to the geological disposal of nuclear waste. Applied Geochemistry 50, 91-105.

Nied, D., Enemark-Rasmussen, K., L'Hopital, E., Skibsted, J. & Lothenbach, B. (2016): Properties of magnesium silicate hydrates (M-S-H). Cement and Concrete Research 79, 323-332.

Rey, M., Bárcena, I. & García-Siñeriz, J.L. (2015): Full Dismantling Sampling Plan. Aitemin, .

Roosz, C., Grangeon, S., Blanc, P., Montouillout, V., Lothenbach, B., Henocq, P., Giffaut, E., Vieillard, P. & Gaboreau, S. (2015) : Crystal structure of magnesium silicate hydrates (M-S-H): The relation with 2:1 Mg–Si phyllosilicates. Cement and Concrete Research 73, 228-237.

Sanchez, L., Cuevas, J., Ramirez, S., Riuizdeleon, D., Fernàndez, R., Vigildelavilla, R. & Leguey, S. (2006) : Reaction kinetics of FEBEX bentonite in hyperalkaline conditions resembling the cement–bentonite interface. Applied Clay Science 33, 125-141.

Savage D., Bateman K., Hill P. (1992): Rate and mechanism of the reaction of silicates with cement pore fluids.- Applied Clay Science, 7, 33-45.

Sawhney, B.L. (1970): Potassium and cesium ion selectivity in relation to clay mineral structure. Clays Clay Miner. 18, 47-52.

Svensson, D., Dueck, A., Nielsson, U., Olsson, S., Sandén, T., Lydmark, S., Jägerwall, S., Pedersen, K. & Hansen, S. (2011): Alternative buffer material – status of the ongoing laboratory investigation of reference materials and test package 1. TR-11-06, SKB, www.skb.se, Stockholm, Sweden.

Techer, I., Bartier, D., Boulvais, P., Tinseau, E., Suchorski, K., Cabrera, J. & Dauzères, A. (2012) : Tracing interactions between natural argillites and hyper-alkaline fluids from engineered cement paste and concrete: Chemical and isotopic monitoring of a 15-years old deep-disposal analogue. Applied Geochemistry 27, 1384-1402.

Tinseau, E., Bartier, D., Hassouta, L., Devol-Brown, I. & Stammose, D. (2006): Mineralogical characterization of the Tournemire argillite after in situ interaction with concretes. Waste Management 26, 789-800.

Tonelli, M., Martini, F., Calucci, L., Fratini, E., Geppi, M., Ridi, F., Borsacchi, S. & Baglioni, P. (2016) : Structural characterization of magnesium silicate hydrate: towards the design of eco-sustainable cements. Dalton Trans. 45, 3294-3304.

Tuller, M., Kulkarni, R. & Fink, W. (2013): Segmentation of X-ray CT data of porous materials: A review of global and locally adaptive algorithms. Soil–Water–Root Processes: Advances in Tomography and Imaging: 157-182.

Turrero, M.J., Torres, E., Garralon, A., Sanchez, L., Alonso, M.C., García Calvo, J.L., Laguna, V.F., Cuevas, J., Ruiz, A.L., Fernandez, R., Ortega, A. & Gonzalez, D. (2016): Shotcrete and Shotcrete/Bentonite Analysis, FEBEX-DP Partner Meeting, May 3rd-4th, 2016, Kartause Ittingen, Switzerland.

Villain, G., Thiery, M. & Platret, G. (2007): Measurement methods of carbonation profiles in concrete: Thermogravimetry, chemical analysis and gammadensimetry. Cement and Concrete Research 37, 1182-1192.

Villar, M.V. (Ed.) et al. (2006): FEBEX Project Final report. Post-mortem bentonite analysis. Publicación Técnica Enresa 05-1/2006, Madrid, 183 pp.

Villar, M.V., Iglesias, R.J., Abós, H., Martínez, V., de la Rosa, C. & Manchón, M.A. (2016a): FEBEX-DP onsite analyses report. NAB 16-12. 106 pp.

Villar, M.V.(ed). (2017): FEBEX-DP Postmortem THM/THC Analysis Report. NAB 16-017. 143 pp.

Villar, M.V., Iglesias, R.J., Gutiérrez-Alvarez, C., Carbonell, B., Campos, R., Campos, G., Martín, P.L. & Castro, B. (2018): FEBEX-DP: Thermo-hydro-mechanical postmortem analysis of bentonite performed at CIEMAT. Technical report CIEMAT/DMA/2G216/2/16. NAB 16-24. Madrid.

Watson, C.E., Savage, D., Wilson, J., Walker, C. & Benbow, S.J. (2012): The long-term cement studies project: the UK contribution to model development and testing. Mineralogical Magazine 76, 3445-3455.

Wersin, P. & Kober, F. (2017): FEBEX-DP – Metal Corrosion and Iron-Bentonite Interaction Studies. Nagra Technical Report NAB 16-016, Nagra, Wettingen, Switzerland

Wolters, F. & Emmerich, K. (2007). Thermal reactions of smectites—Relation of dehydroxylation temperature to octahedral structure. Thermochimica Acta 462, 80-88.

Appendix A: Results of Concrete/rock interface analysis (Obayashi)

Obayashi was the only institution focusing on concrete/rock interface analyses. The aim of their work was to investigate the internal structure and mineralogy of the concrete and granite at the interface level and compare a sample from the dismantling of heater #1 with another from the dismantling of heater #2. The study is based on XRD-CT analyses.

A.1 Sample CG-C-31-OB1

Fig. 169 shows images of cross-section layers of the concrete/rock interface of sample CG-C-31-OB1 (5 sections from layer 100 to 700 each 150 layers) (dismantling of heater #1). The upper half of each layer corresponds to concrete and the lower half to granite. Different grey values in the images correspond to different density crystals and black represents voids and cracks. A net black line is observed separating concrete and granite, what is interpreted as a crack produced by shrinkage after concrete exposition to air for 13 years. This fact is observed in all the samples taken from the first dismantling but is not observed in any of the 2015 dismantling samples. Coarse and homogeneous dark grey grains on the concrete side correspond with aggregates. Fig. 170 shows vertical cross sections acquired by rearrangement of cross-sections. The left side is granite and the right side is concrete. The concrete seems densely packed. Setting the threshold to histogram of brightness and using a cluster labelling method, 3-D image of voids is computed (Fig. 171).

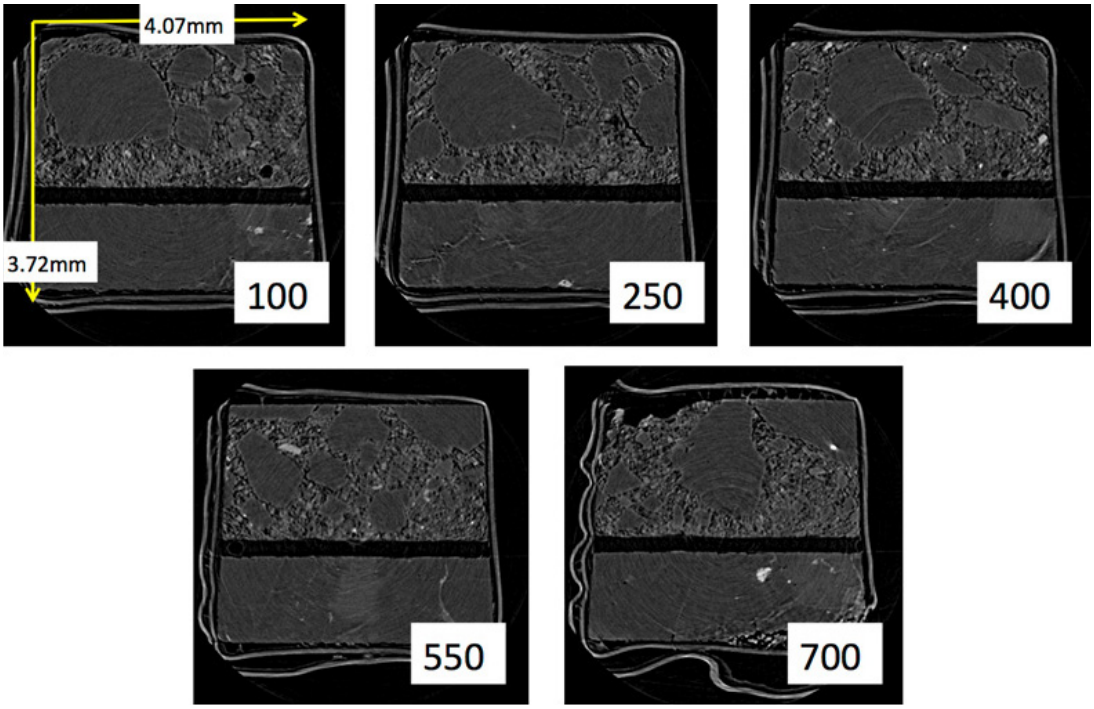

Fig. 169: CT images of different cross sections (layers) of the concrete/rock interface of sample CG-C-31-OB1. Upper half of the images corresponds to concrete and lower half to granite.

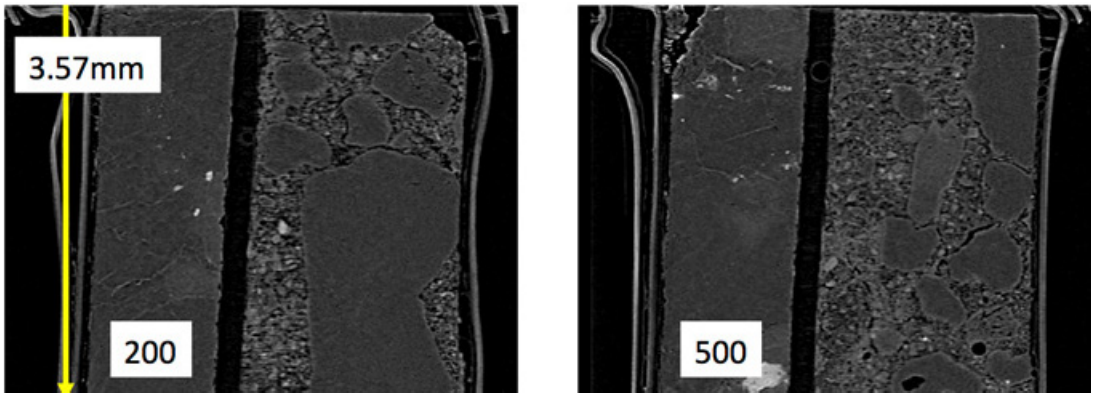

Fig. 170: CT images of two vertical cross sections (layers) of the concrete/rock interface of sample CG-C-31-OB1. Right side of the images corresponds to concrete and left side to granite.

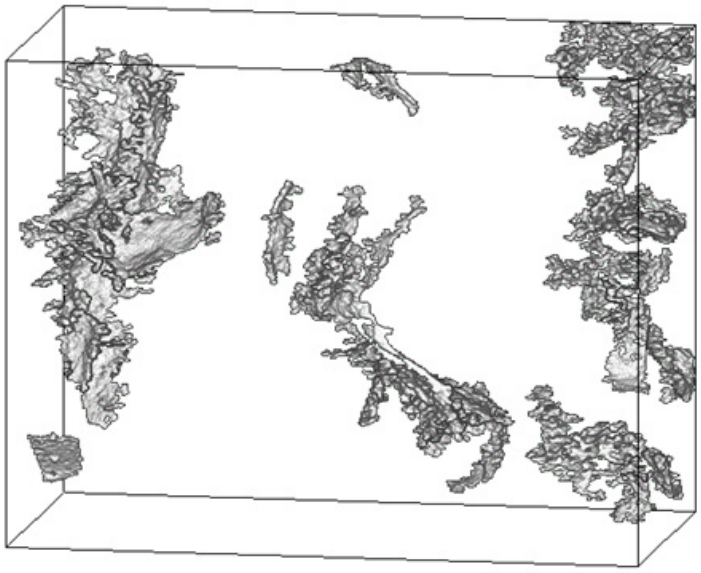

Fig. 171: Example of 3-D image of voids in the concrete/rock sample CG-C-31-OB1.

XRD was performed at layer 200. Fig. 172 shows observation point 1 where the analysis was made and Fig. 173 shows the results of diffraction profiles with the corresponding mineral data. Calcite and clay minerals, specifically illite, are observed. The latter indicates a certain interaction of the concrete with granite during the operation of heater #1. Savage (1992) mentioned argillation (especially illitisation) of granite in high-alkali water immersion tests. The observed feldspars are attributed to aggregates.

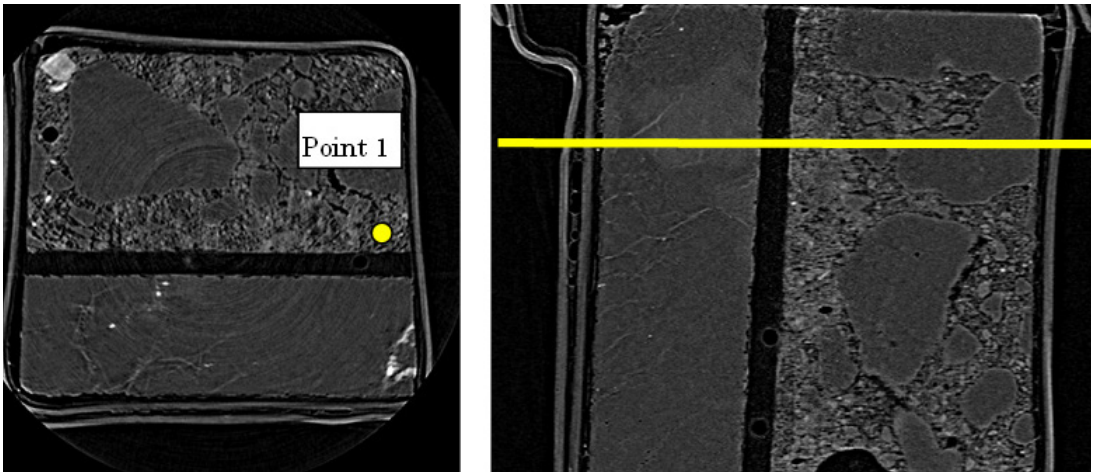

Fig. 172: XRD analysis was made on selected point 1 in layer 200. On the right side the yellow line indicates the vertical cross section.

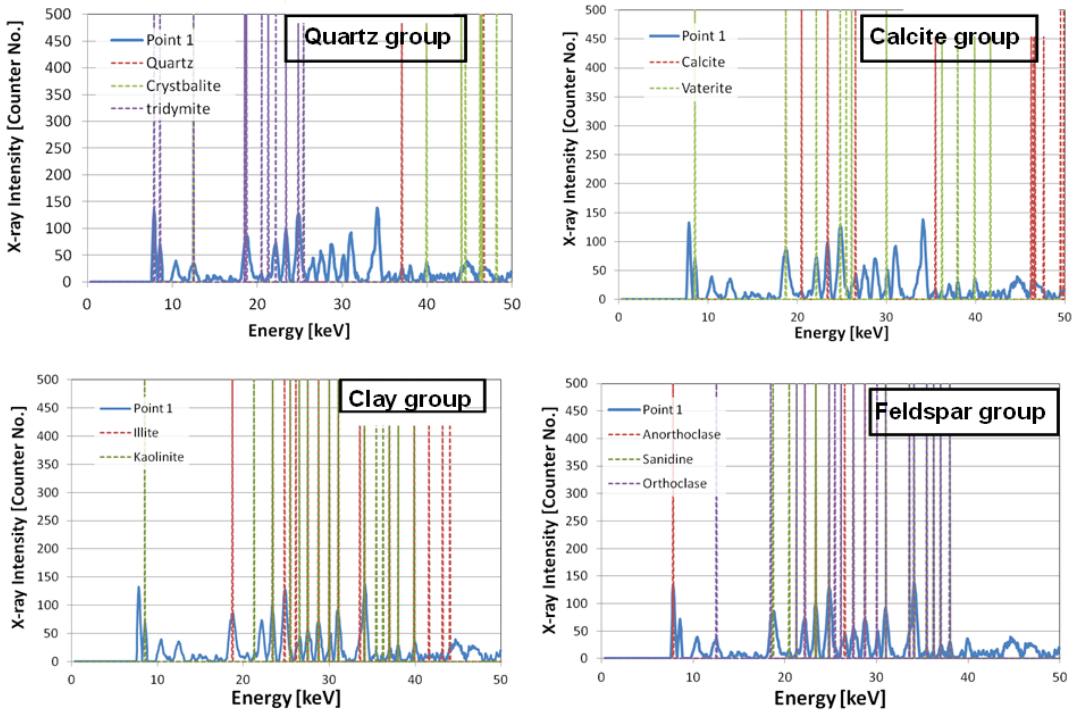

Fig. 173: Diffraction profiles in layer 200, point 1 (see Fig. 172) with mineral data identified.

A.2 Sample CG-C-32-OB5

Fig. 174 shows images of cross section layers of the concrete/rock interface of sample CG-C-32-OB5 (dismantling of heater #2). 5 cross sections from layers 100 to 700, each 150 layers, were made. The upper half of each layer corresponds to concrete and the lower half to granite. Different grey values in the images correspond to different density crystals and black

represents voids and cracks. Porosity in the concrete is very high in all the layers, which is attributed to the shotcreting technique and also to the result of rebound, as seen in previous chapters. Fig. 175 shows a vertical cross sections in which the upper side is granite and the lower side is concrete. The high porosity in the concrete is easily visible in this section as well.

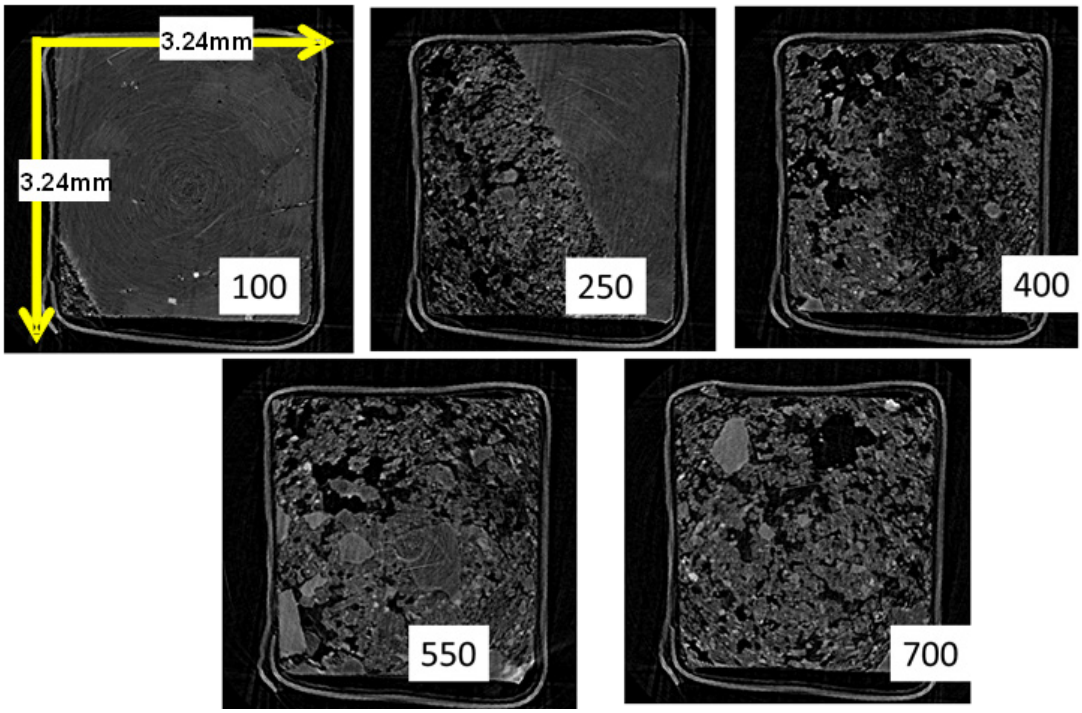

Fig. 174: CT images of different cross sections (layers) of the concrete/rock interface of sample CG-C-32-OB5. Upper half of the images corresponds to concrete and lower half to granite.

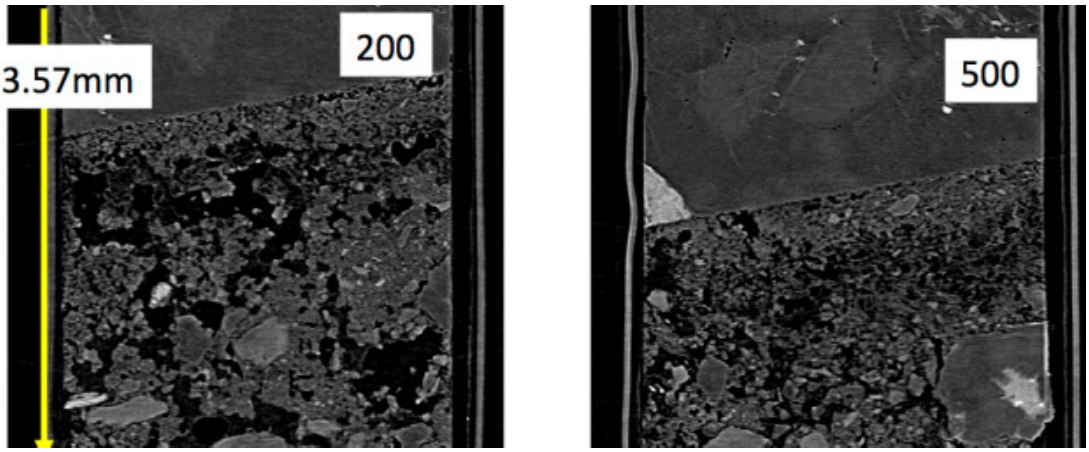

Fig. 175: CT images of two vertical cross sections (layers) of the concrete/rock interface of sample CG-C-32-OB5. Lower part of the images corresponds to concrete and upper part to granite.

Setting the brightness thresholds, the digitized 3-D images of voids are computed. In addition, by combining this with a cluster labelling algorithm, isolated voids are distinguishable. Fig. 176 shows 3-D image of voids. The left picture shows, again, a high porosity and interconnected voids in the concrete at the interface with the rock, what can lead to a high permeability in the boundary area of the concrete/rock.

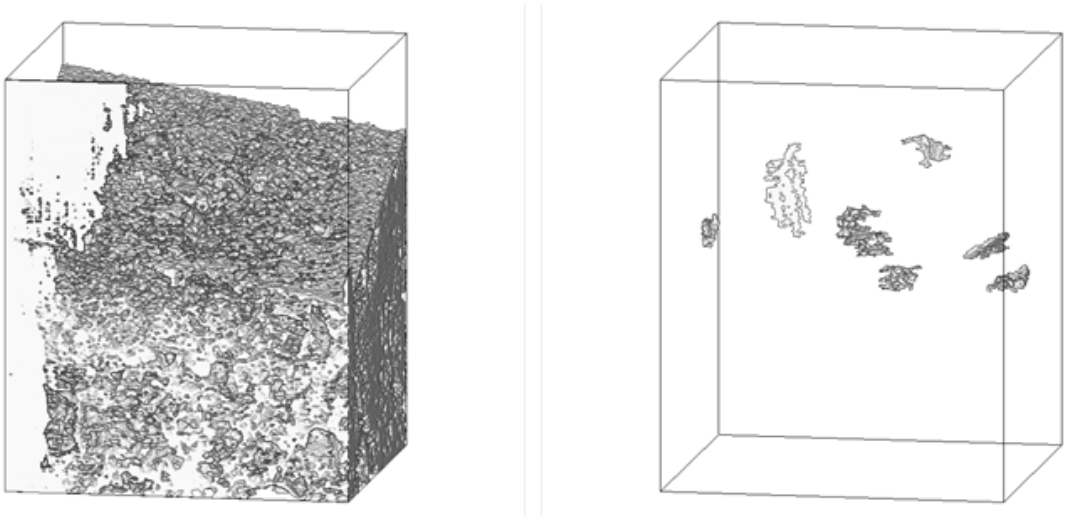

Fig. 176: Example of 3-D image of voids in the concrete/rock sample CG-C-32-OB5.

XRD analysis was performed at the layer 200. Fig. 177 shows observation point 1~4 in a horizontal cross section. The location of layer 200 is shown with a dashed line in a vertical cross section. Point 1~3 are located in concrete area and point 4 is located in the granite area. Point 3 and 4 are close to interface.

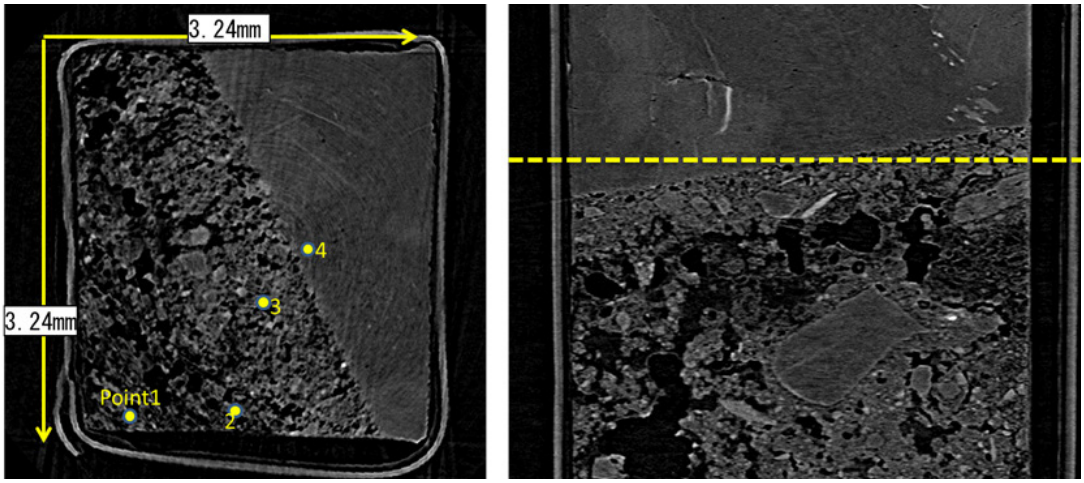

Fig. 177: XRD analysis was made on selected points 1 to 4 in layer 200 of the sample CG-C-32-OB5. On the right side the yellow line indicates the vertical cross section.

Fig. 178 shows the result of diffraction profiles. Similar patterns can be seen at Point 1 and Point 2. Point 3 appears to be a combination of concrete and rock (Points 1 and 4). The intensity of some peaks between ~ 22 keV to ~ 32 keV seem to change gradually (increasing intensity) from point 1 to 4.

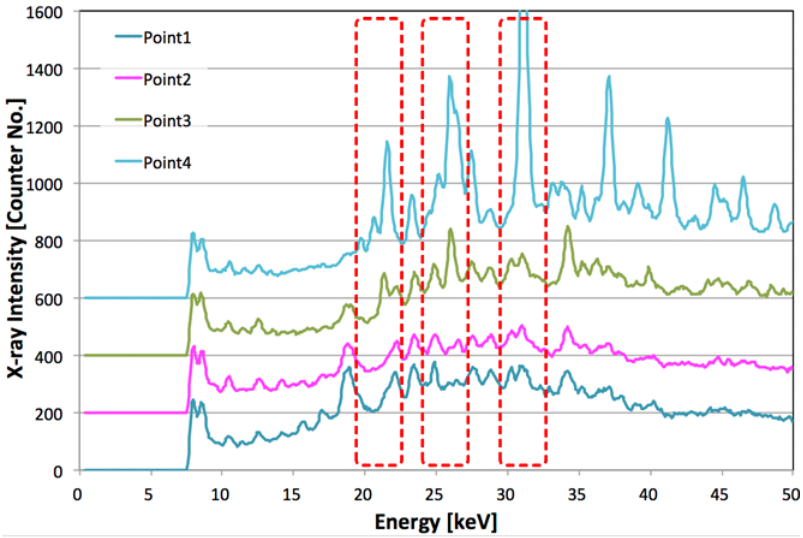

Fig. 178: Diffraction profiles of observed points 1 to 4 in layer 200 of sample CG-C-32-OB5.

Fig. 179 shows the result of diffraction profiles compared to the peaks of the quartz group database. Point 2 is omitted because it is very similar to point 1. All points showed good agreement with the quartz groups peaks.

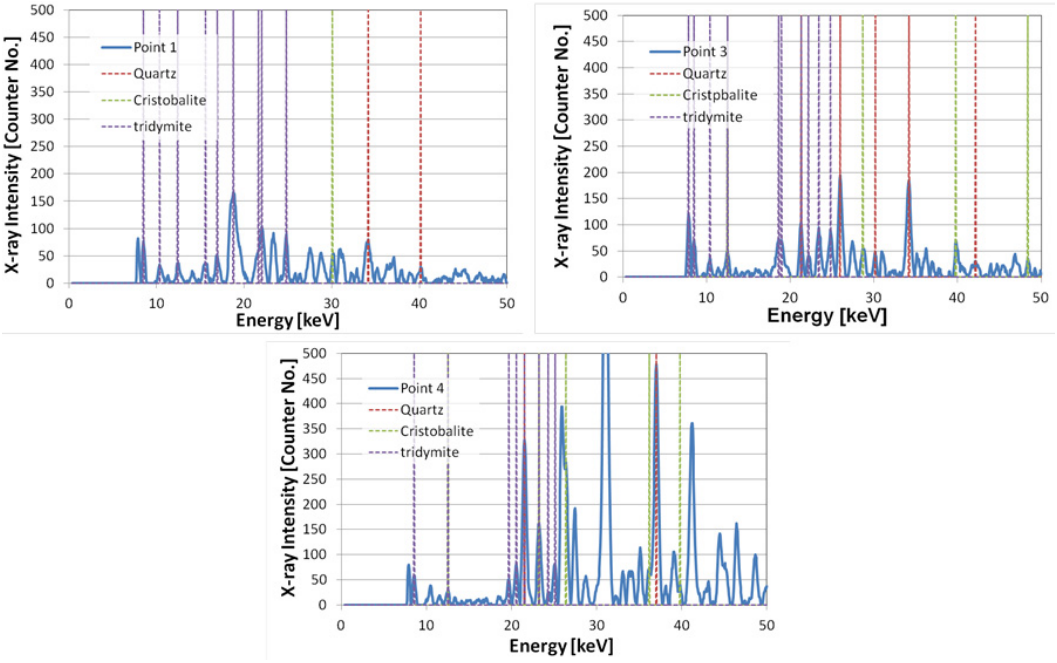

Fig. 179: Diffraction profiles of points 1 to 4 of layer 200 of sample CG-C-32-OB5 compared with quartz group profile database.

Fig. 180 shows the result of diffraction profiles compared to those of the calcite group. Point 1 and point 3, which are in the concrete area, showed good matches with calcite group. Point 4 in granite exhibits a low calcite group content.

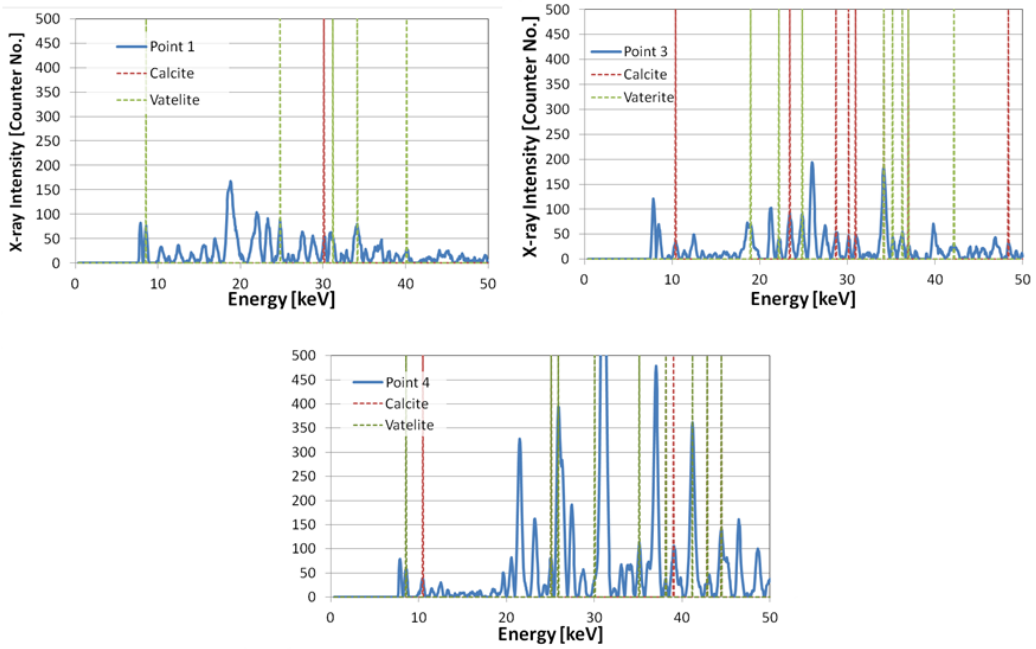

Fig. 180: X-ray profiles of sample CG-C-32-OB5 at the different points of layer 200 compared to calcite group database.

Fig. 181 shows the result of diffraction profiles compared to those of the clay group. All point showed good agreement with kaolinite and low illite content.

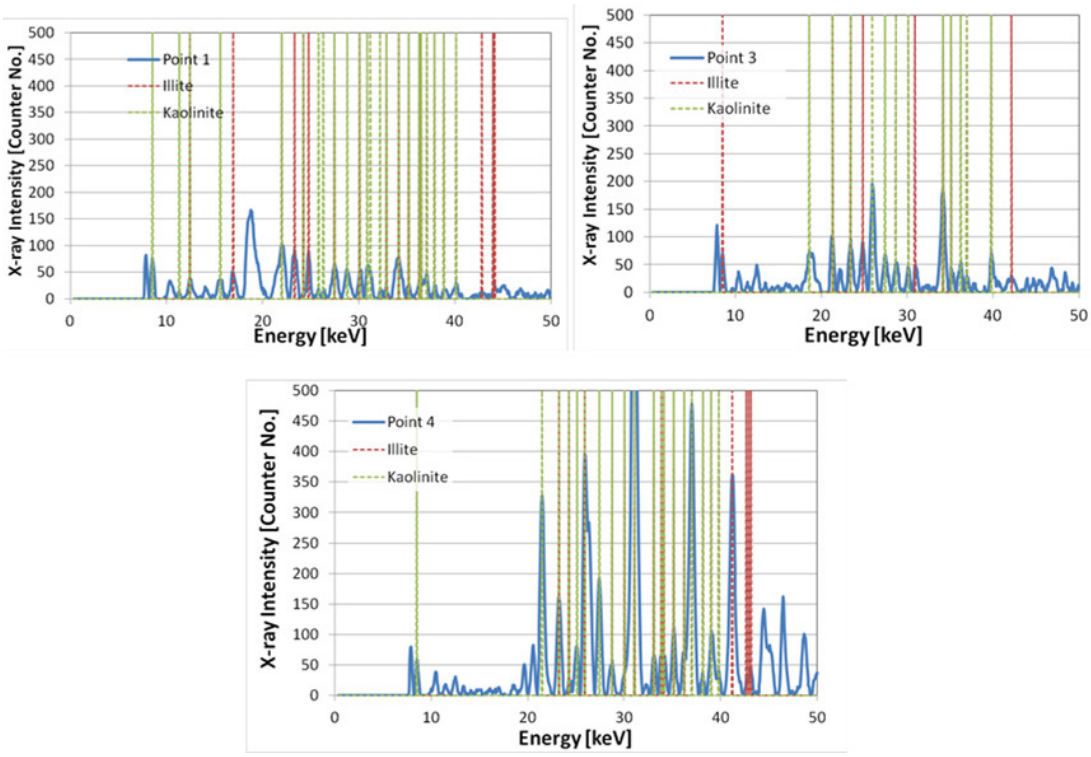

Fig. 181: X-ray profiles of sample CG-C-32-OB5 at different points of layer 200 compared to those of the clay group.

Fig. 182 shows the result of diffraction profiles compared to the feldspar group. All points showed good agreement with orthoclase. Point 1 and 3 consist of cement hydrate and aggregate, so the orthoclase signals from these points are considered to come from aggregates.

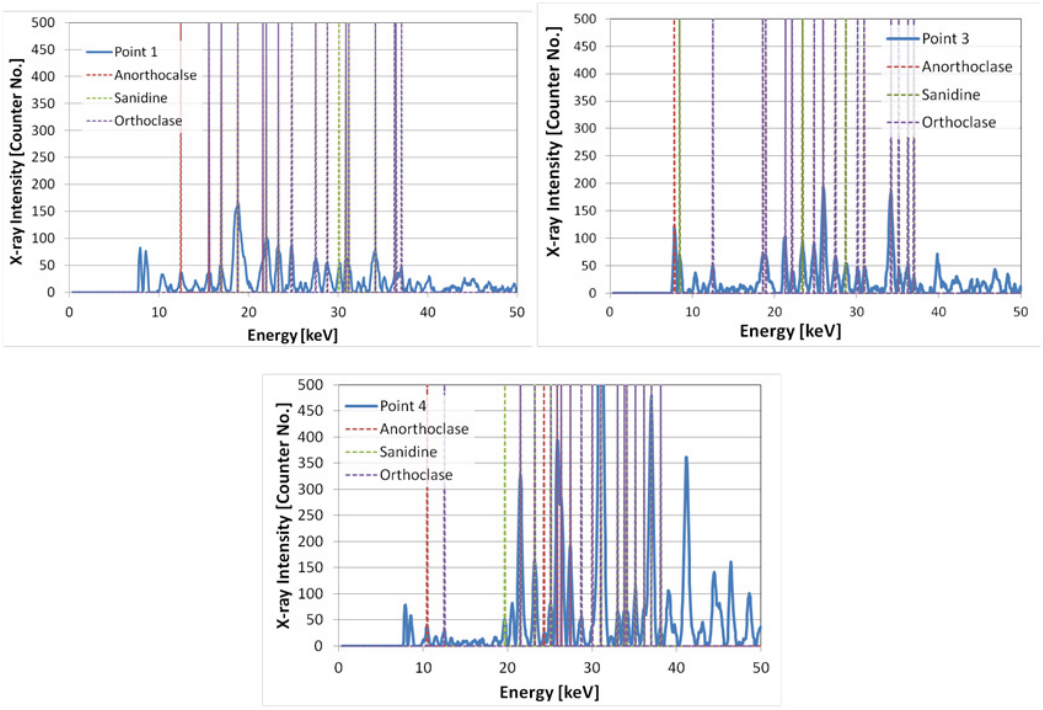

Fig. 182: X-ray profiles of sample CG-C-32-OB5 at different points of layer 200 compared to those of the feldspar group.

A.3 Summary

An integrated XRD-CT method was applied to the concrete/granite interface with the following highlights:

- The concrete/rock interface sampled at the dismantling of heater #1 of the FEBEX experiment presents a space attributed to shrinkage by exposition to air for 13 years. The micro-XRD analysis showed the presence of calcite and clay minerals, specifically illite, which may be the product of the alkaline interaction of the concrete and the granite before first dismantling.

- The concrete/rock interface coming from the dismantling sample of heater #2 of the FEBEX experiment does not have the space between concrete and granite. However, high porosity is observed in the concrete, what may be due to the shotcreting technique and the rebound material when applying it. Calcite is found in the concrete side, but illite is not present.

Appendix B: Data on Concrete Ageing

B.1 Samples

Tab. B-1: Length and characterisation of samples from core C-C-32-1. Last column is a list of all tests executed.

Core Sections	Sample identification	Height/ cm	Core long fraction/ cm	Distance from Bentonite/ cm	Tests
Section 2	**CC 32 1-1**	0.00-0.50	50	296-246	-
	CC 32 1-2	0.50-1.03	53	246-193	-
	CC 32 1-3	1.03-1.92	89	193-104	permeability, compressive strength, ultrasound, capillary suction, microstructure
Section 1	**CC 32 1-4**	1.92-2.10	18	104-86	permeability,
	CC 32 1-5	2.10-2.41	31	86-55	-
	CC 32 1-6	2.41-2.76	35	55-20	compressive strength, ultrasound, capillary suction
	CC 32 1-7	2.76-2.86	10	20-10	compressive strength, ultrasound
	CC 32 1-8	2.86-2.93	7	10-3	Microstructure, capillary suction
	CC 32 1-9	2.93-2.96	3	3-0	Microstructure

Tab. B-2: Length and characterisation of samples from core C-C-32-2. Last column is a list of all tests carried out.

Core Sections	Sample identification	Height/ cm	Core long fraction/ cm	Distance from Bentonite/ cm	Tests
Section 2	**CC 32 2-1**	0.00-0.06	6	291-285	-
	CC 32 2-2	0.06-0.09	3	285-282	-
	CC 32 2-3	0.09-0.34	25	282-257	-
	C-C-32-2-4	0.34-0.61	27	257-230	-
	C-C-32-2-5	0.61-0.83	22	230-208	-
	C-C-32-2-6	0.83-1.05	22	208-186	-
	C-C-32-2-7	1.05-1.93	88	186-98	permeability, compressive strength, ultrasound, capillary suction, microstructure
	C-C-32-2-8	1.93-2.00	7	98-91	
Section 1	**C-C-32-2-9**	2.00-2.06	6	91-85	microstructure
	C-C-32-2-10	2.06-2.22	16	85-69	compressive strength
	C-C-32-2-11	2.22-2.86	64	69-5	permeability, capillary suction
	C-C-32-2-12	2.86-2.91	5	5-0	microstructure

Tab. B-3: Length and characterisation of samples from core C-C-32-3. Last column is a list of all tests carried out.

Core Sections	Sample identification	Height/ cm	Core long fraction/ cm	Distance from Bentonite/ cm	Tests
Section 2	**CC 32 2-1**	0.00-0.06	6	291-285	-
	CC 32 2-2	0.06-0.09	3	285-282	-
	CC 32 2-3	0.09-0.34	25	282-257	-
	C-C-32-2-4	0.34-0.61	27	257-230	-
	C-C-32-2-5	0.61-0.83	22	230-208	-
	C-C-32-2-6	0.83-1.05	22	208-186	-
	C-C-32-2-7	1.05-1.93	88	186-98	permeability, compressive strength, ultrasound, capillary suction, microstructure
	C-C-32-2-8	1.93-2.00	7	98-91	
Section 1	**C-C-32-2-9**	2.00-2.06	6	91-85	microstructure
	C-C-32-2-10	2.06-2.22	16	85-69	compressive strength
	C-C-32-2-11	2.22-2.86	64	69-5	permeability, capillary suction
	C-C-32-2-12	2.86-2.91	5	5-0	microstructure

Tab. B-4: Coordinates of samples studied by UAM. Cores start at X=6.882 and ends approximately 10 cm before the coordinate 7.882. X coordinates in the following table starts at 0 (X = 6.882).

Sample	Coordinates Y (cm)	Coordinates Z (cm)	Coordinates X (m)
CC-34-4	-38	-46	7.882
CC-34-5	-25.41	-26.86	7.882
CC-34-6	-2.35	2.84	7.882
CC-34-7	20.48	25.67	7.882
CC-34-8	40.65	53.17	7.882
CC-34-9	61.05	78.22	7.882
CC-34-10	62.38	88.42	7.882
CC-34-11	67.26	104.16	7.882

B.2 Mineralogical characterization by XRD (UAM)

To carry out the mineralogical analyses by powder diffraction it is necessary to have a well-ground specimen where the particles are randomly oriented in order to produce a uniform intensity. To optimize the XRD analysis for the studied samples, it is necessary to remove, as much as possible, the aggregates of the concrete, the most inert materials, as quartz and feldspar. To obtain a suitable fraction for analysis, the concrete samples were crushed with a vice clamp obtaining small-sized samples. These crushed samples were ground in a HERZOG ring mill at three different grinding times (2, 5 and 10 s), obtaining samples of different fineness by adjusting the milling time. Then, each of these samples was separated into size fractions by sieving through three size-fractions: 1.000, 0.500, 0.125 and 0.050 mm. These fractions were hand-ground in an agate mortar and stored in open polycarbonate tubes during > 48 h in a 50% relative humidity chamber (controlled by $MgNO_3$ saturated solution at 25 °C and by a deposit of NaOH pellets as CO_2 absorbing material). Then, the sieved fractions were analysed by means of random powder XRD.

The best conditions for the analyses were found for a time of 2 s (minimum time) in the mill and sieved through the 0.05 mm sieve because of the lowest observed intensities of the feldspar reflections (Fig. 1).

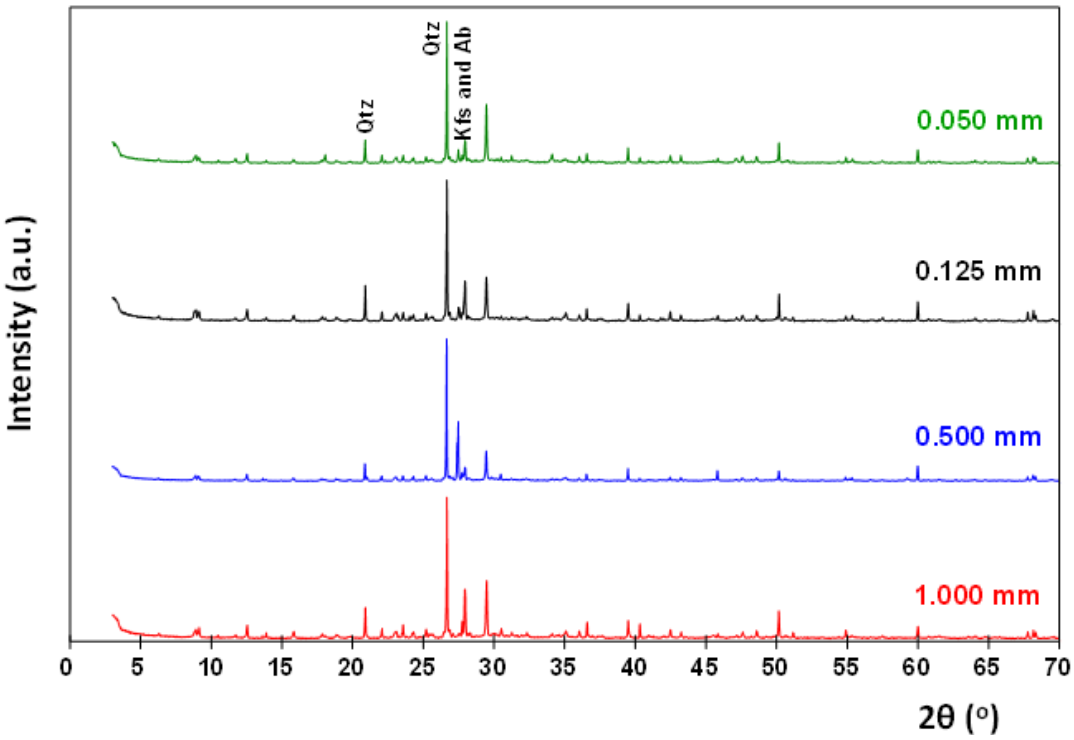

Fig. 183: X-Ray diffraction patterns for CC34-11-12_22 sample for 2s in the mill and four different sieves (1.000, 0.500, 0.125 and 0.050 mm).

The mineral composition in concrete matrix sieved to 0.05 mm was determined by X-ray diffraction (XRD). The XRD patterns registered from bulk, randomly-oriented powders were recorded in an angular range (º2θ) of 3-70º in a θ/2θ X-PERT Panalytical instrument with an X-CELERATOR detector. This set-up allowed taking measurements equivalent to 0.016º

angular steps during 100 s each step. Voltage and Intensity of the operated X-ray Cu tube were 45 Kv and 40 Ma, respectively. The equipment uses monochromatic radiation provided by a Ge 111 monochromator. The slit settings were: soller slit (0.04 rad); divergence and antiscatter slits both 0.5º.

To quantify cement phases, the combination of the Rietveld Structure Refinement (RSR) and semi-quantitative Reference Intensity Ratio (RIR) methods have been used. The quantification obtained by RSR has been used as reference to vary the RIR ratios used for semi-quantitative analysis on the basis of several ICDD powder diffraction files (PDF) standards supported in High Score Expert plus © software 220 (vs. 2.1.b 2005).

Several data registered form C-C-34-11 core were refined using SIROQUANT™. The starting structure models were taken from the database of the program and then the background was successfully fitted. The peak profiles were modeled using a pseudo-Voigt function with one Gaussian and one Lorentzian coefficient. The scale factor, lattice constants, u, v, w and asymmetry parameters were also refined for each phase step by step. Fig. 2 displays the observed, calculated and difference X-ray diffraction profile for CC-34-11 (12-22 cm) of the Rietveld refinement. The difference between the diffraction profiles and the values of the R-factors obtained confirm the validity of the structural models. For this reason, and with the quantification obtained by this method, the RIR factors are recalculated (Tab. B-2) and modified in the database of the X'Pert High Score Plus program. Tab. B-3 show the list of PDF files considered for concrete quantification.

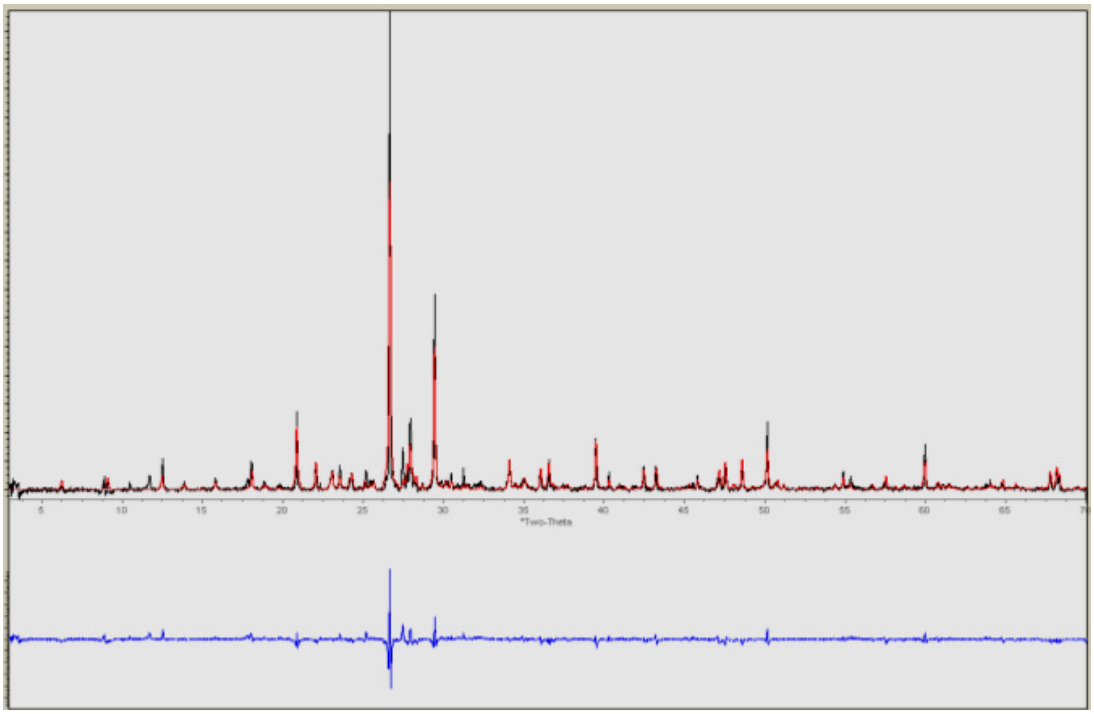

Fig. 184: Calculated and observed XRD patterns and difference spectrum for CC-34-11-(12_22 cm) Using SIROQUANT™ (RF=5.6 and Chi^2=8.5)

Tab. B-5: Mineralogical quantification of sample CC-34-11-(12_22 cm) and recalculated RIR factors used in HighScore Plus XRD analyses software program.

Phase	RIR X'Pert High Score Plus	% Quantification by Siroquant	recalculated RIR	% Quantification with recalculated RIR
Quartz	3.10	34		23
Calcite	3.20	23	1.4	23
Albite	0.62	22	0.7	17
Ettringite	1.0*	5	0.45	5
Clinochlore	1.0*	6	1.0	5
Muscovite	2.0*	1	2.0	2
Portlandite	3.50	4	0.5	13
Biotite	1.43	1	1.37	2
CSH Tobermorite 9Å**	1.0*	0	1.0	<1
Orthoclase	0.82	4		8
Gypsum	1.70	<1	1.7	1
Cordierite***	2.09	0		1

* RIRs for these phases was not found or was find to vary a lot within similar phases in the data base. They were assigned as 1, or 2 in the case of muscovite (RIRs varies from 2-4).

** Some broad reflection effects have been observed near 29-30 º2Θ. The CSH 9Å phase was selected because it has been identified previously in poorly ordered CSH components.

** A phase located in d=8.2 Å was systematically assigned to cordierite by the software. Several amphiboles show this reflection as one of the most intensity peaks. So far, these phases are minority and could not be unequivocally assigned.

Tab. B-6: Minerals identified and RIR values considered for semi-quantitative determination of mineral phases using High Score Plus® panalytical software.

Mineral	Mineral PDF ICDD file	Modified or assigned reference intensity ratio (RIR)
Qtz = quartz	01-085-0796	3.1
Cal = calcite	00-024-0027	0.5
Clc =Clinochlore	00-029-0701	1.0
Ms = Muscovite	00-006-0263	2.0
Bt = Biotite	01-080-1107	1.4
Ab = Albite	01-084-0752	0.6
Or = Orthoclase	01-075-1592	0.8
Crd = Cordierite	01-077-0293	2.1
Etr = Ettringite	00-013-0350	0.5
Gp = Gypsum	00-006-0046	1.7
Port = Portlandite	001-087-0673	0.5
CSH = (tobermorite 9Å)	00-010-0374	0.7

B.3 Soluble ions results (UAM)

Tab. B-7: Soluble (aqueous extractable) ions in concrete. The sum of cations is higher than anions due to the OH- contribution during the dissolution of the cement matrix.

Sample	Coord. X (cm)	Coord. Y (cm)	Coord. Z (cm)	mmol/100g										
				F^-	Cl^-	NO_3^-	SO_4^{2-}	Σ Anion	Na^+	NH_4^+	K^+	Ca^{2+}	Mg^{2+}	Σ Cation
C-C-34-4	5	-38	-46	0.009	0.185	0.009	0.124	0.33	7.55	0.31	6.47	26.76	< 0.01	41.09
	50	-38	-46	0.015	0.153	0.005	0.321	0.49	8.87	< 0.01	4.12	18.95	< 0.01	31.94
	85	-38	-46	0.016	0.179	0.005	0.582	0.78	10.51	0.38	6.85	13.21	< 0.01	30.95
C-C-34-5	5	-25	-27	0.014	0.154	0.017	0.135	0.32	6.61	0.37	5.91	29.60	< 0.01	42.50
	50	-25	-27	0.025	0.137	0.081	0.314	0.56	8.44	0.15	6.91	17.71	< 0.01	33.21
	89	-25	-27	0.017	0.164	0.000	1.024	1.20	12.48	0.32	9.73	10.34	< 0.01	32.86
C-C-34-6	5	-2	3	0.021	0.155	0.007	0.094	0.28	6.06	< 0.01	5.52	44.85	< 0.01	56.44
	50	-2	3	0.018	0.110	0.002	0.892	1.02	7.92	0.41	6.38	25.20	< 0.01	39.91
	88	-2	3	0.019	0.137	0.004	0.144	0.30	8.55	0.33	6.69	33.22	< 0.01	48.79
C-C-34-7	5	20	26	0.020	0.279	0.004	1.321	1.62	3.38	< 0.01	4.78	15.92	< 0.01	24.09
	50	20	26	0.011	0.163	0.000	0.223	0.40	8.52	0.17	7.58	11.21	< 0.01	27.47
	87	20	26	0.018	0.167	0.003	0.202	0.39	11.85	0.31	7.97	22.43	< 0.01	42.56
C-C-34-8	5	41	53	0.013	0.133	0.000	0.341	0.49	5.92	0.24	5.60	28.09	< 0.01	39.86
	50	41	53	0.019	0.281	0.017	0.464	0.78	9.34	0.30	8.17	11.55	< 0.01	29.36
	88	41	53	0.017	0.148	0.003	0.097	0.26	8.72	0.21	7.35	40.71	< 0.01	56.99
C-C-34-9	4	61	78	0.013	0.192	0.002	0.236	0.44	4.63	0.17	3.79	25.29	< 0.01	33.88
	25	61	78	0.018	0.133	0.000	0.333	0.48	7.14	0.14	6.34	27.56	< 0.01	41.19

Sample	Coord. X (cm)	Coord. Y (cm)	Coord. Z (cm)	mmol/100g											
				F^-	Cl^-	NO_3^-	SO_4^{2-}	Σ Anion	Na^+	NH_4^+	K^+	Ca^{2+}	Mg^{2+}	Σ Cation
	50	61	78	0.015	0.122	0.000	0.168	0.30	7.23	0.27	6.48	29.43	< 0.01	43.42
	76	61	78	0.019	0.119	0.000	1.307	1.45	7.97	0.31	6.84	13.84	< 0.01	28.95
	85	61	78	0.014	0.120	0.002	0.232	0.37	7.57	0.27	6.70	25.86	< 0.01	40.40
C-C-34-10	5	62	88	0.021	0.336	0.038	0.222	0.62	3.94	0.09	3.99	31.13	< 0.01	39.15
	50	62	88	0.016	0.222	0.003	0.381	0.62	7.48	0.36	6.38	17.11	< 0.01	31.33
	87	62	88	0.014	0.115	0.000	0.411	0.54	8.20	0.09	6.75	24.84	< 0.01	39.87
C-C-34-11	5	67	104	0.033	1.426	0.000	2.953	4.41	6.11	0.21	5.05	33.59	< 0.01	44.96
	17	67	104	0.032	0.596	0.000	0.262	0.89	8.73	0.57	8.44	24.83	< 0.01	42.56
	28	67	104	0.036	0.856	0.000	3.229	4.12	11.24	0.68	9.91	12.02	< 0.01	33.86
	34	67	104	0.041	0.836	0.000	0.771	1.65	9.32	1.01	8.10	18.17	< 0.01	36.60
	40	67	104	0.024	0.570	0.000	0.810	1.40	10.45	0.44	8.50	11.68	< 0.01	31.07
	45	67	104					-	-	-	-	-	-	-
	51	67	104	0.025	0.531	0.000	0.189	0.74	8.47	0.52	7.51	25.31	< 0.01	41.80
	63	67	104	0.044	0.598	0.015	0.696	1.35	13.23	0.66	9.72	45.02	< 0.01	68.63
	73	67	104	0.024	0.210	0.000	0.136	0.37	8.10	0.28	5.78	43.19	< 0.01	57.35
	85	67	104					-	-	-	-	-	-	-
	93	67	104	0.041	0.416	0.011	1.743	2.21	15.10	0.29	10.75	42.55	< 0.01	68.69

B.4 Mineralogical characterisation (UAM)

Tab. B-8: Mineralogical characterisation by XRD (total sample).

Sample	Coord. X (cm)	Coord. Y (cm)	Coord. Z (cm)	Weigth %											
				Qtz	Cal	Ab	Or	Crd/ Amp	Clc	Ms	Bt	Etr	Gp	CSH	Port
CC-34-4	5	-38	-46	31	25	14	4	-	5	4	2	13	1	1	-
	50	-38	-46	29	27	9	7	1	5	4	2	14	1	1	-
	85	-38	-46	35	25	9	5	-	5	5	3	11	1	-	1
CC-34-5	5	-25	-27	37	25	9	5	-	5	5	2	10	1	-	1
	50	-25	-27	32	28	9	5	1	6	5	2	10	1	1	1
	89	-25	-27	27	29	14	7	-	7	6	1	7	1	1	1
CC-34-6	5	-2	3	38	17	10	9	1	6	4	2	6	1	1	5
	50	-2	3	34	26	9	5	1	4	3	3	7	1	3	3
	88	-2	3	24	26	14	11	1	4	3	3	10	1	1	3
CC-34-7	5	20	26	30	26	15	6	1	4	3	3	6	-	4	1
	50	20	26	27	31	10	5	-	5	3	3	14	1	1	1
	87	20	26	28	23	15	6	1	8	4	3	8	1	-	4
CC-34-8	5	41	53	33	25	13	6	1	5	5	3	6	1	-	3
	50	41	53	33	23	19	5	-	3	3	2	10	1	-	1
	88	41	53	27	25	15	7	-	6	5	-	4	1	1	9
CC-34-9	4	61	78	34	29	10	4	-	3	2	1	12	1	1	3
	25	61	78	30	23	12	4	-	5	4	1	12	1	1	6
	50	61	78	32	27	10	4	1	5	3	2	9	1	1	5
	76	61	78	39	23	10	7	-	5	3	2	9	1	1	1
	85	61	78	30	25	13	8	-	4	3	2	9	1	-	5

Sample	Coord. X (cm)	Coord. Y (cm)	Coord. Z (cm)	Weigth %											
				Qtz	Cal	Ab	Or	Crd/ Amp	Clc	Ms	Bt	Etr	Gp	CSH	Port
CC-34-10	5	62	88	33	27	13	5	-	5	3	2	8	-	1	3
	50	62	88	28	29	9	6	1	5	3	2	14	1	1	1
	87	62	88	33	28	8	6	-	6	5	1	5	2	-	5
CC-34-11	5	67	104	28	26	11	5	-	3	3	2	17	1	1	3
	17	67	104	29	25	8	9	1	4	3	2	5	2	1	13
	28	67	104	28	25	12	6	-	4	3	1	16	1	3	2
	34	67	104	33	20	11	5	-	5	3	1	11	1	1	10
	40	67	104	28	27	11	8	-	4	3	2	12	1	1	3
	45	67	104	32	27	13	7	-	3	3	2	6	1	-	5
	51	67	104	27	30	9	6	-	4	3	2	5	1	1	10
	63	67	104	31	26	11	6	-	4	2	1	13	1	1	3
	73	67	104	23	29	16	7	1	3	2	1	8	2	2	6
	85	67	104	24	27	14	6	-	6	3	2	13	1	1	3
	93	67	104	39	20	11	7	-	7	4	2	8	1	1	1

Tab. B-9: Results for Thermal analysis (TA). Temperature maxima for weight loss and thermogravimetric (TG) data within several temperature intervals (UAM data).

Sample	Coord. X (cm)	Coord. Y (cm)	Coord. Z (cm)	T. maximum (°C)							% weight loss				% Total weight loss
				1	2	3	4	5	6	7	25-300	300-500	500-800	800-1000	
CC-34-9	4	61	78	77	123	366	409	577	717	877	9.2	2.1	8	1.8	21.1
	25	61	78	72	123	374	409	585	709	874	7.6	2.9	7.6	1.3	19.4
	50	61	78	72	123	377	417	577	712	874	6.6	2.9	7.7	1.3	18.6
	76	61	78	77	120	379	417	574	714	872	7.6	2.9	7.8	1.3	19.6
	85	61	78	74	126	374	420	580	712	882	6.9	2.2	7.3	1.3	17.7
CC-34-11	5	67	104	80	120	372	415	564	720	882	9.2	2.3	9.4	2.1	23
	17	67	104	77	123	377	417	585	712	885	10	2.6	8.5	1.5	22.6
	28	67	104	80	123	385	415	574	709	858	11	2.5	7.4	1.3	22.2
	34	67	104	72	126	380	417	568	709	868	8.3	2.6	7.6	1.1	19.6
	40	67	104	72	123	374	415	572	707	866	9	2.3	6.9	1.1	19.3
	45	67	104	74	123	374	415	582	712	872	6.4	2.1	7.7	0.9	17.1
	51	67	104	74	126	377	417	577	712	877	6.7	2.2	7.3	1.2	17.4
	63	67	104	77	126	382	41	572	712	869	9.2	2.5	7.8	1.5	21
	73	67	104	77	126	382	417	582	709	880	8.7	2.7	7	1.7	20.1
	85	67	104	77	126	382	417	572	723	877	7.8	2.3	9.6	1.2	20.9
	93	67	104	74	123	380	420	572	712	890	7.2	2.4	7.5	1.3	18.4

B.5 Carbonation (UAM)

Tab. B-10: Carbonate content, δ13C and δ18O, and specific surface area measured by N2-BET isotherm.

Sample	Coord. X (cm)	Coord. Y (cm)	Coord. Z (cm)	BET m^2/g	BET (error)	$\delta^{13}C_{VPDB}$	$\delta^{18}O_{VPDB}$	$CaCO_3$ Wt.%
C-C-34-4	5	-38	-46	16.3	0.1	-3.78	-8.44	13.42
	50	-38	-46	28.4	0.1	-4.63	-9.59	13.13
	85	-38	-46	17.0	0.1	-4.14	-9.33	15.11
C-C-34-5	5	-25	-27	15.8	0.0	-3.69	-8.37	14.82
	50	-25	-27	15.9	0.1	-4.45	-8.59	15.48
	89	-25	-27	17.0	0.1	-2.64	-7.81	16.14
C-C-34-6	5	-2	3	11.9	0.0	-5.54	-9.25	13.77
	50	-2	3	13.0	0.1	-6.32	-8.70	8.70
	88	-2	3	15.9	0.0	-3.43	-8.23	15.50
C-C-34-7	5	20	26	20.0	0.1	-8.06	-9.15	19.83
	50	20	26	14.3	0.0	-6.27	-8.91	9.01
	87	20	26	17.2	0.0	-2.92	-8.41	14.46
C-C-34-8	5	41	53	16.6	0.1	-5.77	-8.39	15.03
	50	41	53	10.1	0.0	-4.74	-8.50	8.96
	88	41	53	12.9	0.0	-4.71	-8.07	16.83
C-C-34-9	4	61	78	14.2	0.1	-5.58	-8.39	11.74
	25	61	78	8.4	0.1	-5.50	-8.86	10.79
	50	61	78	8.3	0.0	-4.44	-8.03	10.10
	76	61	78	10.7	0.0	-5.25	-8.81	10.05
	85	61	78	5.6	0.1	-5.66	-8.92	10.28

Sample	Coord. X (cm)	Coord. Y (cm)	Coord. Z (cm)	BET m^2/g	BET (error)	$\delta^{13}C_{VPDB}$	$\delta^{18}O_{VPDB}$	$CaCO_3$ Wt.%
C-C-34-10	5	62	88	31.8	0.1	-7.36	-9.00	20.18
	50	62	88	14.4	0.1	-5.03	-8.27	9.03
	87	62	88	20.9	0.1	-5.27	-7.99	15.53
C-C-34-11	5	67	104	16.1	0.1	-6.37	-8.99	15.59
	17	67	104	9.9	0.0	-5.14	-8.63	16.61
	28	67	104	14.6	0.1	-6.35	-8.92	18.18
	34	67	104	9.4	0.1	-4.99	-8.10	19.28
	40	67	104	11.7	0.1	-6.10	-8.68	17.79
	45	67	104	7.6	0.0	-3.62	-8.25	21.50
	51	67	104	7.1	0.1	-4.94	-8.83	25.0
	63	67	104	18.7	0.1	-5.77	-8.84	20.0
	73	67	104	18.2	0.0	-6.88	-9.39	8.76
	85	67	104	12.4	0.1	-4.40	-7.67	22.90
	93	67	104	11.4	0.1	-4.24	-8.75	8.70

Appendix C: Data on Concrete/Bentonite Interface

C.1 Soluble ions by aqueous leaching (Ciemat)

Tab. C-1: Results of soluble salts (mmol/100g) in concrete/bentonite interface samples. Zero corresponds to the concrete/bentonite interface, positive values are for the bentonite side and negative values are for the concrete side.

Sample C-C-34-8												
Distance to the plug (mm)	F^-	Cl^-	NO_2^-	Br^-	NO_3^-	PO_4^{3-}	SO_4^{2-}	Mg^{2+}	Ca^{2+}	Na^+	K^+	NH_4^+
0	0.02	0.85	0.00	0.00	2.01	0.00	26.25	7.07	0.43	5.00	15.1	0.10
3	0.02	0.81	0.00	0.00	0.15	0.00	24.21	0.00	0.00	0.00	22.8	0.00
6	0.07	0.85	0.00	0.00	0.07	0.00	3.66	4.54	0.04	0.05	0.70	5.55
10	0.08	0.84	0.00	0.00	0.00	0.00	3.15	4.67	0.11	0.20	0.45	0.04
14	0.09	0.89	0.00	0.00	0.01	0.00	1.10	3.12	0.06	0.08	0.15	0.03
22	0.10	0.96	0.00	0.00	0.00	0.00	1.04	3.27	0.06	0.07	0.15	0.03
26	0.10	0.89	0.00	0.00	0.00	0.00	0.97	3.10	0.06	0.09	0.14	0.03
34	0.09	0.84	0.00	0.00	0.01	0.00	0.89	2.85	0.05	0.07	0.11	0.03
Sample C-C-34-10												
Distance to the plug (mm)	F^-	Cl^-	NO_2^-	Br^-	NO_3^-	PO_4^{3-}	SO_4^{2-}	Mg^{2+}	Ca^{2+}	Na^+	K^+	NH_4^+
-85	0.14	0.34	0.16	0.01	1.31	0.09	0.00	0.00	1.26	0.11	0.25	1.34
-65	0.15	0.36	0.11	0.01	0.09	0.12	0.00	0.00	1.24	0.11	0.26	1.32
-38	0.12	0.30	0.20	0.01	0.03	0.21	0.00	0.00	1.18	0.11	0.24	1.19
-20	0.17	0.35	0.23	0.01	0.02	0.26	0.00	0.00	1.38	0.12	0.26	1.57
-7.5	0.09	0.23	4.82	0.00	1.13	0.05	0.00	0.00	1.02	0.08	0.18	3.80
-2.5	0.08	0.23	1.28	0.00	0.13	0.04	0.00	0.00	0.89	0.09	0.18	1.12

10	0.08	0.21	2.28	0.00	0.00	0.02	0.03	0.03	0.70	0.03	0.08	0.60
Sample C-C-34-10 (cont.)												
Distance to the plug (mm)	F^-	Cl^-	NO_2^-	Br^-	NO_3^-	PO_4^{3-}	SO_4^{2-}	Mg^{2+}	Ca^{2+}	Na^+	K^+	NH_4^+
20	0.08	0.23	2.38	0.00	0.07	0.08	0.00	0.00	0.00	0.84	0.08	0.79
30	0.09	0.23	2.19	0.00	0.02	0.11	0.00	0.00	0.93	0.07	0.15	0.89
40	0.09	0.22	2.13	0.00	0.01	0.12	0.00	0.00	0.90	0.06	0.13	0.81
Sample C-C-34-12												
Distance to the plug (mm)	F^-	Cl^-	NO_2^-	Br^-	NO_3^-	PO_4^{3-}	SO_4^{2-}	Mg^{2+}	Ca^{2+}	Na^+	K^+	NH_4^+
-80	1.08	16.34	0.06	0.03	0.08	0.00	0.79	17.99	28.40	0.00	13.97	3.22
-74.5	1.18	17.71	0.05	0.03	0.06	0.00	0.92	19.05	25.88	0.07	14.31	3.15
-69	1.75	19.93	0.09	0.03	0.10	0.00	0.58	23.15	27.94	0.05	14.50	4.48
-64	1.72	19.15	0.10	0.03	0.13	0.00	0.60	23.24	19.43	0.04	14.71	4.76
-58.5	1.51	22.73	0.06	0.04	0.05	0.00	0.50	19.46	18.63	0.06	20.91	3.73
-52.5	1.37	19.91	0.07	0.03	0.10	0.00	0.44	16.89	20.11	0.09	23.19	2.94
-48.5	1.59	30.11	0.06	0.04	0.09	0.00	0.39	15.20	12.19	0.19	31.94	3.14
-43.5	1.50	30.70	0.08	0.04	0.08	0.00	0.31	15.28	15.34	0.03	35.96	3.46
-35.5	1.70	11.81	0.07	0.02	0.05	0.00	2.83	26.01	23.65	0.10	14.75	5.07
-29.5	1.52	10.43	0.09	0.02	0.10	0.00	2.50	22.82	20.76	0.10	9.63	4.57
-26	1.42	26.47	0.04	0.04	0.09	0.00	0.80	11.94	12.42	0.04	26.17	2.09
-22	1.41	26.39	0.07	0.04	0.16	0.00	0.79	11.65	10.73	0.06	25.67	2.23
-18	0.91	6.90	0.07	0.02	1.07	0.00	24.57	26.29	19.46	1.59	19.83	0.91
-10	0.85	6.84	0.07	0.02	1.21	0.00	23.40	24.87	22.18	0.17	23.01	1.11
-6	0.77	4.94	0.07	0.00	1.03	0.00	35.74	33.99	17.64	0.19	31.85	1.19

-2	0.72	4.81	0.07	0.01	1.07	0.00	34.91	32.63	17.66	0.07	31.69	1.22
1	0.15	0.32	0.00	0.00	0.04	0.00	0.27	2.79	0.06	0.04	0.11	0.04
Sample C-C-34-12 (cont.)												
Distance to the plug (mm)	F^-	Cl^-	NO_2^-	Br^-	NO_3^-	PO_4^{3-}	SO_4^{2-}	Mg^{2+}	Ca^{2+}	Na^+	K^+	NH_4^+
5	0.22	0.47	0.00	0.00	0.20	0.00	0.47	3.71	0.10	0.03	0.11	0.02
10	0.15	0.45	0.00	0.00	0.01	0.00	0.42	3.34	0.09	0.04	0.09	0.03
15	0.14	0.44	0.00	0.00	0.10	0.00	0.40	2.96	0.08	0.03	0.07	0.01
20	0.10	0.50	0.00	0.00	0.01	0.00	0.63	3.67	0.08	0.04	0.10	0.02
25	0.11	0.45	0.00	0.00	0.01	0.00	0.55	3.51	0.09	0.05	0.09	0.02
30	0.16	0.49	0.00	0.00	0.02	0.00	0.42	3.20	0.08	0.04	0.11	0.02
35	0.14	0.53	0.00	0.00	0.02	0.00	0.48	3.12	0.10	0.04	0.07	0.02
40	0.15	0.48	0.00	0.00	0.02	0.00	0.57	3.23	0.09	0.04	0.09	0.01
45	0.18	0.44	0.00	0.00	0.13	0.00	0.53	3.61	0.09	0.03	0.08	0.03
Sample BC-C-35-1												
Distance to the plug (mm)	F^-	Cl^-	NO_2^-	Br^-	NO_3^-	PO_4^{3-}	SO_4^{2-}	Mg^{2+}	Ca^{2+}	Na^+	K^+	NH_4^+
6	0.06	0.62	0.00	0.00	0.01	0.00	2.00	3.58	0.06	0.09	0.11	0.03
10	0.06	0.61	0.00	0.00	0.01	0.00	2.10	3.82	0.07	0.11	0.19	0.03
12	0.08	0.61	0.00	0.00	0.02	0.00	0.91	2.85	0.05	0.07	0.13	0.03
20	0.08	0.63	0.00	0.00	0.00	0.00	0.79	2.58	0.04	0.06	0.11	0.02
24	0.08	0.59	0.00	0.00	0.01	0.00	0.93	2.94	0.05	0.05	0.11	0.03
32	0.08	0.56	0.00	0.00	0.01	0.00	0.88	2.72	0.05	0.05	0.10	0.02
36	0.06	0.62	0.00	0.00	0.21	0.00	1.07	2.97	0.05	0.06	0.12	0.02
44	0.06	0.60	0.00	0.00	0.00	0.00	1.04	2.84	0.05	0.06	0.10	0.02

Sample BC-C-35-2												
Distance to the plug (mm)	F^-	Cl^-	NO_2^-	Br^-	NO_3^-	PO_4^{3-}	SO_4^{2-}	Mg^{2+}	Ca^{2+}	Na^+	K^+	NH_4^+
-60	0.00	1.74	0.00	0.00	0.01	0.00	0.03	0.80	0.36	0.01	4.63	0.01
Sample BC-C-35-2 (cont.)												
Distance to the plug (mm)	F^-	Cl^-	NO_2^-	Br^-	NO_3^-	PO_4^{3-}	SO_4^{2-}	Mg^{2+}	Ca^{2+}	Na^+	K^+	NH_4^+
-45	0.01	1.77	0.00	0.00	0.00	0.00	0.03	0.69	0.44	0.01	5.03	0.01
-35	0.06	0.27	0.00	0.00	0.03	0.02	0.32	2.56	0.05	0.01	0.09	0.01
-25	0.10	0.26	0.00	0.00	0.01	0.02	0.32	2.64	0.05	0.01	0.13	0.01
-15	0.00	1.94	0.00	0.00	0.01	0.00	0.03	0.52	0.16	0.01	5.88	0.01
-7.5	0.00	1.11	0.00	0.00	0.00	0.00	0.03	0.33	0.09	0.02	4.39	0.01
3	0.07	1.08	0.00	0.00	0.13	0.01	0.20	2.03	0.88	0.00	0.09	0.02
10	0.06	0.15	0.00	0.00	0.00	0.01	0.20	1.97	0.06	0.01	0.08	0.02
15	0.08	0.18	0.00	0.00	0.01	0.01	0.19	2.35	0.08	0.02	0.15	0.01
25	0.10	0.13	0.00	0.00	0.01	0.01	0.10	2.07	0.04	0.01	0.13	0.02
30	0.07	0.13	0.00	0.00	0.01	0.00	0.07	1.73	0.04	0.01	0.08	0.01
40	0.07	0.10	0.00	0.00	0.00	0.00	0.08	1.68	0.03	0.01	0.07	0.01
45	0.07	0.13	0.00	0.00	0.01	0.00	0.08	1.71	0.04	0.01	0.06	0.01
55	0.08	0.10	0.00	0.00	0.00	0.00	0.08	1.73	0.02	0.01	0.06	0.01
Sample BC-S-35-3												
Distance to the plug (mm)	F^-	Cl^-	NO_2^-	Br^-	NO_3^-	PO_4^{3-}	SO_4^{2-}	Mg^{2+}	Ca^{2+}	Na^+	K^+	NH_4^+
-25	0.04	0.34	0.00	0.00	0.40	0.00	0.04	1.96	0.33	0.05	0.15	0.04
-20	0.05	0.14	0.00	0.00	0.14	0.00	0.04	2.65	0.36	0.04	0.14	0.05
-15	0.00	0.00	0.00	0.00	0.00	0.00	0.00	0.00	0.00	0.00	0.00	0.00

-10	0.00	0.00	0.00	0.00	0.00	0.00	0.00	0.00	0.00	0.00	0.00	0.00
-5	0.00	0.00	0.00	0.00	0.00	0.00	0.00	0.00	0.00	0.00	0.00	0.00
2	0.11	0.15	0.00	0.00	0.01	0.02	0.18	3.98	0.15	0.04	0.12	0.11
4	0.11	0.10	0.00	0.00	0.01	0.00	0.09	3.16	0.08	0.04	0.12	0.10
Sample BC-S-35-3 (cont.)												
Distance to the plug (mm)	F^-	Cl^-	NO_2^-	Br^-	NO_3^-	PO_4^{3-}	SO_4^{2-}	Mg^{2+}	Ca^{2+}	Na^+	K^+	NH_4^+
8	0.12	0.10	0.00	0.00	0.01	0.01	0.11	3.19	0.07	0.04	0.13	0.08
12	0.14	0.12	0.00	0.00	0.01	0.00	0.12	3.22	0.07	0.03	0.12	0.08
15	0.13	0.12	0.00	0.00	0.01	0.00	0.12	3.11	0.06	0.02	0.10	0.08
18	0.13	0.12	0.00	0.00	0.00	0.00	0.11	3.37	0.07	0.02	0.12	0.08
21	0.14	0.11	0.00	0.00	0.01	0.00	0.12	3.10	0.05	0.01	0.12	0.07
24	0.19	0.16	0.00	0.00	0.01	0.00	0.18	3.66	0.06	0.02	0.12	0.08
28	0.12	0.09	0.00	0.00	0.01	0.00	0.12	3.11	0.06	0.01	0.10	0.07
31	0.13	0.10	0.00	0.00	0.01	0.00	0.13	3.02	0.06	0.01	0.10	0.08
34	0.17	0.14	0.00	0.00	0.01	0.00	0.20	3.66	0.06	0.01	0.13	0.06
36	0.15	0.13	0.00	0.00	0.01	0.00	0.15	3.25	0.05	0.02	0.11	0.05
Sample BC-S-35-4												
Distance to the plug (mm)	F^-	Cl^-	NO_2^-	Br^-	NO_3^-	PO_4^{3-}	SO_4^{2-}	Mg^{2+}	Ca^{2+}	Na^+	K^+	NH_4^+
0	0.04	0.33	0.00	0.00	0.40	0.00	0.04	1.96	0.33	0.05	0.15	0.04
10	0.03	0.42	0.00	0.00	1.06	0.00	0.08	1.24	0.22	0.17	0.20	0.04
13	0.04	0.07	0.00	0.00	0.03	0.00	0.02	1.94	0.05	0.03	0.13	0.04
18	0.05	0.14	0.00	0.00	0.14	0.00	0.04	2.65	0.36	0.04	0.14	0.05
22	0.06	0.09	0.00	0.00	0.04	0.00	0.06	1.75	0.03	0.01	0.07	0.03

32	0.05	0.09	0.00	0.00	0.12	0.00	0.06	0.82	0.02	0.01	0.06	0.01
Sample BB-36-6												
Distance to the plug (mm)	F^-	Cl^-	NO_2^-	Br^-	NO_3^-	PO_4^{3-}	SO_4^{2-}	Mg^{2+}	Ca^{2+}	Na^+	K^+	NH_4^+
2	0.04	0.25	0.00	0.00	0.00	0.00	0.23	1.59	0.00	0.00	0.00	
4	0.02	0.19	0.00	0.00	0.00	0.00	0.21	1.51	0.00	0.00	0.00	
Sample BB-36-6 (cont.)												
Distance to the plug (mm)	F^-	Cl^-	NO_2^-	Br^-	NO_3^-	PO_4^{3-}	SO_4^{2-}	Mg^{2+}	Ca^{2+}	Na^+	K^+	NH_4^+
7	0.03	0.19	0.00	0.00	0.00	0.00	0.17	1.57	0.00	0.00	0.00	
9	0.09	0.37	0.09	0.00	0.09	0.00	0.21	0.00	0.00	0.00	0.00	
14	0.04	0.21	0.00	0.00	0.00	0.00	0.22	1.77	0.00	0.00	0.39	
18	0.04	0.21	0.00	0.00	0.00	0.00	0.24	1.67	0.00	0.00	0.00	
21	0.05	0.20	0.00	0.00	0.00	0.00	0.27	1.74	0.00	0.00	0.00	
25	0.08	0.23	0.00	0.00	0.00	0.00	0.22	1.86	0.26	0.00	0.25	
30	0.04	0.21	0.00	0.00	0.00	0.00	0.39	2.03	0.00	0.00	0.00	
36	0.05	0.21	0.00	0.00	0.00	0.00	0.39	2.06	0.00	0.00	0.00	
FEBEX REF.*	**0.05**	**1.98**		**0.00**	**0.02**		**0.98**	**0.06**	**0.05**	**5.02**	**0.07**	
CONCRETE REF.**	**0.02**	**0.20**			**0.01**		**0.52**	**<0.01**	**30.12**	**5.35**	**5.40**	

**Data from Fernández et al. 2004.*

***Average from results on Tab. B-7 (and part A.I.3) – samples C-C-34-5 (5cm), C-C-34-6 (5cm) and C-C-34-7 (5cm) were taken as reference as in this samples the impact of granite groundwater or bentonite porewater is assumed to be negligible.*

C.2 Cation exchange capacity and exchangeable cations

Reference material (BGR)

None of the originally used FEBEX bentonite was available as reference material. Therefore, the FEBEX bentonite used for the ABM test (Dohrmann et al. 2013; Kaufhold et al. 2013) was used as reference. In addition, 22 samples of those investigated in the present study were selected and the values were averaged to calculate a reference. These selected samples were taken in a distance of more than 10 cm from the heater and from the granite and did not show any variation with respect to the chemical composition. Reference values, the FEBEX-ABM data and the "average reference" are compared in Tab. C-1. No deviations were found for exchangeable Na^+ and K^+. The slightly lower content of exchangeable Mg^{2+} is close to insignificant. The larger content of exchangeable Ca^{2+}, however, reflects the systematic differences between two slightly different methods used. The ABM reference clay was investigated using the so called "Cu-trien5xcalcite" method in which the exchange solution was pre-saturated with respect to calcite in order to avoid further calcite dissolution during the CEC experiment (Dohrmann et al. 2013). This method however requires a larger sample mass. For the present study this method could not be applied because less sample mass was available. Generally, CEC values can be best compared when measured within one measurement series (same solutions, same calibration of photometer, same temperature,…). Therefore, the values obtained by averaging 22 samples, all with appreciable distance to both heater and granite, are better suited to serve as reference values and for comparison with possible changes that took place during the 18 years of operation. The 5x-calcite-values are marked in grey.

Tab. C-2: CEC data of the CEC references.

	Na^+	K^+	Mg^{2+}	Ca^{2+}	sum	CEC
	[meq/100g]					
REF ABM (5x-Cc)	27.3	2.9	37.0	33.8	100.0	101.0
REF averg. (n=22)	27.6	2.6	35.7	40.9	107.0	98.1

Tab. C-3: CEC and EC data of section 35 samples (BGR data).

	distance from heater surface	Na^+	K^+	Mg^{2+}	Ca^{2+}	sum	CEC
	[cm]	[meq/100g]					
REF ABM (5x-Cc)		27.3	2.9	37.0	33.8	100.0	101.0
REF averg.		27.6	2.6	35.7	40.9	107.0	98.1
BC-S-35-1b	0.1	21.2	3.6	27.8	49.0	101.6	76.8
BC-S-35-1b	1	27.2	4.1	26.4	45.3	103.0	93.6
BC-S-35-1b	3	26.3	4.0	34.4	42.1	106.7	97.1
BC-S-35-1a	0.1	17.3	3.1	33.4	18.3	71.9	55.8
BC-S-35-1a	1	28.1	4.5	21.6	44.5	98.7	90.1
BC-S-35-1b (2) Z	3	1.5	1.0	1.4	61.2	65.0	6.4

Obayashi data

Tab. C-4: Results of the exchangeable cation measurement in sample C-C-32-6-OC (Obayashi data). Results are given in meq/100g. Between brackets is the percentage of each cation related to the total.

Sample	Na	K	Ca	Mg	Total
0	15.1 (23.5)	3.2 (5.0)	35.3 (54.9)	10.6 (16.5)	64.2
1	17.0 (24.4)	3.4 (4.9)	37.5 (53.9)	11.7 (16.8)	69.7
3	19.0 (25.7)	3.7 (5.0)	41.2 (55.9)	9.9 (13.5)	73.8
5	22.6 (26.9)	3.7 (4.5)	48.5 (57.9)	9.0 (10.7)	83.8
7	22.7 (26.0)	4.0 (5.0)	51.9 (59.0)	9.6 (11.0)	88.3
BL	25.3 (27.9)	4.2 (4.7)	49.7 (54.7)	11.6 (12.8)	90.9

Ciemat data

Tab. C-5: Results of exchangeable cations in bentonite samples at the concrete/bentonite interface (Ciemat data).

Sample C-C-34-8						
Distance to the plug (mm)	**Na^+ cmol(+)/Kg**	**K^+ cmol(+)/Kg**	**Mg^{2+} cmol(+)/Kg**	**Ca^{2+} cmol(+)/Kg**	**NH_4^+ cmol(+)/Kg**	**Σcations**
0	13.86	1.82	20.39	59.90	0.26	96.24
3	13.95	1.93	19.29	59.81	0.30	95.27
6	19.65	2.67	28.25	32.75	0.46	83.77
10	21.50	2.69	29.32	33.34	0.80	87.64
14	20.15	2.53	29.36	29.27	0.52	81.83
22	20.95	2.54	29.47	29.47	0.34	82.77
26	23.02	2.82	31.74	31.47	0.79	89.84
34	23.02	2.82	31.74	31.47	0.79	89.84
Sample C-C-34-10						
Distance to the plug (mm)	**Na^+ cmol(+)/Kg**	**K^+ cmol(+)/Kg**	**Mg^{2+} cmol(+)/Kg**	**Ca^{2+} cmol(+)/Kg**	**NH_4^+ cmol(+)/Kg**	**Σcations**
10	2.02	1.96	37.12	57.71	0.00	98.80
20	1.99	1.66	37.45	58.39	0.21	99.70
30	2.44	2.08	37.81	56.49	0.00	98.82
40	2.43	0.64	36.90	56.09	2.60	98.65

Sample C-C-34-12						
Distance to the plug (mm)	**Na^+ cmol(+)/ Kg**	**K^+ cmol(+)/ Kg**	**Mg^{2+} cmol(+)/ Kg**	**Ca^{2+} cmol(+)/Kg**	**NH_4^+ cmol(+)/ Kg**	**Σcations**
1	26.35	5.05	29.06	40.3	0.55	101.31
5	27.74	5.36	27.7	42.87	0.53	104.2
10	27.95	4.89	24.07	42.08	0.5	99.5
15	27.56	4.99	24.14	42.46	0.25	99.4
20	27.65	5.01	24.2	40.44	0.45	97.76
25	29	4.83	24.21	43.87	0.46	102.37
30	27.42	4.94	25.62	42.32	0.49	100.78
35	25.42	4.49	24.1	38.73	0.42	93.16
40	25.36	4.6	25.45	39.31	0.5	95.23
45	27	4.92	26.39	41.26	0.47	100.05
Sample BC-C-35-1						
Distance to the plug (mm)	**Na^+ cmol(+)/ Kg**	**K^+ cmol(+)/ Kg**	**Mg^{2+} cmol(+)/ Kg**	**Ca^{2+} cmol(+)/Kg**	**NH_4^+ cmol(+)/ Kg**	**Σcations**
6	24.63	2.63	30.99	35.05	0.81	94.10
10	26.59	3.37	23.99	38.81	1.05	93.81
12	30.20	3.40	24.38	40.45	0.82	99.25
20	26.55	3.13	31.76	35.78	0.81	98.03
24	26.71	3.15	33.29	36.79	0.82	100.76
32	25.45	3.05	30.28	34.97	1.04	94.80
36	24.80	2.75	29.27	34.43	0.54	91.79
44	26.39	2.96	31.65	37.50	0.58	99.10
Sample BC-C-35-2						
Distance to the plug (mm)	**Na^+ cmol(+)/ Kg**	**K^+ cmol(+)/ Kg**	**Mg^{2+} cmol(+)/ Kg**	**Ca^{2+} cmol(+)/Kg**	**NH_4^+ cmol(+)/ Kg**	**Σcations**
3	28.76	3.89	15.58	49.87	0.00	98.11
10	29.74	3.01	15.33	51.35	0.00	99.43
15	28.54	2.85	14.52	53.02	0.00	98.92
25	28.83	2.59	14.14	51.75	0.48	97.79
30	28.32	2.60	13.21	51.31	0.00	95.44
40	28.43	2.55	12.06	51.61	0.39	95.03
45	28.93	2.45	12.17	52.99	0.00	96.54

55	28.69	2.53	11.94	52.12	0.33	95.61
Sample BC-S-35-3						
Distance to the plug (mm)	**Na^+ cmol(+)/ Kg**	**K^+ cmol(+)/ Kg**	**Mg^{2+} cmol(+)/ Kg**	**Ca^{2+} cmol(+)/Kg**	**NH_4^+ cmol(+)/ Kg**	**Σcations**
2	26.89	3.62	13.80	40.94	0.60	85.55
4	29.91	2.67	9.13	49.53	0.56	91.52
8	30.34	2.95	8.17	52.74	0.77	94.52
12	30.55	2.96	8.25	52.82	0.66	94.91
15	29.99	2.97	8.10	51.56	0.66	92.96
18	30.47	2.88	8.29	52.60	0.63	94.55
21	30.74	3.00	8.23	53.30	0.93	95.74
24	29.79	2.80	8.63	52.04	0.71	93.62
28	31.30	2.89	7.55	53.45	0.82	95.61
31	30.70	2.85	7.74	53.10	0.59	94.68
34	29.42	2.85	8.30	50.87	1.12	92.01
36	30.38	2.92	9.25	52.30	0.51	95.11
Sample BC-S-35-4						
Distance to the plug (mm)	**Na^+ cmol(+)/ Kg**	**K^+ cmol(+)/ Kg**	**Mg^{2+} cmol(+)/ Kg**	**Ca^{2+} cmol(+)/Kg**	**NH_4^+ cmol(+)/ Kg**	**Σcations**
0	22.62	5.36	30.28	39.10	0.00	97.35
10	30.55	4.66	11.81	50.90	0.31	98.23
13	29.72	3.58	11.41	50.36	0.00	95.07
18	29.98	3.20	11.47	51.61	0.84	97.11
22	29.97	3.07	11.73	50.72	0.00	95.49
32	29.35	3.03	12.58	49.31	0.94	95.20

C.3 Carbonates and stable isotope analysis (UAM)

Tab. C-6: Carbonates content, δ13C and δ18O stable isotopes, specific surface area measured by BET N2 isotherm and % of <2µm fraction extracted in distilled water.

Sample	Subsample	Coord. X (cm)	Coord. Y (cm)	Coord. Z (cm)	BET m^2/g	BET (error)	δ^{13} C VPDB	δ^{18} O VPDB	% weight $CaCO_3$	% Fracción <2 µm
CC-34-8	C	-6.1	41	53	13.4	0.0	-4.5	-8.9	15.5	-
	C04	-2.3	41	53	7.2	0.0	-	-	18.8	-
	C03	-1.3	41	53	8.8	0.0	-	-	14.3	-
	C02	-0.8	41	53	9.2	0.0	-	-	17.9	-
	C01	-0.3	41	53	16.4	0.1	-4.7	-8.3	21.3	-
	IC	0.1	41	53	-	-	-	-	-	-
	IB	0.1	41	53	-	-	-	-	-	-
	B01	2.0	41	53	47.7	0.4	-1.8	-6.6	-	18.6
	B02	4.3	41	53	51.0	0.4	-2.6	-7.7	-	18.6
	B03	4.8	41	53	54.4	0.6	-	-	-	23.4
	B	6.4	41	53	54.9	0.5	-3.2	-8.1	-	16.3

CC-34-10	C	-8.8	62	88	18.9	0.1	-4.0	-7.9	19.7	-
	C04	-3.9	62	88	8.7	0.0	-	-	20.1	-
	C03	-2.0	62	88	10.1	0.0	-	-	17.2	-
	C02	-0.8	62	88	11.1	0.0	-	-	19.4	-
	C01	-0.3	62	88	13.4	0.0	-6.8	-9.3	32.7	-
	IC	-0.1	62	88	-	-	-	-	-	-
	IB	0.1	62	88	-	-	-	-	-	-
	B01	0.2	62	88	54.9	0.6	-4.2	-7.3	-	30.5
	B02	0.7	62	88	56.0	0.9	-2.8	-6.5	-	16.2
	B03	1.2	62	88	58.3	0.6	-	-	-	20.4
	B	2.3	62	88	52.3	0.4	-2.8	-7.4	-	24.9
CC-34-12	C	-4.4	-31	-62	18.0	0.0	-3.9	-8.2	30.5	-
	C03	-2.7	-31	-62	17.8	0.1	-	-	19.7	-
	C02	-1.2	-31	-62	13.3	0.1	-	-	20.5	-
	C01	-0.3	-31	-62	39.4	0.1	-5.1	-9.4	25.8	-
	IC	-0.1	-31	-62	-	-	-	-	-	-
	IB	0.1	-31	-62	-	-	-	-	-	-
	B01	0.2	-31	-62	53.3	0.6	-5.5	-9.3		32.0
	B02	0.7	-31	-62	54.0	0.5	-3.4	-7.7		14.8
	B03	1.2	-31	-62	51.5	0.5	-	-	-	11.9
	B04	1.3	-31	-62	49.9	0.4	-	-	-	17.9
	B	2.9	-31	-62	54.1	0.5	-3.4	-9.0	-	19.0

BC-C35-1	C	-4.5	13	88	19.9	0.1	-2.6	-8.2	18.2	-
	C04	-2.5	13	88	22.9	0.1	-	-	21.2	-
	C03	-1.3	13	88	8.3	0.0	-	-	21.7	-
	C02	-0.8	13	88	10.8	0.1	-	-	14.2	-
	C01	-0.3	13	88	12.5	0.0	-4.5	-8.9	25.2	-
	IC	-0.1	13	88	-	-	-	-	-	-
	IB	0.1	13	88	-	-	-	-	-	-
	B01	0.2	13	88	62.2	0.7	-3.8	-7.0	-	5.1
	B02	0.7	13	88	61.7	0.7	-1.8	-8.2	-	4.2
	B03	1.2	13	88	58.2	0.6	-	-	-	10.9
		3.4	13	88	51.2	0.5	-4.1	-5.1	-	4.3
BC-C35-2	C	-4.5	-162	-91	6.9	0.1	-3.4	-7.6	14.8	-
	C04	-2.5	-162	-91	9.0	0.0	-	-	14.2	-
	C03	-1.3	-162	-91	5.6	0.0	-	-	19.4	-
	C02	-0.8	-162	-91	8.1	0.0	-	-	20.3	-
	C01	-0.3	-162	-91	10.4	0.1	-4.7	-7.4	36.5	-
	IC	-0.1	-162	-91	-	-	-	-	-	-
	IB	0.1	-162	-91	-	-	-	-	-	-
	B01	0.2	-162	-91	60.5	0.6	-3.8	-9.3	-	15.6
	B02	0.7	-162	-91	68.8	0.8	-8.4	-8.8	-	6.4
	B03	1.2	-162	-91	65.8	0.7	-	-	-	21.6
	B	3.4	-162	-91	69.9	0.7	-0.5	-5.9	-	13.9

BC-C-35-3	C	-12.1	-62	66	nd		nd	nd	34.5	
	C05	-5.6	-62	66	nd		-4.89	-7.81	22.0	
	C04	-4.8	-62	66	nd		-7.67	-9.23	18.0	
	C03	-3.7	-62	66	nd		-4.55	-7.55	20.5	
	C02	-2.3	-62	66	nd		-2.39	-7.83	18.0	
	C01	-0.7	-62	66	nd		-4.82	-8.47	20.9	
	IC	-0.1	-62	66	nd		-2.69	-8.05	nd	
	IB	0.1	-62	66	15.9	0.0	nd	nd	nd	
	B01	0.3	-62	66	61.3	0.1	-9.14	-8.77	nd	
	B02	0.6	-62	66	nd		nd	nd	nd	
	B03	1	-62	66	nd		nd	nd	nd	
	B04	1.5	-62	66	47.9	0.1	nd	nd	nd	
	B05	2.2	-62	66	65.3	0.1	nd	nd	nd	
	B06	3.2	-62	66	57.5	0.3	nd	nd	nd	
	B07	4.2	-62	66	81.5	0.8	-7.47	-9.62	nd	
	B	5.7	-62	66	62.8	0.0	nd	nd	nd	
	FEBEX ref.				62	0.2	-1.23	-7.32		

C.4 Elemental mapping of polished sections

UAM analysis

Dry polished sections were prepared with materials on both sides of the interface, and hence containing both concrete and bentonite. These sections allowed us to produce chemical maps of composition and to reveal microstructural features of the concrete/bentonite contact. Concrete and bentonite are usually separated by a continuous crack parallel to the interface, produced shortly after a minimum time of ambient exposure. Frequently a thin rim of apparently bentonite material remained in discontinuous crusts at the concrete surface. The preparation of concrete and bentonite samples was needed prior to SEM-EDX analyses for elaboration of compositional profiles and elemental maps. Samples were sliced with a diamond wire saw, freeze-dried in liquid nitrogen, dried in vacuum with P_2O_5 dehydrated atmosphere up to 10^{-4} Pa, and finally polished. Using this preparation, the bentonite slices maintained their consistence in the polishing operation without disaggregation. Therefore, embedding in resin was not required for elemental profiles or mapping. Nevertheless the surfaces were embedded in LR-WHITE resin after analysis in order to compare the visual aspect.

Compositional profiles perpendicular to the concrete-bentonite interface were performed in samples CC-34-10 and CC-34-12 for concrete and for bentonite. Since concrete and bentonite samples were received separated, except for some concrete and bentonite samples where a few millimetres of cemented rims were attached to the samples, the closest border to the interface of each sample was assumed as the contact between both materials.

Elemental maps were performed for an area of 24 x 2.46 mm in a bentonite polished piece of sample CC-34-12, and an area of 28.62 x 2.91 mm in a concrete polished piece of sample BC-S-35-3. The latter sample contains 2-3 mm of bentonite cemented to the concrete.

Additionally, unpolished small concrete and bentonite fresh disaggregate pieces of samples CC-34-10 and BC-S-35-3 were vacuum dried, mounted on carbon-coated tapes and metallized by gold coating for analysis of morphologies and microstructures.

The compositional profiles were elaborated with different incremental length scales from the interface outward. This method thus obtained a detailed view of possible chemical changes closer to the interface: the first 100 µm of sample from the interface were scanned by 5 analyses with high resolution (20 µm in perpendicular length from the interface). The next 5 analyses were extended to approximately a whole length of 250 µm. And finally, from there to the end of each sample, a constant resolution of approximately 400-500 µm was considered per analysis to represent the chemical profiles. A representation of the criteria chosen for sample CC-34-10 on both sides, concrete and bentonite, is given in Fig. 1. Note that for concrete, coarse aggregate grains were intentionally avoided to obtain a better averaged chemical profile of the cement paste matrix.

The morphology, chemical composition and microstructure of selected samples in concrete were performed by INCAx-sight Oxford Instruments® Energy Dispersive X-ray analyser coupled to a Hitachi S-3000N Scanning Electron Microscope (SEM-EDX).

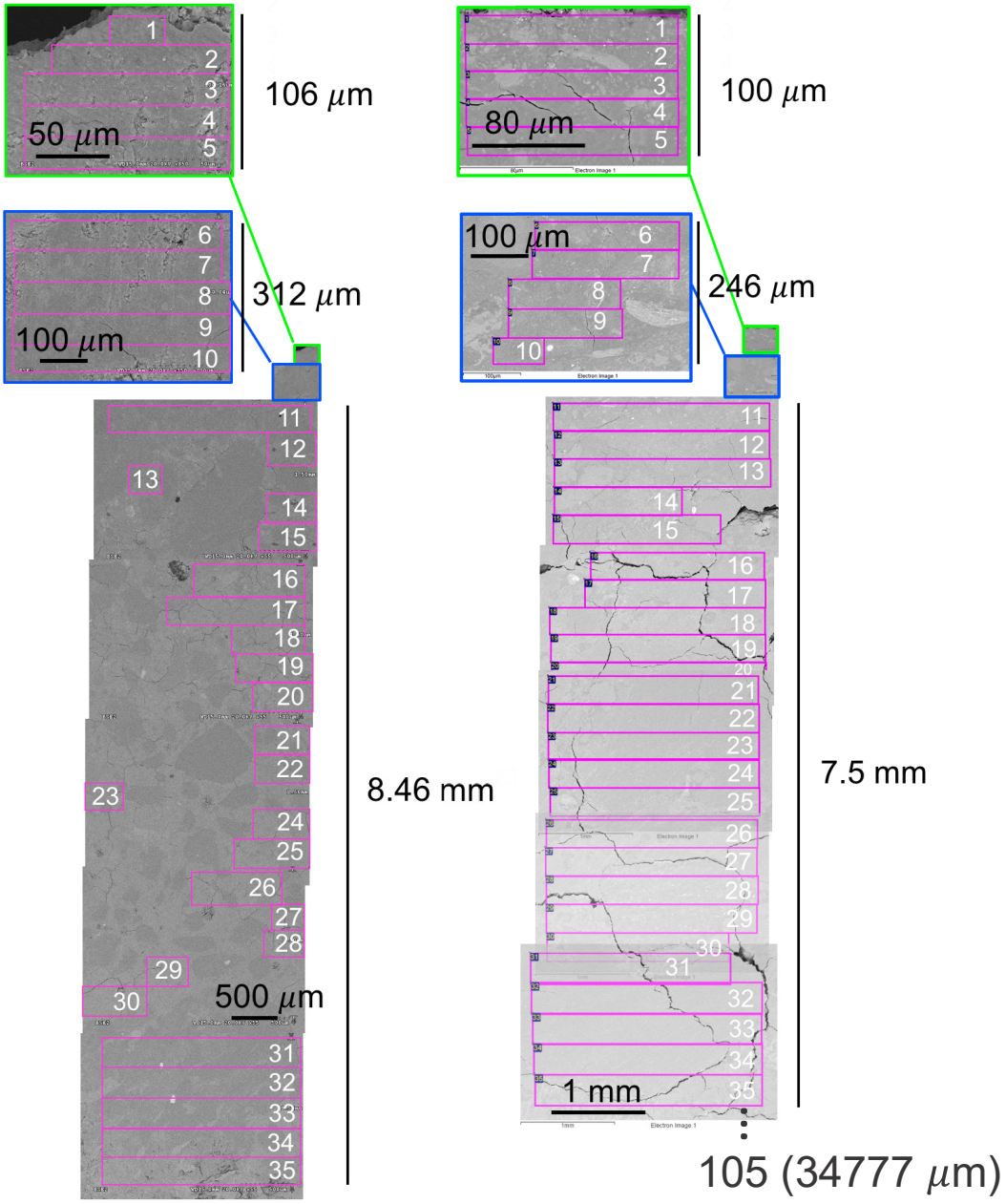

Fig. 185: Reconstitued back-scattering images showing the density and location of chemically analysed fields for EDX-chemical mapping. This is the methodology applied to complete the chemical profile along the concrete (left) and bentonite (rigth) samples CC-34-10 by EDX analyses. The interface is situated at the top.

Tab. C-7: EDX chemical analyses from spots marked in Figure 108 for BC-S-35-3 sample.

Element	**analyses**															
	1	2	3	4	ettr	5	7	8	9	10	11	12	13	14	15	16
C			18.56			8.7	15.31	10.31	16.46	17.87	14.59	13.97	28.07	23.21	24.69	17.99
O	83.15	75.64	60.44	73.86		74.5	63.55	65.41	65.36	57.05	69.65	58.76	63.7	64.2	62.79	67.25
Mg	0.13	0.79	7.46	0.38			0.81		0.74	1.23	0.23	0.98			0.51	0.28
Al	2.70	2.35		2.18		2.37	1.72	0.69	1.79	1.84	2.15	0.84	0.31	1.99	0.46	1.82
Si	1.11	8.61	0.52	9.25		1.01	6.28	8.31	4.95	8.45	2.29	13.3	0.89	0.72	1.61	0.82
S	4.53	1.61		2.37		4.63	1.63	0.26	2.03	1.72	3.31	0.25		2.91	0.19	3.66
K		0.29		0.09							0.1					
Ca	8.23	9.91	12.46	11.58		8.79	10.02	14.65	8.45	10.6	7.45	11.7	7.02	6.95	9.74	8.01
Fe	0.15	0.79	0.56	0.29			0.68	0.36	0.22	1.24	0.25	0.21				0.18
Ca/Si	7.41	1.15	23.96	1.25		8.70	1.60	1.76	1.71	1.25	3.25	0.88	7.89	9.65	6.05	9.77
Al/S	0.60	1.46		0.92	0.7	0.51	1.06	2.65	0.88	1.07	0.65	3.36		0.68	2.42	0.50
Ca/S	1.82	6.16		4.89	2	1.90	6.15	56.35	4.16	6.16	2.25	46.80		2.39	51.26	2.19
Obs.	ettr	CASH	$MgCaCO_3$	CASH		ettr	CSH_CO3	CSH_CO3	ettr-CO_3	CASH; CO_3	ettr	CASH	$CaCO_3$	ettr-CO_3	$MgCaCO_3$	etrr

Ettr: ettringite atomic ratios. Obs: observations; CO_3: carbonates, CSH: calcium silicate hydrates, CASH: calcium-aluminum silicate hydrates, $MgCaCO_3$: rich Mg calcite; $CaCO_3$: calcite.

Tab. C-8: EDX chemical analyses from spots marked in Figure 110 for C-C-34-8.

Element	analyses	IF	IF	IF-B	B	B	B	B	B
	34-1-8	34-1-17	34-2-10	34-2-5	34-1-9	34-1-11	34-1-12	34-1-13	34-1-14
C	23.52	19.87	18.77	20.94	11.46	15.32	13.99	11.51	17.21
O	62.18	64.68	63.26	60.37	59.94	63.64	66.57	66.73	63.47
Na	0.43	0.51	0.8		0.43	0.45	0.24	0.15	0.36
Mg	0.72	0.64	1.09	6.05	3.72	2.7	2.6	2.73	2.61
Al	2.50	1.56	2.5	2.78	5.73	4.56	4.46	4.67	3.89
Si	7.08	5.26	7.52	8.58	17.31	12.08	11.28	13.07	11.14
S	0.34	1.52	0.53	0.14					
K	0.39		0.42	0.14	0.16	0.18	0.09	0.08	
Ca	2.58	5.55	4.61	0.6	0.52	0.5	0.39	0.47	10.02
Fe	0.26	0.41	0.52	0.39	0.72	0.57	0.39	0.59	0.68
Ca/Si	0.36	1.06	0.61	2.79	0.03	0.05	0.09	0.04	0.25
Al/S	7.35	1.03	4.72	61.29					
Ca/S	7.59	0.27	8.70	2.79					
Al/Si	0.35	0.30	0.33	0.32	0.33	0.38	0.40	0.36	0.35
Obs	CO_3	SO_4	CO_3_CSH	CSH_CO_3	clay,CO_3	clay,CO_3	clay,CO_3	clay,CO_3	clay,CO_3

B: bentonite; IF: interface; Obs: observations; CO_3: carbonates, CSH: calcium silicate hydrates, SO_4: sulphates.

Tab. C-9: EDX chemical analyses from spots marked Figure 111 in for C-C-34-10 in the bentonite interface.

Element	analyses	IF-B	IF-B	IF-B	IF-B	IF-B	IF-B	IF-B
	1	2	3	4	5	6	7	8
C	20.04	7.26	7.57	10.65	23.19	23.1	26.24	15.82
O	62.66	68.96	69.53	68.49	63.15	62.56	59.49	59.88
Na	0.91	0.18		0.19	0.39		0.52	0.66
Mg	0.61	8.8	9.38	6.11	0.72	0.37	0.39	0.17
Al	2.38	3.91	3.46	3.4	1.32	0.19	1.03	4.33
Si	8.23	10.3	9.34	10.13	3.31	0.62	5.16	14.5
S	0.28				1.01		0.4	
K	0.45	0.2	0.11	0.29	0.18		0.15	3.69
Ca	4.02		0.1	0.26	6.54	13.15	6.4	0.81
Fe	0.41	0.38	0.51	0.48	0.19		0.23	0.14
Ca/Si	0.49	0.00	0.01	0.03	1.98	21.21	1.24	0.01
Al/S	8.50				1.31		2.58	
Ca/S	14.36				6.48		16.00	
Al/Si	0.29	0.38	0.37	0.34	0.40	0.31	0.20	0.30
Obs	CO_3	MSH	MSH	clay:MSH	SO_4-CO_3	CO_3	CO_3_CSH	clay,K

B: bentonite; IF: interface; Obs: observations, MSH: Magnesium silicate hydrates, CO_3: carbonates; SO_4: sulphates; CSH: calcium silicate hydrates.

Tab. C-10: EDX chemical analyses from spots marked in Fig. 185 for C-C-34-10 in the concrete interface.

Element	IF-C	IF-C	IF-C	IF-C
	9	10	11	12
C	8.14	10.54	16.14	13.62
O	70.29	57.88	58.79	65.03
Na				
Mg				0.48
Al	1.72	1.67	1.43	2.2
Si	1.81	5.14	2.98	6.84
S	4.59	2.21	1.23	1.28
Cl				0.22
K				0.43
Ca	13.46	21.15	19.15	9.55
Fe		1.41	0.29	0.34
Ca/Si	7.44	4.11	6.43	1.40
Al/S	0.37	0.76	1.16	1.72
Ca/S	2.93	9.57	15.57	7.46
Al/Si	0.95	0.32	0.48	0.32
Obs	ettr (CO_3-CSH)	CO_3-CSH ettr	CO_3_CSH	CO3-CSH ettr

C: concrete; IF: interface; Obs: observations, MSH: magnesium silicate hydrates, CO_3: carbonates, CSH: calcium silicate hydrates, ettr: ettringite.

C.5 Mineralogical characterisation

XRD of concrete/bentonite samples (UAM)

Sampling sectioning and labelling was made following the example in Fig. 186 that corresponds to sample C-C-34-12.

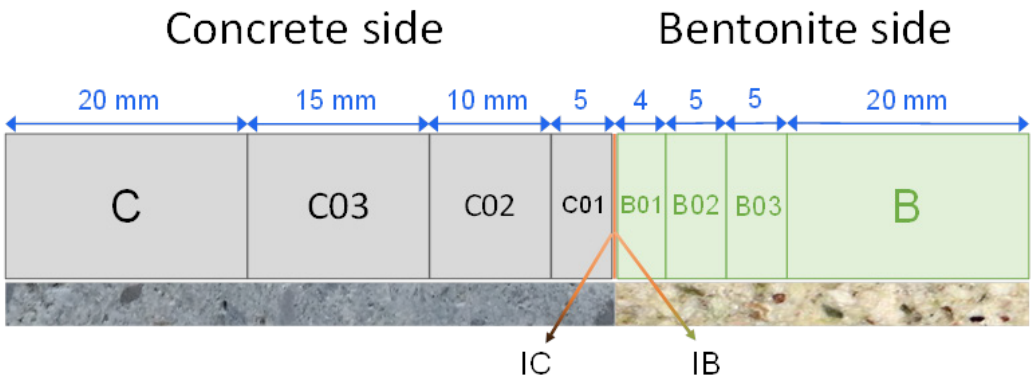

Fig. 186: Sampling sectioning and labeling for C-C-34-12 concrete-bentonite core section. IB or IC samples were very small (< 0.1 g) scrapped samples characterizing the x~0 coordinate position.

The mineralogical quantification performed on raw FEBEX bentonite performed by the standard addition method and SIROQUANT© refinement of concrete crystalline minerals was used as reference to vary the RIR ratios used for semi-quantitative analysis on the basis of several ICDD powder diffraction files (PDF) standards supported in High Score Expert plus © software (vs. 2.1.b 2005); (Tab. C-11).

Tab. C-11: FEBEX bentonite quantification and modified RIR ratios used for the quantification of bentonite in the S45 section (UAM bentonite report) and used in the characterisation of bentonite in the concrete/bentonite interface. ICDD PDF2 files (2001) used as references are included.

Bentonite	**% Mont.**	**% Ilt Mica**	**% Qtz**	**% Crs**	**% Cal**	**% Kfs Or**	**% Pl An**
FEBEX	94±1	1	0.7	1.6	0.9	0.8	0.8
PDF file reference	00-012-0204** 00-013-0135***	01-086-1385	01-085-0796	00-001-0438	01-083-0578	00-031-0966	01-079-1148
RIR(*)	0.3	1	3	1	2	1	1

* RIR modified in High Score Expert plus © programe (vs. 2.1.b 2005) Mont.: montmorillonite. Qtz: quartz; Crs: Cristobalite. Cal: calcite. KFs: orthoclase. Pl: Plagioclase (andesine).

** Na bentonite and

*** Ca-15Å bentonite. The use of both is justified by the observation of a common observation of an asymmetric tail to high 2Θ angles in the (001) montmorillonite basal reflection peak.

Some of the mineral phases identified in the interfaces (in example, IB or IC samples) were not present in the concrete or in the bentonite outside this zone. C-(A)-S-H minerals produced in contact with FEBEX bentonite were characterised to have Al-tobermorite characteristics (Fernández et al. 2014) . C-(A)-S-H have been evaluated by adjusting the scale of the 00-010-

0374 CSH pdf file with respect to the 3.04 Å broad reflection identified as a shoulder near the 3.03 Å calcite peak. Mg trioctahedral 2:1 sheet silicates (M-S-H type minerals) were quantified by using the 00-25-1498 pdf file of saponite. A 0.3 RIR value was used similarly to montmorillonite as long as low crystal size trioctahedral smectite is present, i.e. when a 1.52-1.53 Å broad reflection is detected nearby the characteristic 1.50 Å XRD reflection of montmorillonite.

<2µm size fraction of bentonite was separated from 42 selected samples (B01, B02, B03 and B, Fig. 186) in order to study the variation of basal spacings for montmorillonite and to characterise potential structural alteration in the FEBEX clay. The <2µm fractions were extracted by the dispersion of bentonite in distilled water using an ultrasonic tip. The dispersion was let to settle in a 25 cm high flask during 14 h at 20 ºC in order to aspirate the liquid up to 20 cm height measured from the initial level of the liquid surface. Suspensions in the flask were maintained tightly closed to atmospheric contact with paraffin film in order to avoid carbonation. Clay particles were flocculated by adding ethanol and centrifuged. Basal spacings of smectite in samples were measured by preparing oriented aggregate films using a 0.05g/ml dispersed slurry that was smeared on a 2 cm^2 glass tile, then dried in laboratory conditions. Ethylene Glycol (EG) solvation was performed inside a closed plastic box by adding a EG impregnated filter paper inside. EG vapour enters the clay film deposited on the glass tiles lying on the paper (48 h).

These samples were θ/2θ scanned from 3º to 40º in the same conditions than the powder patterns. Basal spacing reflections were measured using the DRXWin® software (vs. 2.3.22. V. Primo ©).

Tab. C-12: Mineralogical characterisation by XRD (total sample).

Sample	Slice	Coord. X (cm)	Coord. Y (cm)	Coord. Z (cm)	% wt.	% wt.	% wt.	% wt.	% wt.	% wt.	% wt.	% wt.	% wt.	% wt.	% wt.	% wt.	% wt.	% wt.	% wt.	% wt.	% wt.	% wt.	% wt.	
					Crs	Mnt	Or	Pl	Cal	Qtz	Ilt	Ab	Gp	-TRI	7-7.5Å	C-(A)-S-H*	Crd/ Amp	Clc	Ms	Bt	Etr	Port	Obs.
C-C-34-8	C	-6.1	41	53	-	-	9	-	13	25	-	29	-	-	-	-	1	8	4	4	6	-	
	C04	-2.3	41	53	-	-	6	-	10	31	-	33	-	-	-	2	1	7	3	3	4	-	
	C03	-1.3	41	53	-	-	7	-	8	31	-	35	-	-	-	6	1	6	4	3	-	-	
	C02	-0.8	41	53	-	-	6	-	9	27	-	37	-	-	-	3	1	6	4	3	5	-	
	C01	-0.3	41	53	0.5	-	6	-	12	31	-	27	3	-	-	6	-	6	3	3	2	1	
	IC	-0.1	41	53	-	1	4	-	12	28	-	25	5	0.5	-	10	1	4	3	2	-	1	13-12
	IB	0.1	41	53	1	30	2	31	7	17	1	31	-	1	4	5	-	-	-	-	-	-	
	B01	0.2	41	53	1	54	1	12	8	7	1	0.5	-	14	0.5	2	-	-	-	-	-	-	
	B02	0.7	41	53	-	79	-	6	8	2	-	-	-	2	0.5	1	-	-	-	-	-	-	
	B03	1.2	41	53	-	79	-	14	1	3	1	-	-	-	1	-	-	-	-	-	-	-	
	B	6.4	41	53	1	86	1	5	4	3	-	-	-	-	-	-	-	-	-	-	-	-	3.14
C-C-34-10	C	-8.8	62	88	-	-	6	-	13	33	-	25	-	-	-	-	-	8	3	4	8	-	
	C04	-3.9	62	88	-	-	6	-	10	30	-	30	-	-	-	-	1	9	3	3	9	-	
	C03	-2	62	88	-	-	7	-	11	28	-	30	-	-	-	-	1	8	3	3	8	-	
	C02	-0.8	62	88	-	-	6	-	9	35	-	29	-	-	-	-	1	7	3	3	8	-	
	C01	-0.3	62	88	0.5	-	6	-	12	35	-	27	0.5	-	-	0.5	-	5	2	2	11	0.5	3.08

Sample	Slice	Coord. X (cm)	Coord. Y (cm)	Coord. Z (cm)	% wt.	% wt.	% wt.	% wt.	% wt.	% wt.	% wt.	% wt.	% wt.	% wt.	% wt.	% wt.	% wt.	% wt.	% wt.	% wt.	% wt.	% wt.	
					Crs	Mnt	Or	Pl	Cal	Qtz	Ilt	Ab	Gp	-TRI	7-7.5Å	C-(A)-S-H*	Crd/ Amp	Clc	Ms	Bt	Etr	Port	Obs.
	IC	-0.1	62	88	2	10	5	-	13	26	-	21	0.5	7	0.5	7	-	3	2	1	1	-	3.08
	IB	0.1	62	88	2	80	-	2	1	4	1	-	0.5	10	0.5	1	-	-	-	-	-	-	
	B01	0.2	62	88	2	86	-	6	2	3	1	-	-	-	-	-	-	-	-	-	-	-	
	B02	0.7	62	88	1	82	1	6	3	4	1	-	-	-	-	-	-	-	-	-	-	-	
	B03	1.2	62	88	-	88	0.5	4	2	5	-	-	-	-	-	-	-	-	-	-	-	-	
	B	2.3	62	88	1	85	1	5	1	4	-	-	-	-	-	-	-	-	-	-	-	-	
C-C-34-12	C	-4.4	-31	-62	-	-	6	-	10	29	-	20	-	-	-	6	2	10	4	3	8	-	
	C03	-2.7	-31	-62	-	-	6	-	10	29	-	26	-	-	-	-	1	10	3	3	13	-	
	C02	-1.2	-31	-62	-	-	6	-	9	28	-	20	-	-	-	6	1	8	3	3	11	-	
	C01	-0.3	-31	-62	-	-	4	-	12	34	-	24	-	-	-	13	1	4	2	2	3	1	
	IC	-0.1	-31	-62	1	21	2	0.5	18	21	0.5	12	-	12	0.5	6	1	1	1	1	2	-	13-dic
	IB	0.1	-31	-62	6	59	2	4	6	6	1	-	0.5	16	0.5	1	-	-	-	-	-	-	
	B01	0.2	-31	-62	1	84	1	1	3	1	1	-	0.5	9	0.5	-	-	-	-	-	-	-	
	B02	0.7	-31	-62	1	89	1	4	2	3	-	0.5	-	-	-	-	-	-	-	-	-	-	3.13
	B03	1.2	-31	-62	1	91	-	3	1	2	-	-	-	0.5	-	-	-	-	-	-	-	-	
	B04	1.3	-31	-62	1	83	-	5	4	4	2	0.5	-	-	0.5	-	-	-	-	-	-	-	2.84
	B	2.9	-31	-62	1	91	-	3	1	3	1	-	-	-	-	-	-	-	-	-	-	-	

Sample	Slice	Coord. X (cm)	Coord. Y (cm)	Coord. Z (cm)	% wt.	% wt.	% wt.	% wt.	% wt.	% wt.	% wt.	% wt.	% wt.	% wt.	% wt.	% wt.	% wt.	% wt.	% wt.	% wt.	% wt.	% wt.	
					Crs	Mnt	Or	Pl	Cal	Qtz	Ilt	Ab	Gp	-TRI	7-7.5Å	C-(A)-S-H*	Crd/ Amp	Clc	Ms	Bt	Etr	Port	Obs.
BC-C-35-1	C	-4.5	13	88	-	-	6	-	18	29	-	25	0.5	-	-	-	-	7	4	3	7	-	
	C04	-2.5	13	88	-	-	8	-	20	17	-	31	-	-	-	-	1	8	4	3	5	3	
	C03	-1.3	13	88	-	-	4	-	12	29	-	28	-	-	-	-	1	8	4	4	5	5	
	C02	-0.8	13	88	-	-	3	-	9	26	-	25	1	-	-	10	1	6	3	3	7	5	
	C01	-0.3	13	88	-	-	7	-	9	26	-	30	0.5	-	-	8	1	4	4	2	4	4	
	C01’	-0.3	-	-	-	-	7	-	9	22	-	36	2	-	-	12	1	4	4	3	-	-	
	C01’’**	-0.3	-	-	-	-	5	-	9	21	-	37	2	-	-	14	0.5	2	4	2	-	-	
	IC	-0.25	13	88	-	-	2	-	6	26	-	47	1	0.5	-	11	3	-	1	1	2	0.5	
	IC’	-0.2			-	21	1	0.5	10	7	0.5	16	5	19	-	18	-	1	1	-	-	-	13-dic
	IC’’	-0.1			1	40	1	0.5	11	12	0.5	9	2	9	-	12	-	2	-	1	-	-	
	IB	0.1	13	88	1	63	1	18	6	3	1	10	2	4	1	0.5	-	-	-	-	-	-	3.19
	B01	0.2	13	88	1	92	-	3	1	2	-	-	0.5	-	-	0.5	-	-	-	-	-	-	
	B02	0.7	13	88	1	90	-	4	2	3	-	-	-	0.5	0.5	-	-	-	-	-	-	-	
	B03	1.2	13	88	1	89	-	5	2	3	-	-	-	-	-	-	-	-	-	-	-	-	
	B	3.4	13	88	1	91	-	3	1	3	1	-	-	-	-	-	-	-	-	-	-	-	3.22
BC-C-35-2	C	-4.5	-162	-91	-	-	7	-	7	25	-	38	-	-	-	-	1	7	4	4	3	5	
	C04	-2.5	-162	-91	-	-	7	-	6	25	-	33	-	-	-	3	1	7	4	3	6	4	

Sample	Slice	Coord. X (cm)	Coord. Y (cm)	Coord. Z (cm)	% wt.	% wt.	% wt.	% wt.	% wt.	% wt.	% wt.	% wt.	% wt.	% wt.	% wt.	% wt.	% wt.	% wt.	% wt.	% wt.	% wt.	% wt.	
					Crs	Mnt	Or	Pl	Cal	Qtz	Ilt	Ab	Gp	-TRI	7-7.5Å	C-(A)-S-H*	Crd/ Amp	Clc	Ms	Bt	Etr	Port	Obs.
	C03	-1.3	-162	-91	-	-	3	-	8	29	-	43	-	-	-	-	1	5	4	3	-	5	
	C02	-0.8	-162	-91	-	-	10	-	9	30	-	33	-	-	-	-	1	8	3	3	4	-	
	C01	-0.3	-162	-91	0.5	-	8	-	8	33	-	39	-	-	-	-	0.5	5	3	2	2	0.5	
	IC	-0.1	-162	-91	1	8	6	0.5	10	17	0.5	41	-	2	-	2	-	2	2	3	1	0.5	13-dic
	IB	0.1	-162	-91	1	30	2	31	7	17	1	17	-	1	4	5	-	-	-	-	-	-	10.8, 1.51
	B01	0.2	-162	-91	1	54	1	12	8	7	1	0.5	-	14	0.5	2	-	-	-	-	-	-	
	B02	0.7	-162	-91	-	79	-	6	8	2	-	-	-	2	0.5	1	-	-	-	-	-	-	3.13
	B03	1.2	-162	-91	-	79	-	14	1	3	1	-	-	-	1	-	-	-	-	-	-	-	
	B	3.4	-162	-91	1	86	1	5	4	3	-	-	-	-	-	-	-	-	-	-	-	-	3.14
BC-S-35-3	C	-12.1	-62	66	-	-	8	-	8	29	-	34	-			-	2	7	2	2	5	3	
	C05	-5.6	-62	66	-	-	3	-	5	20	-	57	-	-	-	-	1	4	2	2	3	3	
	C04	-4.8	-62	66	-	-	16	-	5	24	-	40	-	-	-	-	1	4	3	3	4	-	
	C03	-3.7	-62	66	-	-	9	-	7	23	-	45	-	-	-	-	1	6	3	2	4	-	
	C02	-2.3	-62	66	-	-	9	-	6	17	-	48	-	-	-	-	1	8	3	2	5	2	
	C01	-0.7	-62	66	0.5	-	11	-	6	32	-	36	-	-	-	1	-	5	4	2	2	0.5	7.9
	IB	0.1	-62	66	1	54	-	4	6	6	1	0.5	0.5	21	0.5	4	-	1	-	-	-	-	
	B01	0.25	-62	66	0.5	78	5	7	3	4	0.5	0.5	-	1	-	1	-	-	-	-	-	-	11.4, 10.4, 9
	B02	0.6	-62	66	0.5	80	1	5	10	3	0.5	0.5	-	-	0.5	-	-	-	-	-	-	-	

Sample	Slice	Coord. X (cm)	Coord. Y (cm)	Coord. Z (cm)	% wt.	% wt.	% wt.	% wt.	% wt.	% wt.	% wt.	% wt.	% wt.	% wt.	% wt.	% wt.	% wt.	% wt.	% wt.	% wt.	% wt.	% wt.	
					Crs	Mnt	Or	Pl	Cal	Qtz	Ilt	Ab	Gp	-TRI	7-7.5Å	C-(A)-S-H*	Crd/ Amp	Clc	Ms	Bt	Etr	Port	Obs.
	B03	1	-62	66	1	88	1	4	5	2	0.5	-	-	-	0.5	-	-	-	-	-	-	-	
	B04	1.45	-62	66	0.5	87	1	6	3	2	0.5	-	-	-	-	-	-	-	-	-	-	-	3.01
	B05	2.2	-62	66	1	82	1	5	9	4	0.5	-	-	-	-	-	-	-	-	-	-	-	
	B06	3.2	-62	66	1	93	-	2	2	2	-	-	-	-	-	-	-	-	-	-	-	-	
	B07	4.2	-62	66	-	90	1	6	1	2	0.5	0.5	-	-	-	-	0.5	-	-	-	-	-	
	B	5.7	-62	66	1	90	1	2	2	4	0.5	-	-	-	-	-	-	-	-	-	-	-	

Crs: Cristobalite; Mnt: montmorillonite; Or: Orthoclase (also microcline in concrete slices); Pl: plagioclase (andesine); Cal: calcite; Qtz: quartz; Ilt: illite (referenced to muscovite PDF standard); Ab: albite; Gp: gypsum (below 1 wt.% is marked at 0.5, (-) absence of reflection at 7.6 Å); -TRI: trioctahedral smectite referenced to the 1.53-1.52 Å reflection of saponite (RIR = Mnt); 7-7.5Å: (-) indicates absence of this reflection, which may confirm intercalation of brucite in montmorillonite or possible chrysotile (Cuevas et al., 2013), and C-(A)-S-H: wide reflections at 11-11.5 Å and 3.08-3.04 Å indicative of Al tobermorite-clinotobermorite in bentonitic material (Fernández et al., 2014), (*) 9Å tobermorite C-S-H phase has been used for quantification by adjusting the scale of the 3.04 shoulder in the 3.03 calcite peak, both in concrete or in bentonite at the interface (Chapter 6.3 of main text); Clc: Clinochlore, Ms: Muscovite, Bt: Biotite, Crd/Amp: Cordierite/amphibole group, Etr: Ettringite, Port = Portlandite; (**), in BC-C-35-1, several scraps were obtained for fragmented separate concrete interfaces. It contained varied amount of bentonitic material indicative of increasing depths of bentonite.

Tab. C-13: Results for Thermal analysis (TA). Temperature maxima for weight loss and thermogravimetric (TG) data within several temperature intervals (UAM data).

Sample	Subsample	Coord.	Coord.	Coord.	T. maximum (°C)											% wt loss				Total wt%
		X (cm)	Y (cm)	Z (cm)	1	2			3	4	5	6	7	8		25-300	300-500	500-800	800-1000	
CC-34-8	C	-6.1	41	53	nd	nd	nd	nd	nd	nd	nd	nd	nd	nd	nd	nd	nd	nd	nd	nd
	C01	-0.3	41	53	60	108	-	-	-	-	576	702	768	-	-	4.91	1.38	9.84	0.40	16.53
	B01	2.0	41	53	nd	nd	nd	nd	nd	nd	nd	nd	nd	nd	nd	nd	nd	nd	nd	nd
	B	6.4	41	53	nd	nd	nd	nd	nd	nd	nd	nd	nd	nd	nd	nd	nd	nd	nd	nd
CC-34-10	C01	-0.3	62	88	80	191	-	-	368	-	-	685	792	-	-	10.03	2.18	5.54	1.16	18.91
	B01	0.2	62	88	61	133	-	-	-	-	**489**	614	-	-	-	10.87	1.90	3.31	0.00	16.08
	B	2.3	62	88	67	136	-	-	-	-	563	-	-	835	-	12.17	1.33	2.87	0.03	16.40
CC-34-12	C01	-0.3	-31	-62	59	134	-	283	-	418	505	732	785	-	-	3.93	1.69	12.78	0.40	18.80
	B01	0.2	-31	-62	72	135	-	-	-		**490**	620	758	818	-	11.68	2.11	4.02	0.04	17.85
	B	2.9	-31	-62	75	136	-	-	-	407	-	617	-		-	12.58	1.35	2.96	0.00	16.89
BC-C35-1	C01	-0.3	13	88	68	134	-	-	-	-	556	703	-		-	5.04	1.41	9.46	0.31	16.22
	B01	0.2	13	88	67	140	-	-	-	-	485	610	-	861	-	13.17	1.41	3.06	0.05	17.69
	B	3.4	13	88	69	132	-	-	-	-	-	613	-	961	-	14.57	1.25	3.02	0.00	18.84
BC-C35-2	C01	-0.3	-162	-91	67		-	-		400	560	687	-	852	-	4.15	1.45	4.33	0.53	10.46
	B01	0.2	-162	-91	64	124	-	-			**489**	625	729	-	-	10.40	2.07	4.42	0.00	16.89
	B	3.4	-162	-91	67	132	-	-	-		-	612	750	-	-	12.37	1.23	3.20	0.00	16.80
BC-C-35-3	C	-12.1	-62	66	69	119	199	266	379		492	708		887	-	6.69	2.88	6.68	1.16	17.41
	C05	-6.2	-62	66	67	108	-	-	-	405	526	682	745	-	891	5.31	1.60	4.27	0.78	11.96

Sample	Subsample	Coord.	Coord.	Coord.	T. maximum (°C)											% wt loss				Total wt%
		X (cm)	Y (cm)	Z (cm)	1	2			3	4	5	6	7	8		25-300	300-500	500-800	800-1000	
	C04	-5.4	-62	66	76	109	154	-	367	444	532	656	744	840	920	3.22	1.21	2.78	0.74	7.95
	C03	-4.3	-62	66	64	108	-	-	368		499	678	-	800	-	5.25	1.36	4.11	0.81	11.53
	C02	-3.0	-62	66	63	97	295	349	394	454	559	673	756	809	-	3.12	0.92	3.53	0.47	8.04
	C01	-0.7	-62	66	70	110	206	-	-	405	564	670	756	890	-	5.92	1.81	4.19	0.71	12.63
	IB	0.1	-62	66	nd	nd	nd	nd	nd	nd	nd	nd	nd	nd	nd	nd	nd	nd	nd	nd
	B01	0.3	-62	66	64	120		-	-	**489**	-	609	-	808	-	9.21	2.15	3.81	0.00	15.17
	B02	0.6	-62	66	66	122		-	-	**482**	-	609	-	821	-	9.56	1.97	3.50	0.03	15.06
	B	5.7	-62	66	68	128		-		497	-	627	779	-	-	8.65	4.07	4.37	0.29	17.38
	Febex				68	136		-	-	-	-	621	757	860	-	12.87	1.21	3.05	0.00	17.13

Note: numbered T maximum are the corresponding maximum found in concrete materials (see Appendix A, part A.I.4, Tab.9). Values in bold letter are significant TG peaks in bentonite. Sometimes concrete exhibit the 490 °C maximum peak with low relevance.

C.6 X-ray diffraction

Results of the reference material (BGR)

The carbonate content of the "reference material" based on XRD Rietveld analysis (calcite 1 mass%) is in good agreement with the LECO data (0.1 mass% C which equals 0.8-0.9 % calcite). The evolved gas analysis of thermally induced gases indicated the presence of at least traces of a sulphate mineral, sulfide minerals could not be identified (< 0.01 mass%). The K_2O content can be explained by 5 % K-feldspar resulting in about 0.85 mass% K_2O and some exchangeable K^+ of the smectite (about 0.14 mass% K_2O). No K is available for illitic layers in a hypothetic interstratified mineral. Instead FEBEX bentonite as used in the ABM test in Äspö contains smectite with different hydration states when analysed in air-dry conditions. This can be described as a kind of interstratification of smectite with different water layers. Ferrage et al. (2005) demonstrated that the coexistence of different hydration states is a common phenomenon in smectites. Overall the chemical data confirm the mineralogical composition determined by Rietveld analysis. The quantitative mineralogical composition is given in Tab. C-8. The results are in good agreement with those published by Nagra (NAB 13-096) except for the different feldspar contents. BGR Rietveld refinement yielded 14 mass % feldspar while about 3 mass % were reported in previous studies.

The mineralogical composition as determined by Rietveld analysis could be slightly modified based on chemical data but the data was used as it is because for Rietveld refinement the same parameters were used for all samples. This is the prerequisite for a possible identification of differences of samples based on quantitative XRD.

Tab. C-14: Mineralogical composition of the ABM references.

	Febex REF (ABM) [mass%]
quartz	1
K-fsp	5
smectite	84
plagioclase	9
calcite	1
sum	100